# RAMAN SPECTROSCOPIC INVESTIGATION ON ELECTROCHEMICAL ENERGY STORAGE FOR PSEUDO-CAPACITORS AND LI-ION BATTERIES

A Dissertation

Presented to

The Academic Faculty

By

Dongchang Chen

In Partial Fulfilment

of the Requirements for the Degree

Doctorate of Philosophy in the

School of Chemistry and Biochemistry

Georgia Institute of Technology

May 2017

# RAMAN SPECTROSCOPIC INVESTIGATION ON ELECTROCHEMICAL ENERGY STORAGE FOR PSEUDO-CAPACITORS AND LI-ION BATTERIES

Approved by:

Dr. Meilin Liu, Advisor
School of Materials Science and Engineering
*Georgia Institute of Technology*

Dr. Mostafa A. El-Sayed, Advisor
School of Chemistry and Biochemistry
*Georgia Institute of Technology*

Dr. Angus P. Wilkinson
School of Chemistry and Biochemistry
*Georgia Institute of Technology*

Dr. John Z. Zhang
School of Chemistry and Biochemistry
*Georgia Institute of Technology*

Dr. Gleb Yushin
School of Materials Science and Engineering
*Georgia Institute of Technology*

Date Approved: [Jan 11th, 2017]

This dissertation is dedicated to my parents and my beloved. Thank you for your love and encouragement.

# ACKNOWLEDGEMENTS

First of all, I would like to express my deepest appreciation to my advisor, Dr. Meilin Liu, for his guidance and financial support on my research as well as being the principal guiding teacher during my doctoral study. I would also like to extend my deepest gratitude to my co-advisor, Dr. Mostafa A. El-Sayed, for providing me with the opportunity to learn and practice in the Laser Dynamic Laboratory. Moreover, I would like to acknowledge my undergraduate advisors, Drs. Shuiming Hu, Anwen Liu, and Zude Zhang, all of whom exposed me to the world of chemistry and physics.

Also, I would like to extend my sincere thanks to my thesis committee members: Drs. Angus Wilkinson, John Zhang, and Gleb Yushin. Their knowledge and critical feedback greatly improved the consistency of my work. During my first year of PhD study, Drs. Angus Wilkinson, John Zhang, Zhonglin Wang, and Larry Bottomley greatly enriched my knowledge of crystallography, electrochemistry, and physical characterization. Knowledge from their lectures played a critical role in formulating my research. I really appreciate their great instruction.

Moreover, I would like to express my appreciation to my collaborators and colleagues. My colleagues Mingfei Liu, Dong Ding, Kevin Blinn, Xiaxi Li, Jung-pil Lee, Samson Lai, Gordon Waller, Yu Chen, Ben Rainwater, Liang Huang, Yong Qin, Xunhui Xiong, Renzong Hu, Bote Zhao, and Lei Zhang offered generous help, shared their strong expertise, and had numerous fruitful discussions with me, which were very important to the progress of my research. In the Laser Dynamic Laboratory, Dr. Mahmoud offered considerable assistance to me in the part of plasmonic material research as well as other aspects of spectroscopy, which were extremely helpful. Outside of Georgia Tech, Dr. Jeng-

Han Wang and Tsung-Fu Chou offered me tremendous help on theoretical vibrational calculations and relevant knowledge. Their theoretical backup was critical for the consistency of my experimental vibrational analyses.

Finally, I would like to thank the graduate program of the School of Chemistry and Biochemistry and the School of Materials Science and Engineering at Georgia Tech. They offered this invaluable opportunity for me to study abroad and to pursuit my goal in the United States.

# TABLE OF CONTENTS

Page

# LIST OF TABLES

# LIST OF FIGURES

# LIST OF ABBREVIATIONS AND SYMBOLS

| | |
|---|---|
| $a$ | Coefficient for irreducible representation and Activity |
| $c$ | Concentration |
| $C$ | Capacitance |
| CE | Counter electrode |
| CV | Cyclic voltammetry |
| $D$ | Diffusion constant |
| DOF | Degree of freedom |
| DFT | Density functional theory |
| DMC | Dimethyl carbonate |
| $E$ | Energy, Potential, and Electric field strength |
| $E_a$ | Activation energy |
| EC | Ethylene carbonate |
| EDLC | Electrochemical double layer capacitance |
| $F$ | Faradaic constant |
| FWHM | Full width half maximum |
| G | Gibbs free energy |
| GGA | Generalized Gradient Approximation |
| $h$ and $\hbar$ | Planck Constant and Reduced Planck constant |
| $H$ | Hamiltonian |
| $I$ | Current density and Intensity |
| $i$ *and* $j$ | Current density |
| $k$ | Photon wavefront |
| $k_B$ | Boltzmann constant |
| LSPR | Localized surface Plasmon resonance |
| $n$ | Quantum number |
| $p$ | Momentum |
| $P$ | Polarization |
| $q$ | Phonon wavefront |
| $Q$ | Normal coordinate and Charge |
| RE | Reference electrode |

| | |
|---|---|
| SEM | Scanning electron microscopy |
| SERS | Surface enhanced Raman spectroscopy |
| TEM | Transmission electron microscopy |
| $u$ | ion mobility |
| $v$ | Scan rate |
| WE | Working electrode |
| XAS | X-Ray absorption spectroscopy |
| XRD | X-ray diffraction |
| $Z$ | Impedance |
| $\alpha$ | Polarizability |
| $\Gamma$ | Representation |
| $\varphi$ | Phase angle |
| $\lambda$ | Wavelength |
| $\sigma$ | Conductivity |
| $\chi$ | Character for irreducible representation |
| $\Psi$ | Wave function |
| $v$ and $\omega$ | Frequency and Angular Frequency |

# SUMMARY

Electrochemical energy storage devices, such as batteries and pseudocapacitors, are the most promising power supply for many emerging technologies, from portable electronics to electrical vehicles and smart grids. While incremental progress in performance of these devices has been made in recent years, dramatic advancement is hindered by the lack of a profound understanding of the atomic level energy storage mechanism of Li-ion batteries and pseudocapacitors. This dissertation carries out a series of fundamental mechanism studies for a few important electrode materials of Li-ion batteries and supercapacitors using *in operando* Raman spectroscopy. This study revealed the detailed structural changes of electrode materials during energy storage from the evolution of vibrational structures as a function of electrochemical operations. To better explain this rationale, this dissertation discusses briefly the fundamental concepts and principles, including electrochemistry, Raman spectroscopy, and *in operando* configurations as well as basic experimental setups, prior to the chapters of detailed research results. The first material studied in this dissertation is layered manganese oxide ($MnO_2$), the most characteristic pseudocapacitive material. The cation size effects observed in the *in operando* Raman evolution of $MnO_2$ clearly proved the interlayer cation storage mechanism. Secondly, the dissertation also probed the energy storage of layered nickel hydroxide/oxo-hydroxide ($NiO_2H_x$), which has a structure similar to that of layered $MnO_2$ and features the transitional electrochemical behavior between the pseudocapacitor and the battery with very high energy density. Correlations between Raman spectroscopic evolution and electrochemical behavior proved that the break/formation of O-H bonds in $NiO_2H_x$ contribute to the electrochemical energy storage primarily while cation

incorporation between $NiO_2H_x$ layers plays a minor role. Thirdly, this dissertation investigated the mechanism of energy storage of T-$Nb_2O_5$, which can store Li ions at an exceptionally fast rate similar to a capacitor. Through a comparison between *in operando* Raman spectroscopic evolution and a theoretical calculation of the vibrational structure of the proposed model, it is found that Li ions are preferably stored on the 2D voids of Nb-O bonding facets similar to the surface-bound capacitive behavior, which unravels the Li-ion incorporation mechanism responsible for fast energy storage. In addition to the research results, a few recommendations are provided about more aspects of energy storage/conversion mechanisms, the application of advanced Raman spectroscopy, and the advanced *in operando* mechanism analyses.

The research work described in this dissertation has contributed significant new discoveries for fundamental chemistry and physics relevant to energy science. Moreover, information about mechanisms unraveled in this dissertation can be helpful for rational design of material structures and compositions for unique functionalities, which will ultimately contribute to engineering developments in the energy storage industry. Finally, the general methodology of this dissertation can be readily applied to other research fields to probe the correlation between external functionalities and intrinsic properties of materials.

# 1. INTRODUCTION

## 1.1. Motivation

The world has an extremely urgent demand for efficient and reliable mobile electrical energy storage systems. Undoubtedly, the most critical aspect of this demand is for transportation. Currently, not only transportation, but also a large portion of the stationary electrical power supply (e.g., household and commercial), heavily rely on fossil fuels, which are being consumed at an astounding rate worldwide.[1] Besides this critical fact, the consumption of fossil fuels (coal, oil, and natural gases) generates a massive amount of greenhouse gases and pollutants that are irreversibly destroying the global environment.[2-4] In the past few decades, electricity generated by renewable energy (wind, water, and solar) has been progressively replacing that by fossil fuels for household and commercial electrical power supply.[5-7] However, for transportation, completely replacing fossil fuel is a significant challenge since the electrical energy generated by renewable sources needs to be effectively stored. Besides the demand from transportation, other vital fields, such as portable electronic devices, also strongly rely on portable electrical energy storage. Therefore, as efficient and reliable mobile electrical energy storage systems are urgently needed,[8-10] research and development of electrical energy storage systems is one of the most important topics of modern industry.

The most realistic method of meeting the demand of mobile electrical energy storage is to store electrical energy electrochemically. Remarkable progress in the development of electrochemical energy storage has taken place in the applications of rechargeable batteries (i.e., secondary batteries). Since the discovery of the first

rechargeable battery (lead-acid) in 1859, various types of rechargeable batteries have been developed and applied to various areas.[11,12] As the most promising batteries, Li-ion batteries, which were developed in 1980s,[13-15] have substantial advantages over the other types of batteries developed earlier and have been proven highly successful.[16-18] Currently, Li-ion batteries are the most likely candidate to totally replace internal combustion engines for vehicles and the major power sources for portable electronics.[16-21] Besides Li-ion batteries, supercapacitors, including electrochemical double layer capacitors and pseudocapacitors, which were developed in the 1980s, are another type of promising electrical energy storage device.[22-27] Supercapacitors could deliver much higher power density than most batteries and much higher energy density than conventional capacitors.[23,25] Owing to these unique features, supercapacitors could be applied to power components requiring many rapid charge/discharge cycles.[22,25] In recent years, numerous types of novel materials have been developed as electrode materials for Li-ion batteries and supercapacitors. The performance of electrical energy storage is progressively improving, in terms of energy density, power density, cycling life, lower cost, and safety as well as the prevention of self-discharge and the memory effect.

However, for a large number of discoveries of electrode materials for Li-ion batteries and supercapacitors in recent years, the performance of electrical energy storage has not been comprehensively enhanced for all aspects.[18,28] It has often been found that although a few aspects of performance have been significantly enhanced (most likely capacity or energy density), a few other aspects of performance have been compromised (e.g., safety and cost), Thus, many novel materials invented in recent years cannot be widely applied on a large scale. For example, early Li-ion battery materials developed in

the 1980s and the 1990s (i.e., $LiCoO_2$ and its derivatives, $LiMn_2O_4$, $LiFePO_4$ with graphite anodes) still contribute to a vast majority of commercially available Li-ion batteries.[10,21,29,30] Thus, energy storage systems (e.g., for electrical vehicles and portable electronics) powered by Li-ion batteries and supercapacitors are relatively expensive (~300-500 USD/kWh for Li-ion batteries, more expensive for supercapacitors).[10,29,30] Therefore, because of the absence of new Li-ion battery and supercapacitor materials with comprehensive enhancement on all aspects of performance, the energy storage industry has not been subject to revolutionary progress, such as the replacement of internal combustion engines with cheap and reliable battery/capacitor-powered engines.

The stagnant development of Li-ion battery and supercapacitor materials mentioned above is solely because most of the research related to novel materials is based on trial-and-error iterative experiments without rational design. Designing a material is very challenging and needs to be guided by certain principles. The key to obtaining these vital principles is the systematic understanding of the mechanism of electrochemical energy storage for Li-ion batteries and supercapacitors. From a scientific perspective, understanding the mechanisms of energy storage is an important topic for fundamental physical science research. More importantly, fundamentally understanding these mechanisms is vital to the development of the new-generation of electrochemical energy storage material, which is the key to revolutionizing the industry of energy storage.

## 1.2. Research objectives

Research on the electrochemical energy storage mechanisms need an efficient physiochemical method is needed to unravel the structural features caused by energy storage. Among all physiochemical methods, Raman spectroscopy is very efficient for

probing the details of materials by revealing material features from vibrational spectroscopy.[31-35] In the past few decades, the application of Raman spectroscopy in the field of physical science has proven extremely successful.[36-39] Moreover, a combination of Raman spectroscopy with a real-time probing configuration (*in situ* and *in operando*) further enhances capabilities of Raman spectroscopy to probe material properties as a function of time. Owing to these strong capabilities, Raman spectroscopy could be a critical tool for probing the structural details of supercapacitor and Li-ion battery materials, thus providing vital information about energy storage mechanisms.

The objective of this dissertation is to understand the mechanism of energy storage for a few important supercapacitor and Li-ion battery materials using Raman spectroscopy. In particular, this study will combine *in operando* techniques with Raman spectroscopy to reveal the dynamics of structural changes during electrochemical operations. The research topics in this dissertation include the pseudocapacitive energy storage mechanism of layer-structured $MnO_2$, the electrochemical energy storage mechanism of $NiO_2H_x$, and the ultrafast Li ion storage mechanism of T-$Nb_2O_5$. All of these materials are promising candidates for the new-generation of electrical energy storage. Further chapters will discuss the detailed properties of each type of material and the rationale of mechanism studies.

## 1.3. Dissertation structure

Chapter 1 briefly introduces the motivation of the dissertation and explains the urgent demand for cheap and reliable electrochemical energy storage devices and the importance of mechanism study for electrochemical energy storage. It also includes the general research objectives of this dissertation. Chapter 2 introduces the theoretical backgrounds and principles vitally needed in this dissertation. It emphasizes the physical

concepts and the principles of their physical meanings without complicated algebra. The first part of the chapter explains fundamental electrochemistry and electrochemical energy storage. The second part briefly introduces the concepts and principles of Raman spectroscopy, and the third part briefly introduces the concepts of *in operando* Raman spectroscopy, which is vital for this dissertation. Chapter 3 introduces basic experimental configurations for electrochemical tests, Raman spectroscopic tests, and *in operando* Raman configurations. Other types of experiments such as sample preparations and electron microscopic tests, which are not systematically used, will be mentioned in other chapters.

Chapter 4 describes the study of the charge storage mechanism of pseudocapacitive $MnO_2$. This chapter will elaborate the rationale of the study by the background introduction of $MnO_2$-based pseudocapacitors, the experimental approaches, cation size effects on spectroscopic analyses, theoretical calculations, mechanism information, and a few insights on rational design. This chapter uses excerpts from the following paper[40]: Chen, D., Ding, D., Li, X., Waller, G. H., Xiong, X., El-Sayed, M. A., Liu, M., "Probing the charge storage mechanism of a pseudocapacitive $MnO_2$ electrode using *in operando* Raman spectroscopy ", *Chem. Mater.* **2015,** 27, 6608-6619. Chapter 5 describes the study of the charge storage mechanism of $NiO_2H_x$. This chapter will elaborate the rationale of the study by the background introduction of $NiO_2H_x$-based electrochemical energy storage, experimental approaches, spectroscopic evolution as a function of electrolyte properties, and obtained mechanism information. This chapter uses excerpts from the following paper[41]: Chen, D., Xiong, X., Zhao, B., Mahmoud, M. A., El-Sayed, M. A., Liu, M., "Probing Structural Evolution and Charge Storage Mechanism of $NiO_2H_x$ Electrode

Materials using *In Operando* Resonance Raman Spectroscopy ", *Advanced Science* **2016,** 3, 1500433.

Chapter 6 describes the study of the ultrafast Li ion storage mechanism of T-$Nb_2O_5$. This chapter will elaborate the rationale by an introduction of the exceptionally fast Li ion storage behavior of T-$Nb_2O_5$, sample preparation, *in operando* spectroscopic analyses, the model of Li ion incorporation, theoretical calculations of vibrational properties, conclusions on Li ion storage mechanism of T-$Nb_2O_5$, and insights on rational design. This chapter uses excerpts from a paper (unpublished as of Jan 13$^{th}$ 2017):[42] Dongchang Chen, Jeng-Han Wang, Tsung-Fu Chou, Mostafa A. El-Sayed, Meilin Liu, "Unraveling the nature of anomalously fast energy storage in T-$Nb_2O_5$". Chapter 7 briefly concludes the research results of this dissertation and presents recommendations about more aspects of energy storage/conversion mechanism studies, applications of advanced Raman spectroscopy, and advanced *in operando* mechanism probing techniques.

# 2. FUNDAMENTAL PRINCIPLES

## 2.1. Fundamentals of electrochemistry

### 2.1.1. Basic thermodynamic concepts

Electrochemistry describes the fundamental rules about the relationship between redox chemical reactions, chemical energies associated with the redox chemical reactions, and electricity.[43] Despite the variety of emerged electrochemical energy storage or energy conversion systems, the fundamental principles of these systems are solely based on electrochemistry. In this section, the basic aspects of thermodynamics of electrochemistry will be discussed.

A reduction-oxidation (redox) reaction is defined as a chemical process, during which an electron transfer is occurred. The result of the redox reaction is that the oxidation states of elements change. Generally, a redox reaction can be expressed as the equation below:

$$\mathrm{Ox}_1 + \mathrm{Red}_1 \leftrightarrow \mathrm{Ox}_2 + \mathrm{Red}_2 \ . \tag{1}$$

In this equation, $\mathrm{Ox}_1$ is the oxidizing agent, which is the acceptor of electrons. The product corresponding to the oxidizing agent is $\mathrm{Red}_2$. Similarly, $\mathrm{Red}_1$ is a reducing agent, which is the donor of electrons. The product corresponding to the reducing agent is $\mathrm{Ox}_2$. Theoretically, any reactions involving the transfer of redox reaction can be realized by an electrochemical cell. In an electrochemical cell, the chemical energy can be transformed into electrical energy. The Gibbs free energy ($\Delta G$) of the redox reaction can be expressed in the form of an electrochemical cell potential ($E$):

$$\Delta G = -nFE \ . \tag{2}$$

In this equation, $n$ is the number of electrons involved in the redox reaction; $F$ is the Faradaic constant, which is the amount of charge of one mole of electrons:

$$F = eN_A = 96485\,C/mol \quad . \tag{3}$$

On the basis of an electrochemical cell, the redox reaction can be separated into two half reactions in terms of electrochemistry. Each half redox reaction is processed at separated electrodes. The electrode material is mostly in the solid state. The reactants on each electrode can be in the solid, liquid, or gaseous phase. To generate a current flow from the electrochemical reaction on each half cell, the cathode and the anode are separated by an electrolyte, which is ionically conductive. The electrolyte can be in the form of a solution, an ionic liquid, a gel, a solid state, or other forms. The process in which the gain of electrons occurs is the cathodic reaction:

$$\mathrm{Ox}_1 + ne^- \rightarrow \mathrm{Red}_2 \quad . \tag{4}$$

The corresponding electrode is a cathode. The process in which the loss of electrons occurs is the anodic reaction:

$$\mathrm{Red}_1 - ne^- \rightarrow \mathrm{Ox}_2 \quad . \tag{5}$$

The corresponding electrode is an anode. Each half reaction has an associated equilibrium electrochemical potential. The value of the potential is determined by the Nernst equation. For a the half redox reaction (equation (4)), the Nernst equation is

$$E = E^0 + \frac{RT}{nF}\ln\left(\frac{a_{\mathrm{Ox}_1}}{a_{\mathrm{Red}_2}}\right) \quad , \tag{6}$$

where $E^0$ is the standard electrode potential and $a$ is the activities of reactants and products. Once the electrochemical cell forms, the equilibrium electrochemical potential is determined by the potential difference between the cathode and the anode:

$$E_{cell} = E_{cathode} - E_{anode} \ . \tag{7}$$

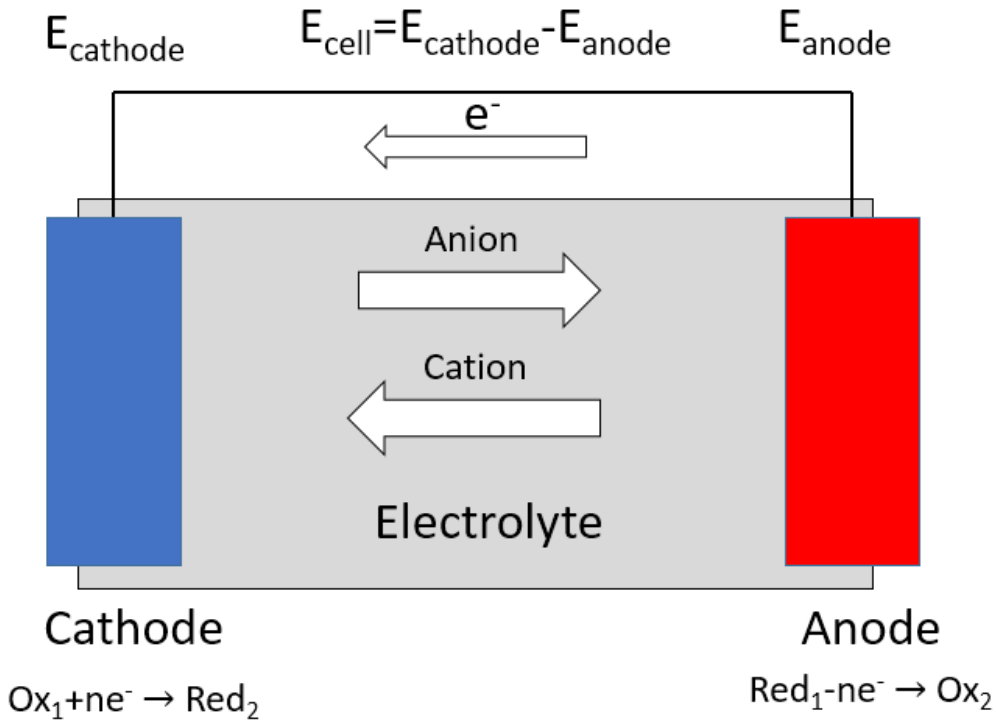


**Figure 2-1.** A schematic of an electrochemical cell. The components (the cathode, the anode, and the electrolyte) and corresponding reactions are labeled.

On the basis of the schematic configuration of electrochemical cell, various redox reactions can be applied to realize electrochemical energy storage and energy conversion. With regard to energy storage, for example, the chemical reaction

$$PbO_2 + Pb + 2H_2SO_4 \leftrightarrow 2PbSO_4 + 2H_2O \ , \tag{8}$$

can be used for a battery to store electrical energy using $PbO_2$ as the cathode, Pb as the anode, and $H_2SO_4$ as the electrolyte. When the forward direction of the reaction is processed, the electrochemical cell is discharged; the chemical energy is transformed into electrical energy. When the backward direction of the reaction is processed, the electrical energy is stored in the form of chemical energy. With regard to energy conversion, for example, the chemical reaction

$$2H_2 + O_2 \leftrightarrow 2H_2O \ , \tag{9}$$

can be realized electrochemically by using catalytically active electrodes. The forward direction of the reaction leads to the generation of electricity (fuel cells). The backward direction of the reaction leads to the generation of fuel and oxygen (electrolytic cell). This dissertation will discuss only the energy storage. Specifically, it focuses on two types of energy storage, pseudocapacitors, and Li-ion batteries. The details of the pseudocapacitors and Li-ion batteries will be discussed in the following sections.

### 2.1.2. Basic physicochemical processes for an electrochemical cell

Thermodynamic rules, as briefly mentioned in the previous section, describe the relationship between a redox reaction and an electrochemical cell as well as the equilibrium electrochemical potential without a current flow. As a realistic electrochemical cell generates electrochemical current, a variety of physicochemical processes may occur (Figure 2-2). The fundamental principles of each process are briefly described in this section.

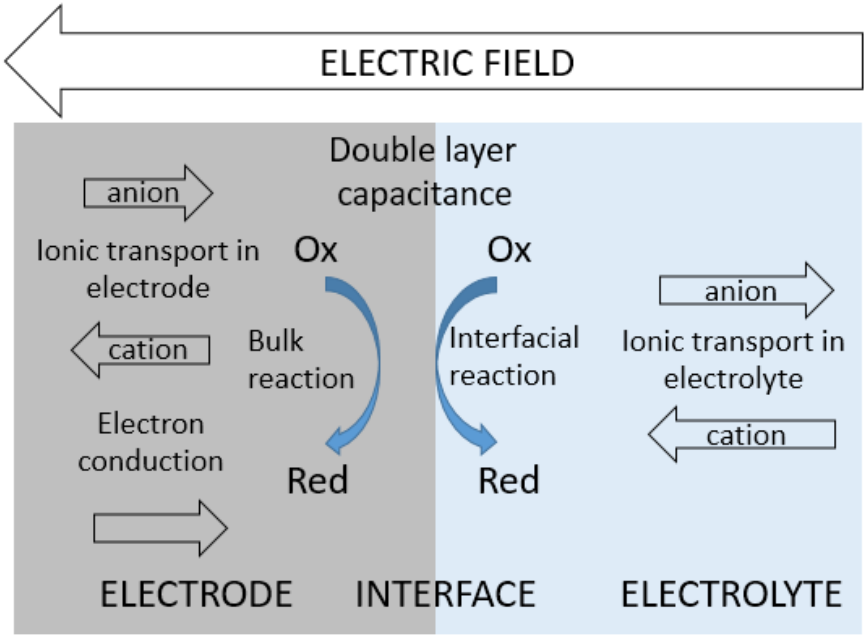

**Figure 2-2.** Schematics of physicochemical processes associated with an electrochemical cell.

#### *2.1.2.1. Electronic conduction in an electrode*

When an electric field forms between an electrode and an electrolyte and an external electrochemical current is applied or generated, electrons will flow in the opposite direction of the electric field. The current density ($j$) is a function of electronic conductivity ($\sigma$) and the strength of the electric field ($E$) [44] :

$$\vec{j} = \sigma \vec{E} \ . \tag{10}$$

Electronic conductivity varies greatly with the type of material and depends on the band gap of an electronic structure.[44] For metallic materials, electronic conductivity ranges from $10^3$-$10^6$ S/cm. For carbonaceous materials (e.g., graphene, graphite, and activated carbon), $\sigma$ is generally no less than $10^1$ S/cm. These materials are highly conductive and are often contributed as current collectors. However, most metal oxides (e.g., $MnO_2$ and $LiCoO_2$) are electronic insulators with electronic conductivity that ranges from $10^{-3}$-$10^{-9}$ S/cm. Some metal oxides (e.g., rutile $RuO_2$) are metallically conductive with considerably high electronic conductivity (~$10^4$ S/cm).[45]

#### *2.1.2.2. Ionic transport in an electrode*

Ionic transport in electrodes is applicable only to ionic crystals. The ionic conductivity of a particular type of ion ($i$) is a function of the concentration of mobile charge carrier ($n$), the number of charges ($Z$), and charge carrier mobility ($u$) [44]:

$$\sigma_i = Z_i n_i u_i e \ . \tag{11}$$

Charge carrier mobility depends on the diffusion constant ($D$):

$$u_i = \frac{D_i}{k_B T} \ , \tag{12}$$

where $k_B$ is the Boltzmann constant, $T$ is the temperature. The diffusion constant is experimentally proven directly correlated to the temperature (i.e., the Arrhenius equation):

$$D = D_0 e^{(-\frac{Ea}{RT})} \quad . \tag{13}$$

The diffusion of ionic species in bulk electrodes can be generally classified into two categories: the vacancy/defect-mediated mechanism and the interstitial site-mediated mechanism.[44] The value of a diffusion constant depends on a large variety of factors such as the types of ions, the structures of ionic crystals, the doping of heteroatoms, and the morphologies of electrodes. With regard to the effect of crystal structures, for example, the diffusion constant of a Li ion in layer-structured $LiCoO_2$ ($10^{-10}$ to $10^{-8}$ $cm^2/s$) is generally higher than spinel-structured $LiMn_2O_4$ ($10^{-11}$ to $10^{-9}$ $cm^2/s$), partially leading to the higher Li-ion conductivity of $LiCoO_2$ (~ $10^{-4}$ S/cm) than $LiMn_2O_4$ (~ $10^{-6}$ S/cm). For the same crystal structure (e.g., $LiCoO_2$), the diffusivity of Li ions greatly changes with the stoichiometry of Li, doping (e.g., Al and Ni), and morphologies (e.g., a thin film or a single particle), as demonstrated by various publications.[44] On the basis of diffusion, the transport of ionic species is governed on Fick's Law:

$$\begin{aligned} j_i &= -D_i \nabla c_i \\ \frac{\partial c_i}{\partial t} &= \nabla \cdot (D \nabla c_i) \end{aligned} \quad . \tag{14}$$

#### *2.1.2.3. Ionic transport in an electrolyte*

As mentioned in Section 2.1.1. , electrolytes for electrochemical cells can be in the form of solutions or solid states. A solid-state electrolyte is most likely composed of an ionic crystal. The conduction of ionic species in a solid-state electrolyte is exactly the same as that in a bulk electrode, as mentioned earlier. A solution-type electrolyte is composed of a polar solvent, cations, and anions. The description of current density is equation (11), and

the transport of ions is also controlled by diffusion (Fick's second law). Since ionic species are dispersed in an isotropic liquid matrix (a solvent) instead of an anisotropic solid matrix (a crystalline lattice), the Einstein-Stokes equation, is mostly used to describe the diffusion constant, simply assuming the spherical shape of the ionic species:

$$D = \frac{k_B T}{6\pi\eta r} \ , \tag{15}$$

where η is the viscosity of solvent and $r$ is the radius of the dispersed spherical particles. Since the solution-type electrolyte requires ionization and solvation of the dissolved salt, the observable ionic conductivity depends not only on the sizes of ions and viscosity of the solvent, but also on the concentration, the dielectric constant, and the molecular structure of solvent molecules.[44] For example, strong electrolytes (such as $NaNO_3$) with a high molarity (e.g., 2 M) dissolved in water, which has a high dielectric constant, can offer ionic conductivity more than 0.1 S/cm. Also, same type of salt can lead to various conductivity values when various types of solvents are used.[46] For example, 1 M $LiClO_4$ has slightly higher ionic conductivity in mixed solvent of ethylene carbonate/dimethyl carbonate than propylene carbonate owing to optimized balance between solvent polarity and viscosity.

#### *2.1.2.4. Diffusion models of ionic transport*

The ionic transport in both electrodes and electrolytes is governed by diffusion as mentioned above and the behavior can be described by Fick's Law (equation 14), which is a partial differential equation. Boundary conditions are needed to fully describe distribution of ionic species, which can be expressed by a few diffusion models.[43] The following are three common models to describe a diffusion process. First, when the concentration of ions or species (i.e., C(x)) equals to the concentration of a bulk electrolyte (a constant value) only at an infinite distance from an electrode surface or a current collector (i.e., $C(x)=C_0$,

when x=∞), such boundary condition is semi-infinite diffusion. This model is often used to describe an electrochemical reaction at the electrode surface from the electrolyte (e.g., reduction of Fe(III) ion to Fe(II) at an electrode) or ionic intercalation in a very thick electrode. Second, if $C(x)=C_0$ at a non-infinite distance from an electrode, the model is named finite diffusion. In this case, another boundary condition needs to be concerned.[47-49] When the concentration of ions or species is zero at the electrode surface or at the end of an electrode (i.e., C(0)=0), the model is finite length diffusion and often used to describe the diffusion in fuel cells where species are completely consumed at the end of an electrode. When the surface or the end of an electrode is non-permeating (i.e., dC/dx=0 when x=0), the model is finite space diffusion and often used to describe the diffusion of intercalated ions into an electrode of which one side is connected to a current collector. Different configurations of electrochemical reactions have various models to describe their diffusion processes.

#### *2.1.2.5. Double layer capacitance*

As an electrode and an electrolyte physically contacts, a charge separation across the electrode-electrolyte interface instantly forms, which is called double layer effect.[43] The first layer is composed of surface charge of the electrode and adsorbed solvent molecules bound on surface. The second layer is composed solvated ions attracted to the surface charge resulting from the columbic force. The double layer effect is a non-Faradaic process and does not involve a change in oxidation states. Because of the resemblance between a classic capacitor, the double layer effect essentially leads to a capacitance where charge storage can be realized:

$$Q = C_{dl} A(E_{applied} - E_{open\ circuit}) \ , \tag{16}$$

where $C_{dl}$ is the normalized double layer capacitance, $Q$ is stored charge, $A$ is the surface area of the electrode. Evidently, the total stored charge increases with electrode surface area. For the electrode materials with moderate surface area, the charge storage of double layer is very limited; the double layer capacitance is mostly considered as surface effect that influence electrochemical kinetics rather than energy storage. In recent years, through engineering of nanostructures, porous conductive materials with a high surface area (e.g., carbonaceous type) have successfully been utilized for the energy storage by maximizing the double layer effect (electrochemical double layer capacitance, EDLC).[12,24,26,50] Also, the EDLCs generally can be charged and discharged with a very high rate, almost comparable with classic dielectric and electrolytic capacitors. Thus EDLCs are applicable to high power applications. However, the energy density of EDLC is still far less than state-of-art energy storage devices (e.g., batteries), which will be elaborated in following sections of dissertation.

#### *2.1.2.6. Interfacial reactions*

Despite the double layer effect, at the interface between an electrode and an electrolyte, the electrode material, solvent molecules of the electrolyte, and ionic species of the electrode and the electrolyte may involve chemical reactions. Unlike the double layer effect, interfacial reactions are redox processes and involve the transfer of electrons. Depending on the source of electrons of interfacial reactions, these redox reactions can either be spontaneous or can be induced by electrochemical current. On one hand, some interface-bound chemical reactions are generally viewed as side-reactions, blocking electronic and ionic transport, and should be eliminated as much as possible. On the other hand, some interface-bound reactions can be utilized for electrochemical energy storage.

#### *2.1.2.7. Bulk redox reactions*

On the basis of electronic and ionic transport, the bulk phase of an electrode can be electrochemical reduced or oxidized. Generally, bulk-phase redox reactions can be the major contributor to the electrochemical energy storage. These redox reactions can be classified to different categories and will be discussed in detail in further sections of the dissertation.

### 2.1.3. Fundamental principles of electroanalytical techniques

In order to characterize physicochemical reactions in an electrochemical cell, various experimental techniques are needed to describe aspects of these reactions. This section briefly describes common electrochemical techniques frequently used for the characterization of electrochemical energy storage.[43]

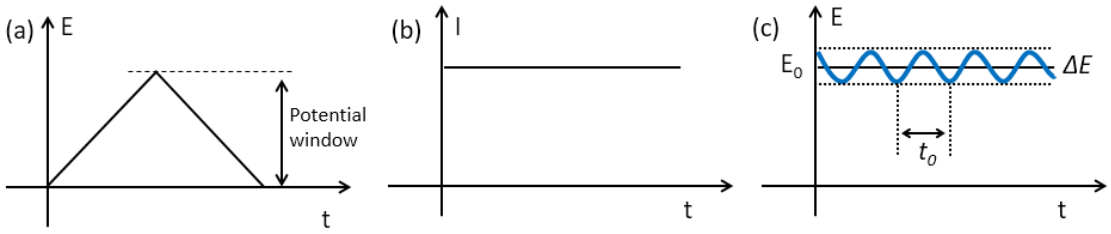


**Figure 2-3.** Schematics of control factors as a function of time for (a) cyclic voltammetry, (b) galvanostatic charge/discharge, and (c) Impedance spectroscopy.

#### *2.1.3.1. Cyclic voltammetry*

Cyclic voltammetry is one of the most common techniques to probe the thermodynamics and the kinetics of electrochemical reactions. During a cyclic voltammetry measurement, the electrode potential is repeatedly scanned as a linear function with time with a constant scan rate within a potential window (Figure 2-3). The

process when the potential is scanned positively or negatively is anodic or cathodic process, respectively.

Different electrochemical processes will show various responses of currents as a function of potentials. For example, first, for an ideal capacitor, the current will display a square shape as a function of electrode potentials (Figure 2-4a). As the scan rate of CV ($v$) increases, the constant current in the CV profile increases linearly (equation (17)) [43]:

$$i \propto v \ . \tag{17}$$

Second, for a redox reaction controlled by semi-infinite diffusion, a pair of current peaks will appear. The peaks are as cathodic and anodic peaks, corresponding to cathodic and anodic processes, respectively (Figure 2-4b). The average sum of cathodic and anodic peak positions often can represent the Nernst potential of the particular electrochemical reaction. The peak separation ΔE is determined by the number of electrons of the redox reaction. As the scan rate of CV increases, the peak current increases with the square root of the scan rate (equation (18)) [43]:

$$i \propto v^{1/2} \ . \tag{18}$$

Third, for a redox reaction controlled by finite space diffusion with a characteristic diffusion length L and a diffusion constant D, a characteristic scan rate $v_0$ can be obtained [51,52]:

$$v_0 = \frac{RT}{nF}\frac{D}{L^2} \ . \tag{18}$$

If the scan rate $v$ is much lower than the characteristic scan rate $v_0$, the diffusion can be considered fast enough that the diffusion process doesn't limit the kinetics. In this case, the

CV current increases linearly with the scan rate (equation (17), i.e., the system is reduced to a capacitor). If the scan rate $v$ is much higher than the characteristic scan rate $v_0$, the diffusion can be considered slow enough that the kinetics is diffusion-controlled. In this case, the CV current increases with the square root of the scan rate (equation (18), i.e., the system is reduced to semi-infinite diffusion). Otherwise ($v$ is comparable with $v_0$), the CV current can be roughly considered proportional to a power function of $v$, with the power index ranges between 0.5-1.

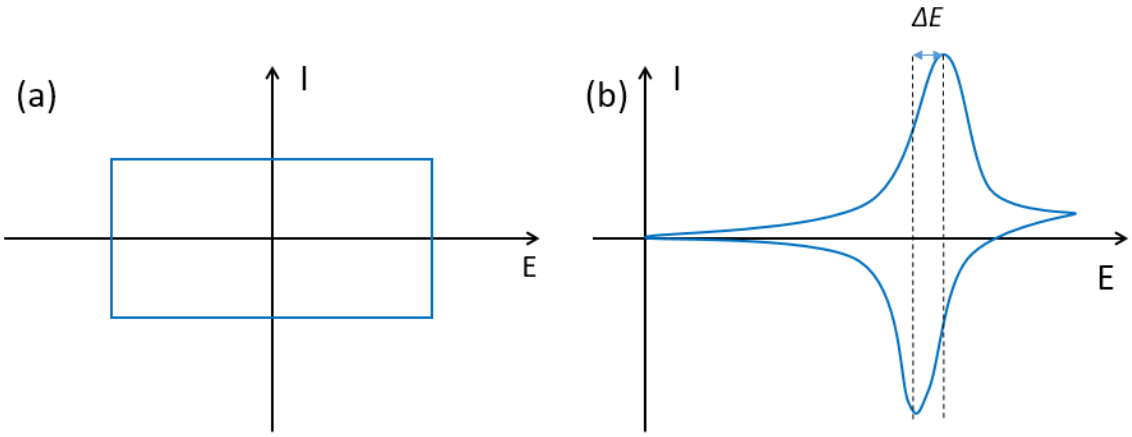


**Figure 2-4.** Schematics of current response during a CV measurement for (a) a capacitor and (b) an electrochemical redox reaction governed by semi-infinite diffusion.

#### *2.1.3.2. Galvanostatic measurements*

As a supplementary method for cyclic voltammetry, galvanostatic tests are also often used to evaluate behavior of electrochemical processes. The electrode potential is monitored when a constant current is applied (Figure 2-3b). During a galvanostatic test, the electrode potential is controlled within a potential window. In most occasions, the amount of charges applied during the cycling between a potential window can be calculated to evaluate performance of charge storage.

#### *2.1.3.3. Impedance spectroscopy*

Impedance spectroscopy is a powerful tool to study thermodynamics and kinetics of electrochemical reactions. A schematic of an impedance spectroscopy measurement is shown in (Figure 2-3c). Generally, the electrode potential is controlled at a constant DC potential ($E_0$) with an AC perturbation $E_t$ [53]:

$$E = E_0 + E_t, \quad E_t = \left|E_t\right| e^{i\omega t} \ . \tag{19}$$

In this equation, $\omega$ is the angular frequency of the AC potential. During an impedance measurement, the current is observed as a sum of a DC ($I_0$) and an AC current ($I_t$):

$$I = I_0 + I_t \ . \tag{20}$$

The complex impedance Z is:

$$Z = \frac{E_t}{I_t} = Z_0 e^{i(2\varphi)} = Z_0 \cos(\varphi) + iZ_0 \sin(\varphi) = Z' + iZ'', \tag{21}$$

where φ is the phase angle of the impedance. The complex impedance can be separated into a real part (Z') and an image part (Z''). The real part and the imaginary part can be plotted together, which a Nyquist plot.

In order to analyze the kinetics of electrochemical reactions, each elementary process can be simulated by a number of equivalent circuit elements. For a resistor (R), the impedance is always a constant. The phase angle is $0^o$:

$$Z = R. \tag{22}$$

For a capacitor (C), the phase angle is always $90^o$:

$$Z = \frac{1}{i\omega C} \ . \tag{23}$$

For a constant phase element (CPE):

$$Z = R\frac{1}{(i\omega \cdot s/rad)^P}, 0 \le P \le 1 \ , \tag{24}$$

where ωs/rad is the dimensionless frequency. Constant phase elements are often used to describe the double layer capacitance of a rough surface. Also, when P is 0.5, CPE can be used to describe the semi-infinite diffusion process. In this case, the phase angle is 45°. For a finite space Warburg element [48,49,54]:

$$Z = R\frac{\coth((iT\omega)^P)}{(iT\omega)^P}. \tag{25}$$

When P is 0.5, the finite space Warburg can be used to describe the finite space diffusion. At high frequencies, the phase angle is roughly 45°; at low frequencies, finite space Warburg element is similar with a capacitor with an approximate phase angle of 90°. For finite length Warburg element [54]:

$$Z = R\frac{\tanh((iT\omega)^P)}{(iT\omega)^P}. \tag{26}$$

When P is 0.5, the finite length Warburg can be used to describe the finite length diffusion. At high frequencies, the phase angle is roughly 45°; at low frequencies, finite space Warburg element is similar with a resistor with an approximate phase angle of 0°. Figure 2-5 describes Nyquist plots of common equivalent circuit elements. These elements can be applied to model electrochemical kinetic processes.

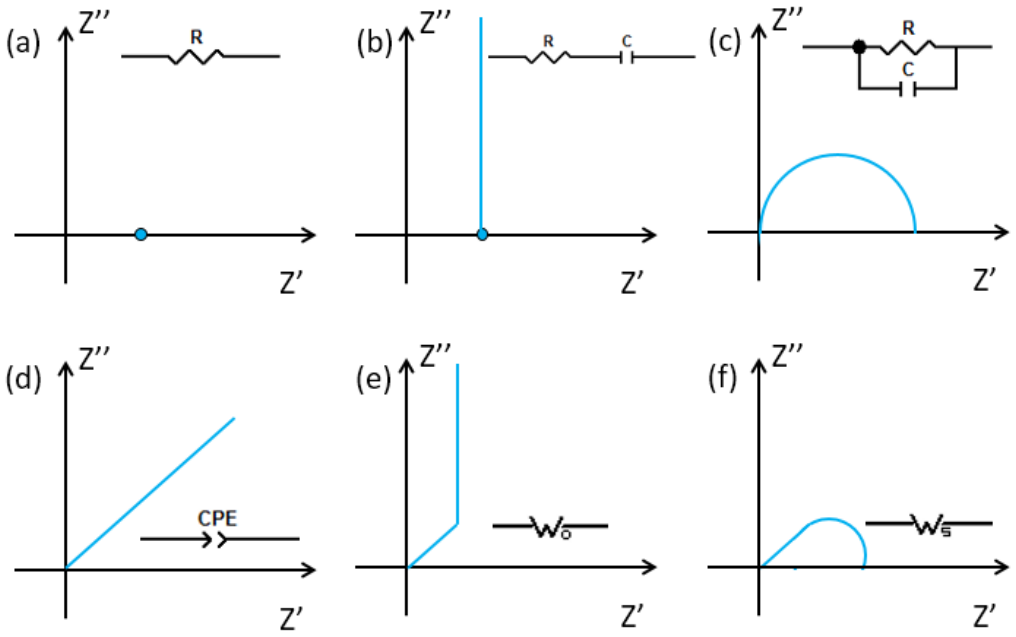


**Figure 2-5.** Schematics of Nyquist plots for different elements. (a) a resistor, (b) a resistor and a capacitor in series, (c) a resistor and a capacitor in parallel, (d) a constant phase element with a phase angle of 45°, describing semi-infinite diffusion. (e) a finite space Warburg element (f) a finite length Warburg element**.**

### 2.1.4. Electrochemical energy storage

As mentioned in Section 2.1.1. and Section 2.1.2. , electrochemical reactions and the associated physicochemical processes can lead to stored electrical energy. Through proper selection and engineering of electrode materials, an energy storage device can be constructed. Stable electrochemical storage must obey the rule that the chemical potentials of the electrodes must be within the stability window of the electrolyte.[28,55,56]

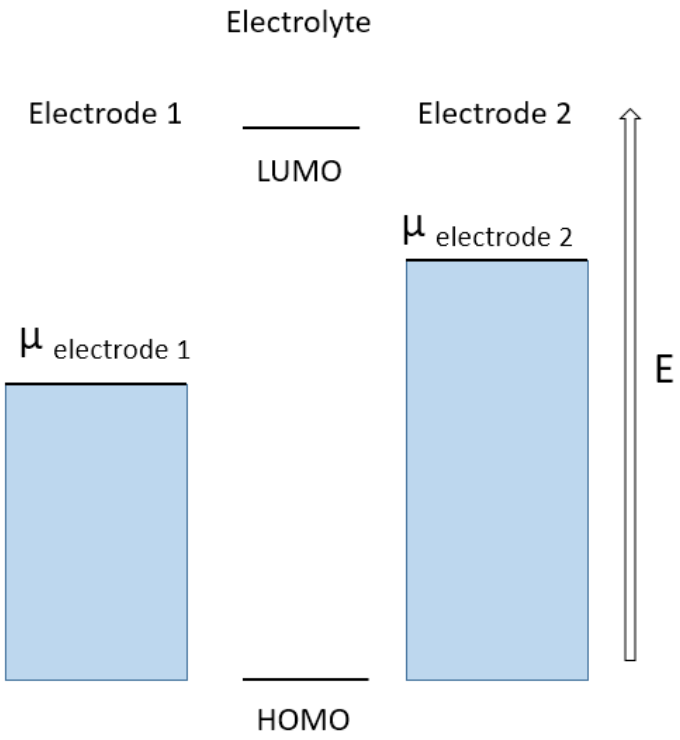


**Figure 2-6.** A schematic energy level diagram of a stable electrochemical energy storage device.

During an operation of an electrochemical storage device, the chemical potential of each electrode may change. Chemical potentials of electrodes should be always higher than the HOMO (highest occupied molecular orbital) energy level and lower than the LUMO (lowest unoccupied molecular orbital) energy level of the electrolyte. Otherwise the electrolyte will be oxidized or reduced electrochemically or simultaneously, leading to instability of the electrochemical energy storage device.

#### *2.1.4.1. Fundamental configurations of Li-ion batteries*

When both electrodes utilize bulk redox-active materials for energy storage, the device is called a battery. A basic configuration of a battery can be essentially described as Figure 2-1, which includes a cathode, an anode, and an electrolyte.[24,57,58] If the redox reaction is reversible, the battery can be recharged, which is a secondary battery. Through decades of research and developments, a number of batteries have been proven extremely

successful, such as Ni-MH batteries, lead-acid batteries, and Zinc-carbon batteries. Among all types of existing rechargeable batteries, Li-ion batteries have a great perspective owing to a few currently irreplaceable merits.[16,17,58] A schematic configuration of a Li-ion battery is shown in Figure 2-7.

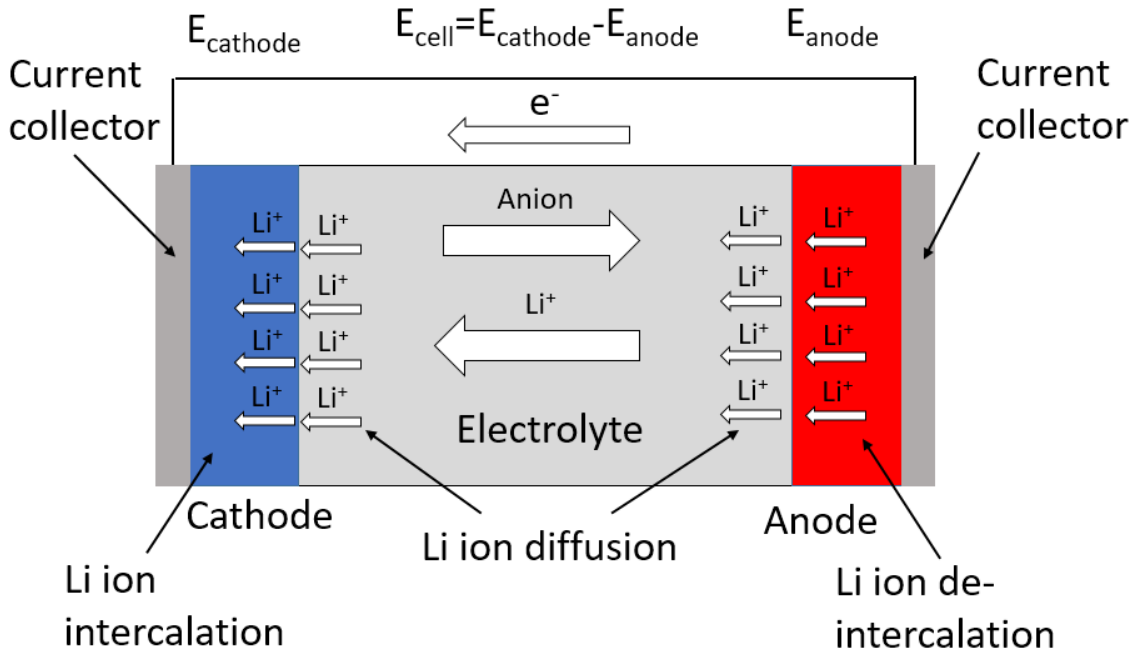


**Figure 2-7.** A Schematic of a Li-ion battery during a discharge process.

The cathode materials of Li-ion batteries are mostly transitional metal oxide-based, including $LiFePO_4$, $LiMO_2$ (M=Mn, Co, Ni, and Al), and $LiM_2O_4$ (M=Mn and Ni).[15,59] The Nernst potentials of these cathodes approximately range from 3-4.5 V vs $Li^+/Li$ (or 0-1.5 V vs Standard Hydrogen electrode approximately). For anode materials, graphite is most often used with an electrochemical potential about 0.2 V vs $Li^+/Li$ (approximately -3.0 V vs Standard Hydrogen electrode). In recent years, a few novel electrode materials were developed, such as sulfur and silicon.[18,60] For electrolyte solvents, non-aqueous solvents are generally used.[46,61] The most common solvent is the 1:1 mixture of ethylene carbonate (EC) and dimethyl carbonate (DMC). The electrolyte salts for Li-ion batteries mainly

include $LiPF_6$, $LiClO_4$, $LiBF_4$, and other types. During the discharge process (Figure 2-7), Li ions deintercalate from anode bulk material along with the oxidation of the anode. At the same time, Li ions intercalate into the bulk cathode along with the reduction of the cathode. The charge process is the reverse of the discharge process. The Nernst potential of each electrode usually determines the Li intercalation potential of which charge is stored/released. The theoretical specific capacity of each electrode is determined by the number of electrons involved in the redox reaction per formula ($n$) and the molar weight of the electrode material (M) [58]:

$$Specific\ capacity = \frac{nF}{M}\ , \tag{27}$$

where F is the Faraday constant (96485 C/mol).

The characteristics of Li-ion batteries mentioned above essentially contribute to a number of merits. First, as a result of the low redox potential of Li-ion battery anodes, a high working voltage can be achieved. Also, owing to the low molecular weight of electrode materials, the specific capacities of Li-ion batteries are pretty high. Moreover, Li-ion batteries have low memory effect and self-discharge. In recent years, through developments of nanotechnologies, performance and reliability of Li-ion batteries are being progressively optimized.

For evaluations of capacity for a Li-ion battery, galvanostatic cycling is often applied. By applying a constant positive/negative current ($I$), the potentials of electrodes are repeatedly charged/discharged between a potential window. The charge/discharge capacity can be easily derived from the product of the charge/discharge current and the charge/discharge time ($t$):

$$Experimental\ capacity = I \times t\ . \tag{28}$$

Also, cyclic voltammetry is also commonly used to determine the lithiation potential from the CV peak positions and corresponding currents. The integration of the CV current over time can also lead to a capacity value:

$$Experimental\ capacity = \int_{E_1}^{E_2} i(E)\frac{dE}{v} \ . \tag{29}$$

Moreover, to evaluate the kinetics of Li-ion batteries at different conditions (e.g., open circuit, charge, and discharge), impedance spectroscopy is frequently used as well. To interpret the impedance data, the equivalent circuit (Randle's circuit, Figure 2-8) can interpret electrode kinetics reasonably.[62]

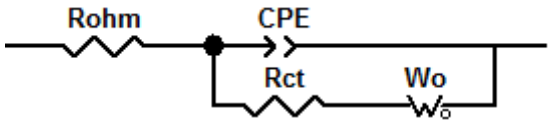


**Figure 2-8.** Randle's circuit as an equivalent circuit for a Li-ion battery

In the Randle's circuit, $R_{ohm}$ represents the Ohmic resistance of the electrode and the electrolyte. CPE represents the double layer capacitance of electrode-electrolyte interface. $R_{ct}$ is the charge transfer resistance for redox reactions. $W_o$ is the open Warburg element to describe the ionic diffusion process. In recent years, other types of equivalent circuits based on the modification of Randle's circuit are proposed to simulate the Li-ion battery kinetics more accurately. Through fitting of this equivalent circuit, the value of each circuit element can be obtained, thus generating important kinetic information of the Li-ion battery.

#### *2.1.4.2. Fundamental configurations of electrochemical capacitors*

In recent decades, electrochemical capacitors gradually emerged as a new type of electrochemical energy storage devices.[24-27] Since capacitances of electrochemical

capacitors are much higher than those of conventional capacitors, electrochemical capacitors are also named as supercapacitors. Unlike batteries, which have a defined cathode and an anode, capacitors (including supercapacitors) use symmetric electrodes, the capacitance of a capacitor is defined as the amount of charges it can store in a particular potential range [24,63]:

$$C = \frac{\Delta Q}{\Delta V} \ . \tag{30}$$

The first type of electrochemical capacitors is named as electrochemical double layer capacitors, which utilize the electrochemical double layer effect without involving a Faradaic process (Figure 2-9 left), generating capacitor-like electrochemical behavior similar with Figure 2-4a (a rectangular CV profile).[25,26] Owing to the rapid developments of nanotechnology, various conductive materials (especially carbonaceous materials) with extraordinarily high surface area have been fabricated, such as activated carbon, carbon nanotubes, and graphene.[24,64-68] When applied as supercapacitors, these materials exhibit impressive capacitance values. Since formation/release of electrochemical double layer capacitance is much faster than charge-transfer of a redox process, EDLCs can store/release charges in a much faster rate than batteries. However, since EDLC doesn't involve redox reactions, the amount of charges EDLC can store generally is generally not higher than batteries. Also, because of the same reason, EDLCs usually don't have a defined theoretical capacitance value.

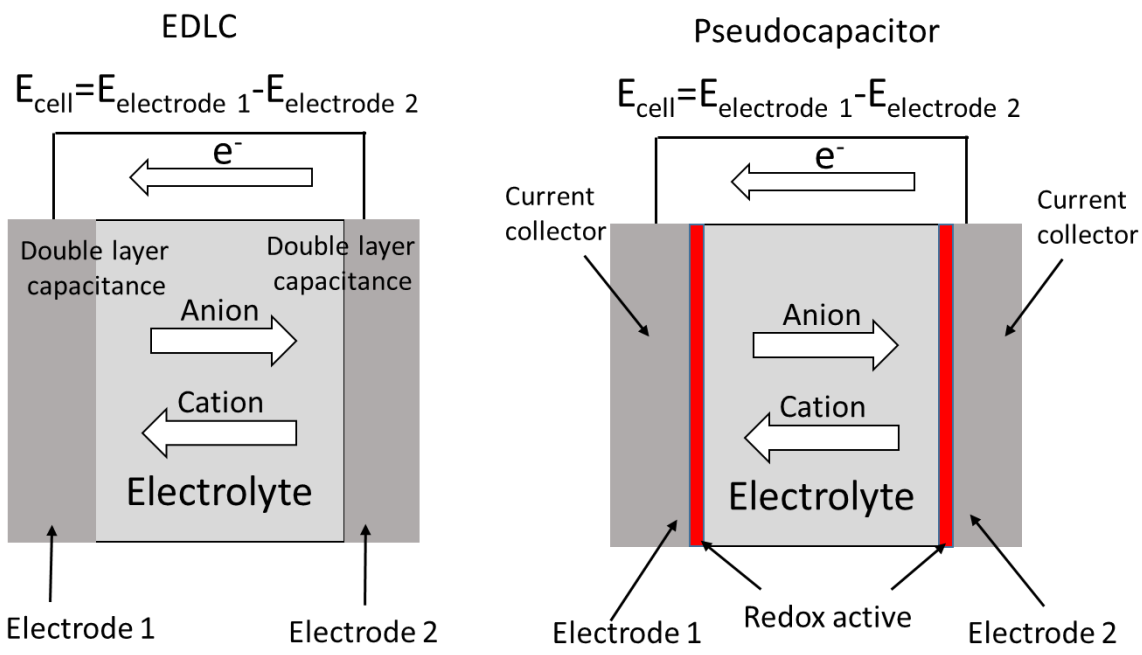


**Figure 2-9.** Schematic configurations and operation of an EDLC (left) and a pseudocapacitor (right)

The second type of electrochemical capacitors is called pseudocapacitors (Figure 2-9b). The term "pseudocapacitor" was firstly named for a few charge storage systems through surface-bound reversible redox reactions.[24,27,69,70] Electrochemically, these surface-bound redox reactions behave similar with capacitors. Since its charge storage is not capacitive intrinsically, the prefix "pseudo" is added. The first renowned pseudocapacitive material is ruthenium oxide ($RuO_2$), which is operated under acidic electrolyte solutions.[69,70] During an operation of a $RuO_2$-based pseudocapacitor, one $RuO_2$ electrode is oxidized with an increased oxidation state of Ru:

$$H_xRuO_2\text{-}yH^+\text{-}ye^- \leftrightarrow H_{x\text{-}y}RuO_2 \ ; \tag{31}$$

another $RuO_2$ electrode is reduced with a reduced oxidation state of Ru:

$$H_xRuO_2+yH^++ye^- \leftrightarrow H_{x+y}RuO_2 \ . \tag{32}$$

As the direction of current flow is flipped, the roles of two electrodes can be switched, leading to the symmetric capacitor-like electrical energy storage. Since the discovery of $RuO_2$-based pseudocapacitive energy storage, other transition metal-oxide materials were applied as pseudocapacitors to lower the cost. For most pseudocapacitive materials, unlike batteries of which charge storage is processed near a stable electrochemical potential (Nernst potential), the redox reactions for pseudocapacitors (e.g., equation (31) and (32)) usually don't have well-defined Nernst potentials, making the charge storage occurs within a wide range of potentials. This characteristic makes behavior of pseudocapacitors very similar with that of conventional capacitors and EDLCs. The theoretical specific capacitance of a particular pseudocapacitive material is defined as [25,26]:

$$Specific\ capacity = \frac{nF}{M\Delta E}\ , \tag{33}$$

where $\Delta E$ is the potential window of the pseudocapacitive electrode.

For evaluations of performance of a supercapacitor, similar with Li-ion batteries, galvanostatic cycling is mostly often applied to calculate capacitance values. As mentioned above, since both EDLCs and pseudocapacitors don't have a defined potential for charge storage, the unit capacitance is used instead of capacity, to evaluate the amount of charges stored within a specific range of potentials:

$$Experimental\ capacitance = \frac{I \times t}{\Delta E}\ . \tag{34}$$

Aside from galvanostatic cycling, CV measurements can characterize behavior of supercapacitors feasibly. According to equation (30), the capacitance value as a function of time can be directly derived from the current of a CV measurement:

$$C(V) = \frac{i(V)}{v}\ . \tag{35}$$

The total capacitance value can be calculated by integrating the CV profile similar with calculating the capacity value of a battery:

$$Experimental\ capacitance = \frac{\int_{E_1}^{E_2} i(E)\frac{dE}{v}}{E_2 - E_1}. \quad (36)$$

In addition, impedance spectroscopy can be used to probe the kinetics of a supercapacitor. One common type of equivalent circuit is to add one capacitor element after a Randle's circuit to simulate the charge storage contribution from a supercapacitor (Figure 2-10).[71,72] Through equivalent circuit fitting, the value of each element can be obtained.

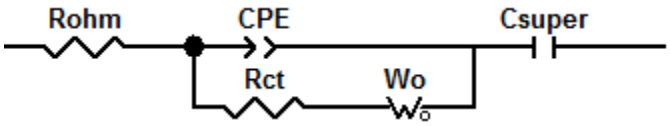


**Figure 2-10. A** common equivalent circuit for a supercapacitor.

## 2.2. Fundamentals of Raman spectroscopy

### 2.2.1. Basics of spectroscopy

Spectroscopy is based on the interaction between light and matter. During the interaction process, properties of incident light change, offering information about properties of the matter.[73] Light is subject to wave-particle duality, which makes light both an electromagnetic wave and a particle (photon). The energy and momentum of a photon are solely determined by the wavelength of the photon (electromagnetic wave):

$$E = h\upsilon\ , \quad (37)$$

$$k = \frac{2\pi}{\lambda}\ , \quad (38)$$

$$\vec{p} = \hbar\vec{k}\ , \quad (39)$$

$$\text{and } \lambda = \frac{\upsilon}{c} \ . \tag{40}$$

In these equations, $E$, $p$, $\lambda$, and $\upsilon$ are the energy, the momentum, the wavelength, and the frequency of a photon respectively; $h$ and $c$ are the Planck constant and speed of light respectively. Electromagnetic waves with certain ranges of wavelengths are designated as different categories. As the most important range for spectroscopic study, the wavelength of visible light ranges from 400 nm to 750 nm, for Infrared light, it ranges from 750 nm to 1mm, for ultraviolet light, it ranges from 10 nm to 400 nm.

### 2.2.2. Principles of molecular and crystalline vibration.

As a category of spectroscopy, vibrational spectroscopy is the study of interaction between electromagnetic waves and vibrational properties of matter.[73] In this section, the fundamental concepts of vibrational spectroscopy, which is vital to this dissertation, will be briefly discussed.

#### *2.2.2.1. Vibration of a diatomic molecule*

A diatomic molecule is the simplest case to describe fundamental principles of molecular vibration (Figure 2-11). In this model, only one vibration mode, which is along the axis of diatomic molecule, can exist. The vibration of this diatomic molecule can be approximated as a harmonic oscillator. The force applied to each molecule is proportional to the displacement of each atom from its equilibrium position.

**Figure 2-11.** A schematic of a diatomic molecule under harmonic oscillator approximation.

Under harmonic oscillator approximation, the energy of the harmonic oscillator (i.e., vibrational energy, the sum of kinetic energy (E) and potential energy (V)) can be expressed as:

$$\hat{H} = \hat{E} + \hat{V} = \frac{\hat{p}^2}{2m} + \frac{1}{2} m\omega^2 \hat{x}^2 \quad , \tag{41}$$

where $H$ is the Hamiltonian of the oscillator, $m$ is the mass of the atom, $p$ is the momentum of oscillator, $x$ is the displacement. By solving the Schrödinger equation:

$$\hat{H} \left| \Psi(x) \right\rangle = E \left| \Psi(x) \right\rangle \quad , \tag{42}$$

the eigenvalues of vibrational energy are discrete levels (e.g., energy levels) instead of a continuous distribution[73] :

$$E(n) = (n + \frac{1}{2}) \hbar \omega_0 \, . \tag{43}$$

The energy levels are evenly spaced with a constant value $\hbar\omega_0$. The $\omega_0$ is the intrinsic property of the molecule. The harmonic oscillator approximation is a rough model to describe vibrational behavior. Other more complicated models can describe vibrational properties more accurately, leading to a few correction terms for equation (43).

#### *2.2.2.2. Vibration of a 1D crystal*

The combination of atoms with periodic translation symmetry essentially forms a crystal. The simplest model for crystal vibration is a 1D atomic chain with a constant equilibrium distance,[74] which can be considered as an infinite expansion of a diatomic molecule (Figure 2-12).

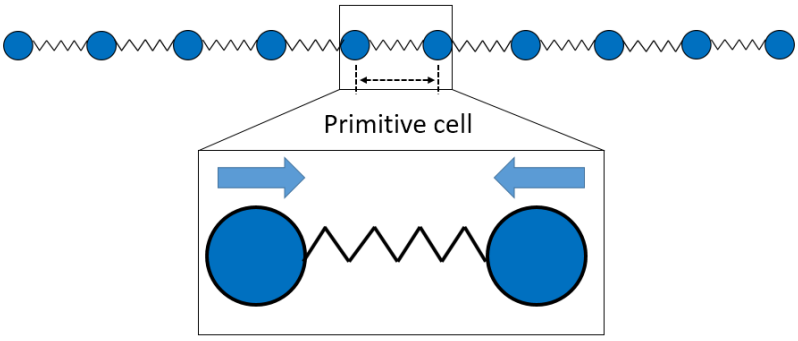


**Figure 2-12.** A schematic of a 1D crystal under harmonic oscillator approximation.

Since a primitive cell contains only one atom, only one vibration mode exists in the primitive cell (Figure 2-12). The entire 1D crystalline vibration can also be considered as propagation of this vibration mode of a primitive cell, leading to lattice vibrational waves with a wavelength λ and a frequency ω (Figure 2-13). Because of the particle-wave duality, the wave of the propagation of a vibrational mode is also considered as a particle, which is called a phonon.[74]

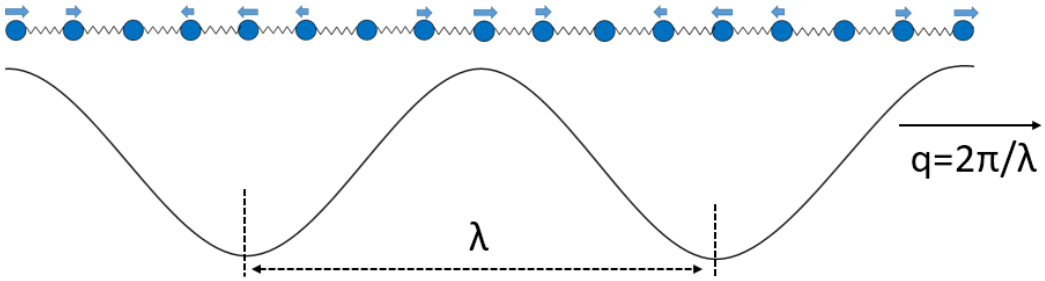


**Figure 2-13.** A Schematic of a phonon formed by vibration of a 1D crystal with a wavelength λ. In this figure, q is the wave vector of the phonon.

The correlation between phonon frequencies and wavelengths is called a phonon dispersion relation [74]:

$$\omega_{phonon}=\omega(\vec{q}) \ , \tag{44}$$

where $q$ is the wave vector of phonon:

$$q = \frac{2\pi}{\lambda} \ . \tag{45}$$

The phonon dispersion relation is an intrinsic property of a particular phonon. The momentum of phonon is:

$$\vec{p} = \hbar \vec{q} \ . \tag{46}$$

Under harmonic oscillator approximation, the phonon dispersion relation of a 1D atom chain is roughly shown in Figure 2-14. When q=0 (the wavelength is infinity, the momentum is zero, all atoms vibrate with same a direction and an amplitude), the frequency is zero.

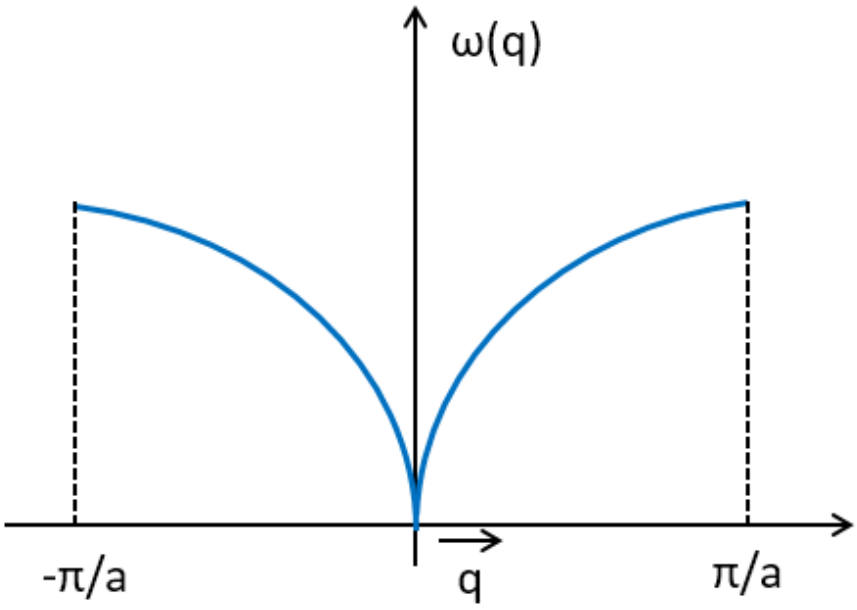


**Figure 2-14.** A phonon dispersion relation of a 1D crystal with harmonic oscillator approximation.

In a phonon dispersion relation, each point on the phonon dispersion relation represents a phonon. For each phonon, the energy is also a series of discrete energy levels. On the basis of harmonic oscillator approximation, the energy of a particular phonon is described in equation (47) [74]:

$$E(n)_{phonon} = (n + \frac{1}{2})\hbar\omega_{phonon} \ . \tag{47}$$

For a 1D atom chain with two different atoms, the primitive cell has two atoms. The linear combination of the coordinations of the two atoms can form two mutually independent (i.e., orthonormal) vibration modes.[74] If neighboring atoms vibrate with the same direction, the mode is an acoustic mode (Figure 2-15). If neighboring atoms vibrate with the opposite direction, the mode is an optical mode (Figure 2-15). The propagation of the two vibration modes gives rise to two lattice waves (phonons), which are acoustic phonons and optical phonons (Figure 2-16). Under harmonic oscillator approximation, rough phonon dispersions of an optical phonon and an acoustic phonon for a 1D atom chain are shown in Figure 2-17. When q=0, (i.e., infinite wavelength), optical phonons have the maximized energy (frequency) whereas energies (frequency) of acoustic phonons are zero.

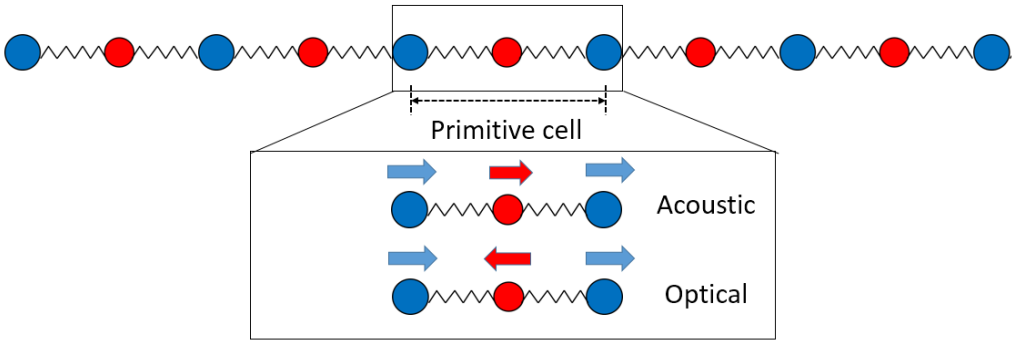


**Figure 2-15.** A Schematic of two phonons formed by vibration of a 1D crystal with two atoms in one primitive cell. The vibration of an acoustic mode and an optical mode is highlighted.

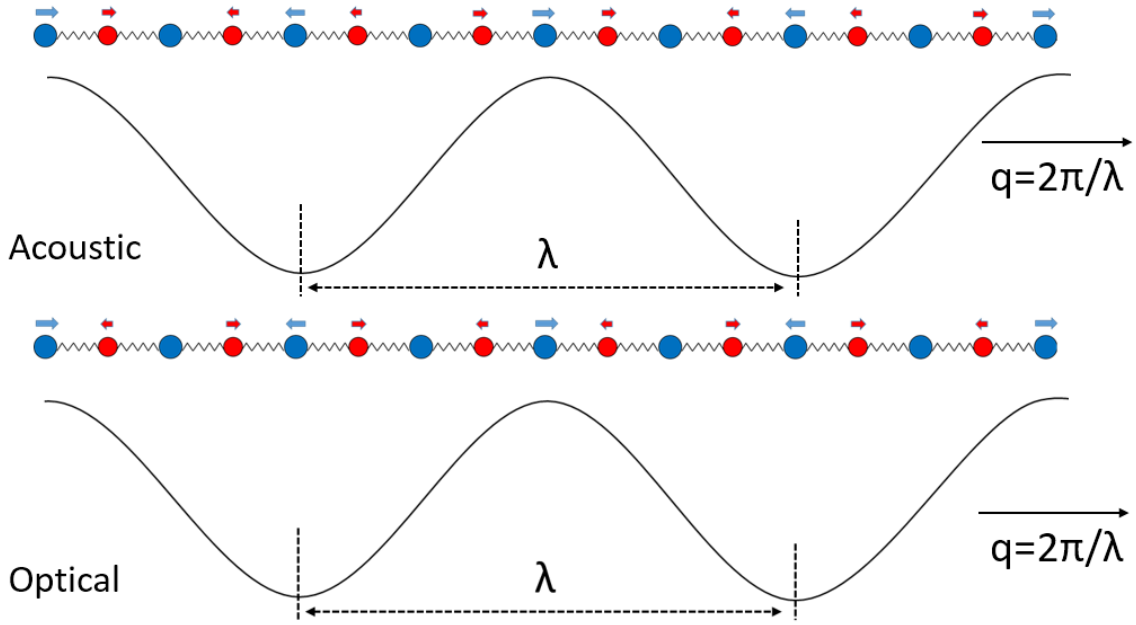


**Figure 2-16.** Schematics of an acoustic phonon and an optical phonon formed by vibration of a 1D crystal with two atoms in one primitive cell. The wavelength is λ.

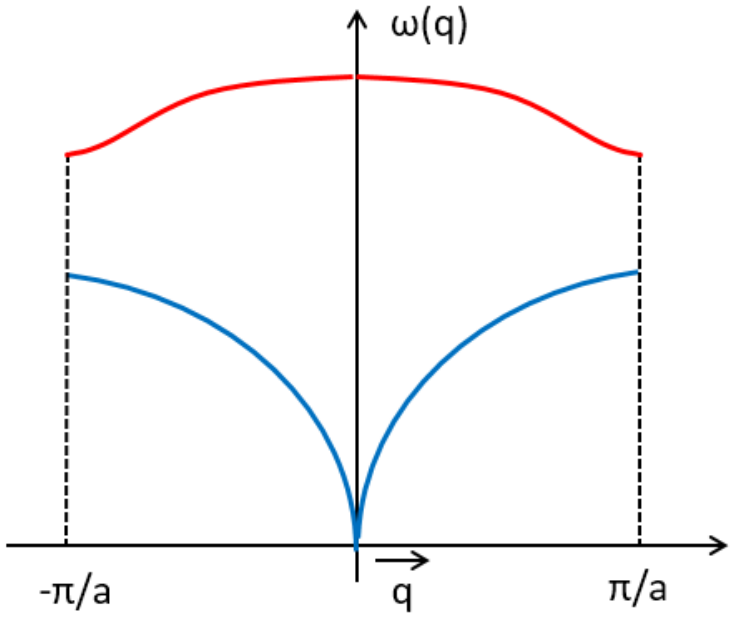


**Figure 2-17.** Phonon dispersion relations of a 1D crystal with two atoms in one primitive cell under harmonic oscillator approximation (red: an optical mode, blue: an acoustic mode).

As a summary of the fundamental concepts discussed in this section, energy of molecular/crystalline vibration is quantized. For crystalline vibration, the vibration forms a wave (phonon) with specific relations between frequencies and wavelengths. In the next section, vibration of 3D molecules and 3D crystals, which can represent the realistic molecules and crystals more accurately, will be discussed.

#### *2.2.2.3. Vibration of a 3D molecule and a crystal: Degree of freedom*

For a diatomic molecule mentioned above, vibrational motions can be described by a single coordinate (the displacement from the equilibrium position). Therefore, the energy of a system has only one variable, which leads to a single series of energy levels. For a 1D crystal, the case is similar, and the single coordinate, which describes the vibration in one primitive cell, propagates as a wave. For the case of a 1D atom chain with two atoms in one primitive cell, vibrational motions can be separated into two independent modes (i.e., acoustic and optical) through linear combination of the coordinates of the two atoms.

For a molecular system or a primitive cell that contains N atoms (atom number: 1...N), vibrational motions cannot be feasibly described as the mutually independent (i.e., orthonormal) vibration modes, since the potential energy of a particular atom is intertwined with that of other atoms. To describe the vibrational behavior, the degree of freedom (DOF), which is the number of independent coordinates involved in vibrational motions, needs to be analyzed first. For a three-dimensional molecule, every atom (i) in the molecule can move three dimensionally ($x_i$, $y_i$, $z_i$). Therefore, 3N independent coordinates are needed to fully describe the whole system. Since the entire molecule can move and rotate freely as a whole, three independent coordinates are needed to describe the translational movements. Three or two independent coordinates are needed to describe the rotational movements for

non-linear and linear molecules, respectively. Therefore, the degree of freedom (DOF) of vibrational motions for a molecule with N atoms is [34,35,73,75,76]:

$$\begin{aligned} DOF_{vibration} &= 3N-6\ (non-linear) \\ DOF_{vibration} &= 3N-5\ (linear) \end{aligned} . \tag{48}$$

For the case of a three-dimensional crystal, a primitive cell has N atoms. A crystal doesn't have translational or rotational movement. All of the DOF belongs to vibrational motions. Three independent coordinates are needed to describe the vibrational motions of which atoms in one primitive cell move with a same direction. Thus the acoustic modes have a degree of freedom of 3:

$$DOF_{acoustic} = 3. \tag{49}$$

The rest of DOF belongs to optical modes [34,35,74-77]:

$$DOF_{optical} = 3N-3. \tag{50}$$

#### *2.2.2.4. Symmetry and normal modes of 3D molecules/crystal*

On the basis of principles of DOF mentioned above, multiple coordinates ($x_1 \ldots x_{DOF}$) are needed to describe vibrational behavior. Through a coordinate transformation, the atomic coordinates ($x_1 \ldots x_{DOF}$) can be transformed to a series of normal coordinates ($Q_1 \ldots Q_N$) to make the kinetic energy and potential energy of each normal coordinate mutually independent. The principles of the coordinate transformation process will be briefly discussed.

For a 3D molecule, the bonding between each atom may makes the spatial distribution of atoms has a symmetry property. In this case, the structure of the entire molecule belongs to a point group. As a simplest example, a water molecule belongs to $C_{2V}$ point group. Each point group has a series of symmetry operations, such as inversion

(*i*), reflection (σ), rotation (C).[78] Under the confinement of a particular point group, a series of irreducible representations of a particular point group can be considered as the normal coordinates, which are orthogonal and complete. Each irreducible representation has a character for each symmetry operation, which leads to a character table. The character value of one irreducible representation is the sum of diagonal elements of a matrix form of the irreducible representation. Depending on the number of independent variables of each irreducible representation (e.g., dimension), an irreducible representation can be one dimensional (A or B, symmetry or anti-symmetry with respect to a principal axis, respectively), two dimensional (E), or three dimensional (T). Subscript g or u (symmetry or anti-symmetry with respect to an inversion center, respectively), subscript 1 or 2 (symmetry or anti-symmetry with respect to a reflection plane, respectively), and superscript ' or " (symmetry or anti-symmetry with respect to a non-principal axis, respectively) are often added to describe symmetry properties.[78] For example, the character table of the $C_{2v}$ group is:[79]

**Table 2-1. An example character table ($C_{2v}$)**

| $C_{2v}$(mm2) | # | E | $C_2$ | $\sigma_y$ | $\sigma_x$ | functions |
|---|---|---|---|---|---|---|
| $A_1$ | $\Gamma_1$ | 1 | 1 | 1 | 1 | z, $x^2$, $y^2$, $z^2$ |
| $A_2$ | $\Gamma_3$ | 1 | 1 | -1 | -1 | xy, $J_z$ |
| $B_1$ | $\Gamma_2$ | 1 | -1 | 1 | -1 | x, xz, $J_y$ |
| $B_2$ | $\Gamma_4$ | 1 | -1 | -1 | 1 | y, yz, $J_x$ |

In this table, $A_1$, $A_2$, $B_1$, and $B_2$ are irreducible representations. E, $C_2$, $\sigma_y$, and $\sigma_x$ are symmetry operations. Each irreducible representation may have corresponding linear functions, rotational functions, and quadruple functions. The representation of a 3D

molecule (Γ, i.e., the movements of the 3D molecule in Cartesian or other coordinates, $x_1 \ldots x_{DOF}$) can be considered as the sum of irreducible representations ($\Gamma_{irr}$) with coefficients ($a_\Gamma$):

$$\Gamma = \sum_{irr} a_\Gamma \Gamma_{irr} \,. \tag{51}$$

Each irreducible representation can be considered as a mode of movement (e.g., a vibrational mode, Q). The energy of each mode (kinetic and potential) is mutually independent. The coefficient of a particular irreducible representation ($a_\Gamma$) can be obtained from the character of the representation ($\chi_i$) for each symmetry operation (i) [34,35,75,76]:

$$a_\Gamma = \frac{1}{h} \sum_{symm\ ops} \chi_i \chi_\Gamma \,. \tag{52}$$

For example, the 3D movements of a water molecule (DOF=9) are:

$$\Gamma_{H_2O} = 3A_1 + A_2 + 2B_1 + 3B_2 \,. \tag{53}$$

Any movements of a water molecule can be considered as the sum of these normal modes. Each mode (irreducible representation) can be visualized (Figure 2-18). Water molecule has three vibrational normal coordinates ($Q_1$-$Q_3$).

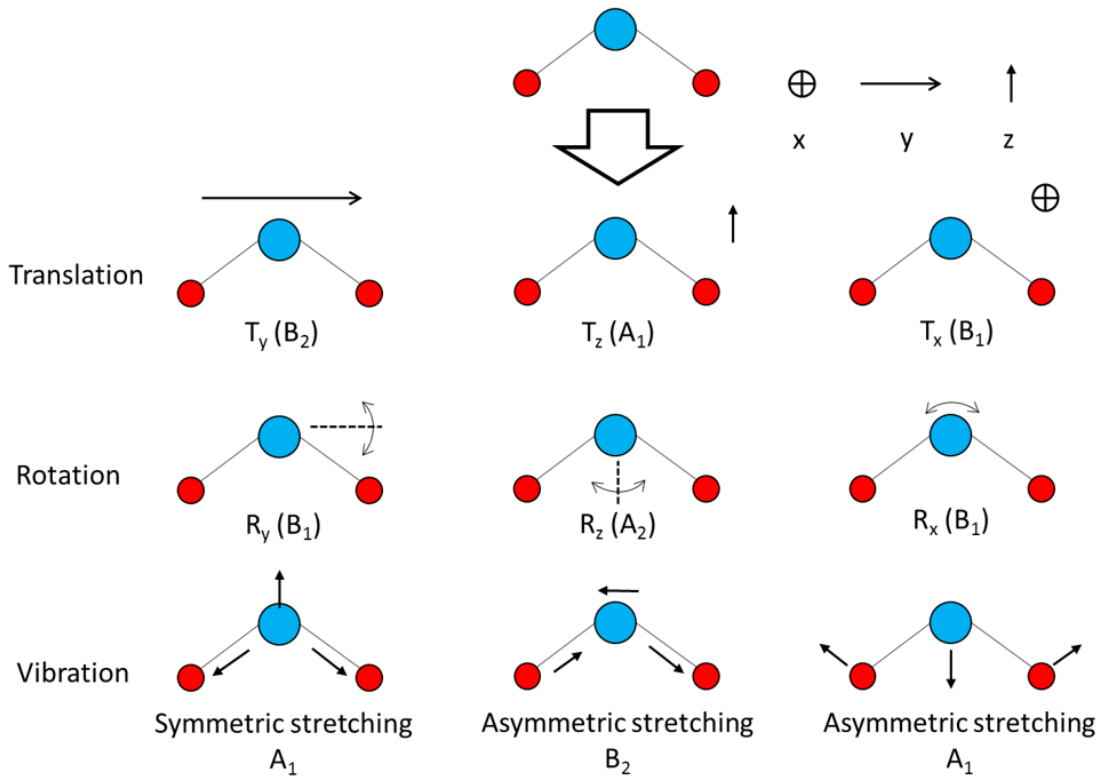


**Figure 2-18.** Visualization of normal modes of a water molecule.

For the vibration of a 3D crystal, the analyses of normal modes are essentially the same, except a crystal doesn't have translational and rotational motions. The combination of a point group symmetry with a translational symmetry leads to a space group symmetry.[74] The motions of each Wyckoff position can be deduced to a series of irreducible representations (normal modes), same with equation (52) and (51). Then a sum of irreducible representations for all Wyckoff positions give rise to the vibration modes of the crystal. [75-77] For example, crystalline silicon has $T_d$ point group symmetry and *Fd-3m* space group symmetry. The primitive cell has two Si atoms (DOF=6). Si atoms locate at Wyckoff position 8a. Therefore, atomistic motions of Si can be described as a sum of two irreducible representations (e.g., normal modes $Q_1$ and $Q_2$):

$$\Gamma_{Si} = T_{1u} + T_{2g} \ , \tag{54}$$

where $Q_1$ corresponds to $T_{1u}$ (an acoustic mode) and $Q_2$ corresponds to $T_{2g}$ (an optical mode).

#### *2.2.2.5. Vibration energy levels of 3D molecule/crystal*

As mentioned above, a coordinate transformation of a 3D molecule and a 3D crystal can describe the movements as a sum of normal modes. Since the energy of each normal mode is mutually independent, the Schrodinger equation of the system is:

$$\hat{H}\left|\Psi(Q_1...Q_N)\right\rangle = E\left|\Psi(Q_1...Q_N)\right\rangle. \tag{55}$$

Under harmonic oscillator approximation, the energy level of a mode *i* for a 3D molecule is:

$$E_i(n_i) = (n_i + \frac{1}{2})\hbar\omega_i; \tag{56}$$

the energy level of a mode *i* for a 3D crystal is:

$$E_i(n_i)_{phonon} = (n_i + \frac{1}{2})\hbar\omega_{i\,phonon}\ . \tag{57}$$

The value of the characteristic frequency of each normal mode (for a 3D molecule) and the function of the phonon dispersion of each normal mode (for a 3D crystal) are intrinsic properties of the molecule or crystal. The energy of the system can be considered as the sum of energy of each vibration mode.

### 2.2.3. Raman scattering theory

As mentioned in the previous section, for a particular normal mode $Q_i$, the energy level is:

$$E_i(n_i) = (n_i + \frac{1}{2})\hbar\omega_i. \tag{58}$$

Most molecules are at the ground state ($n_i$=0) according to Bose-Einstein distribution; a small amount of molecules are at the first excitation state ($n_i$=1). When a molecule is scattered by an incident photon, the molecule can be excited to a virtual state then transit back to a higher vibrational energy state; generating a scattered photon. Also, a molecule at the first excited state can be excited to a virtual state and transit to the ground state. The scattering process is called Raman scattering.[31-33] Under harmonic oscillator approximation, the change of the vibration quantum number must be ±1 [73]:

$$\Delta n_i = \pm 1 \ . \tag{59}$$

During this process, the energy of the scattered photon will change in a unit of $\hbar\omega_i$:

$$\Delta E = E_{incident} - E_{scattered} = \pm\hbar\omega_i \ . \tag{60}$$

Transition from ($n_i$=0 to 1) is named Stokes scattering; transition from ($n_i$=1 to 0) is called Anti-Stokes scattering. Also, the scattering process may not lead to change of energy state, which is called Raleigh scattering. Raleigh scattering has a much higher probability than Stokes and Anti-Stokes scattering do. The schematics of the three scattering processes are shown in Figure 2-19. It should be noted that $\Delta n_i$=±1 is applicable only to harmonic oscillator approximation. For a realistic molecule or crystal, $\Delta n_i$=±2 is occasionally observed ($\Delta E=2\hbar\omega_i$) with a much lower probability than normal Stokes scattering, which is often named overtone signal.

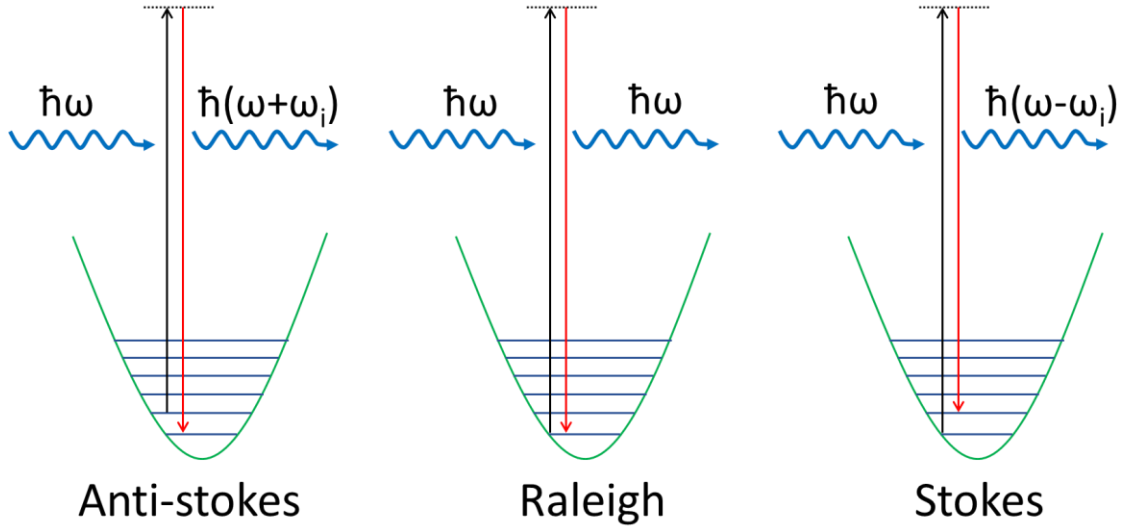


**Figure 2-19.** Schematics of light scattering processes with a normal mode $Q_i$. Left: Anti-Stokes scattering. Middle: Raleigh scattering. Right: Stokes scattering.

Besides the schematics mentioned above, Raman scattering processes can be described mathematically. During a scattering process, an oscillating electric field of incident photons ($E$) can lead to an oscillating polarization of a molecule [34,35]:

$$\vec{P} = \alpha \vec{E}\,, \tag{61}$$

where $\alpha$ is the polarizability tensor:

$$\alpha = \begin{pmatrix} \alpha_{xx} & \alpha_{xy} & \alpha_{xz} \\ \alpha_{yx} & \alpha_{yy} & \alpha_{yz} \\ \alpha_{zx} & \alpha_{zy} & \alpha_{zz} \end{pmatrix}. \tag{62}$$

The polarizability tensor is an intrinsic property of the molecular vibration; it can be approximated as a sum of a static term $\alpha_0$ and contributions from each normal mode:

$$\alpha(Q) = \alpha_0 + \sum \left( \frac{\partial \alpha}{\partial Q_i} \right)_0 Q_i + \ldots\,. \tag{63}$$

Since the vibration of a normal mode ($Q_i$) is also in a form of wave with a frequency $\omega_i$. The oscillation of polarization of a molecule as a result of an electromagnetic wave with frequency $\omega$ is:

$$\vec{P} = \alpha_0 \vec{E} e^{-i\omega t} + \sum_k \left( \frac{\partial \alpha}{\partial Q_i} \right)_0 Q_i \vec{E} (e^{-i(\omega+\omega_i)t} + e^{-i(\omega-\omega_i)t}) . \quad (64)$$

Equation (64) describes a Raman scattering process mathematically. The first term contributes to the oscillation of polarization with same frequency of incident electromagnetic wave, which corresponds to Raleigh scattering. The oscillations of polarization with frequencies $\omega + \omega_i$ and $\omega - \omega_i$ correspond to Anti-Stokes and Stokes scattering, respectively. Obviously, for a normal mode $Q_i$, the requirement for being Raman active (generating oscillations of polarization with frequencies of $\omega + \omega_i$ and $\omega - \omega_i$) is [34,35]:

$$\textit{Raman tensor for } Q_i : \alpha_i' = \left( \frac{\partial \alpha}{\partial Q_i} \right)_0 \neq 0 . \quad (65)$$

The derivative of the polarization tensor $\alpha$ to a normal mode $Q_i$ is defined as the Raman tensor $\alpha_i'$. The value of each element of the Raman tensor for a particular normal mode $Q_i$ is an intrinsic property of the material (similar with characteristic frequency $\omega_i$). The intensity of Raman scattering can be considered generally proportional to the square of Raman tensor. Also, the intensity is proportional to $\omega^4$ ($\omega$: incident photon frequency) and a term describing the effect of temperature [34,35]:

$$I_i \propto |\alpha_i'|^2 \propto \omega^4 \propto \frac{1}{\exp(-\frac{\hbar \omega_i}{kT}) + 1} . \quad (66)$$

The determination of Raman activity of a normal mode can be analyzed through a character table. If a particular normal mode (irreducible representation) has an associated quadruple

function in the character table, then the Raman tensor is not equal to zero theoretically (Raman active). On the other hand, if a particular mode has an associated linear function, then this mode is IR active (IR spectroscopy will not be discussed in this dissertation). In addition, if the point group has an inversion center, a normal mode cannot be both Raman-active and IR-active. [34,35]

According to the equation (61), the polarization direction of scattered photons (vector P) is dependent on each value of a Raman tensor. The diagonal elements of a Raman tensor will keep the polarization direction of scattered photons same as that of incident photons, while non-diagonal element will make the polarization direction of scattered photons different from that of incident photons. On the basis of this rationale, Raman scattering can be performed with a particular configuration, which defines the propagation direction and the polarization direction for both incident and scattered light. The notation of such configuration is:

$$Notation = A(ji)B \ , \tag{67}$$

where A and B are propagation directions of incident and scattered light, respectively; j and i are polarization directions of incident and scattered light, respectively. In this configuration, the intensity of Raman scattering for a particular normal mode $Q_i$ is:

$$I_i^{ij} = \left| \overrightarrow{e_i} \cdot \alpha_i' \cdot \overrightarrow{e_j} \right|^2 \ . \tag{68}$$

Based on equation (68), a helpful deduction can be achieved for Raman scattering of molecules, which are generally isotropically oriented. In this case, similar to polarizability tensor, Raman tensor of a mode $Q_i$ can be divided to contributions of an isotropic part ($\alpha_i'^{s}$) and an anisotropic part ($\alpha_i'^{a}$) [80,81]:

$$\alpha_i'^{s} = \frac{1}{3}(\alpha_i'_{xx} + \alpha_i'_{yy} + \alpha_i'_{zz})$$
$$\alpha_i'^{a} = \frac{1}{2}((\alpha_i'_{xx} - \alpha_i'_{yy})^2 + (\alpha_i'_{yy} - \alpha_i'_{zz})^2 + (\alpha_i'_{xx} - \alpha_i'_{zz})^2 + 6(\alpha_i'^{2}_{xy} + \alpha_i'^{2}_{xz} + \alpha_i'^{2}_{yz})) \quad . \tag{69}$$

To evaluate the change of the polarization direction for Raman scattering, the polarization direction of scattered photons (i) can be adjusted perpendicular or parallel to the polarization direction of incident photons (j). The depolarization ratio can be measured [80,81]:

$$Depolarization\ ratio = \frac{I_j}{I_i} = \frac{m \cdot (\alpha_i'^{a})^2}{(\alpha_i'^{s})^2 + n \cdot (\alpha_i'^{a})^2} \quad . \tag{70}$$

Obviously, according to equation (69) and equation (70), if the anisotropic part $\alpha_i'^{a}$ is zero (i.e., the Raman tensor is a diagonal matrix and elements are equal, $\alpha_i'^{a}=0$), polarization direction of Raman scattered photons is same as that of incident photons (i.e., depolarization ratio=0). If the isotropic part $\alpha_i'^{s}$ is zero (i.e., Raman tensor has no diagonal elements, $\alpha_i'^{s}=0$), Raman scattered photons are completely depolarized (i.e., the depolarization ratio is maximized). If both isotropic part and anisotropic part are non-zero, the Raman scattered photons will get depolarized to a certain degree but not completely depolarized. Therefore, for molecular samples, a rough Raman band assignment judging from the elements of Raman tensors can be made on the basis of polarized Raman experiments.

For the Raman scattering of a crystal, besides the rules mentioned above (Stokes scattering, Raman tensors of normal modes, polarization of Raman scattering), the phonon dispersion relations needs to be considered,[74] since vibrations in primitive cell propagate through the entire crystal. As mentioned in previous sections, a phonon has momentum

($\hbar q$). According to the rule of momentum conservation, photon(k)-phonon(q) scattering can occur only when their wavelengths are comparable (i.e., $k \approx q$). Since wavelengths of visible light (~$10^{-6}$-$10^{-7}$ m) are generally orders higher than those of primitive cell sizes (~$10^{-10}$ nm), an incident photon (using visible light) can scatter only with a long-wavelength phonon (i.e., the phonon has low momentum, $q \approx 0$). Therefore, only phonons near the center of the Brillouin Zone (Γ-point) can involve with Raman scattering.[74] Phonon modes in other parts of a dispersion curve (i.e., phonons with shorter wavelengths, not near Γ-point) can be probed using incident photons with shorter wavelengths (e.g., X-ray and neutron).

For the Raman scattering of crystals (solid-state materials), a few implications can be made on the basis of the above-mentioned principles. First, generally, since solid state materials can be fabricated as single crystals with specific orientations, according to equation (68), scattered light of a normal mode with non-diagonal Raman tensor elements will be depolarized, which offers an approach to determine the value of each element of Raman tensors. For randomly oriented polycrystalline materials, determination of polarization properties is same as that for molecules (equation (69) and equation (70)). Another implication is that most metallic crystals are not Raman active. For a metallic crystal, its crystalline structure is often very simple (e.g., FCC). Only one atom exists in one primitive cell, making all DOF belongs to acoustic modes. As mentioned above, for a space group with an inversion center, acoustic modes are not Raman-active. Even if the associated space group doesn't have an inversion center, frequencies of acoustic modes near Γ point are zero, which cannot lead to changes of energy of scattered photons.

### 2.2.4. Raman spectroscopy

On the basis of fundamentals of Raman scattering mentioned above, frequencies of scattered photons are depicted as the difference with the frequency of incident photons, named Raman shift:

$$Raman\ shift = \omega_{incident} - \omega_{scattered} \ . \tag{71}$$

To properly determine Raman shift values, incident light should have a fixed frequency (e.g., monochromatic). Besides the position (characteristic frequency $\omega_i$) and intensity (Raman tensor values) of a normal mode $Q_i$, for a realistic Raman spectrum, the intensity profile needs to be concerned. The scattering of the mode $Q_i$ will experimentally lead to a Raman band corresponding to $Q_i$. Sum of all Raman bands contributes to a Raman spectrum. Theoretically, for a Raman-active normal mode $Q_i$, the intensity of Raman band of $Q_i$ can be depicted by a Lorentzian distribution [82]:

$$I(\omega) \propto \frac{\Gamma_L}{(\omega - \omega_i) + \Gamma_L^{\,2}} \ . \tag{72}$$

The profile is a peak with maximum intensity at $\omega_i$, the full width half maximum (FWHM) is:

$$\mathrm{FWHM_L} = 2\Gamma_L \ . \tag{73}$$

For a realistic case, the peak profile can be broadened because of different factors (e.g., material disorder, instrumentation issues, etc.). The broadening effect can be depicted by a Gaussian function [82]:

$$I(\omega) \propto \exp(-\frac{(\omega - \omega_i)^2}{\Gamma_G^{\,2} / \ln 2}) \ . \tag{74}$$

The full width half maximum is:

$$FWHM_G = 2\Gamma_G \ . \tag{75}$$

The two types of profiles (Gaussian and Lorentzian) with a same FWHM are compared in Figure 2-20. For a realistic Raman peak, the broadening effect can be considered as a convolution between a Gaussian function and a Lorentzian function [82]:

$$I \propto \int_{-\infty}^{\infty} G(\omega', \Gamma_G) L(\omega' - \omega', \Gamma_L) d\omega' \ . \tag{76}$$

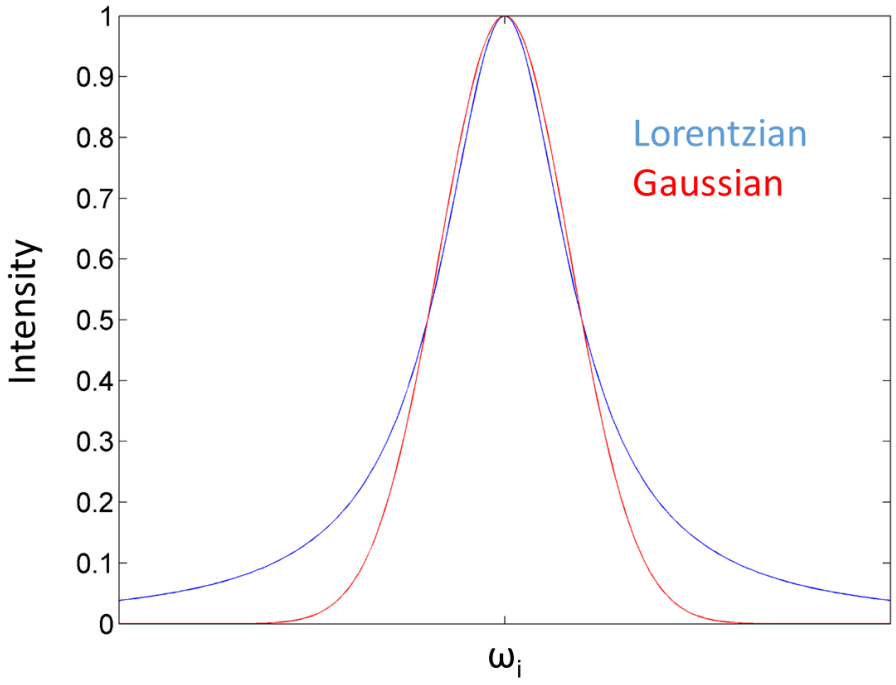


**Figure 2-20.** Schematics of a Lorentzian and a Gaussian profile centered at $\omega_i$ with a same band width.

Thus, based on the fundamental principles mentioned above, Raman scattering of vibrational normal modes of molecules and crystals leads to a Raman spectrum; aspects of a Raman spectrum (positions, intensities, and profiles) are closely related to material properties, which offers theoretical support of this dissertation.

### 2.2.5. Resonance Raman and Fluorescence

During the Raman scattering process, photon excitations may lead to other types of transitions. As mentioned above, molecules/crystals are excited to a virtual state during

Raman scattering. Probability of Stokes scattering is very low, since the virtual state doesn't exist physically (Figure 2-21 left). However, if the incident photon frequency is properly tuned, a molecule/crystal can be excited to a real state (most likely a particular vibrational level of a different electronic state (i.e., a vibronic state Figure 2-21 middle). Probability of Stokes scattering will be greatly enhanced. This process is named as Resonance Raman scattering.[83] To probe a proper excitation wavelength, an UV-Vis absorption spectrum can be measured first to analyze the proper frequency range, which can lead to a significant electronic state transition. Utilizing incident photons with a matched frequency with the electronic state transition frequency can potentially lead to a strong Resonance Raman enhancement. On the other hand, if a molecule/crystal is excited to a different vibronic state (e.g., Figure 2-21 middle), vibration energy relaxations, internal conversions, and intersystem crossings may occur and the molecule/crystal may transit from the first excited electronic state to the ground state, generating photons with a wide range of frequencies (fluorescence, Figure 2-21 right).[83,84] The fluorescence effect is unfavorable for Raman spectroscopic study since the fluorescence frequencies and Raman frequencies may overlap. By choosing high-wavelength or low-wavelength incident photons, the fluorescence effect can be avoided or pushed away from Raman effect, respectively. Therefore, to utilize the resonance Raman effect and minimize the fluorescence effect, a careful selection of photon wavelength is needed.

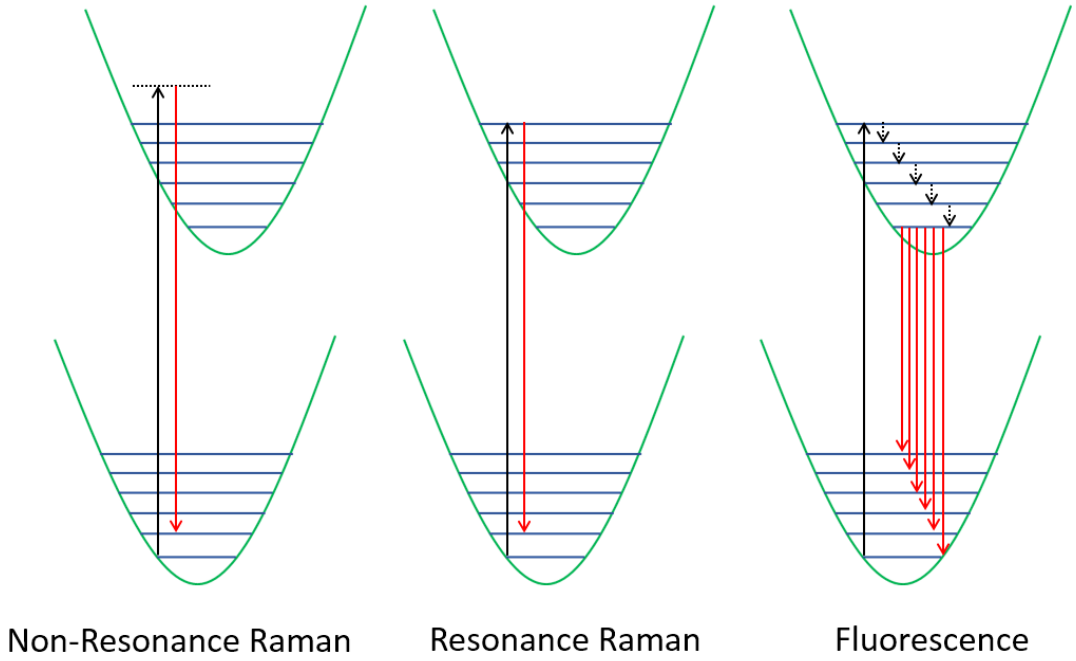


**Figure 2-21.** Schematics of non-resonance Raman, resonance Raman, and fluorescence.

### 2.2.6. Surface-enhanced Raman spectroscopy

Surface-enhanced Raman spectroscopy is an efficient tool to enhance Raman signal of materials. The fundamental concepts of surface-enhanced Raman spectroscopy were found and developed in the 1970s.[85,86] For a nanoparticle or a rough surface made of noble metal (e.g., Au and Ag), free electrons usually have high mobility. The oscillation of an electric field with a particular frequency (i.e., a photon) can lead to the oscillation of free charges of rough surface and nanoparticles. This process can be interpreted as an incident photon excites a local surface plasmon of a rough surface or a nanoparticle, or can be interpreted as an incident electromagnetic wave is in resonance with a local surface plasmon (LSPR), which leads to an enhanced local oscillating electrical field. At a particular frequency, the degree of resonance is maximized, leading to the maximized intensity of the local electromagnetic field. A schematic diagram of an excitation of local surface plasma and an enhancement of a local electric field is shown in Figure 2-22.

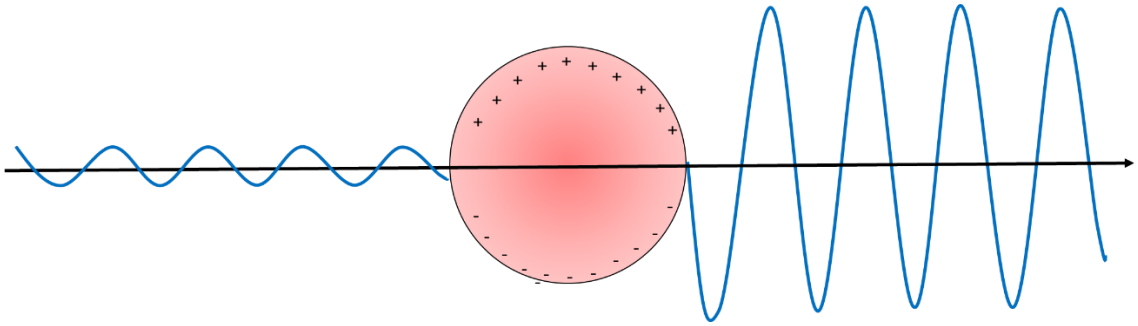

**Figure 2-22.** A schematic of an excitation of local surface plasma and an enhancement of a local electrical field by a noble metal nanoparticle.

If a material is in the vicinity of a nanoparticle or a rough surface, when the incident photon frequency is in resonance with the surface plasma frequency, the enhanced electromagnetic field will significantly enhance the Raman intensity (equation (64)). This method, which utilizes local surface plasmon resonance (LSPR) effect, is named surface-enhanced Raman spectroscopy (SERS). When a probed material is of extremely low amount or has extremely low Raman activity, SERS is a very powerful tool to realize efficient Raman analyses of the probed material.

## 2.3. Fundamentals of *in operando* Raman spectroscopy

Based on the fundamental concepts discussed in the previous section, vibrational structures of a particular type of material are intrinsic properties: the structure of the material determines the number of Raman-active normal modes, characteristic frequencies of normal modes, and Raman tensor values of each normal mode. These vibrational features will be translated to the number, positions, and intensities of Raman bands. Also, a particular material will have certain degree of other effects (e.g., disorders), which will influence the profiles of Raman bands.

In terms of dynamics of structural evolution, when the structure of a material is changed as a result of an external or an internal source, these changes will influence vibrational properties consequently. To be specific, if the structural evolution generates new Raman-active normal modes, changes Raman-active normal mode frequencies, changes Raman tensor values of each mode, or changes the degree of disorder, experimentally, new Raman bands, shift of Raman band positions, changes of relative Raman band intensities, and changes of Raman band profiles, will be observed, respectively. The correlation between spectroscopic properties and structural properties makes Raman spectroscopy applicable under operating conditions for an electrochemical energy storage device, which is *in operando* Raman spectroscopy. In this dissertation, *in operando* Raman spectroscopy is focused on the operation of pseudocapacitors and Li-ion batteries. The schematic diagram of the *in operando* Raman spectroscopic setup is shown in Figure 2-23.

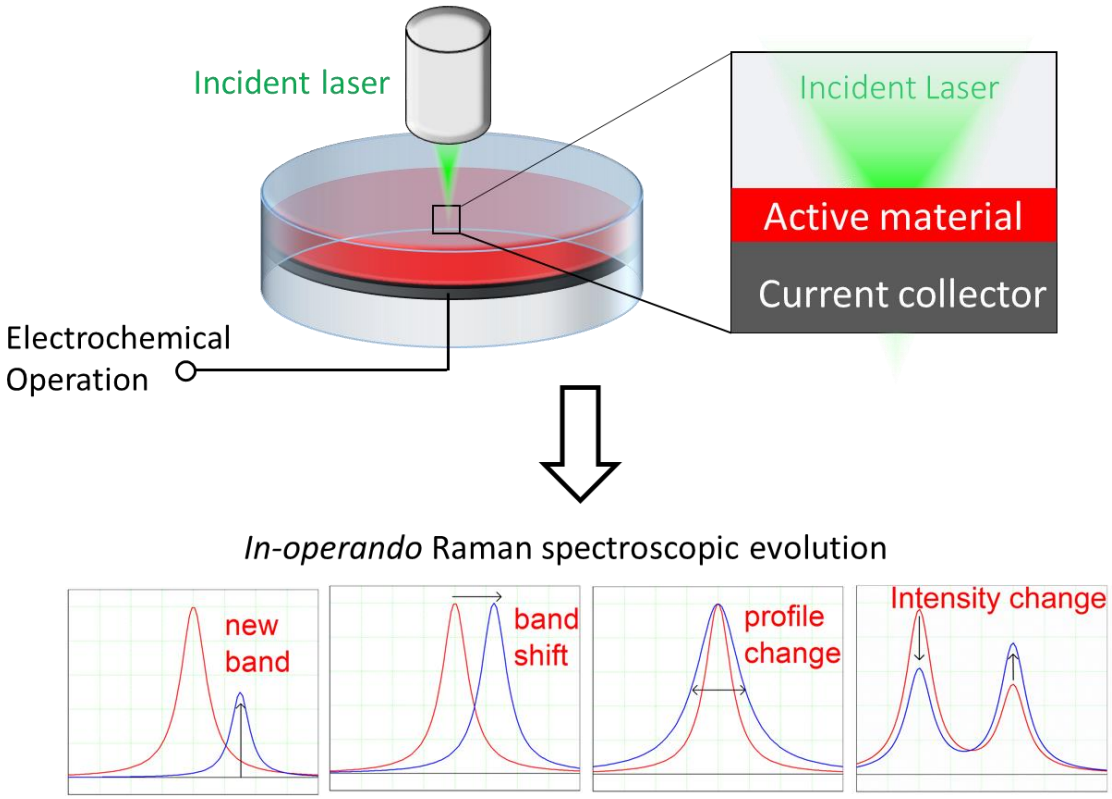


**Figure 2-23.** A schematic diagram of the *in operando* Raman spectroscopic configuration used in this dissertation.

As an electrochemical operation is applied to an electrode, the electrochemical reactions may lead to various structural changes; the spectroscopic evolution is a function of electrochemical parameters (potential *E*, current *I*, charge *Q*, time *t*, and etc.) :

$$I(\omega,n) = f(E,I,Q,t,....). \tag{77}$$

In this function, $I(\omega,n)$ is the spectroscopic evolution while $\omega$ is the Raman shift frequency and $n$ is the number of spectra. By carefully analyzing spectroscopic features, detailed structural changes can be unraveled, meeting the objective of mechanism probing of Li-ion battery and pseudocapacitive materials. Moreover, the information of different spectroscopic features (e.g., band positions, intensities, and profiles) can be quantitatively

correlated to electrochemical properties, which can offer valuable quantitative interpretation of energy storage mechanisms.

# 3. EXPERIMENTAL APPROACHES

## 3.1. Electrochemical measurements

The fundamental concepts of electrochemical analytical methods were briefly introduced in Section 2.1.3. To realize electrochemical measurements, the practical electrochemical cell configurations need to be considered.[43] Figure 3-1 shows the schematic configurations of two common types of measurements. To accurately evaluate properties of a specific material, a three-electrode configuration should be used. For a three-electrode measurement (Figure 3-1 right), the electrochemical potential of the working electrode (i.e., WE, the electrode to be analyzed) is referenced to a reference electrode (RE). Ideally, a reference electrode has a constant electrochemical potential. For aqueous electrolytes, common reference electrodes include Ag/AgCl, Hg/HgO, and other types. The electrochemical current for the operation of the WE is compensated by another electrode (counter electrode). An ideal counter electrode can supply an infinite current without interfering the electrochemical reactions of the WE. Common counter electrodes are platinum, activated carbon, and other types. In a three-electrode configuration, the electrochemical potential of working electrode can be accurately controlled, making three-electrode configurations well suited for fundamental electrochemical analyses. But, three-electrode configurations cannot be feasibility constructed since more electrical components are involved, also leading to the fact that the sizes of three-electrode configurations are generally bulky. Also, for three-electrode configurations, the bias between the working electrode and the counter electrode, which are responsible for current flow of the system, is unknown, which makes it not applicable as a device for energy storage.

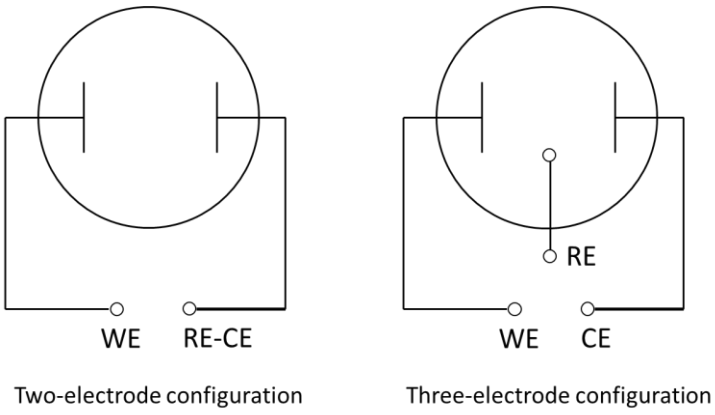


**Figure 3-1.** Schematics of two-electrode and three-electrode configurations.

For a two-electrode configuration (Figure 3-1 Left), beside the working electrode, another electrode is applied as both RE and CE, which supplies electrochemical current and serves as the potential reference for the WE at the same time. The major shortcoming of this configuration is that the potential of RE-CE may change with current output, which makes the potential of the WE not accurately controlled. Therefore, two-electrode configurations are not suited for fundamental investigations. However, two-electrode configurations can be feasibly fabricated with smaller sizes, and the bias between the two electrodes can be measured, although the exact potential of each electrode cannot be probed. Two-electrode configurations are very well suited for practical energy storage applications (such as supercapacitors and Li-ion batteries).

## 3.2. Raman spectroscopic measurements

Fundamental concepts of Raman spectroscopy were discussed in Section 2.2. To realize Raman spectroscopic measurements, Figure 3-2 shows the schematic configuration of a Raman spectroscopic system. The entire system can be separated into optics of illumination and optics of spectroscopic acquisition.

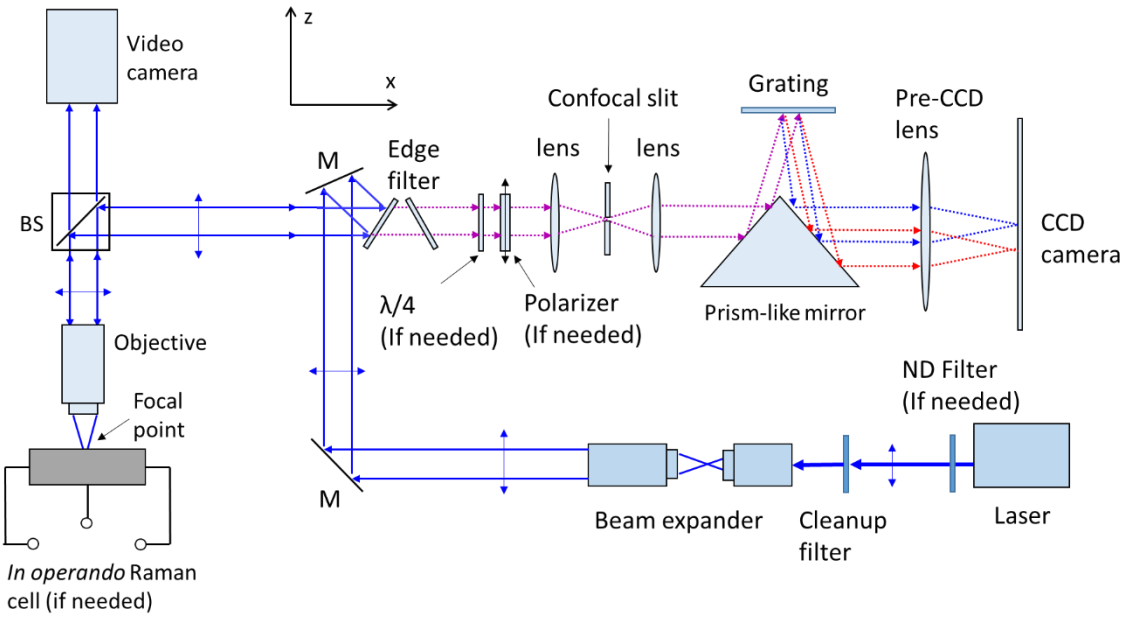


**Figure 3-2.** An experimental schematic of Raman spectroscopic measurements. Label of each beam: incident laser and scattered light (blue solid lines), Raman scattered light (purple dash lines), dispersed Raman scattered light (red and blue dash lines). The polarization direction and coordinates of the system are labeled.

### 3.2.1. The configuration of illumination

Optics of light illumination experimentally realizes Raman scattering between materials and photons. For the source of photons, lasers are mostly often used for Raman spectroscopic experiments, since lasers are highly collimated and monochromatic. In comparison, power of monochromatized broadband light is very little. The lasers used in this dissertation are Ar-ion lasers with wavelengths of 457 nm, 488 nm, and 514 nm, and He-Ne laser with wavelength of 632.8 nm. All incident lasers have a fixed polarization direction (labeled Figure 3-2), which makes the system suitable for polarized Raman study.

Since lasers are often not perfectly monochromatic, a cleanup filter is needed to eliminate all other frequencies except the frequency for Raman excitation. Also, a neutral density filter is often applied to adjust laser power, to eliminate possible effects such as sample burning. Then the laser is guided to a beam expander constructed by two objectives,

which enlarges the laser beam size for the confocality of spectroscopic acquisition (to be discussed in the next section). Then the laser with enlarged beam is guided to an edge filter. The edge filter has full reflection if the light frequency is below a critical value and a full transmission if the light frequency is above the critical value. This critical frequency is usually slightly higher than the laser frequency (approximately tens of $cm^{-1}$). After being fully reflected by the edge filter, the laser is focused on the sample surface (or an *in operando* Raman cell) by an objective. The numeric aperture (N.A.) of the objective is defined as:

$$N.A. = n\sin(\theta) \ . \tag{78}$$

In this equation, $\theta$ is the angle of focus cone, $n$ is the reflective index of the immersion matrix of the objective (for air, $n$=1). The minimum size of the focused laser beam is determined by light diffraction [87]:

$$d_{\min} = 1.22\frac{\lambda}{N.A.} \ . \tag{79}$$

Obviously, the spot will have a larger size for a long-wavelength laser and a low-N.A. objective, and *vice versa*.

### 3.2.2. The configuration of signal acquisition

At the focal spot of laser illumination, Raman scattered light will be collected by the objective. The efficiency of light collection is determined by *N.A.* value. Then the scattered light will be guided to a beam splitter with 99.9% reflection, which transmits a small fraction of light to the video camera of the microscope. The majority of scattered light is reflected to the edge filter. The edge filter will block the Raleigh scattering, Anti-Stokes scattering, and diffuse-reflected laser.

The scattered light will be focused by a lens, which will reconstruct the focal point of the sample at the confocal slit. Limiting the size of the slit comparable to the size of the focal spot (~ a few μm) can make sure that Raman scattering at the focal point of the sample is collected exclusively without other contributions. Increasing the size of the slit can increase the intensity of Raman scattering while leading to Gaussian broadening of Raman bands, decreasing confocality, and increasing chances of bringing in other non-confocal signal. After the focused scattered light is re-collimated by another lens, the collimated light will be dispersed by a reflection grating, which casts light with different wavelengths to different diffraction angles:

$$l\sin(\theta) = n\lambda \ . \tag{80}$$

In this equation, $l$ is the width of the grating groove; in this dissertation, $l$=1/1800 mm. $\theta$ is the diffraction angle and, $n$ is the diffraction order ($n$=1 for first order diffraction).

Then the collimated beams with different diffraction angles are focused at different locations of a CCD camera by a pre-CCD lens. The CCD camera collection area is made of a matrix of pixels. The signal acquired by different pixels is translated to a Raman spectrum. The refractory grating, pre-CCD lens, and CCD camera determine the resolution of a spectrum. The resolution of a spectrum can be derived from equation (80):

$$resolution = d\lambda = \frac{l\cos(\theta)dx}{f} \ . \tag{81}$$

In this equation, $f$ is the focal lens of the pre-CCD lens; $dx$ is the size of the CCD pixel. Obviously, a longer laser wavelength, a longer focal length, a smaller grating groove width, and a smaller CCD pixel size can lead to a higher resolution of a Raman spectrum, and *vice versa*.

Besides the spectroscopic acquisition, polarized Raman experiments can also be performed. By applying a polarizer with a polarizing direction same as that of the incident laser (*X* direction), then the polarization configuration of the system is (the propagation directions of the incident and the scattered beams are -*Z* and *Z*, respectively):

$$Configuration = \bar{Z}(XX)Z \ . \tag{82}$$

If a λ/4 wave plate is applied in front of the polarizer, the polarization direction will change π/4 accordingly. Thus the polarization configuration is:

$$Configuration = \bar{Z}(XY)Z \ . \tag{83}$$

## 3.3. *In operando* Raman spectroscopic setups

Fundamental concepts of *in operando* Raman spectroscopy were briefly introduced in Section 2.3. In this section, the technical approaches, which experimentally realize *in operando* Raman spectroscopic configurations for pseudocapacitors and Li-ion batteries, will be discussed.

### 3.3.1. The *in operando* Raman cell for pseudocapacitors

For *in operando* Raman studies of pseudocapacitor materials, systematic correlation between the *in operando* Raman spectroscopic evolution and the electrochemical potential is needed, which cannot be realized if the electrochemical potential of the WE is not well-controlled. Therefore, the *in operando* Raman cell should have the capability to perform three-electrode electrochemical tests and spectroscopic acquisitions at the same time. In this dissertation, the structure of the three-electrode *in operando* Raman cell is shown in Figure 3-3.[40,41] The cell body was made of Teflon PTFE to ensure electrical insulation. Then two series of concentric holes with different diameters were drilled on the cell body with accurate dimension control. A 316-stainless steel rod

was inserted from the bottom of the cell body, which is electrically connected to the working electrode (WE). A Pt mesh was applied as the counter electrode (CE) and the electrical connection of the CE is a Pt-wire inserted in a PTFE tube filled with epoxy. The WE and the CE are separated by a separator. The reference electrode (RE), which was wrapped by a PTFE tube, was inserted into the other side of the cell. The tip of the RE was located exactly near the edge of the WE and the CE. Both RE body, CE connection, and WE connection were wrapped by thin PTFE tapes to prevent leakage. To make it available for spectroscopic acquisition, a quartz window was adhered on a PTFE shim on the top of the cell. A cell cap was bolted to the cell body with a PTFE gasket using six bolts to prevent electrolyte evaporation. After the *in operando* Raman cell is configured, it can be mounted on the test stage (Figure 3-2) for *in operando* Raman spectroscopic analyses.

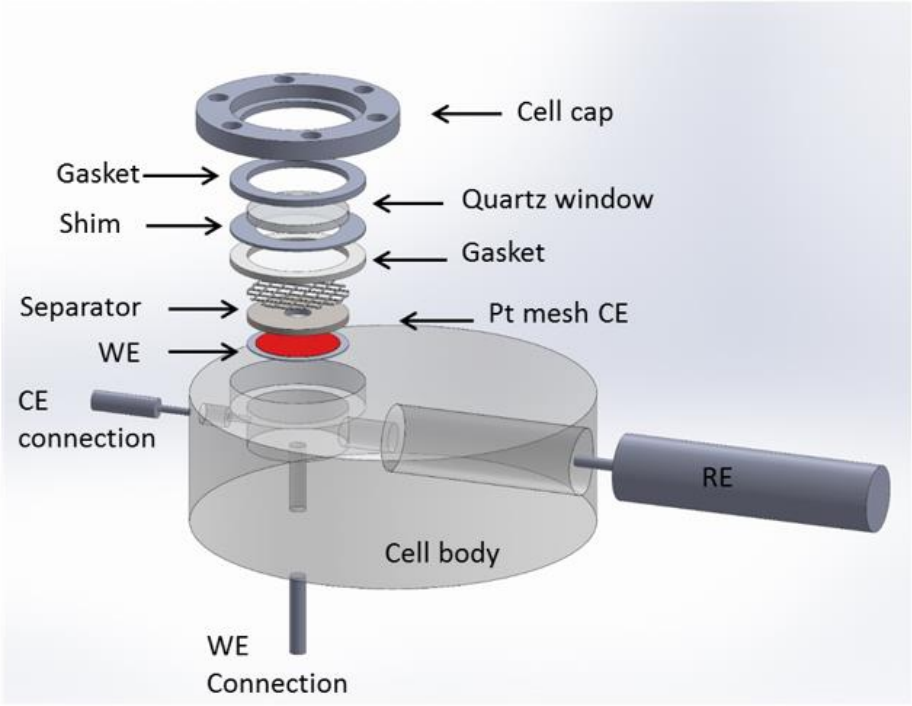


**Figure 3-3.** A schematic diagram of the *in operando* Raman cell for pseudocapacitors.

### 3.3.2. *In operando* Raman cell for Li-ion batteries

To study behavior of a Li-ion battery electrode, the potential is often referenced to Li metal ($Li^+/Li$). Therefore, Li metal is often applied as the counter electrode. During electrochemical operations of the WE, the potential of the Li metal (CE) can be considered almost stabilized at a constant value. Therefore, the Li ion metal can be considered as both the CE and the RE (i.e., pseudo-reference). In this case, a two-electrode configuration can basically provide an accurate potential of the WE. On the other hand, in non-aqueous electrolytes, an ideal reference electrode (similar with Ag/AgCl for aqueous electrolytes) is not available. Therefore, the *in operando* Raman configuration for Li-ion batteries in this dissertation is based on a two-electrode configuration.

For Li-ion battery applications, as mentioned above, the electrolytes are generally non-aqueous solution and anodes of Li-ion batteries are highly reductive. Therefore, hermetic air-tightness is strictly needed. The detailed construction of the *in operando* Raman cell for Li-ion battery application is shown in Figure 3-4. An ultrahigh-vacuum CF-flanged viewport and a blank CF flange were applied as the top part and the bottom part of the cell respectively. To ensure electrical insulation between the two parts, an ultrathin insulation tape was used to cover the bottom cell part. The hermetic airtightness sealing was achieved using a PTFE gasket. The WE is directly connected to the bottom cell part. The CE is connected to the top part of the cell with a series of meshes, shims, and springs. These electric components are fixed in a PTFE insulation ring to prevent electrical connection with other parts of the cell body. Then, the top part and the bottom part were clamped using six bolts to seal the entire cell. All of the bolts are wrapped by ultrathin insulation tapes to prevent electrical connection between the top part and the bottom part.

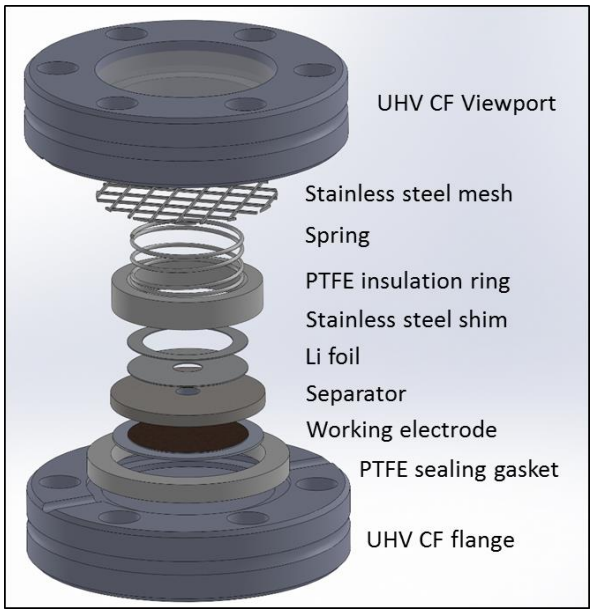


**Figure 3-4.** A schematic construction of the *in operando* Raman cell for Li-ion battery applications.

# 4. PROBING THE CHARGE STORAGE MECHANISM OF PSEUDOCAPACITIVE MANGANESE OXIDE

## 4.1. Introduction

As mentioned in previous chapters, a pseudocapacitor can store electrochemical energy on the basis of fast and reversible redox reactions, leading to capacitor-like electrochemical behavior. The first transitional-metal oxide-based pseudocapacitive material is $RuO_2$. The application of $RuO_2$ is strongly limited by its high cost and numerous other types of pseudocapacitive materials were explored, aiming for a replacement for $RuO_2$. Among all the explored pseudocapacitive materials, layered manganese oxide, which is often denoted as $\delta$-$MnO_2$, is very attractive, because the $\delta$-$MnO_2$ is non-toxic, extremely cheap, and has typical capacitive behavior in aqueous electrolytes.[88-91] Proven by a few early works [92], $\delta$-$MnO_2$ generally incorporate a certain amount of cations and water molecules and its chemical formula is $X_\delta MnO_2.nH_2O$ (X=cation, $\delta$~0.3). The valence state of Mn generally ranges from Mn (III) to Mn (IV).[92,93] The structure of $\delta$-$MnO_2$ features a layered structure composed of edge-sharing $MnO_6$ octahedra. The interlayer spacing is able to incorporate various types of cations and molecules, leading to the formula $X_\delta MnO_2.nH_2O$ mentioned earlier.[92-95] The crystalline structure of $\delta$-$MnO_2$ is shown in Figure 4-1.

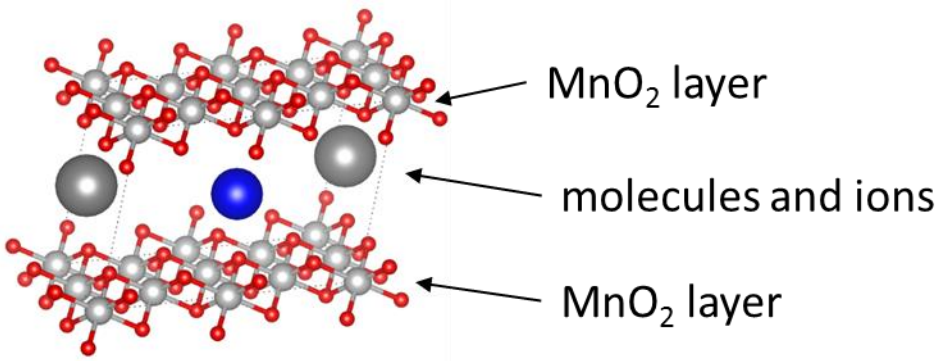


**Figure 4-1.** A schematic crystalline structure of pseudocapacitive δ-$MnO_2$.

In the past decades, the layered $MnO_2$ described above has been widely engineered to different types of pseudocapacitors by modifying morphologies or by modifying current collectors to enhance performance of electrochemical energy storage [89,91,96-98] However, the exact energy storage mechanism, especially the structural change associated with charge storage, is poorly understood. Generally, the energy storage in pseudocapacitive $MnO_2$ was simply explained as the change of the oxidation state: [88]

$$Mn(III) + e^{-} \leftrightarrow Mn(IV) \ . \tag{84}$$

Obviously, the simple valence change mentioned above do not provide any information on the structural evolution that contributes to energy storage. It is generally believed that various types of structural evolution can lead to changes in oxidation state of Mn, including phase transformations, cation incorporations, phase decompositions, and interfacial effects[56]. It is still not systematically clear which type of mechanism or combination of mechanisms contribute to the pseudocapacitive energy storage of $MnO_2$. Unlike Li-ion batteries, which solely rely on Li-ion-based electrolytes, charge storage of $MnO_2$ can be performed in electrolytes with a various types of cations. Therefore, understanding the structural evolution of $MnO_2$ in different types of electrolytes is vital for large-scale applications of $MnO_2$-based pseudocapacitors. More importantly, the current

level of the structural engineering of pseudocapacitive $MnO_2$ is mostly based on trial-and-error experiments rather than scientific theories, just because of the poor understanding of charge storage mechanisms.

## 4.2. Sample preparation and characterization

### 4.2.1. Sample preparation

Fabricating an electrode with simple and controlled geometry is very important for a fundamental mechanism study. In this chapter, the $MnO_2$ film electrodes were fabricated using sol-gel coating technique.[92,99] Firstly, $KMnO_4$ (oxidative precursor) was reduced by either fumaric acid or $MnSO_4$ (reductive precursor) to produce stable $MnO_2$ sol (0.001 M). When fumaric acid was applied as reductive precursor, a diluted $KMnO_4$ solution (20 mL, 0.001 M) was mixed with 50 μL of 1 M KOH solution and 200 μL of fumaric acid solution (0.033 M) with vigorous stirring for 30 min at room temperature. When $MnSO_4$ was applied as reducing precursor, the diluted $KMnO_4$ solution was mixed with 50 μL of 1 M KOH solution and 30 μL of 0.3 M $MnSO_4$ solution with vigorous stirring for 30min at room temperature. During this process, $KMnO_4$ was reduced to a golden brown stable $MnO_2$ sol (approximately 0.001 M). Subsequently, 150 μL of the resulting sol was drop-coated step-wisely on flat Ni foils with 7/16'' diameter. A hydrophobic cover slip (Hybri-slips, Sigma) was then placed on the drop, leaving a uniform layer of $MnO_2$ sol between the coverslip and Ni substrate. The sol-coated Ni foils (with cover slip on top) were then dried at room temperature, leaving a golden brown uniform film of $MnO_2$ on Ni foil. The films were then carefully rinsed by DI water for several times and finally dried in air at room temperature.

### 4.2.2. SEM characterizations.

Figure 4-2 shows the typical morphology of the model $MnO_2$ electrode used in this study. Obviously, the film is non-porous with a flat surface, as shown by the cross-sectional view of the thin film (Figure 4-2). Using the electrode with controlled geometry rather than a composite electrode or complex 3D nanostructures can reduce the uncertainties resulting from morphological complexity. Also, the mass and charge transport associated with the cycling of this electrode can be well controlled and monitored owing to the simple electrode geometry, which can offer unambiguous correlation between the structural features and the corresponding electrochemical properties.

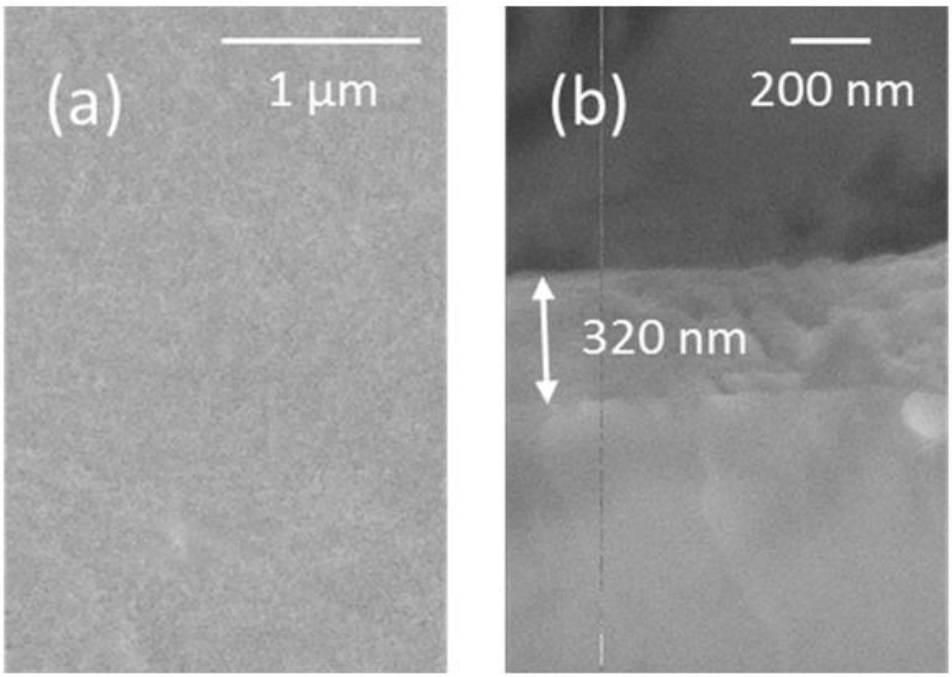


**Figure 4-2.** Morphology of a pseudocapacitive $MnO_2$ model electrode used in this chapter: (a) Top view of the thin-film $MnO_2$ electrode (b) Cross-sectional view of the thin-film $MnO_2$ electrode

### 4.2.3. Phase analyses:

To confirm the structure of the $MnO_2$ model electrode, X-ray diffraction (XRD) was used for phase analysis. The thickness of the model $MnO_2$ electrode is much thinner than the sampling thickness of the X-ray. To overcome this problem, $MnO_2$ powder derived

from the $MnO_2$ sol was used for identification of the phases. As shown in Figure 4-3, the obtained XRD patterns match well with those reported for birnessite layered $MnO_2$.[100,101] The interlayer spacing (i.e., $d_{001}$) can be determined from the angle of the (001) diffraction peak.[92,93] As demonstrated by a variety of reported studies, the $d_{001}$ is sensitive to the sizes, charges, and stoichiometry of the species incorporated into the structure.[92-95] To be specific, first, the incorporated cations can lead to significant electrostatic attraction between the cations and the negatively charged layers, leading to a contraction of interlayer spacing.[102] Second, the size of the incorporated species may affect the d-spacing sterically because of steric hindrance and charge density,[94,95,103] as demonstrated by experimental observation that the interlayer spacing of $MnO_2$ with incorporation of organic cations (e.g., $N(C_nH_{2n+1})_4^+$ or polyelectrolytes) synthesized under aqueous conditions.[94,95,104] The interlayer spacing ($d_{001}$) of the $N(C_nH_{2n+1})_4$-$MnO_2$ increases in the order of $d_{001}$-$N(C_2H_5)_4^+$ (0.96 nm), $d_{001}$-$N(C_3H_7)_4^+$ (1.03 nm), and $d_{001}$-$N(C_4H_9)_4^+$ (1.26 nm),[94] significantly higher than the $d_{001}$ of $MnO_2$ incorporated with neutral $H_2O$ (0.72 nm).[93,94] For the samples used in this chapter, the $d_{001}$ was calculated to be 0.71 nm, which is in the normal range of $d_{001}$ for as-synthesized hydrated $MnO_2$.[92,93]

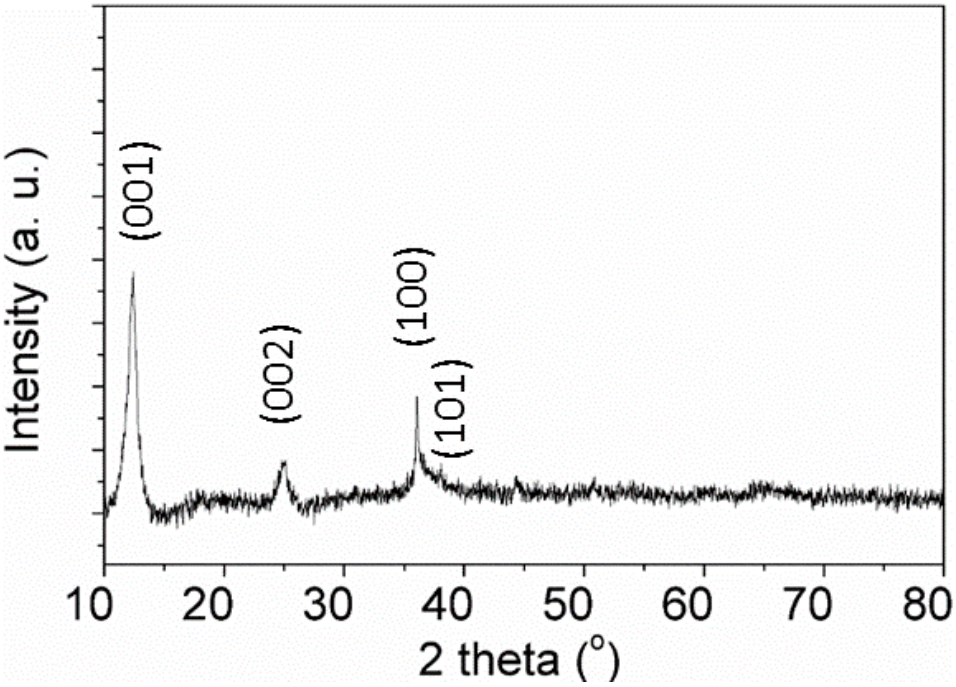


**Figure 4-3.** X-ray diffraction patterns of $MnO_2$ powder derived from $MnO_2$ sol and peak assignment.

### 4.2.4. Raman spectroscopic analyses

Figure 4-4 shows a full-range Raman spectrum of the $MnO_2$ model electrode, suggesting that the sample had pure phase since all noticeable Raman bands belong to $MnO_2$. The Raman bands within 200-700 $cm^{-1}$ describe the intrinsic vibration modes of $MnO_2$, while the Raman bands in the range 800-1400 $cm^{-1}$ should belong to the overtones of vibrational modes. In particular, the four major Raman bands in the range of 200-700 $cm^{-1}$ were marked as $\nu_1$ to $\nu_4$ as shown in Figure 1e. According to the preliminary assignments of Julien *et al*, the $\nu_1$ band (620-650 $cm^{-1}$) was assigned to the symmetric stretching vibration of Mn-O bond in the $MnO_6$ octahedral whereas the $\nu_2$ band (570-590 $cm^{-1}$) was assigned to the Mn-O vibration along the chains of the $MnO_2$ framework.[100,105,106] The properties of both bands were proven to be sensitive to the types of interlayer species.[100] This experimental dependence is mainly because different

interlayer species will lead to different d-spacing of the lattice structure (because of steric hindrance and electrostatic effects as mentioned above), which in turn affect the phonon properties, including the hardening/softening of different phonon modes (Raman band shifts), changes of polarizabilities of different modes (Raman band relative intensities), and different degree of structural disorder (Raman band widths). Such detailed and systematic correlation offers the possibility to systematically investigate the cation-incorporation mechanism from the effects of cation-sizes on Raman spectra.

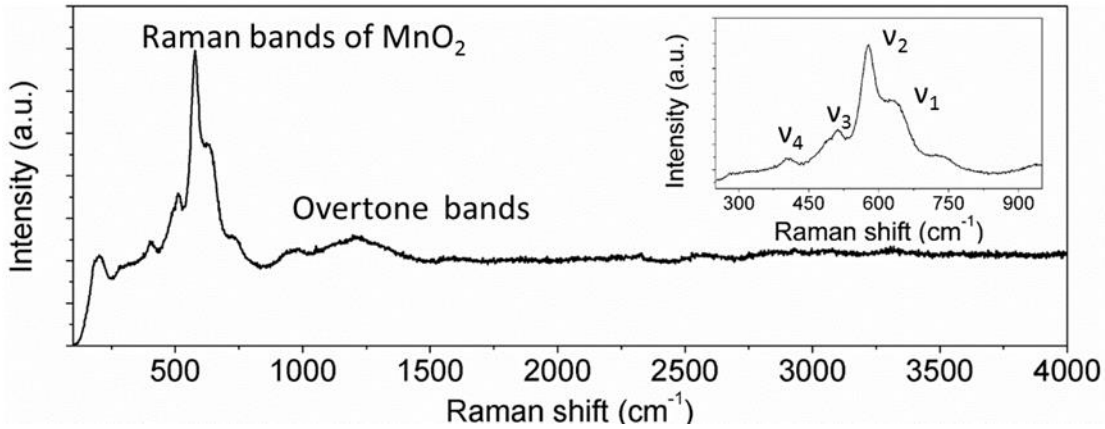


**Figure 4-4.** Raman spectrum of the $MnO_2$ thin film electrode. The inset includes the enlarged Raman spectrum, which shows four characteristic Raman bands and their corresponding labels $\nu_1$ to $\nu_4$.

### 4.2.5. General electrochemical behavior

To unravel the charge storage mechanism, the electrochemical behavior of the $MnO_2$ model electrode in a series of electrolytes was characterized with different cations prior to Raman spectroscopic study. Figure 4-5 shows the electrochemical behavior of the $MnO_2$ model electrode tested in 2M $LiNO_3$, $NaNO_3$, and $KNO_3$ aqueous electrolytes in the potential window between -0.1 V and 0.8 V (vs Ag/AgCl). Regardless of the type of electrolyte cations, the $MnO_2$ thin film model electrode exhibited excellent square-shape CV profile, suggesting that the $MnO_2$ model electrode display an ideal capacitive behavior.

Moreover, the excellent square-shape could be maintained as the scan rate was increased to 500 mV/s in all cases, regardless of the types of electrolyte cations used (Figure 4-6). The current increases when the potential of WE approaches 0.8 V in the anodic scan and -0.1 V in the cathodic scan are results of irreversible electrochemical reactions of the $MnO_2$ electrode, which are due likely to oxidative and reductive dissolution of $MnO_2$ to Mn compounds with higher oxidation states and $Mn^{2+}$, respectively.[107-109] Shown in Figure 4-5b are some typical charge-discharge curves of the $MnO_2$ model electrode in 2 M $LiNO_3$, $NaNO_3$, and $KNO_3$ aqueous electrolytes in the same potential window. The decreasing slope when the WE potential approaches -0.1 V in the cathodic process is attributed to the reductive dissolution of $MnO_2$. Obviously, electrochemical behavior of the $MnO_2$ model electrode is similar in different electrolytes, further confirming that the capacitive behavior is independent of the types of electrolyte cations and the same structural transformation contributes to the capacitive reaction.

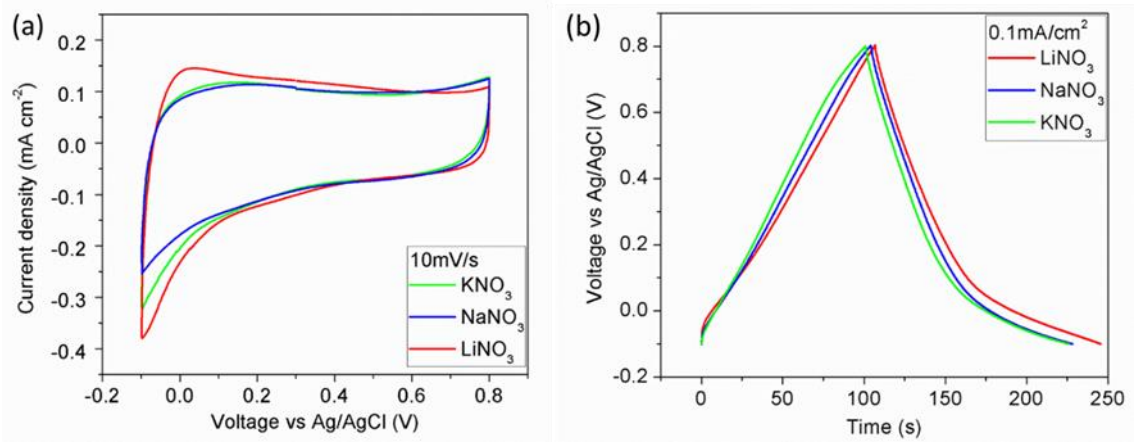


**Figure 4-5.** (a) The cyclic voltammograms (CV) of the pseudocapacitive $MnO_2$ thin film electrode in 2 M $LiNO_3$, 2 M $NaNO_3$ and 2 M $KNO_3$ aqueous electrolytes. The scan rate was 10 mV/s. (b) The charge-discharge curves of the model electrode in 2 M $LiNO_3$, 2 M $NaNO_3$, and 2 M $KNO_3$ aqueous electrolytes.

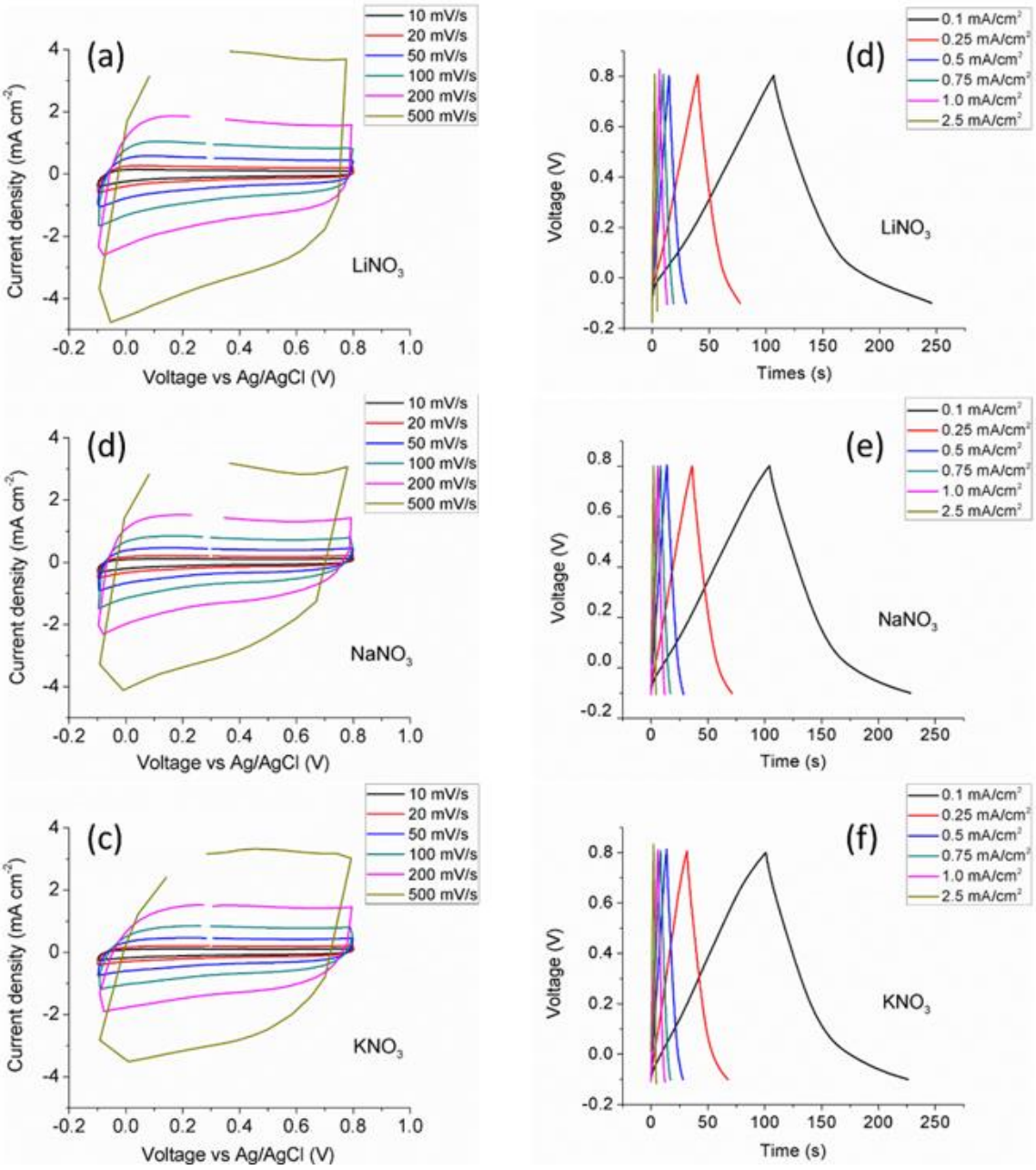


**Figure 4-6.** Cyclic voltammogram (CV) of pseudocapacitive $MnO_2$ thin film model electrodes with different scan rates in (a) 2 M $LiNO_3$ (b) 2 M $NaNO_3$ (c) 2 M $KNO_3$ aqueous electrolytes. The charge-discharge profiles with different current densities in (d) 2 M $LiNO_3$, (e) 2 M $NaNO_3$, and (f) 2 M $KNO_3$ aqueous electrolytes.

## 4.3. *In operando* Raman spectroscopy and vibrational analyses

### 4.3.1. Experimental aspects of *in operando* Raman measurements

#### *4.3.1.1. Technical details*

The *in operando* Raman spectroscopic experiments for $MnO_2$ in this chapter are performed using the three-electrode *in operando* Raman cell shown in Section 3.3.1. An Ar ion laser with wavelength of 514 nm was used as excitation of Raman spectra. The electrolytes are 2M $LiNO_3$, $NaNO_3$, and $KNO_3$ solutions, same as the electrochemical test mentioned above. Technically, during the *in operando* Raman spectroscopic acquisition, a potential stair-step experiment was applied to the $MnO_2$ thin film model electrode. A holding time of 100 seconds was used for each potential step to ensure satisfactory signal-to noise ratio for Raman data collection. The potential window of the potential stair-step experiment varied from 0 V to 0.7 V (with respect to Ag/AgCl) to avoid oxidative and reductive decomposition of the $MnO_2$ model electrode. To demonstrate the effects of irreversible reactions on Raman spectra, Raman spectra are collected beyond the potential window. As shown in Figure 4-7, the Raman band intensity decreased significantly at -0.1 V and 0.8 V, leading to significant error in quantitative Raman spectroscopic analyses of the cation sizes effects.

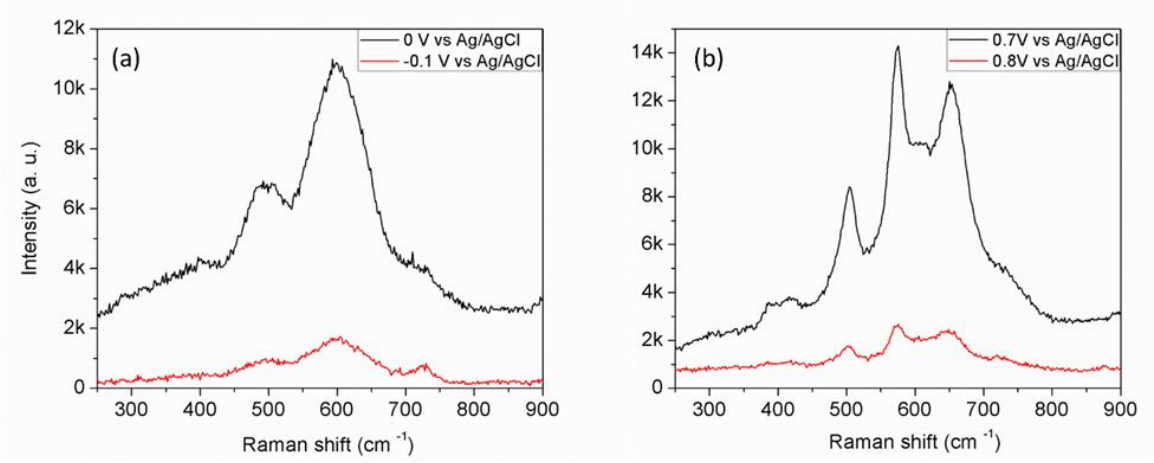


**Figure 4-7.** Comparison of *in operando* Raman spectra acquired at a given potential (vs Ag/AgCl): (a) at 0 V and -0.1 V (b) at 0.7 V and 0.8 V. The electrolyte was 2 M $LiNO_3$.

#### *4.3.1.2. Subtraction of Raman spectroscopic signal of electrolytes*

During an *in operando* Raman experiment, both Raman spectra of the electrode and the electrolyte can contribute to the as-collected Raman spectrum. As a result of the higher Raman activity of $NO_3^-$, the as-collected Raman spectra were dominated by Raman bands of the electrolyte (Figure 4-8). Also, the Raman bands of $MnO_2$ (below 700 $cm^{-1}$) had overlap with the band of $NO_3^-$ at 720 $cm^{-1}$. In order to perform precise spectroscopic analyses, the contribution of the electrolyte was subtracted on the basis of the Raman spectrum of the pure electrolyte. The $NO_3^-$ bands at 1047 $cm^{-1}$ were used as the internal standard to evaluate the contribution of the $NO_3^-$. The subtraction of Raman signal of the electrolyte was based on the equations below:

$$spectra(MnO_2) = (spectra(sample) - R * spectra(electrolyte)) \quad . \quad (85)$$

$$R = \frac{I_{1047}(sample)}{I_{1047}(electrolyte)}$$

The effect of the electrolyte subtraction is shown in Figure 4-8. The Raman band of the electrolyte at 720 $cm^{-1}$, which had overlap with Raman bands of $MnO_2$, was substantially reduced.

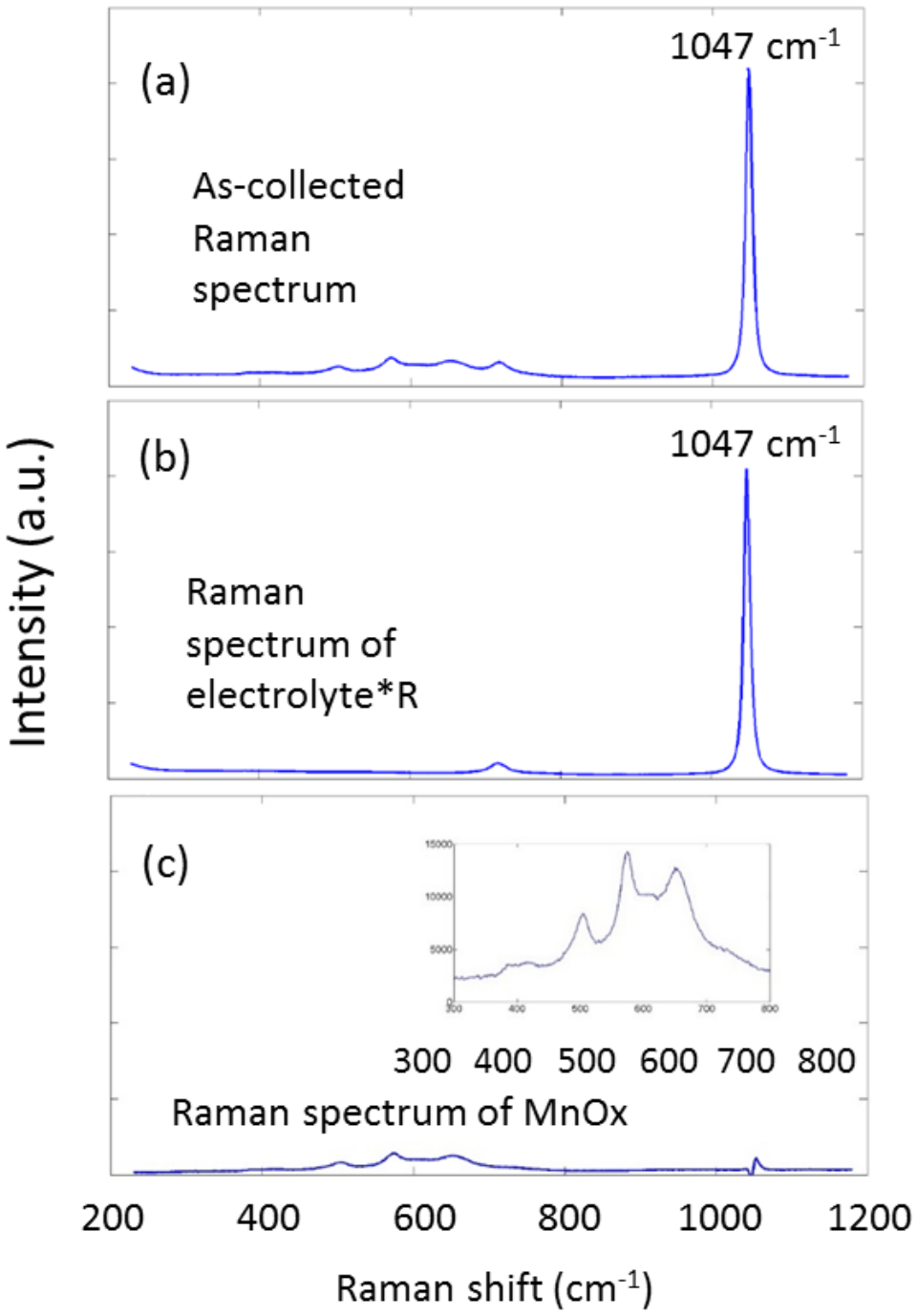


**Figure 4-8.** A schematic demonstration of subtraction of Raman signal from the electrolyte. (a) An as-collected *in operando* spectrum of $MnO_2$. 2 M $LiNO_3$ was used as the electrolyte. (b) The Raman spectrum of 2 M $LiNO_3$. (c) The spectrum of $MnO_2$ after subtraction of the electrolyte signal.

### 4.3.2. ***In operando*** **Raman spectroscopic evolution**

The Raman spectroscopic evolution of the $MnO_2$ model electrode was firstly investigated in a 2 M $NaNO_3$ aqueous electrolyte (Figure 4-9b). Before the cycle started (0.7 V vs Ag/AgCl), the Mn had the highest oxidation state within the range of Mn(III) to Mn(IV); the interlayer spacing was largely filled with water molecules from solvent. As the potential of WE was decreased from 0.7 V to 0 V (during the cathodic process), the oxidation state of the Mn was progressively lowered and more $Na^+$ ions are progressively incorporated into the interlayer space. During this process, the replacement of larger $H_2O$ (2.8 Å) by smaller $Na^+$ (0.99 Å) [102,110] would lead to more contraction of the interlayer spacing because of less steric hindrance and more electrostatic attraction. The overall effect is that the interlayer spacing will decrease gradually as the potential of WE gradually approach 0 V. It is noted that some water molecules may be always present within the interlayer space since the electrode was tested in an aqueous electrolyte. However, the existence of interlayer water molecules should not influence the incorporation of $Na^+$ since the amount of interlayer $Na^+$ is determined primarily by the oxidation states of Mn.

During the operation of the $MnO_2$ electrode, a few changes in spectroscopic features were observed. First, no new bands were observed, indicating that no new phases/species were generated during the process, which agrees with previous *in situ* X-ray adsorption (XAS) studies. The consecutive shift of the Mn K-edge XANES spectra without a change of the K-edge profile indicates systematic evolution of oxidation state without a phase change, regardless of the morphology of the $MnO_2$ electrode. [107,111] Second, the $\nu_1$ and $\nu_2$ bands are more prominent since they have higher signal to noise ratio and hence higher sensitivity to the cycling conditions than other bands in the spectra. The evolution of the $\nu_1$ and $\nu_2$ bands could be summarized as follows. First, the positions of the

$\nu_1$ band underwent a red shift while that of the $\nu_2$ band experienced a blue shift during the cathodic process. On the basis of the empirical facts that the $\nu_1$ band position has a positive correlation with interlayer spacing while the $\nu_2$ band has a negative correlation with interlayer spacing as mentioned by Julien *et al* [100], the band shifts during the cathodic process imply that the interlayer spacing decreases as water molecules are replaced by $Na^+$ ions, which was also observed by Hsu *et al.*[112] These consecutive band shifts are consistent with the change in $d_{001}$ of an $MnO_2$-based composite electrode as revealed by *in situ* XRD measurements, where significant differences in $d_{001}$ between the most-reduced state and the most oxidized state were observed.[102] Second, the $\nu_2$ and $\nu_1$ bands were also broadened gradually, which is ascribed to the increasing degree of Jahn-teller disorder upon cation incorporation during the cathodic process.[113-115] Third, the intensity ratio of $\nu_2$ band to $\nu_1$ band ($I(\nu_2)/I(\nu_1)$) increased first and then decreased as the potential of the WE was varied from 0.7 V to 0 V. Such band intensity ratio evolution is a direct result of the polarizability changes of the two vibrational modes resulting from the substitution of neutral water molecules by positively charged cations. The overall effects of the bands-shifts, band broadening, and intensity changes of $\nu_1$ band and $\nu_2$ band are a broad band centered at 582 $cm^{-1}$ with a shoulder band (Figure 4b). Besides the two stronger bands ($\nu_1$ and $\nu_2$), other two weaker bands ($\nu_3$ and $\nu_4$ band) also exhibited obvious evolution. During the cathodic process, the $\nu_3$ band evolved from a singlet peak to a doublet peak; the $\nu_4$ evolved from a doublet peak to a singlet peak. However, because of the relatively low intensity of the two bands, it is difficult to systematically analyze the evolution of the two bands. As expected, during the anodic process, the spectroscopic evolution of the Raman bands presented the reverse behavior of the cathodic process, including the red shift of $\nu_1$ band, the blue shift

of the $\nu_2$ band, band sharpening, and the change of $I(\nu_2)/I(\nu_1)$. The evolution of $\nu_3$ band and $\nu_4$ band was reversible as well, indicating that the cations incorporation mechanism is reversible when $Na^+$ was used as the electrolyte cation.

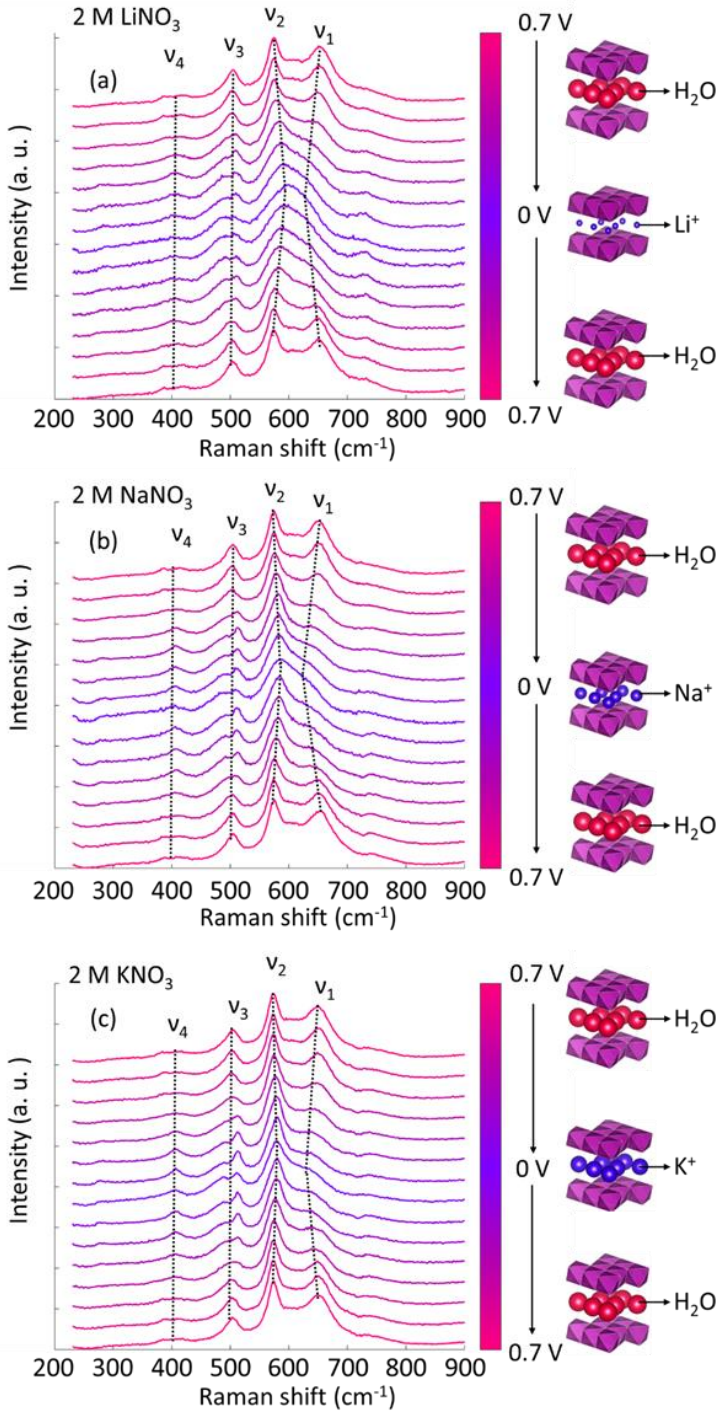

**Figure 4-9.** The Raman spectroscopic evolution of pseudocapacitive $MnO_2$ thin film when WE is cycled between 0.7 V, 0 V, and 0.7 V (vs Ag/AgCl) in (a) 2 M $LiNO_3$, (b) 2 M $NaNO_3$, and (c) 2M $KNO_3$ aqueous electrolytes. The dash lines were applied to show the evolution of band positions ($\nu_1$ to $\nu_4$) as function of the WE potential approximately. A color bar was used to depict the WE potential. The schematic sketches of cation-incorporated $MnO_2$ and water-incorporated $MnO_2$ corresponding to high-potential state and low-potential state respectively are also shown.

It should be noted that the charge storage mechanism cannot be concluded by the Raman spectroscopic evolution in one particular type of electrolyte cations. Unlike Li-ion batteries, whose charge storage could solely be completed in Li-based electrolytes, pseudocapacitive energy storage could be realized in different types of electrolytes for one particular material. The cation incorporation mechanism for one particular type of electrolyte cation is not necessarily valid for other electrolyte cations. Therefore, the *in operando* Raman experiment was performed in $LiNO_3$ and $KNO_3$ electrolytes as well, aiming to analyze the spectroscopic evolution in different sizes of electrolyte cations comprehensively (Figure 4-9a, c). Apparently, the spectroscopic evolution of $MnO_2$ in $LiNO_3$ and $KNO_3$ electrolytes is similar to the spectroscopic evolution in $NaNO_3$. First, the evolution of the cathodic process is the reverse of the anodic process, indicating the reversible electrochemical reactions regardless of the size of cations. Second, the band evolution exhibited same trends when different electrolyte cations were used: red shift of $\nu_1$ band, blue shift of $\nu_2$ band, band broadening, and changes of intensity ratios were observed during cathodic process. Third, the band evolution of the weaker bands ($\nu_3$ and $\nu_4$) also exhibited same evolution in different electrolyte cations. These experimental observations indicate that the same charge storage behavior prevails in electrolytes with different size of cations for pseudocapacitive $MnO_2$. However, since the Raman spectrum of $MnO_2$ is sensitive to the interlayer spacing, which is affected by the steric effect and electrostatic effect as mentioned earlier, the evolution of Raman bands (such as band

position and peak intensity ratios) may exhibit systematic trends when $Li^+$ (0.59 Å), $Na^+$ (0.99 Å), and $K^+$ (1.37 Å) are used.[110] In particular, such spectral trends may be more obvious at a more reduced state since more changes in interlayer spacing may be induced (besides interlayer water molecules), which may lead to more significant steric hindrance effects. Apparently, without quantitative band fitting, the band shift and band broadening are most significant when $Li^+$ ion was used (Figure 4-9a); at 0 V, the $\nu_1$ band and $\nu_2$ band merged as one broad band at approximately 600 $cm^{-1}$. For the case of $K^+$, the band shift and band broadening are least significant; the $\nu_1$ band and $\nu_2$ band are well separated at 0 V (Figure 4-9c). The apparent difference in band evolution when different electrolytes are used could be understood as a direct consequence of cation-size effect. Therefore, systematic and quantified Raman band analyses at different potentials are needed to systematically understand the cation-incorporation mechanism.

### 4.3.3. Cation size effect

The cation-size effects were evaluated for Raman spectra at different potentials when different electrolyte cations were used. To analyze the cation-size effects on Raman spectra quantitatively, systematic band fitting was performed for spectra at different potentials on the basis of Lorentzian profiles (Section 2.2.4. ). Especially, the Raman spectra at highest potential state (0.7 V vs Ag/AgCl) and the lowest potential state (0 V vs Ag/AgCl) are most valuable since Raman spectra at these two potential states represent the structure of the $MnO_2$ model electrode at the most oxidized/reduced state.

#### *4.3.3.1. High potential state*

Figure 4-10 shows the comparison of Raman spectra of the $MnO_2$ model electrodes in different electrolyte cations at the highest potential state (0.7 V vs Ag/AgCl). At 0.7 V,

Mn has the highest oxidation state within the potential window. The interlayer spacing is expected to be mostly filled with water molecules from aqueous electrolytes, regardless of the types of electrolyte cations. As expected, no difference in the Raman spectra of the $MnO_2$ electrode is observable, including the positions and intensity ratios for $\nu_1$ band and $\nu_2$ band. The position of $\nu_1$ band is 651 $cm^{-1}$ regardless of the electrolytes used. The position of $\nu_2$ band is 574 $cm^{-1}$ for $Li^+$ and 573 $cm^{-1}$ for $Na^+$ and $K^+$. These are in good agreement with the observation that no obvious structural difference at high potential state when different electrolyte cations were used.

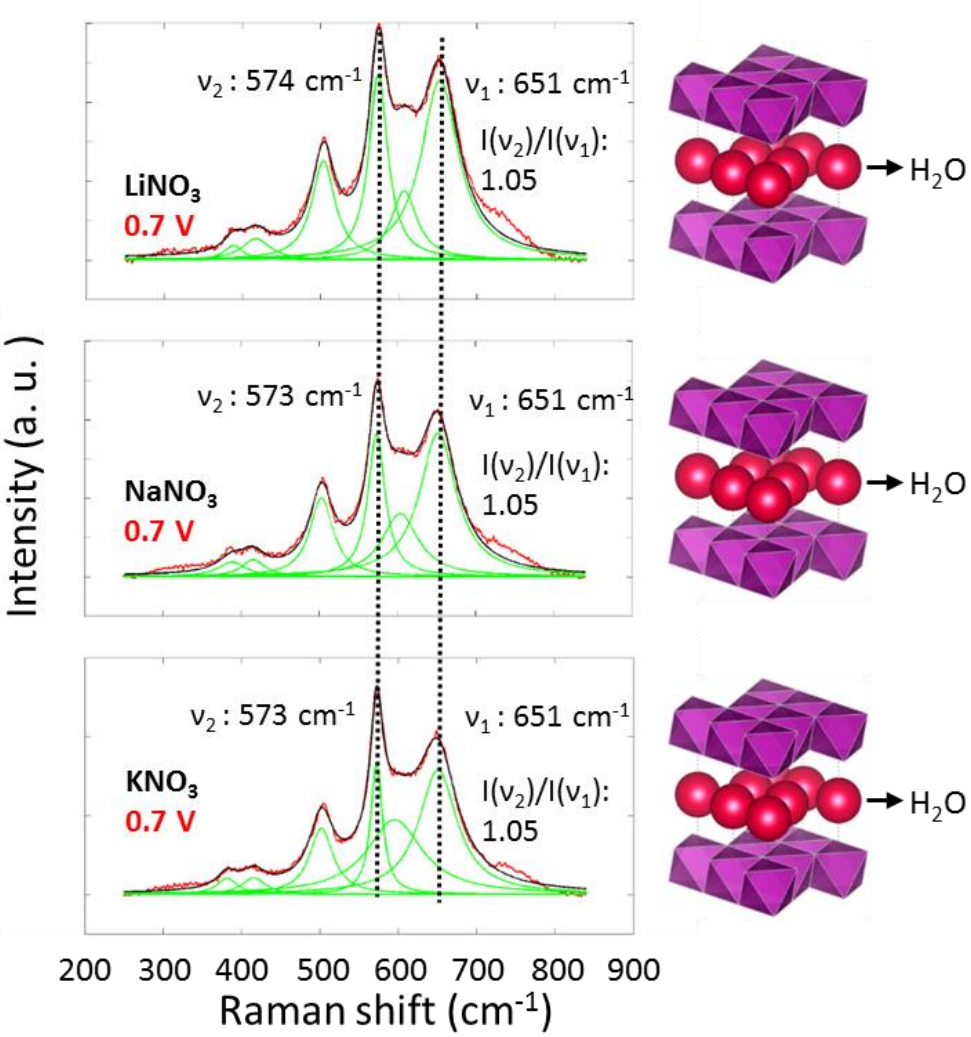

**Figure 4-10.** Raman spectra of the $MnO_2$ thin film model electrode when the potential of WE was 0.7 V in 2 M $LiNO_3$, $NaNO_3$, and $KNO_3$ aqueous electrolytes. The positions of $\nu_1$ band and $\nu_2$ band and $I(\nu_2)/I(\nu_1)$ are marked. The schematic sketches of water-incorporated $MnO_2$ corresponding to high-potential state when different electrolyte cations were used are also shown.

#### *4.3.3.2. Low potential state*

However, at a lower potential state, the oxidation state of Mn is lower and the interlayer space is filled with more electrolyte cations (in addition to some water molecules). Therefore, stronger steric hindrance effect is expected to lead to a greater change in interlayer spacing for a given cation, as demonstrated by a series of *ex-situ* XRD measurements of hydrated $MnO_2$ incorporated with different size of cations, even though the $MnO_2$ used in these ex-situ studies was not fully reduced.[94,95,104,116] The dependence of interlayer spacing on cation sizes is expected to induce systematic trends of phonon mode hardening/softening, polarizabilities, and degree of disorder. Figure 6 shows the comparison of Raman spectra at the low potential state (0 V and 0.1 V vs Ag/AgCl) in different electrolytes. As expected, the Raman spectra in different electrolytes exhibited significantly different features. At 0 V (Figure 4-11a), the position of $\nu_1$ band are located at 632 $cm^{-1}$, 626 $cm^{-1}$, and 616 $cm^{-1}$ for the case of $K^+$, $Na^+$, and $Li^+$, respectively. For the $\nu_2$ band, the positions are at 578 $cm^{-1}$, 582 $cm^{-1}$, and 586 $cm^{-1}$ for the case of $K^+$, $Na^+$, and $Li^+$, respectively. This observation systematically agrees with the phenomena that the $\nu_1$ band positions have positive correlation with interlayer spacing while $\nu_2$ band positions have negative correlation with interlayer spacing [100,117]. Besides the cation-size effect on band positions, the band intensity ratios also exhibited systematic correlation. The band intensity ratio $I(\nu_2)/I(\nu_1)$ are 1.84, 1.59, and 0.94 when $K^+$ (1.37 Å), $Na^+$ (0.99 Å), and $Li^+$ (0.59 Å) electrolyte cations were used, respectively. Such correlation may be attributed to the effect of cation size on charge density and polarizability of the vibrational modes.

Furthermore, the band width at 0 V is maximized for $K^+$ and minimized for $Li^+$, due likely to the fact that the cation size will significantly influence of the Jahn-Teller distortion of the $MnO_2$ structure. Similarly, the band positions, band intensities, and band widths at 0.1 V for different electrolyte cations exhibited similar correlation with cation sizes as shown in the Figure 4-11b.

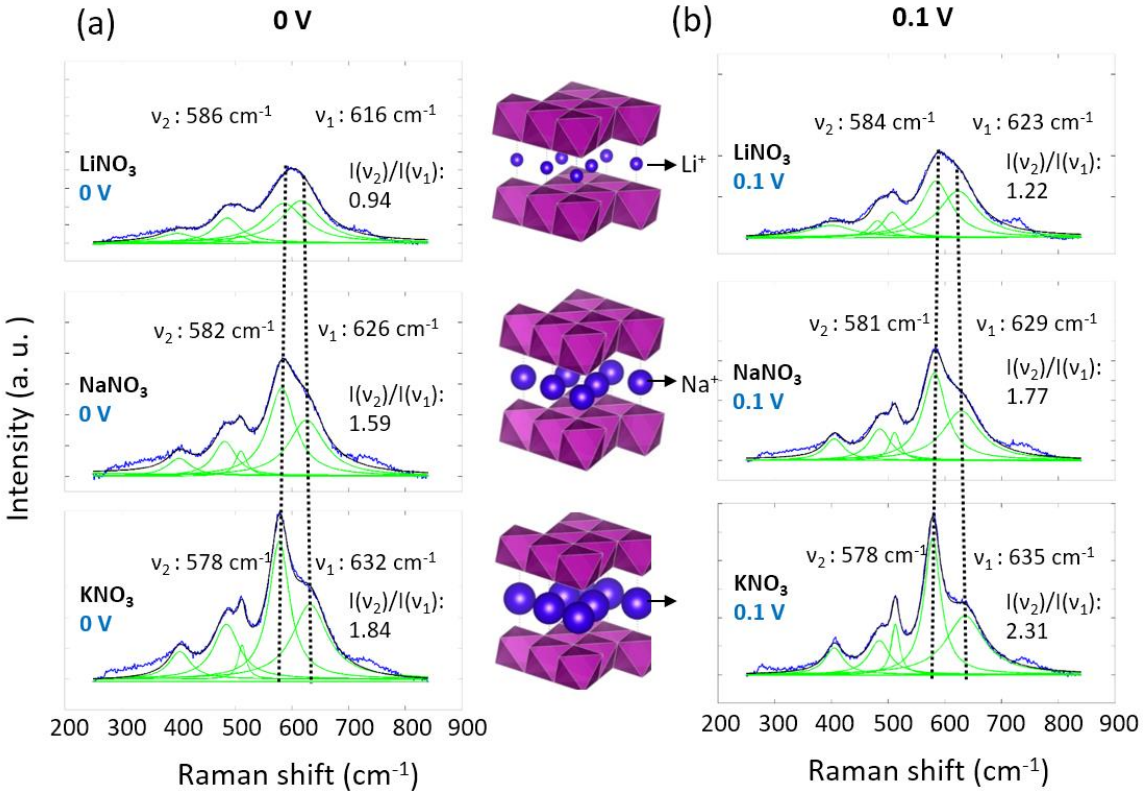


**Figure 4-11.** Raman spectra of the $MnO_2$ thin film model electrode when the potential of WE was (a) 0 V and (b) 0.1 V in 2 M $LiNO_3$, $NaNO_3$, and $KNO_3$ aqueous electrolytes. The positions of $\nu_1$ band and $\nu_2$ band and I($\nu_2$)/I($\nu_1$) are marked. The schematic sketches of cation-incorporated $MnO_2$ corresponding to low-potential state when different electrolyte cations ($Li^+$, $Na^+$, and $K^+$) were used are also shown.

It is noted that at 0 V (vs Ag/AgCl), the interlayer space is filled with more electrolyte cations as mentioned earlier (besides interlayer water molecules). In this case, the formula of the $MnO_2$ could be expressed as $X_{1.0-\delta}MnO_2.nH_2O$ at 0 V (X=$Li^+$, $Na^+$, and $K^+$), which is analogous to the most lithiated state for a Li-ion battery electrode. Particularly

for $Li^+$, the structure of $MnO_2$ at 0 V should be close to layered $Li_{1.0}MnO_2$, which is a fully lithiated Li-ion battery cathode material.[118,119] As expected, the Raman spectrum at 0 V (Figure 4-11a, top) showed significant similarity with the Raman spectrum of $Li_{1.0}MnO_2$;[117,120,121] a strong broad peak located at 600 $cm^{-1}$ (the overlap of $\nu_1$ band and $\nu_2$ band) and a weaker peak ($\nu_3$ band) located at 480 $cm^{-1}$ could match the Raman spectrum of non-hydrated $Li_{1.0}MnO_2$ very well.[117,120] While the $\nu_1$, $\nu_2$, and $\nu_3$ band are consistent, the weak $\nu_4$ band at 0 V is located at 402 $cm^{-1}$, which is different from that for the non-hydrated $Li_{1.0}MnO_2$ reported in literatures (420 $cm^{-1}$). [117,120] This minor discrepancy could be a result of the fact that the amount of the incorporated cations could be close to, but still less than, 1.0 and the inevitable presence of interlayer water molecules. Therefore, the similarity between the Raman spectrum of $MnO_2$ at 0 V in the $Li^+$-based electrolyte and that of $Li_{1.0}MnO_2$ indicates that the structure of $X_{1.0}MnO_2$ (X is electrolyte cation) could be used as a reasonable approximation to the structure of the cation-incorporated $MnO_2$ at 0 V.

## 4.4. Theoretical vibrational analyses

### 4.4.1. Cation-incorporated $MnO_2$ model

To further confirm the cation-size effect at the lowest potential (0 V) state, which is most significant within the potential window as observed experimentally, the vibration mode energies were calculated on the basis of a simple model, which is a cation-incorporated $MnO_2$ with a stoichiometry of $X_{1.0}MnO_2$ (X=Li, Na, or K). This $X_{1.0}MnO_2$ model simplifies the stoichiometry of cation at the most reduced state to make the theoretical phonon energy calculations executable. Recently, similar simplified models, which are based on tunnel-structured $MnO_2$ with incorporation of stoichiometric amount

of cations with different sizes, has been successfully used to explain the effect of cation sizes on charge storage properties.[110,122]

In our simplified model, the $X_{1.0}MnO_2$ model has a monoclinic structure (C2/m space group, No. 12), which is most common for Jahn-Teller distorted layered $MnO_2$ (Figure 4-12).[119,123,124] On the basis of the cell structure of $Li_{1.0}MnO_2$, the cations ($Li^+$, $Na^+$, and $K^+$) are positioned at the face centers (2d site) of monoclinic unit cells (Figure 4-12a). The monoclinic layered structure is a result of Jahn-Teller distortion of hexagonal layered $LiCoO_2$. $LiCoO_2$ has two Raman active modes: $A_{1g}$ and two-fold degenerate $E_g$ [115,117]. With Jahn-Teller distortion, the R-3m layered structure is lowered to a C2/m structure; the Eg mode will split to one $A_g$ mode and one $B_g$ mode, suggesting three Raman active modes for $X_{1.0}MnO_2$ (two $A_g$ modes and one $B_g$ mode).[117,120,121] However, more than three Raman bands were observed for $X_{1.0}MnO_2$, which was also reported by different previous works.[105,121] The reason for the fact is that the unit cell cannot fully describe the translational symmetry of monoclinic $X_{1.0}MnO_2$, since the incorporated cations are not located at the exact site (face center of the unit cell shown in Figure 4-12a), leading to the break of ideal translational symmetry and more observed Raman bands than predicted ones. Therefore, on the basis of the unit cell shown in Figure 4-12a, a 2x2x1 supercell was used to describe the cell structure and to perform phonon calculations (Figure 4-12b). For the lattice parameters, the cell parameters of $LiMnO_2$ was applied for Li-incorporated $MnO_2$.[119] The cell parameters of Na-birnessite and K-birnessite were used for Na-incorporated and K-incorporated $MnO_2$, respectively.[125] It is noted that these lattice parameters were initial values for geometry optimization calculations and adjusted during the geometry optimization process. Also, the coordinates of atoms would be adjusted accordingly.

For the details of DFT calculations, the energies, geometry optimizations, and phonon energies was calculated out using CASTEP module in Materials Studio 6.0. [126] The generalized gradient approximation (GGA) with PBE exchange-correlation functional was used for the calculations of electronic energies.[127,128] The norm-conserving pseudo-potentials were applied with an energy cutoff 750 eV. The k-points were set as 1x1x3 for the supercell. After the geometry optimization process, the lattice parameters and coordinates would be optimized. On the basis of the optimized structure, the phonon energy calculations were based on density functional perturbation theory (DFPT) using a CASTEP module.[126,129]

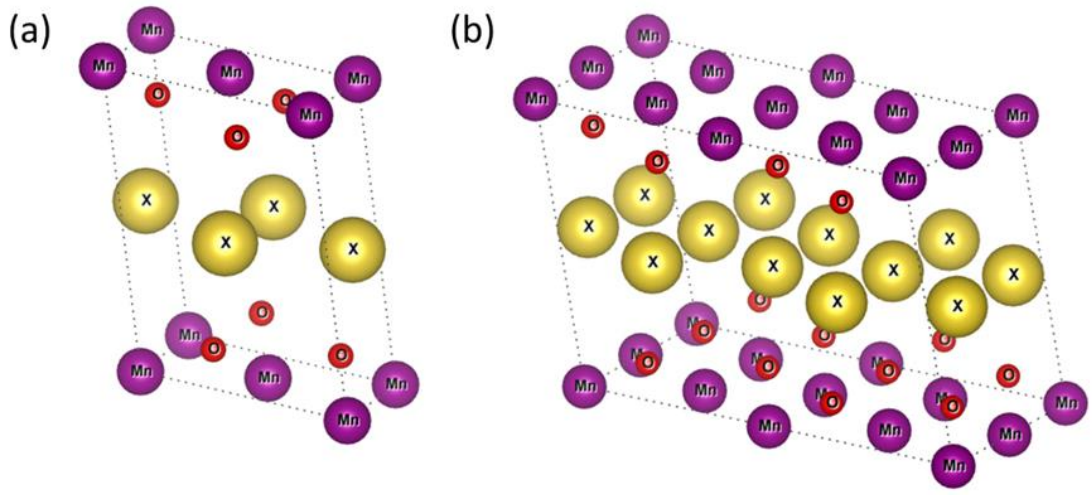


**Figure 4-12.** Cell structures of cation-incorporated $MnO_2$ model. (a) Primitive C2/m monoclinic cell. (b) The 2x2x1 supercell used for theoretical calculations.

### 4.4.2. Vibrational analyses

On the basis of the cell structures and space group (C2/m, No. 12) of cation-incorporated $MnO_2$ (Figure 4-12b), theoretical vibrational analyses can be performed. The space group (C2/m, No. 12) is based on 3D point group $C_{2h}$. The character table of $C_{2h}$ group is shown in Table 4-1.

**Table 4-1. The character table of the $C_{2h}$ point group**

| $C_{2h}$(2/m) | # | E | $C_2$ | i | σ | functions |
|---|---|---|---|---|---|---|
| $A_g$ | $\Gamma_1^+$ | 1 | 1 | 1 | 1 | $x^2$, $y^2$, $z^2$, xy, $J_z$ |
| $B_g$ | $\Gamma_2^+$ | 1 | -1 | 1 | -1 | xz, yz, $J_x$, $J_y$ |
| $A_u$ | $\Gamma_1^-$ | 1 | 1 | -1 | -1 | z |
| $B_u$ | $\Gamma_2^-$ | 1 | -1 | -1 | 1 | x, y |

For the cell structure shown in Figure 4-12b, the total number of atoms or ions is 32. Considering the multiplicity of C2/m group is 2, the number of independent atoms or ions is 16. Thus the total degree of freedom (DOF) is 48. The mechanical representations of cell model could be classified as the sum of the following irreducible representations:[79,130-132]

$$\Gamma = 12A_u + 18B_u + 10A_g + 8B_g \ . \tag{86}$$

Both $A_g$ and $B_g$ modes are Raman active while $A_u$ and $B_u$ modes are Raman inactive. Therefore, on the basis of theoretical calculations, theoretically the cation-incorporated $MnO_2$ has 18 Raman active bands, assuming the 2x2x1 cell structure. On the basis of elucidated symmetry properties of phonon modes, the energies of the phonon modes at Γ point were calculated on the basis of density function perturbation theory (DFPT) as listed in Table 4-2. Possibly because of the limited Raman activities for some modes, less than six bands were observed as mentioned in the main text. Particularly, the two $A_g$ modes, which have the highest energies, could be assigned as $\upsilon_1$ and $\upsilon_2$ mode (highlighted in Table 4-2).

**Table 4-2. Calculated frequencies of Raman active modes of $X_{1.0}MnO_2$ (X=Li, Na, and K) with corresponding mode assignments. The two Ag modes assigned as $\nu_1$ band and $\nu_2$ band are highlighted.**

| Li-incorporated $MnO_2$ | | Na-incorporated $MnO_2$ | | K-incorporated $MnO_2$ | |
|---|---|---|---|---|---|
| Calculated wavenumber (cm-1) | Symmetry properties | Calculated wavenumber (cm-1) | Symmetry properties | Calculated wavenumber (cm-1) | Symmetry properties |
| 284.6 | $B_g$ | 199.3 | $A_g$ | 138.4 | $B_g$ |
| 285.3 | $A_g$ | 199.8 | $B_g$ | 138.5 | $A_g$ |
| 368.5 | $A_g$ | 295.0 | $A_g$ | 211.8 | $B_g$ |
| 371.9 | $B_g$ | 295.4 | $B_g$ | 211.9 | $A_g$ |
| 381.9 | $B_g$ | 329.6 | $B_g$ | 251.9 | $B_g$ |
| 386.0 | $A_g$ | 330.0 | $A_g$ | 310.9 | $A_g$ |
| 420.9 | $A_g$ | 344.8 | $B_g$ | 311.5 | $B_g$ |
| 421.3 | $B_g$ | 411.6 | $A_g$ | 354.8 | $B_g$ |
| 429.3 | $A_g$ | 413.0 | $B_g$ | 355.3 | $A_g$ |
| 432.4 | $B_g$ | 435.8 | $A_g$ | 408.1 | $A_g$ |
| 439.4 | $A_g$ | 456.4 | $A_g$ | 426.6 | $A_g$ |
| 453.2 | $B_g$ | 457.1 | $B_g$ | 428.2 | $B_g$ |
| 495.4 | $A_g$ | 457.9 | $A_g$ | 432.2 | $A_g$ |
| 495.8 | $B_g$ | 460.2 | $B_g$ | 437.0 | $B_g$ |
| 567.4 | $A_g$ | 536.5 | $A_g$ | 516.6 | $A_g$ |
| 573.1 | $B_g$ | **583.1** | $A_g$ | **555.6** | $A_g$ |
| **597.9** | $A_g$ | 583.9 | $B_g$ | 555.6 | $B_g$ |
| **625.0** | $A_g$ | **630.5** | $A_g$ | **632.5** | $A_g$ |

To explain this assignment, Raman spectroscopic analyses under different configurations of polarization were conducted. Since the $MnO_2$ film sample is polycrystalline and isotropically oriented, the assignment rules based on polarization described in equation (69) can be applied. Raman tensors of $B_g$ modes don't have diagonal element (completely depolarized) while the all of three diagonal element of Raman tensor

of $A_g$ mode are non-zero (partially depolarized). Since the incident laser is polarized in x-direction (Figure 3-2), the intensities of $A_g$ modes in the $\bar{Z}(XY)Z$ configuration will be much lower than that in the $\bar{Z}(XX)Z$ configuration. On the other hand, the intensities of the $B_g$ modes will exhibit similar intensities in both $\bar{Z}(XY)Z$ and $\bar{Z}(XX)Z$ configurations. As expected, as the Raman spectra of the $MnO_2$ model electrode were collected in both configurations (Figure 4-13), the intensities of $\upsilon_3$ band are similar for both configurations, indicating that $\nu_3$ band is not an $A_g$ mode. However, the intensities of both $\nu_1$ band and $\nu_2$ band in the $\bar{Z}(XY)Z$ configuration are significantly damped compared to that in the $\bar{Z}(XX)Z$ configuration, which proved that the symmetry of both $\nu_1$ band and $\nu_2$ band belong to $A_g$.

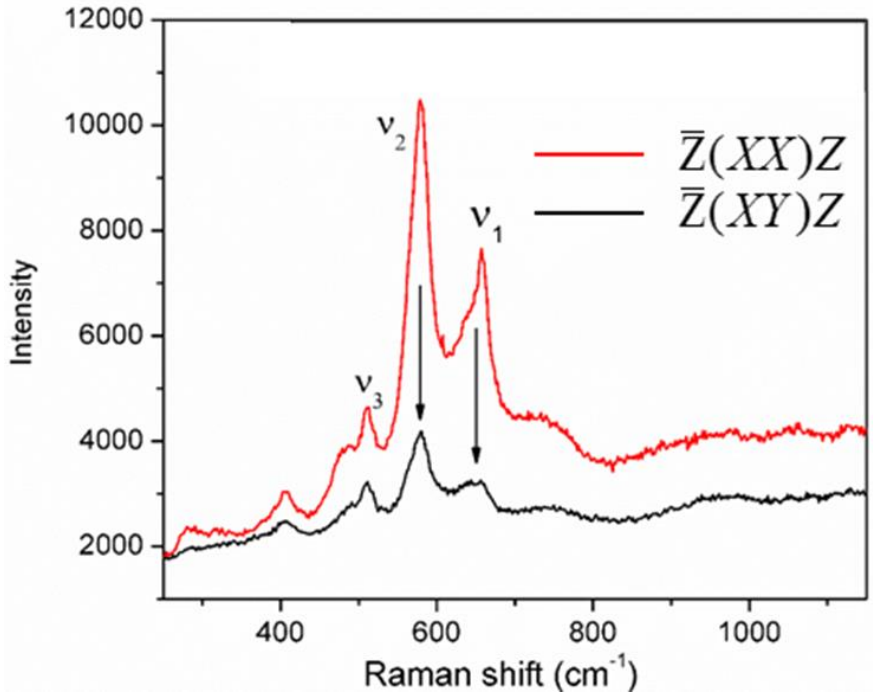


**Figure 4-13.** Raman spectra of the $MnO_2$ model electrode in $\bar{Z}(XX)Z$ and $\bar{Z}(XY)Z$ polarization configurations.

### 4.4.3. Calculated and experimental cation size effect

On the basis of the vibrational calculation and assignments, the experimental and calculated key band positions can be compared for charge storage mechanism analysis. The comparisons of the calculated vibrational modes frequency are shown in the right panel of Figure 4-14. For the $\nu_1$ band frequencies, the mode frequencies are calculated to be 625 $cm^{-1}$, 630 $cm^{-1}$, and 632 $cm^{-1}$ for X=Li, Na, and K, which matches the order of the band positions at 0 V obtained experimentally although the exact values of the calculated vibrational modes energies have discrepancies with experimental values. For the $\nu_2$ band frequencies, the mode frequencies were calculated to be 597 $cm^{-1}$, 583 $cm^{-1}$, and 555 $cm^{-1}$ for X=Li, Na, and K, also matching the order of $\nu_2$ band positions at 0V. It is noted that the calculated frequency of $\nu_2$ band (555 $cm^{-1}$) for X=K is quite different from the experimental value (578 $cm^{-1}$), since the simple $X_{1.0}MnO_2$ model cannot fully describe structures and properties of $MnO_2$ at 0 V, because of the variation in the amount of $K^+$ cations and the existence of interlayer water molecules as mentioned previously. Therefore, theoretical calculations of vibrational modes based on cation-incorporated $MnO_2$ model comprehensively corroborated the size effect on Raman spectra of cations from different electrolytes.

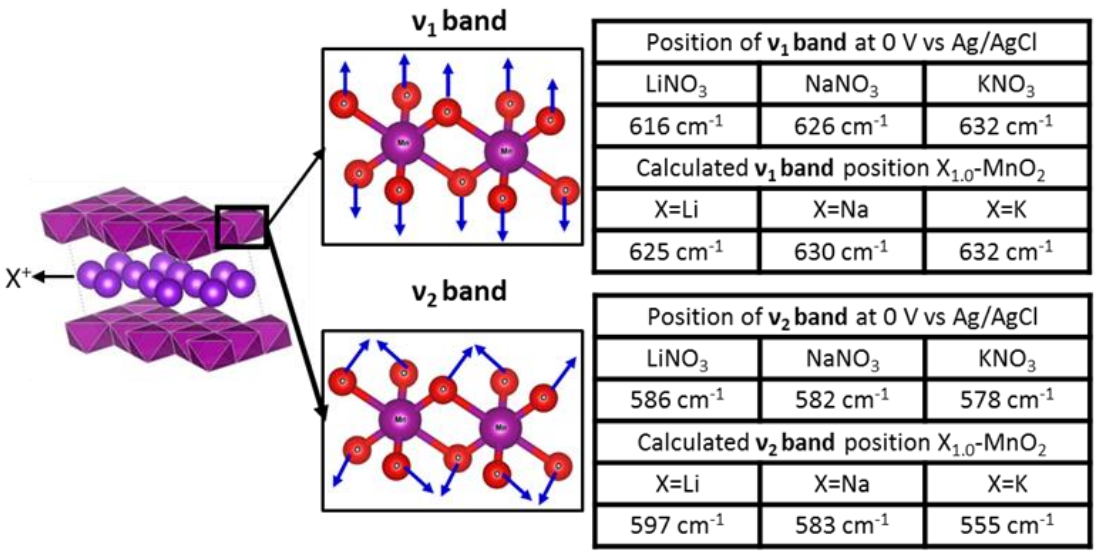


| Position of $\nu_1$ band at 0 V vs Ag/AgCl | | |
|---|---|---|
| $LiNO_3$ | $NaNO_3$ | $KNO_3$ |
| 616 $cm^{-1}$ | 626 $cm^{-1}$ | 632 $cm^{-1}$ |
| Calculated $\nu_1$ band position $X_{1.0}$-$MnO_2$ | | |
| X=Li | X=Na | X=K |
| 625 $cm^{-1}$ | 630 $cm^{-1}$ | 632 $cm^{-1}$ |

| Position of $\nu_2$ band at 0 V vs Ag/AgCl | | |
|---|---|---|
| $LiNO_3$ | $NaNO_3$ | $KNO_3$ |
| 586 $cm^{-1}$ | 582 $cm^{-1}$ | 578 $cm^{-1}$ |
| Calculated $\nu_2$ band position $X_{1.0}$-$MnO_2$ | | |
| X=Li | X=Na | X=K |
| 597 $cm^{-1}$ | 583 $cm^{-1}$ | 555 $cm^{-1}$ |

**Figure 4-14.** Left panel: The model $X_{1.0}MnO_2$ used for the calculation of vibration modes with schematic sketches of $\nu_1$ mode and $\nu_2$ mode. Right panel: The comparison of the positions of $\nu_1$ band and $\nu_2$ band at 0 V and calculated values based on DFPT calculations.

## 4.5. Correlation between spectroscopic and electrochemical behavior

### 4.5.1. Correlation with state of charge

As the cation-size effects were elucidated on the basis of the spectroscopic analyses and theoretical calculations mentioned above, the evolution of Raman band properties at different potentials can be correlated with the charge stored in the $MnO_2$ electrode. The fraction of the cations stored in the $MnO_2$ electrode can be described by the state of discharge (SOD), which can be calculated from the integration of the CV curves in Figure 4-15. To be specific, the SOD at the high potential state (0.7 V vs Ag/AgCl) and the low potential state (0 V vs Ag/AgCl) are defined as 1 and 0 in this work, respectively. When plotted as a function of potentials (Figure 4-15), the SOD curve is largely linear, but with a slight convex shape because of some deviation from ideal capacitive behavior. Also plotted with the SOD curve in Figure 4-15 are $\nu_1$ band positions, $\nu_2$ band positions, band intensity ratios $I(\nu_2)/I(\nu_1)$, and band widths of $\nu_2$ band as a function of potentials for

different electrolyte cations. At 0.7 V, all band properties are almost the same for different electrolyte cations when it is fully discharged (the SOD is 1) because the interlayer spacing is filled mostly with water molecules. As shown in Figure 4-15a, the positions of $\nu_1$ exhibited red shifts as the SOD was decreased; the effect was most significant for Li and least significant for K, since smaller cation can lead to more significant steric effects as mentioned in previous sections. Similarly, the positions of $\nu_2$ band exhibited blue shifts (Figure 4-15b) as cations were gradually incorporated; the significance of the shifts for different cations followed the same order as that for the red shifts of the $\nu_1$ band. The *in situ* phonon hardening/softening effect (Figure 4-15 a and b) is consistent with the change in d-spacing revealed from *in situ* XRD analysis of a composite electrode based on $MnO_2$ in KCl and LiCl electrolyte solutions, where the $d_{001}$ at the most oxidized state remained the same for both electrolytes but the $d_{001}$ at the most reduced state is smaller for $Li^+$ incorporation than that for $K^+$ incorporation.[102]

Meanwhile, the evolution of the intensity ratios followed a different trend; it became most pronounced at an intermediate stage of discharge (Figure 4-15c). While the most significant band shifts were observed for $Li^+$ (and the least significant for $K^+$), the most noticeable intensity ratio changes were observed for $K^+$ (and lease significant for $Li^+$). Raman bands intensities depend strongly on the charge of the interlayer species, which influence the distribution of the charge density within the $MnO_2$ crystal structure. The insertion/extraction of larger cations may lead to a more significant change in polarizability of the vibrational modes. Finally, the evolution of band width also exhibited significant cation-size effects (Figure 4-15d); the significance of band broadening of $\nu_2$ band is most obvious for $Li^+$ and least obvious for $K^+$. Such experimental observation matches the fact

that smaller-size cations will lead to stronger Jahn-Teller distortion, which leads to more band broadening effect. In summary, the cation sizes effect is quantified as a function of the electrochemical charge storage, providing systematic correlation of phonon mode hardening/softening, changes of phonon polarizability, and changes of structural disorder with the steric effects of the incorporating cations from the electrolyte.

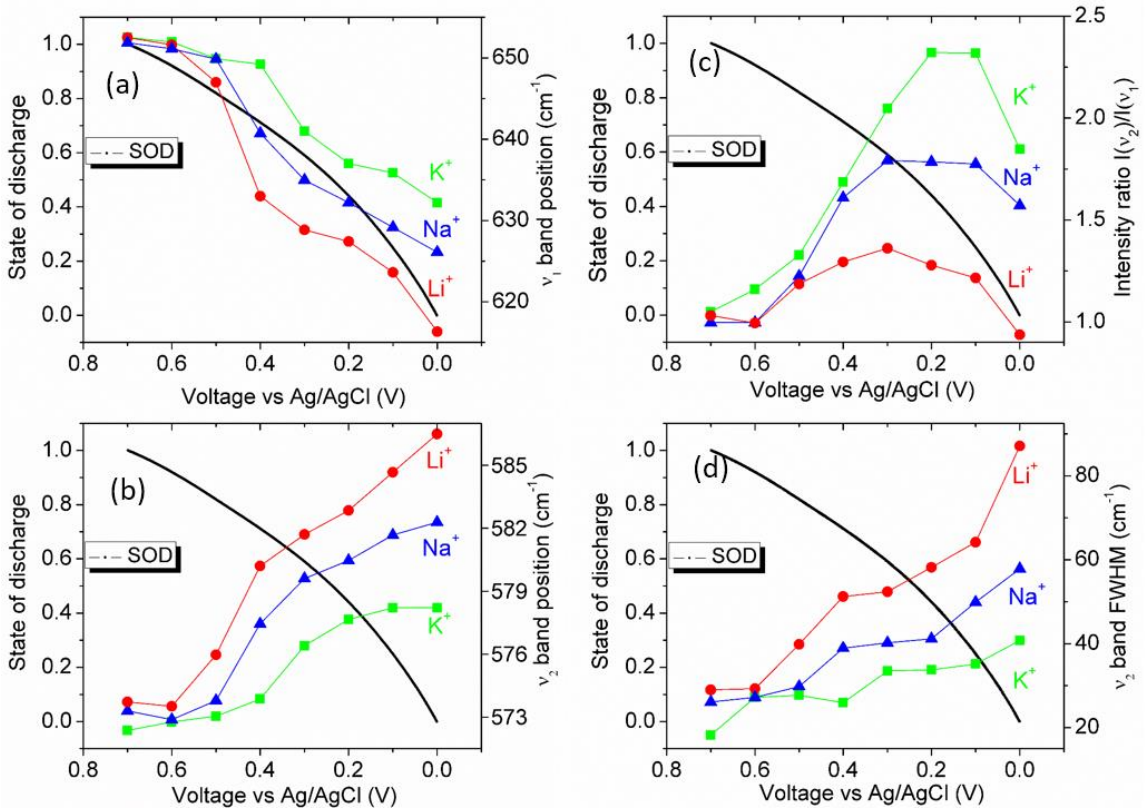


**Figure 4-15.** The key spectroscopic features of the pseudocapacitive $MnO_2$ model electrode as functions of the WE potential when $LiNO_3$, $NaNO_3$, and $KNO_3$ were used as electrolytes. The state of discharge (SOD) is also plotted in each subplot to correlate with spectroscopic features. (a) The $\nu_1$ band positions as function of the WE potential. (b) The $\nu_2$ band positions as function of WE potential. (c) $I(\nu_2)/I(\nu_1)$ as function of the WE potential. (d) The FWHM of $\nu_2$ as function of the WE potential.

### 4.5.2. Cation size effect on general electrochemical behavior

In the previous sections, *in operando* Raman spectroscopy has revealed the details of the structural changes during incorporation of cations of different size in a model

pseudocapacitive $MnO_2$ electrode. While the cation incorporation mechanism and structural evolution remain the same as electrolytes (hence cation sizes) were changed, the use of cations with different sizes ($Li^+$, $Na^+$, and $K^+$) may influence the electrochemical performance of the electrode, including specific capacitances, rate capabilities, and cycling stability. The dependence of electrochemical behavior on cation sizes was investigated by a number of researchers starting with different morphologies of $MnO_2$.[116,133-136] The experimental observations of these studies have significant discrepancies, due mostly likely to the variation in material morphologies, which may critically impact the rates of charge and mass transport. With regard to the cation sizes effects on the electrochemical performance of the thin film model electrode used in this study, at a moderate scan rate (0.1 $mA/cm^2$), the specific capacitances were 881, 858, and 835 F/g (Figure 4-16a), respectively, when electrolytes of 2 M $LiNO_3$, $NaNO_3$, and $KNO_3$ were used, suggesting that the use of smaller cations results in slightly larger specific capacitances. This agrees with the trends reported in other studies using different morphologies of $MnO_2$.[134-136] Moreover, the difference in specific capacitances become more significant at higher cycling rates (Figure 4-16b) because it is easier for smaller cations to be inserted into or extracted out of the layered structure. As a result, the obtainable capacitance of $MnO_2$ is the highest in $LiNO_3$ and the lowest in $KNO_3$ (Figure 4-16c). However, the capacitance retention of the $MnO_2$ electrode during cycling is the worst in the $LiNO_3$ electrolyte and the best in the $KNO_3$ electrolyte (Figure 4-16d). This is because the insertion and extraction of smaller cations induce greater structural changes (as inferred from the more drastic shifts of Raman band features). Greater structural changes during cycling are likely to result in more significant degradation of the $MnO_2$ structure, such as partial collapse of the $MnO_2$

layers, which is potentially detrimental to long-term reversible operation of the supercapacitor electrodes. Accordingly, the cycling stability of $MnO_2$ is the best in the $KNO_3$ electrolyte and the worst in the $LiNO_3$ electrolyte. This dependence of cycling stability and cation sizes is consistent with previously reported observation that the best cycling reversibility is realized with $K^+$, due primarily to the minimum structural change during charge storage.[134] The key electrochemical properties as determined from charge-discharge measurements and the shifts of Raman band features within the potential window are summarized in Table 4-3.

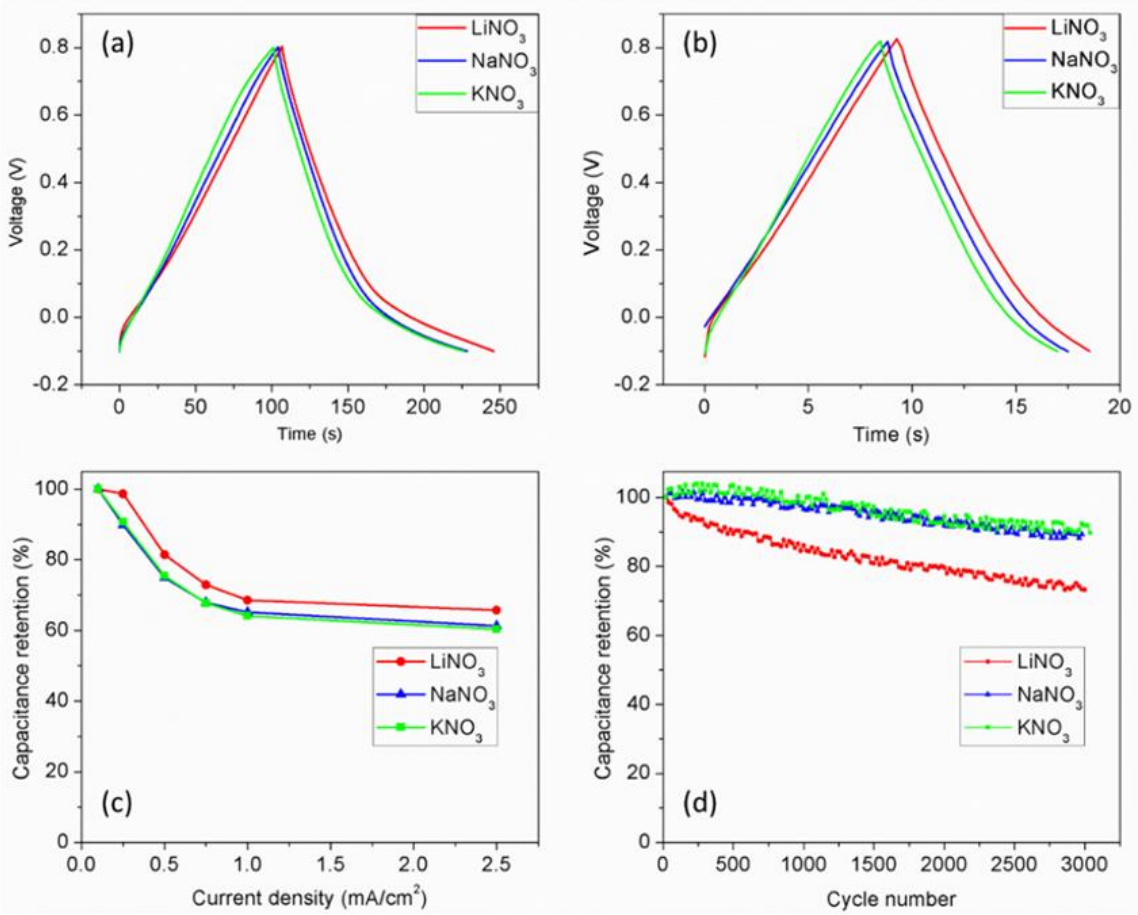


**Figure 4-16.** The comparison of electrochemical performance of a $MnO_2$ electrode in 2 M $LiNO_3$, $NaNO_3$, and $KNO_3$ electrolytes. (a) charge-discharge curves at a current density of 0.1 mA $cm^{-2}$, (b) charge-discharge curves at a current density of 0.75 mA $cm^{-2}$, (c) capacitance

retentions as functions of current densities, (d) capacitance retentions as a functions of cycle numbers. The current density is 0.1 mA $cm^{-2}$.

**Table 4-3. Comparison of the key electrochemical performance parameters and shifts of Raman band features between the potential window for $LiNO_3$, $NaNO_3$, and $KNO_3$.**

| | **Electrochemical properties** | | | **Raman band features shifts (0-0.7 V)** | | | |
|---|---|---|---|---|---|---|---|
| Electrolyte cations | $C_{ps}$ (F $g^{-1}$) | Retention 2.5 A $cm^{-2}$ vs 0.1 A $cm^{-2}$ | Retention-$3000^{th}$ cycle vs $1^{st}$ cycle | $\nu_1$ position ($cm^{-1}$) | $\nu_2$ position ($cm^{-1}$) | $\nu_2$ FWHM ($cm^{-1}$) | $I(\nu_2)/I(\nu_1)$ |
| $Li^+$ | 881 | 65.7 | 73.3 | 37 | 13 | 48 | -0.11 |
| $Na^+$ | 858 | 61.3 | 89.3 | 27 | 9 | 32 | 0.54 |
| $K^+$ | 835 | 60.3 | 92.4 | 21 | 5 | 23 | 0.81 |

### 4.5.3. Cation size effect on impedance spectroscopy

More importantly, the impedance spectra were directly with the Raman spectra collected in 3 different types of electrolytes at a particular polarization potential under *in operando* conditions. Shown in Figure 4-17 are some typical impedance spectra and the corresponding Raman spectra for a $MnO_2$ electrode immersed in electrolytes of 2M $LiNO_3$, $NaNO_3$, and $KNO_3$ while the potential was kept at 0.3 V (vs Ag/AgCl), which represents an intermediate stage of charge. The spectral features of $\nu_1$ band and $\nu_2$ band (including band positions, band intensity ratio, and band width) in the Raman spectra can be correlated with the key features of the impedance spectra, including the characteristic transition frequencies and cell resistance. The first transition frequency ($f_{CT}$), which represents the shift from charge transfer region (high frequency region) to diffusion region (mid frequency region), for $LiNO_3$ (501 Hz), is much higher than that for $NaNO_3$ (63 Hz) and $KNO_3$ (50 Hz). Similarly, the second transition frequency $f_W$, which represents the shift from diffusion region (mid frequency region) to capacitive storage region (low frequency region), is also the highest for $LiNO_3$ (5.01 Hz) and the lowest for $KNO_3$ (2.51 Hz),

suggesting that the smaller cations such as $Li^+$ move faster within the interlayer spacing than the larger ones and, thus, offer a higher rate capability. Also, the extrapolated cell resistance, the intercept with the real axis at low frequencies, are the smallest for the $LiNO_3$ electrolyte (8.4 $\Omega cm^2$) and the largest for the $KNO_3$ electrolyte (14.3 $\Omega cm^2$). At a given frequency (e.g., 0.05 Hz), the real part of the impedance is also the smallest for the $LiNO_3$ electrolyte (74.3 $\Omega cm^2$) and the largest for the $KNO_3$ electrolyte (85.0 $\Omega cm^2$), consistent with other electrochemical measurements.

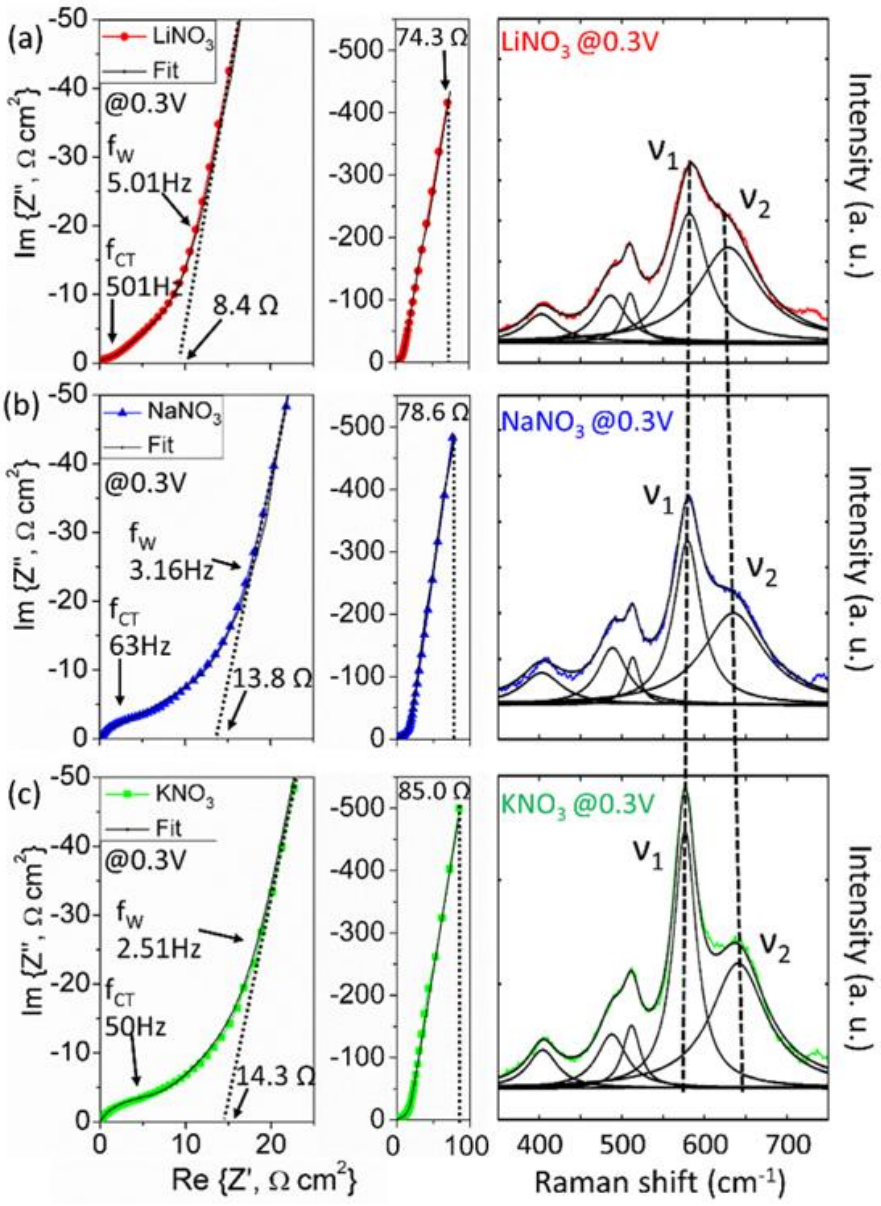


**Figure 4-17.** Some typical impedance spectra (left and middle panel) and Raman spectra (right panel) collected at 0.3 V vs Ag/AgCl in 2 M of (a) $LiNO_3$, (b) $NaNO_3$, and (c) $KNO_3$ electrolytes. The left panel shows the high/mid frequency part and the mid panel shows the low frequency part. The transition frequencies ($f_{CT}$ and $f_W$), the cell resistance, the real part of the impedance at 0.05 Hz, and the key Raman band positions ($\nu_1$ band and $\nu_2$ band) are marked for direct comparison.

Also, equivalent circuit fitting of the impedance spectra was performed to form quantitative correlation between the electrochemical performance (rate capabilities and specific capacitances) with Raman band features at a particular potential. The equivalent

circuit used to fit the impedance spectra was shown in Figure 2-10, where $R_{CT}$, $R_W$, $T_W$, and $C_{ps}$ represent the charge transfer resistance, the diffusion resistance, the diffusion time constant, and the specific capacitance, respectively. Summarized in Table 4-4 are the key parameters of electrochemical performance and Raman bands for $LiNO_3$, $NaNO_3$, and $KNO_3$ at an intermediate charged stage (0.3 V). Smaller cation size leads to smaller $R_{CT}$, $R_W$, and $T_W$, which agree well with the experimental fact that better rate capabilities was achieved when smaller size cations are used (Figure 4-16c). In addition, the specific capacitance values estimated from the impedance data also displayed a trend that smaller cations ($Li^+$) lead to slightly higher capacitance values, also consistent with the results of charge-discharge measurements discussed earlier.

**Table 4-4. Comparison of the key electrochemical properties of a $MnO_2$ electrode measured at 0.3 V (vs Ag/AgCl) in 3 different types of electrolytes ($LiNO_3$, $NaNO_3$, and $KNO_3$) and the corresponding spectral features of Raman spectra collected at the same time.**

| | Electrochemical properties | | | | Raman band properties | | | |
|---|---|---|---|---|---|---|---|---|
| cations | $R_{CT}$ ($\Omega$ $cm^2$) | $R_W$ ($\Omega$ $cm^2$) | $T_W$ (s) | $C_{PS}$ (F $cm^{-2}$) | $\nu_1$ position ($cm^{-1}$) | $\nu_2$ position ($cm^{-1}$) | $\nu_2$ FWHM ($cm^{-1}$) | $I(\nu_2)/I(\nu_1)$ |
| $Li^+$ | 2.06 | 22.7 | 0.32 | 0.0110 | 629 | 582 | 52 | 1.36 |
| $Na^+$ | 5.67 | 31.2 | 0.37 | 0.0105 | 635 | 580 | 40 | 1.79 |
| $K^+$ | 6.44 | 33.1 | 0.39 | 0.0103 | 641 | 576 | 33 | 2.05 |

## 4.6. Insights on rational design

Finally, the elucidated charge storage mechanism could offer potential insights on the engineering the structure of $MnO_2$ electrodes. The electrochemical characterization results (summarized in Table 4-3 and Table 4-4) show that the diffusion resistance is quite significant, implying that the resistance to cation insertion and extraction makes the major contribution to the capacitance loss at high cycling rates. Accordingly, reducing the

diffusion resistance is essential for efficient cation incorporation to better realization of a theoretical capacitance and better rate capabilities. Therefore, in this chapter, the rational design strategy by engineering the crystalline orientation of $MnO_2$ is proposed. If the layers of $MnO_2$ are aligned vertically to the surface of the current collector, as schematically shown in Figure 4-18a, the electrode surface exposed to the electrolyte is fully accessible for electrolyte cation incorporation into the interlayer spacing. Thus, a $MnO_2$ electrode with this orientation is expected to have minimized diffusion resistance thus provide better rate capabilities and high usable capacitances. In contrast, if the layers of $MnO_2$ are aligned parallel to the surface of the current collector as seen in Figure 4-18b, it will potentially lead to significant diffusion resistance and thus poorer electrochemical performance.

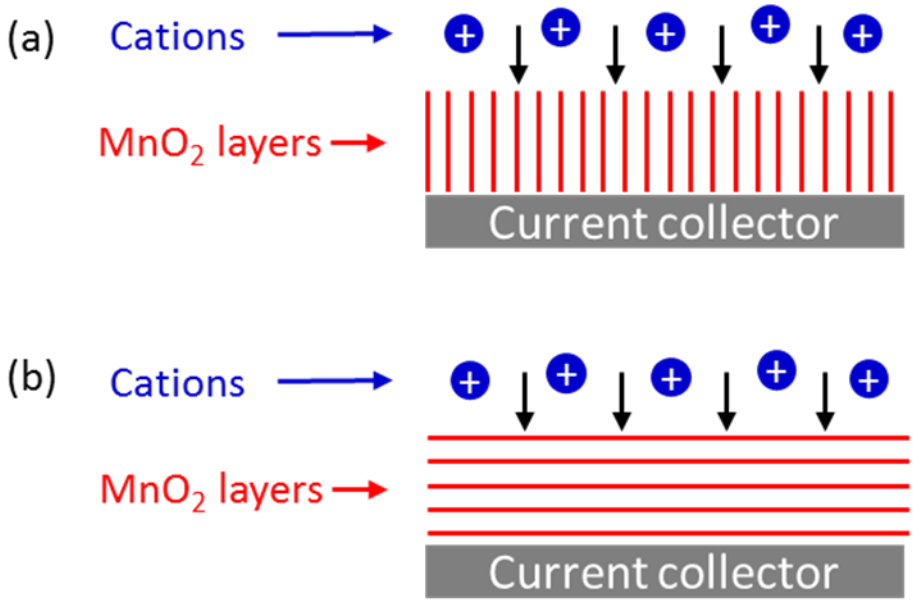


**Figure 4-18.** Two proposed thin film templates of $MnO_2$-based pseudocapacitors and schematics of cation transport. (a) $MnO_2$ films with vertically aligned $MnO_2$ layers. (b) $MnO_2$ film with horizontally aligned $MnO_2$ layers.

Similar strategy has been adopted by other types of energy storage materials where electrolyte ion diffusion is the key to electrochemical performance. As a typical example,

the charge storage mechanism Li-ion battery cathode materials, layered $LiMO_2$ (M=Mn, Co, or Ni), is also based on Li ion incorporation within the interlayer spacing of $LiMO_2$, which is similar to the pseudocapacitive cation incorporation mechanism for $MnO_2$ in this study. By engineering the crystalline orientation of $LiMO_2$ to maximize the accessible interlayer spacing for electrolyte cations, the electrochemical performance (especially the rate capability) can be greatly improved as reported by a number of recent works.[137-139] Besides layer-structured Li-ion batteries based on Li-ion incorporation, other types of materials based on this design strategy has proven enhanced electrochemical performance as well; the graphene layers that are aligned vertically on current collectors exhibited by much better rate capabilities and specific capacitances than graphene layers aligned horizontally.[140] Moreover, similar to our design strategy, the vertically aligned layer-structured $Ni(OH)_2$-based pseudocapacitor also exhibited outstanding electrochemical performance with excellent rate capabilities.[141] Thus, on the basis of the charge storage mechanism study, it is expected that controlling the orientation of the $MnO_2$ layers growth and better engineered nanostructures could dramatically enhance the performance of $MnO_2$-based pseudocapacitors.

## 4.7. Conclusions

In this chapter, the charge storage mechanism of pseudocapacitive $MnO_2$ was systematically investigated using *in operando* Raman spectroscopy performed on a well-controlled thin-film model $MnO_2$ electrode. The unravelled mechanism is shown schematically in Figure 4-19.By adjusting sizes of electrolyte cations ($Li^+$, $Na^+$, and $K^+$), similar Raman spectroscopic evolution was observed. Careful analyses of the spectral features (e.g., band position, width, and intensity) under different conditions (degree of

discharge) in electrolytes with different cations offer insights into the correlation between the structural changes and the charge storage mechanism in pseudocapacitive $MnO_2$. Further, the cation-size effects on band positions were validated by theoretical calculations of phonon energies for $MnO_2$ incorporated with different sizes of cations. Also, the band features were quantitatively correlated with the state of discharge of pseudocapacitive $MnO_2$ for different electrolyte cations. Finally, the elucidated cation incorporation mechanism revealed by the cation size effects from Raman spectroscopic analyses is directly correlated to cation size effects on the electrochemical performance characteristics of $MnO_2$.


**Figure 4-19.** Schematics of energy storage mechanism of pseudocapacitive $MnO_2$.

# 5. PROBING ELECTROCHEMICAL CHARGE STORAGE MECHANISM OF NICKEL HYDROXIDE/OXO-HYDROXIDE ELECTRODE MATERIAL

## 5.1. Introduction

Nickel hydroxides/oxo-hydroxides compounds ($NiO_2H_x$) are a class of electrode materials, which features transitional behavior between a battery and a supercapacitor. This family of materials is among the most attractive candidates for a new-generation of energy storage systems because of their unprecedented theoretical capacity (e.g., ~3000 F $g^{-1}$ for capacitors and ~450 mAh $g^{-1}$ for batteries) and superior stability within a wide range of potentials owing to low equivalent mass and a broad oxidation state window of Ni (Ni(II)-Ni(IV)).[142-145] In recent years, various nanostructured electrode materials (e.g., low dimension nanomaterials and heteroatom-doped 3-D nanostructures),[146-149] have been created to enhance the electrochemical performance,[150-153] resulting in larger capacity, higher rate capabilities, and longer cycling life. Despite the impressive progress on electrochemical performance achieved so far, a fundamental understanding of the structural evolution, the charge storage mechanism, and the contributions of redox reactions to the capacity of $NiO_2H_x$ is still lacking, due primarily to the complex crystalline structures of the redox active $NiO_2H_x$ under cycling conditions.[154] The basic structural element of the $NiO_2H_x$ crystal is $NiO_2$ layers composed of edge-sharing $NiO_6$ octahedra. On one hand, hydrogen atoms can be bonded to oxygen atoms, which forms O-H bonds in the layered framework.[154] On the other hand, the interlayer spacing can accommodate different types of species (e.g., ions and water molecules as schematically shown Figure 5-1).[154] The

stoichiometry of H and interlayer ions are in accordance with the oxidation state of Ni, thus leading to a variety of polymorphs: when x is close to 2 and interlayer species are incorporated, the structure is named as α-$Ni(OH)_2$;[155,156] the extraction of interlayer species from α-$Ni(OH)_2$ leads to a closely packed layered structure, denoted as β-$Ni(OH)_2$;[156-158] the oxidized form of α-$Ni(OH)_2$ is named as γ-NiOOH (with interlayer species);[144,157-159] the extraction of interlayer species from γ-NiOOH leads to the structure called β-NiOOH.[154,159] The completely dehydrogenated form of $NiO_2H_x$ with large amount of incorporated cations (e.g., $Li_{1-\delta}NiO_2$) can also be categorized into this class of material.[15,154,160] These types of polymorphs can be readily interconverted from one to another. [157,158]

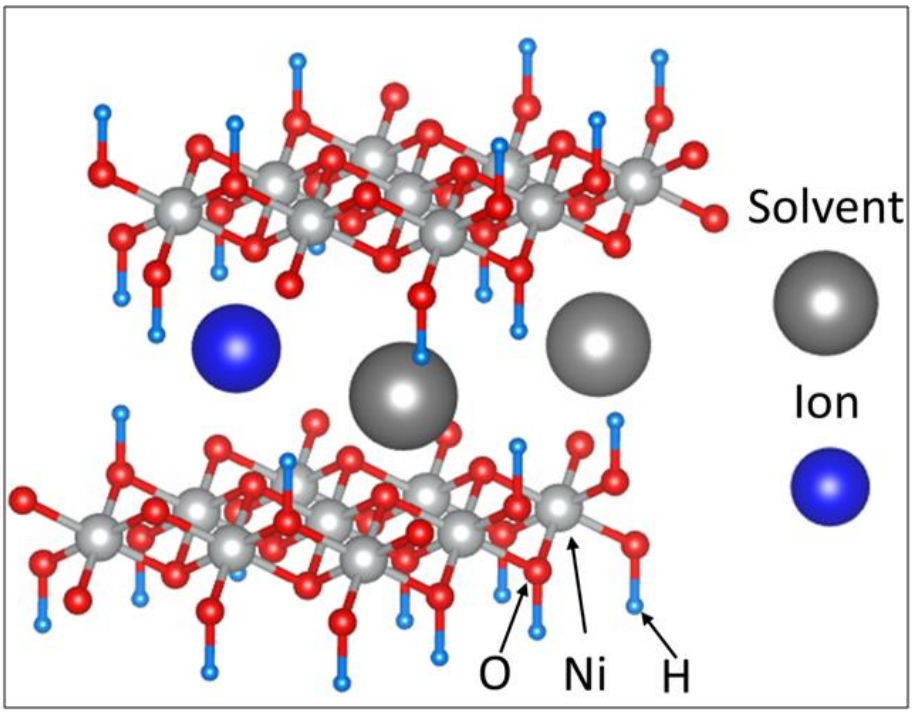


**Figure 5-1.** A schematic sketch of $NiO_2H_x$ layered structure showing bonded hydrogen and interlayer species (ions and solvent molecules).

Despite the complicated polymorphs of $NiO_2H_x$, the basic structure (Figure 5-1) on which various polymorphs are based has two possible mechanisms to store charge (i.e., to change the oxidation states of Ni); the breaking/formation of O-H bond and insertion/extraction of electrolyte cations. On one hand, since the energy storage of $NiO_2H_x$ is primarily operated in KOH electrolytes, the $OH^-$-assisted breaking/formation of O-H bond is expected to play a significant role.[144,150,161] On the other hand, a lot of researches suggested cation insertion/extraction can also contribute considerably to charge storage,[162-164] since it has been revealed that the stoichiometry of $NiO_2H_x$ can accommodate large amount of cations between the layers (e.g., $Na_{0.32}H_{0.22}(H_2O)_{0.25}NiO_2$ and other similar forms).[144,157,165,166] Cation insertion/extraction is also responsible for charge storage of other types of layer-structured pseudocapacitive and battery materials (e.g., layered $MnO_2$-based pseudocapacitors and $LiCoO_2$/$LiNiO_2$-based Li-ion battery cathodes).[15,40,102] Therefore, the detailed contribution of both breaking/formation of O-H bond and cation insertion/extraction should be systematically evaluated. More importantly, it is imperative to quantitatively correlate the charge storage with the structural features of $NiO_2H_x$ in order to gain a fundamental understanding of the charge storage mechanism.

In this chapter, relying on resonance enhancement, *in operando* resonance Raman spectroscopy was applied to evaluate the charge storage contribution of two possible redox mechanisms for $NiO_2H_x$ by adjusting properties of electrolyte solutions. Key phonon properties were quantitatively analysed and correlated with the amount of stored charge, providing important insight into the mechanism of charge storage and scientific basis for knowledge-based design of better electrode materials.

## 5.2. Sample preparation and characterizations

### 5.2.1. Sample preparation

In this study, a thin film model electrode was fabricated by electrochemically oxidizing the bare Ni foil. When the bare Ni foil was immersed in a 2 M KOH electrolyte, a thin layer of nickel hydroxide will form on the surface, because Ni metal starts to be unstable as long as the potential of Ni is higher than -0.7 V vs Ag/AgCl in strong base solution according to the Pourbix diagram of $Ni/NiO_2H_x/NiO_2$.[167,168] During extensive cycling of the Ni foil between 0 V and 0.6 V, the foil surface will be gradually oxidized to form γ-NiOOH with water molecule and cations incorporated between its layers eventually.[158,168,169] Figure 5-2 shows the CV profile of the electrochemical oxidation of Ni foil within 3000 cycles. The foil exhibited negligible current density in the first cycle. However, it is obvious that the current density gradually increases with cycles numbers and doesn't change significantly when the cycle number approach 3000. It is also noted that the overpotential of the redox peak gradually increase with current density, which is owing to the increased thickness of the nickel hydroxide film caused higher ohmic resistance.

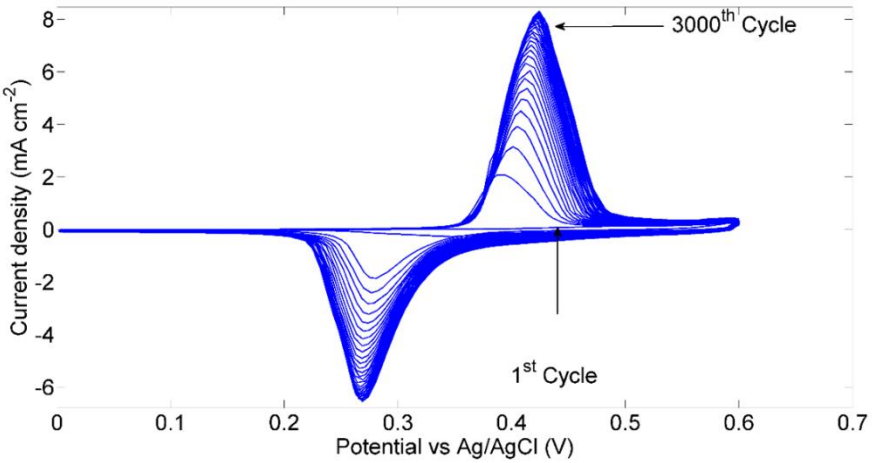


**Figure 5-2.** CV profiles of Ni foil within 3000 cycles with an interval of 50 cycles. The scan rate was 50 mV $s^{-1}$.

### 5.2.2. Electron microscopic characterization

Figure 5-3 shows the morphology of the model electrode, indicating a flat surface, which is beneficial for acquisition of Raman spectra and unambiguous correlation of structural properties and electrochemical behavior. A closer view of the surface (Figure 5-3 inset) clearly shows the flake-like morphology, similar to the typical morphologies of $NiO_2H_x$ reported elsewhere.[150,152]

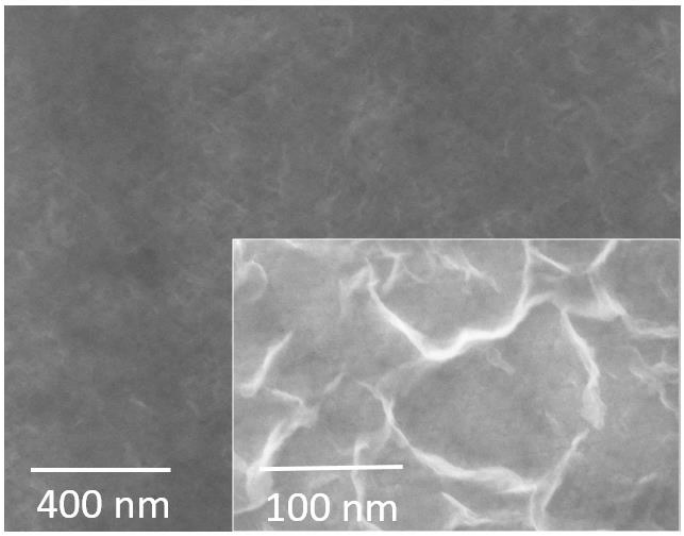


**Figure 5-3.** Scanning electron microscope (SEM) images of $NiO_2H_x$ thin film model electrode.

Because of the limited thickness of the $NiO_2H_x$ film, the X-ray diffraction pattern of the film barely exhibited diffraction signal of $NiO_2H_x$. Therefore, TEM was applied for the phase analyses. Figure 5-4 left shows the TEM image of the scraped thin film of $NiO_2H_x$, which exhibits clear layered fringes. The SAED pattern is shown in Figure 5-4 right, which indicates three weak diffraction rings. Based on the XRD patterns of layer-structured γ-NiOOH based complex (JCPDS 23-1407, JCPDS 27-0764, JCPDS 06-0075) and the sizes of the diffraction rings shown in Figure 5-4, [159,165] the three diffraction rings in the SAED pattern were assigned as the 001, 002, and -201 diffractions of γ-NiOOH.

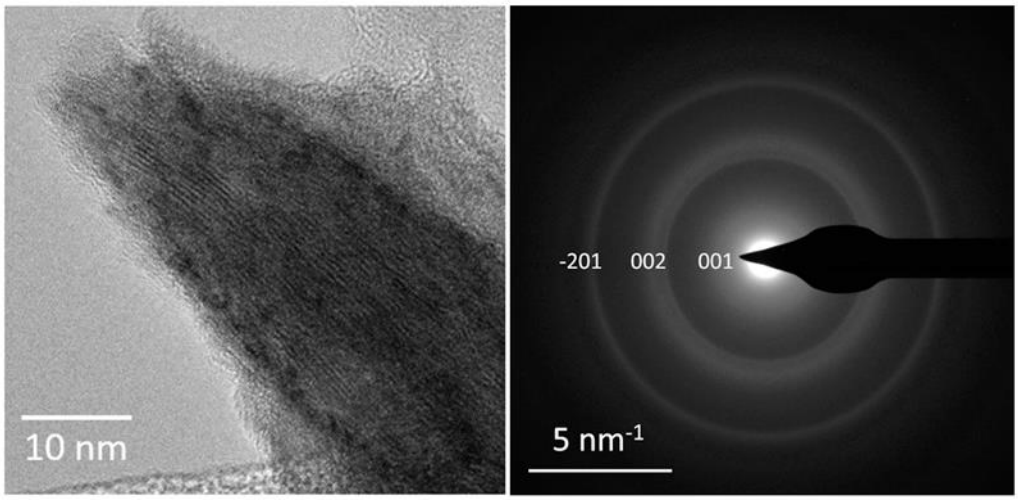


**Figure 5-4.** (left) Transmission electron microscope (TEM) image of the scraped $NiO_2H_x$ thin film. (right) SAED pattern and diffraction ring assignments of scraped $NiO_2H_x$ thin film.

### 5.2.3. Raman spectrum and vibrational analyses

Figure 5-6 shows the Raman spectrum of the thin film model electrode. Two Raman bands (labeled as $\nu_1$ band and $\nu_2$) can be clearly observed and match very well with Raman spectrum of γ-NiOOH.[168,170,171] To assign the two Raman bands, group theory analyses and polarized Raman study is needed. As mentioned above, the layer-structured $NiO_2H_x$ has complicated structures and stoichiometry, regarding the amount of the bonded hydrogen and interlayer ions. Depends on the bond length and coordination of oxygen, the space group of the $NiO_2H_x$ complex was reported as a variety of types (e.g., hexagonal R-3m or monoclinic C2/m).[158,159,165,166] In order to simplify the phonon band assignment, the simple model of $NiO_2$ layer with highest order of symmetry (R-3m, No. 166) was applied, which doesn't take the bonded hydrogen and interlayer ions into account (Figure 5-5). The space group (R-3m, No. 166) is based on point group $D_{3d}$. The character table of $D_{3d}$ point group is shown in Table 5-1.

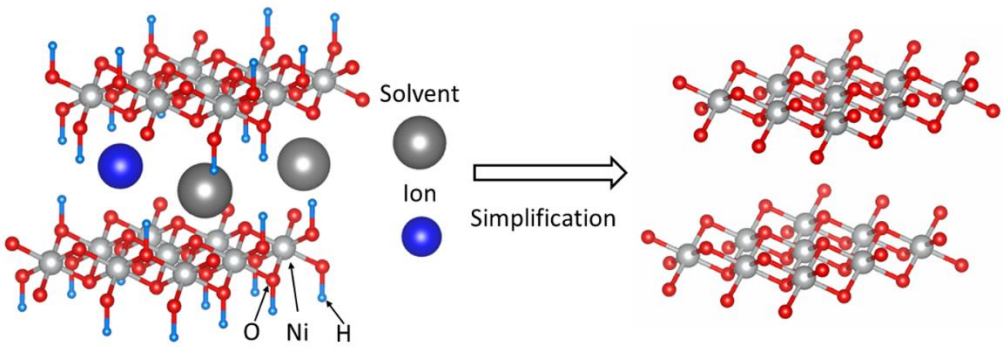


**Figure 5-5.** An illustration of simplification of a $NiO_2$ layer structure model for Raman band assignment based on group theory.

**Table 5-1. The character table of the $D_{3d}$ point group**

| $D_{3d}$(-3m) | # | E | $C_3$ | $C_2$ | i | $S_6$ | $\sigma_d$ | functions |
|---|---|---|---|---|---|---|---|---|
| Multiplicity | - | 1 | 2 | 3 | 1 | 2 | 3 | · |
| $A_{1g}$ | $\Gamma_1^+$ | 1 | 1 | 1 | 1 | 1 | 1 | $x^2+y^2$, $z^2$ |
| $A_{2g}$ | $\Gamma_2^+$ | 1 | 1 | -1 | 1 | 1 | -1 | $J_z$ |
| $E_g$ | $\Gamma_3^+$ | 2 | -1 | 0 | 2 | -1 | 0 | $(x^2-y^2, xy)$, $(xz, yz)$, $(J_x, J_y)$ |
| $A_{1u}$ | $\Gamma_1^-$ | 1 | 1 | 1 | -1 | -1 | -1 | · |
| $A_{2u}$ | $\Gamma_2^-$ | 1 | 1 | -1 | -1 | -1 | 1 | z |
| $E_u$ | $\Gamma_3^-$ | 2 | -1 | 0 | -2 | 1 | 0 | (x, y) |

Since one unit cell contains 3 Ni and 6 oxygens, considering the multiplicity of R-3m group (3), the total number of independent atoms or ions is 3. Threfore, the total degree of freedom (DOF) is 9. Based on group theory analyses, the mechanical representation of the $NiO_2$ layer can be classified as the sum of the following irreducible representations [79,130-132]:

$$\Gamma = A_{1g} + 2A_u + 2E_u + E_g \ . \tag{86}$$

One $A_{1u}$ mode and one $E_u$ mode are acoustic modes. Among the four optical modes, the $A_{1g}$ and $E_g$ modes are Raman active, which basically match the experimental results that

only two Raman bands were observed. For the $A_{1g}$ mode, the oxygens vibrate perpendicular to the plane formed by oxgyen; whereas the oxygens vibrate along this plane for the $E_g$ mode (Figure 5-6). The Raman tensors of the two modes are:

$$A_{1g} = \begin{pmatrix} a & 0 & 0 \\ 0 & a & 0 \\ 0 & 0 & b \end{pmatrix} \quad E_{g1} = \begin{pmatrix} c & 0 & 0 \\ 0 & -c & d \\ 0 & d & 0 \end{pmatrix} \quad E_{g2} = \begin{pmatrix} 0 & -c & -d \\ -c & 0 & 0 \\ -d & 0 & 0 \end{pmatrix}. \qquad (86)$$

It is noted that the Raman tensor of the $A_{1g}$ mode is a diagonal matrix, whereas the Raman tensor of the $E_g$ mode has no diagonal elements. Therefore, the scattered light of the $A_{1g}$ mode will largely maintain the polarization direction of the incident laser and the scattered light of the $E_g$ mode will be completely depolarized because of the polycrystalline nature of the film (69). By switching the polarization configuration from $\bar{Z}(XX)Z$ to $\bar{Z}(XY)Z$ , the relative intensity of the $\nu_1$ band is greatly reduced (Figure 5-6), confirming the Raman band assignments that $\nu_2$ band belongs to the $E_g$ mode and $\nu_1$ band belongs to $A_{1g}$ mode.

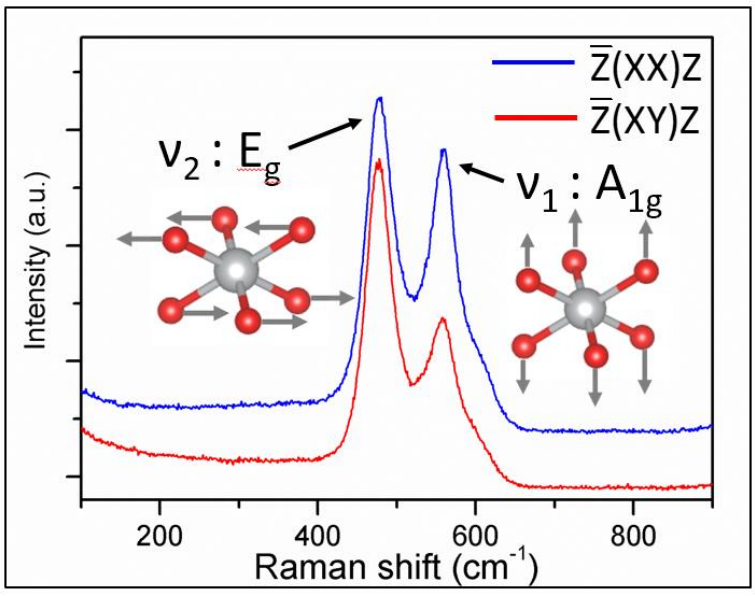


**Figure 5-6.** Raman spectra of the $NiO_2H_x$ thin film model electrode under $\bar{Z}(XX)Z$ and $\bar{Z}(XY)Z$ polarization configurations. The corresponding band assignments ($E_g$ and $A_{1g}$) and the sketches of the two bands are also shown.

More importantly, since these two phonon modes are directly related to the lattice vibration of $NiO_2$ framework, the structural changes as a result of charge storage (e.g., Ni-O bond length, electron cloud distribution, and structural disorder) will inevitably lead to the evolution of phonon properties, including phonon hardening/softening, polarizability changes, and degeneration of symmetry, which will be observed as evolution of band positions, band intensities, and band profiles experimentally. The quantification of these phonon properties provides solid basis to correlate structural changes with charge storage contributions unambiguously, which makes *in operando* Raman spectroscopy perfectly suited for this study.

### 5.2.4. Resonance Raman behavior

To optimize the sensitivity of probing subtle changes in phonon bands during *in operando* experiments, the light absorption properties and resonance Raman effect of the $NiO_2H_x$ model electrode were examined.

#### *5.2.4.1. Adsorption spectrum*

The absorption spectrum of the $NiO_2H_x$ model electrode was obtained by comparing the reflection spectra of a reference standard and the model electrode. Since the $NiO_2H_x$ model electrode has no light transmission, the absorbance can be expressed by the following equation (R is reflectance):

$$Absorbance = 1 - R_{sample} / R_{reference} \quad . \tag{86}$$

Figure 5-7 shows the reflection spectra of both reference standard and the model electrode measured by the customization of Raman spectrometer using white light illumination (a halogen lamp). The reflected light was collected by a high NA objective (50X/0.75) and was then guided to grating chamber. The reflection spectrum of an Ocean Optics reference

standard describes the intensity profile of the light source used for white light illumination. The reflection spectrum of the model electrode indicates strongly reduced reflectance in the visible light range, especially in the region between 600-700 nm where a clear reflectance minimum is observed. The resulting absorption spectrum shows wide absorbance profile in the visible light range with a maximum between 650-700 nm (Figure 5-8a).

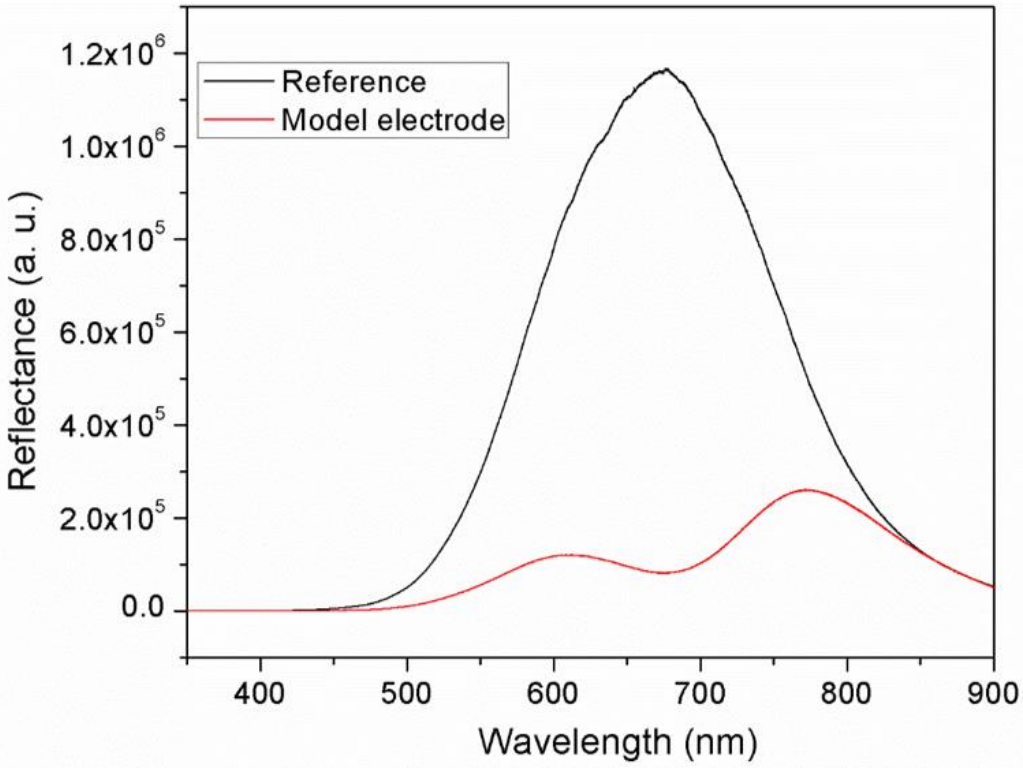


**Figure 5-7.** Reflection spectra of an Ocean Optics reference standard and the $NiO_2H_x$ model electrode acquired by customization of Raman spectrometer using white light illumination.

Since the reflection spectra acquired by the customization of Raman spectrometer was collected by an objective (50x/0.75), a small portion of reflected light cannot be collected. Therefore, a standard Ocean Optics UV-vis spectrometer (DH-2000) equipped with an integration sphere (Ocean Optics ISP-50) was applied to the measurement of the

reflection spectra. An Ocean Optics DH-2000 light source and a QP450-1 optical fiber were applied as light source and light transmission fiber respectively. The reference spectrum was acquired using an Ocean Optics reference standard. The acquisition time was 65 s with boxcar value of 3 to smooth the spectrum. Because of the limited efficiency of integration sphere and much lower sensitivity of CCD detector of UV-vis spectrometer than that of Raman spectrometer, the signal-to-noise ratio of the absorption spectra (Figure 5-8b) acquired by Ocean Optics is much lower than that of the spectra acquired by customization of Raman spectrometer (Figure 5-8a). However, it is obvious that the two spectra show same absorption characteristics generally, which is the broad absorbance profile with a maximum near 700 nm.

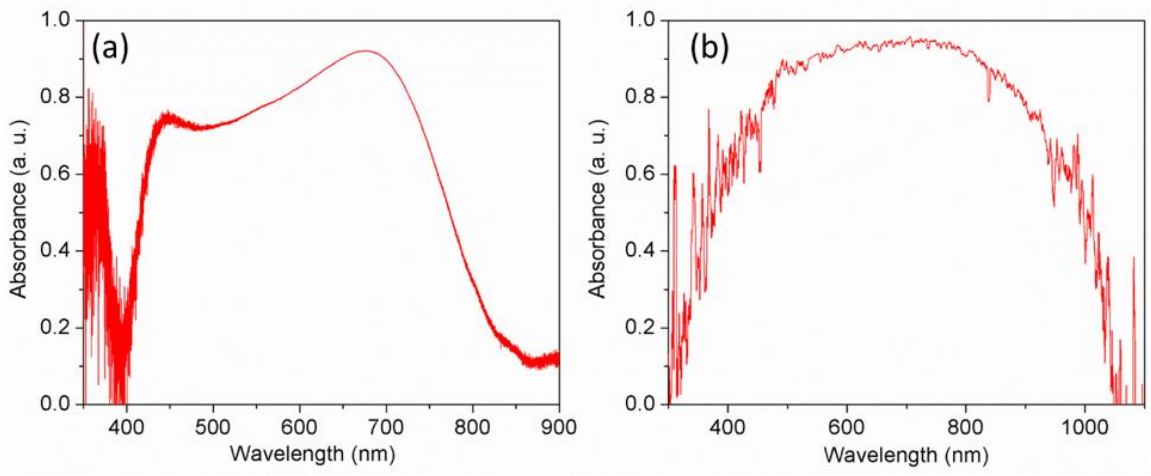


**Figure 5-8.** The absorption spectra acquired by (a) the customization of Raman spectrometer using white light illumination and (b) Ocean Optics UV-vis spectrometer equipped with an integration sphere.

#### *5.2.4.2. Resonance Raman effect*

On the basis of the measurement of absorption spectrum, the resonance Raman effect can be analysed. Among the wavelengths of commonly used lasers in the visible range, the wavelength of He-Ne laser (633 nm) is the closest to the absorbance maximum

(Figure 5-9a), which is closer than those of the Argon ion lasers (488 nm and 514 nm). Consequently, much stronger resonance enhancement was observed under excitation of 633 nm laser than 488 nm or 514 nm laser of equivalent laser power (Figure 5-9b), despite the fact that normal Raman scattering efficiency is proportional to the fourth power of the excitation laser frequency (equation (66)). Because of the strong resonance enhancement under the excitation of 633 nm laser, the sensitivity and specificity of *in operando* Raman spectroscopy has provided unambiguous correlation between phonon and electrochemical properties.

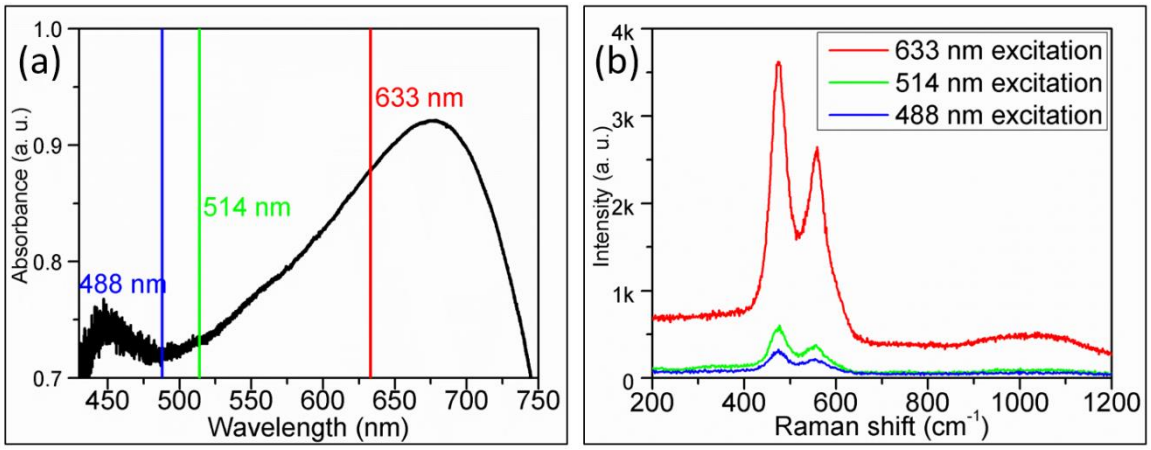


**Figure 5-9.** (a) UV-vis absorption spectrum of $NiO_2H_x$ thin film model electrode marked with available excitation laser wavelengths. (b) Raman spectra of the $NiO_2H_x$ thin film model electrode using different excitation lasers with equivalent laser power of 4 mW.

## 5.3. *In operando* Raman spectroscopic analyses

### 5.3.1. Analyses of general energy storage

The *in operando* Raman spectroscopic evolution was tested first in a 2 M KOH aqueous electrolyte, which is aimed to evaluate the structural change of $NiO_2H_x$ in general charge storage applications. It is noted that in the KOH electrolyte both cation insertion/extraction ($K^+$ ions) and breaking/formation of O-H bond are likely to contribute

to the charge storage process. Figure 5-12 shows the *in operando* resonance Raman spectroscopic evolution along with the CV profile in the potential window of 0-0.5 V. It is observed that a pair of redox peaks appeared in the range of 0.3-0.5 V (vs Ag/AgCl), which is in accordance with the electrochemical behavior of most reported works of $NiO_2H_x$.[150,172] This CV profile can be well maintained as the scan rate increased up to 500 mV $s^{-1}$ (Figure 5-10 left). Similarly, the charge-discharge experiment with different current densities was also performed to calculate the capacitance/capacity retention (Figure 5-10 right and Figure 5-11). Because of the prescence of strong CV peaks for $NiO_2H_x$, this electrochemical behavior can be considered as a transitional behavior between a battery and a capacitor. Therefore, the units for the charge storage of battery system (Ah or C) were used for charge storage capacity calculation. According to Figure 5-11, more than 80% of the charge storage capacity (261 mAh $g^{-1}$) was retained when the current density was increased from 0.025 to 5 mA $cm^{-2}$ (2.1 to 427 A $g^{-1}$ with respect to mass of active material). The calculated areal and specific capacity are 10.98 mC $cm^{-2}$ and 261 mAh $g^{-1}$ (or 1,877 F $g^{-1}$), respectively (considering the fact that a large number of reported works about battery-like materials have already used Farad as unit, the charge storage capacity calculated using the unit "F $g^{-1}$" is 1877 F $g^{-1}$). The superior rate capability mentioned above indicate the flat geometry of the $NiO_2H_x$ model electrode can greatly reduce the kinetic hindrance caused by electrolyte mass transport, which is crucial for unambiguous and quantitative correlation between phonon properties and electrochemical features.

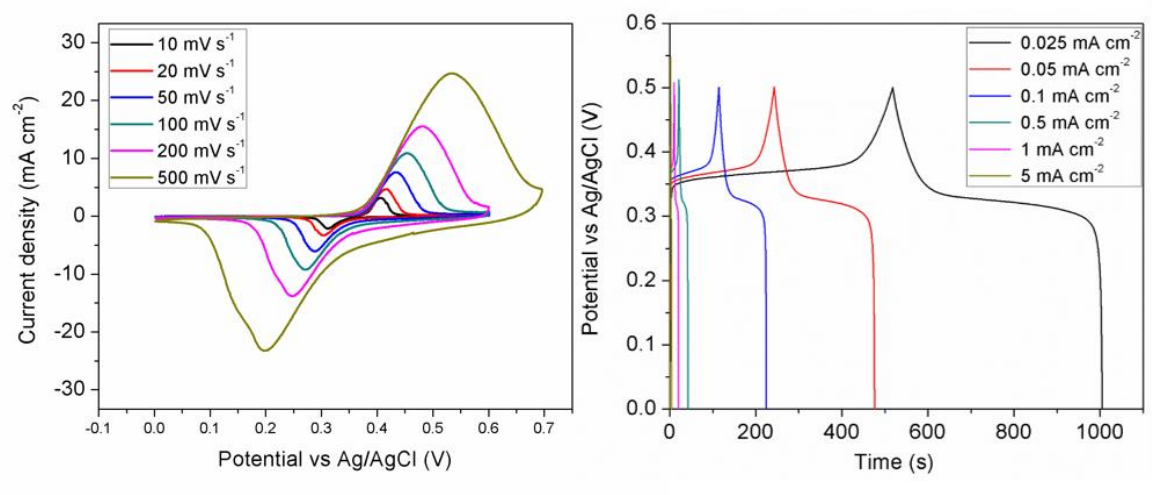


**Figure 5-10. (**Left) Cyclic voltammogram (CV) of the $NiO_2H_x$ thin film model electrode with different scan rates in a 2 M KOH aqueous electrolyte. (Right) The charge-discharge profiles of the $NiO_2H_x$ model electrode with different current densities in a 2 M KOH aqueous electrolyte.

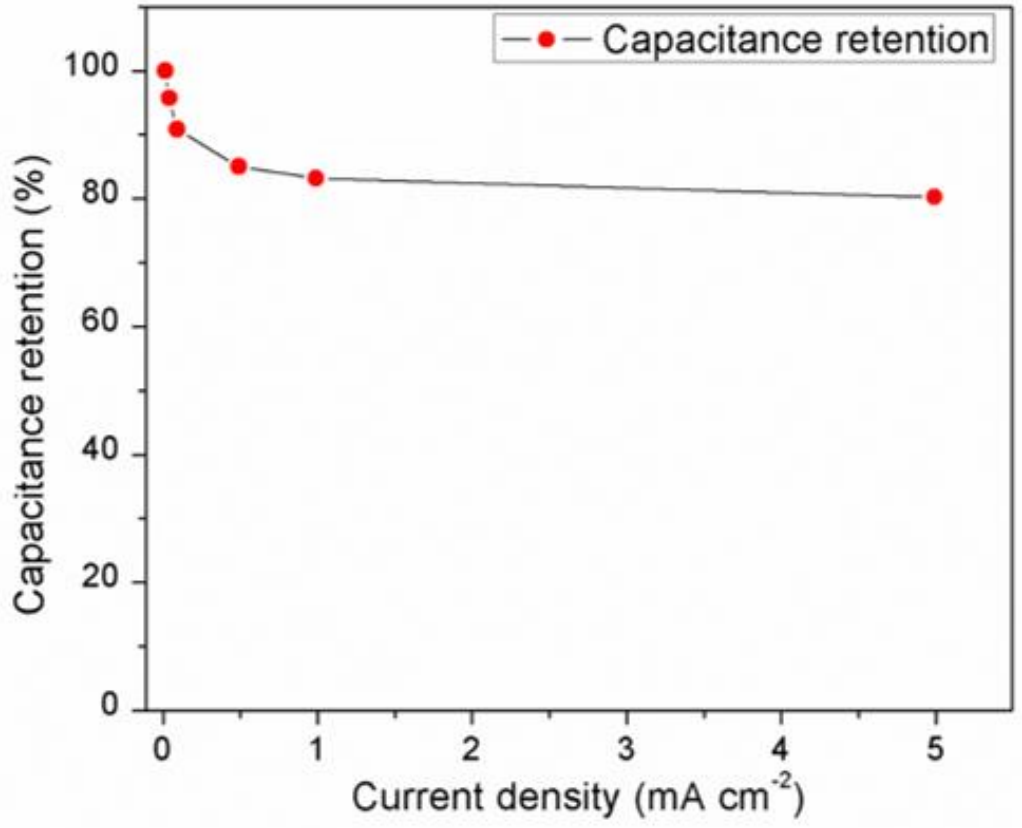


**Figure 5-11.** The capacity/capacitance retentions of the $NiO_2H_x$ model electrode tested in a 2 M KOH aqueous electrolyte as functions of current densities.

The *in operando* Raman spectra were acquired with an interval of 0.05 V during the CV test (Figure 5-12). First, no new bands were observed, proving no extra phases were produced during charge storage. Second, it is clearly shown that the Raman spectra didn't present significant evolution in the potential range where no obvious charge storage is observed (0-0.35 V in anodic process, 0.3-0 V in cathodic process). Third, however, in the potential range between 0.35-0.5 V in anodic process, the energy of $E_g$ mode, denoted as $\omega(E_g)$, was blue-shifted from 474 $cm^{-1}$ to 480 $cm^{-1}$. Similarly, $\omega(A_{1g})$ was blue-shifted to 554 $cm^{-1}$ to 558 $cm^{-1}$. The intensity ratio, denoted as $I(A_{1g})/I(E_g)$, increased from 0.50 to 0.69. These phenomena clearly indicate massive positive charge storage lead to the stiffening of both the $A_{1g}$ mode and the $E_g$ mode, as a straightforward indication of shortening of Ni-O bond, and an increase of the polarizability of the $A_{1g}$ mode, which is resulting from the change of electron cloud distribution within $NiO_2$ layer. Reversibly, significant red shift of both the $A_{1g}$ mode and the $E_g$ mode and a decrease of $I(A_{1g})/I(E_g)$ were observed in the range between 0.5-0.3 V in the cathodic process along with significant reductive current, which suggest the release of the stored positive charge restored the Ni-O bond length and electron cloud distribution within $NiO_2$ layer. In addition, the Raman spectroscopic evolution remained largely the same as the electrolyte was changed from KOH to NaOH and LiOH, implying that the charge storage mechanism is independent of the types of the electrolyte cations studied (Figure 5-13).

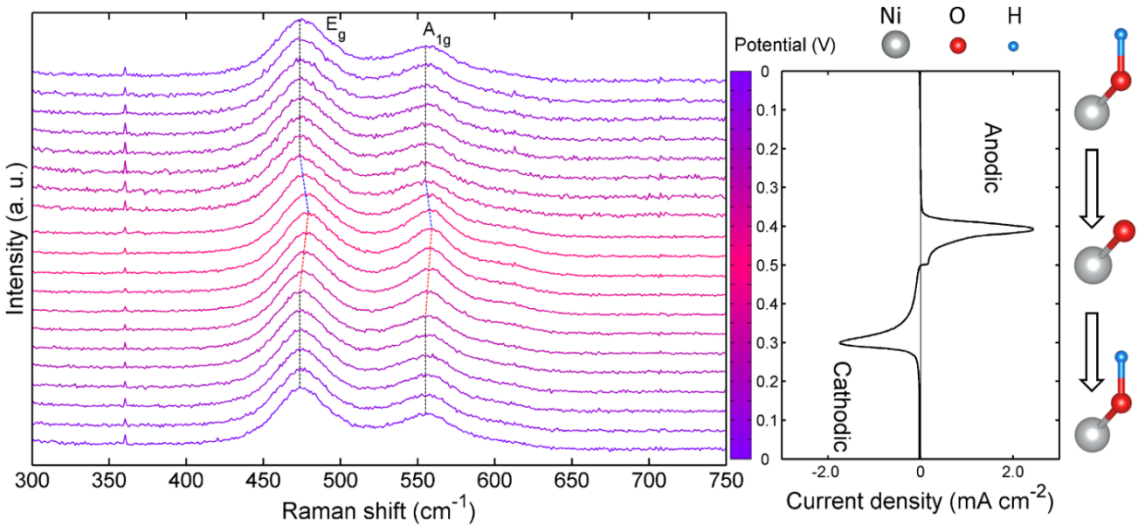


**Figure 5-12.** *In operando* Raman spectroscopic evolution of the $NiO_2H_x$ thin film model electrode operated in a 2 M KOH aqueous electrolyte. The corresponding CV profile (10 mV $s^{-1}$) is shown on the right panel. The potential of each spectrum is indicated by the color bar located between the spectra and the CV curves. The color bar is separated into 20 grids. Each grid represents a potential interval of 0.05 V, over which, the spectrum was acquired during the *in operando* measurements. The red shifts and blue shifts of the $A_{1g}$ mode and the $E_g$ mode are marked on the spectra. A schematic sketch of breaking/formation of O-H bond is also shown to illustrate the redox behavior on the basis of quantitative analyses.

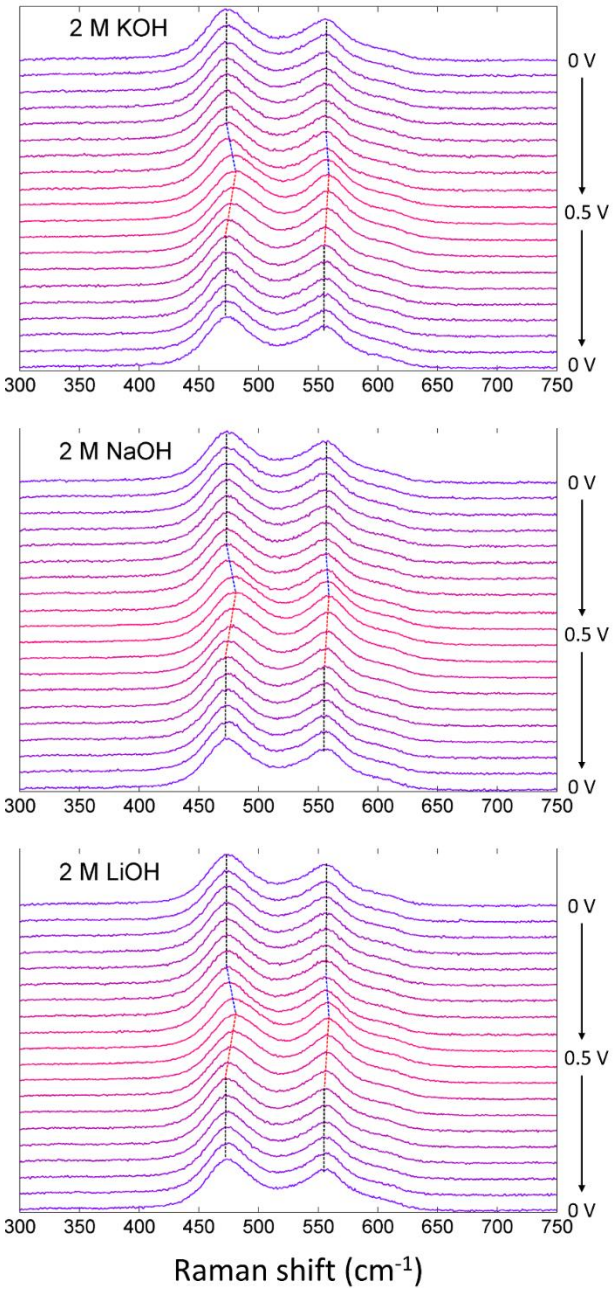


**Figure 5-13.** Evolution of in operando Raman spectra of a thin-film model $NiO_2H_x$ electrode cycled in 2 M aqueous KOH, NaOH, and LiOH aqueous electrolytes.

In order to corroborate the analyses obtained from *in operando* Raman spectroscopic measurements, the reflectance of the model electrode under *in operando* conditions was measured. Light reflection is complementary to light absorption, which corresponds to the electronic structure of the materials (i.e., reflecting the oxidation state).

Figure 5-14 shows the reflectance profile of the electrode as the potential (vs Ag/AgCl) of the working electrode (WE) was changed from 0 V to 0.5 V in a 2 M KOH electrolyte solution. A signficant red shift of the reflection profile (correpsonding to a blue shift of absorption) is clearly observed as the WE potential was switched from 0 V to 0.5 V. This shift suggests an increase in the energy gap of electronic state transition and evolution of the oxidation state of Ni, consistent with the Raman spectroscopic evolution as a function of electrochemical potentials. It is noted that the reflection profile under the *in operando* condition shown in Figure 5-14 exhibited discrepancies with the light reflectance profile under ex-situ condition shown in Figure 5-7, since the existence of the electrolyte will strongly interfere with light absorption/reflection. Also, the light reflectance profile under *in operando* condition cannot be converted to the light absorption profile because of the lack of the light reflectance behavior of a reference standard under the same operando condition. However, the evolution of light reflectance alone can provide strong evidence of changes in oxidation state during cell operation.

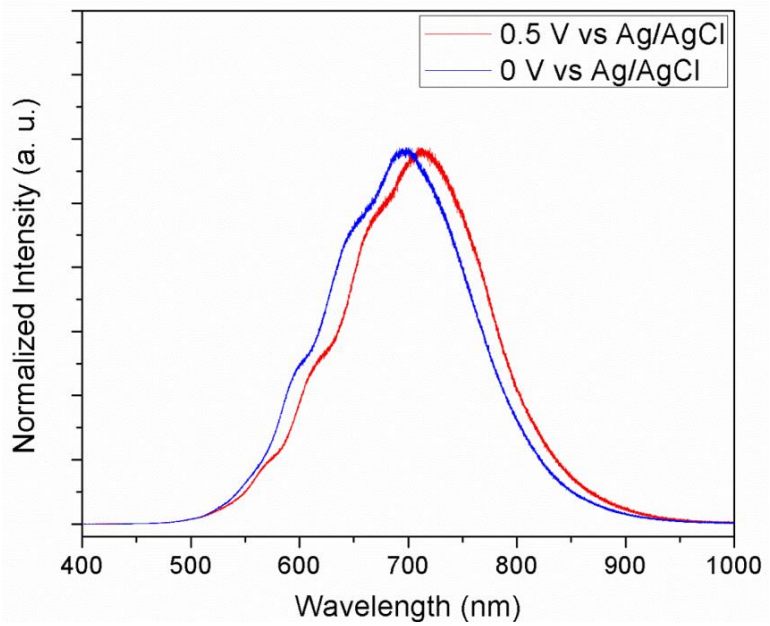

**Figure 5-14.** Light reflection measurements of the $NiO_2H_x$ thin film model electrode at 0 V and 0.5 V in a 2 M KOH aqueous electrolyte solution.

### 5.3.2. Analyses of the contribution from cation incorporation

In the KOH electrolyte, it cannot unambiguously distinguish the contribution of charge storage and structural evolution of possible redox mechanisms, since both cation insertion/extraction and breaking/formation of O-H bond are likely to contribute to the charge storage as mentioned above. Thus, to unambiguously unravel this issue, the *in operando* Raman spectroscopic evolution was performed in a neutral electrolyte (2 M $KNO_3$) to evaluate the charge storage contribution from cation insertion, since the anion of the neutral electrolyte ($NO_3^-$) cannot be involved in the reaction of breaking/formation of O-H bond. **Figure** 3 shows the *in operando* Raman spectroscopic evolution along with the CV profiles. The potential window used in 2 M $KNO_3$ was shifted to a higher potential range (0.5-1.0 V) compared to the potential window used in the 2 M KOH electrolyte (0-0.5 V), since the stability window of $NiO_2H_x$ will shift to higher potentials as pH decrease according to the Pourbix diagram.[167,168] It is clearly noted that the CV exhibited a rectangular-like profile, which can be maintained up to 500 mV $s^{-1}$ (Figure 5-15), similar with the case of layer-structured pseudocapacitive $MnO_2$,[40] indicating cation insertion/extraction can contribute to charge storage of $NiO_2H_x$.

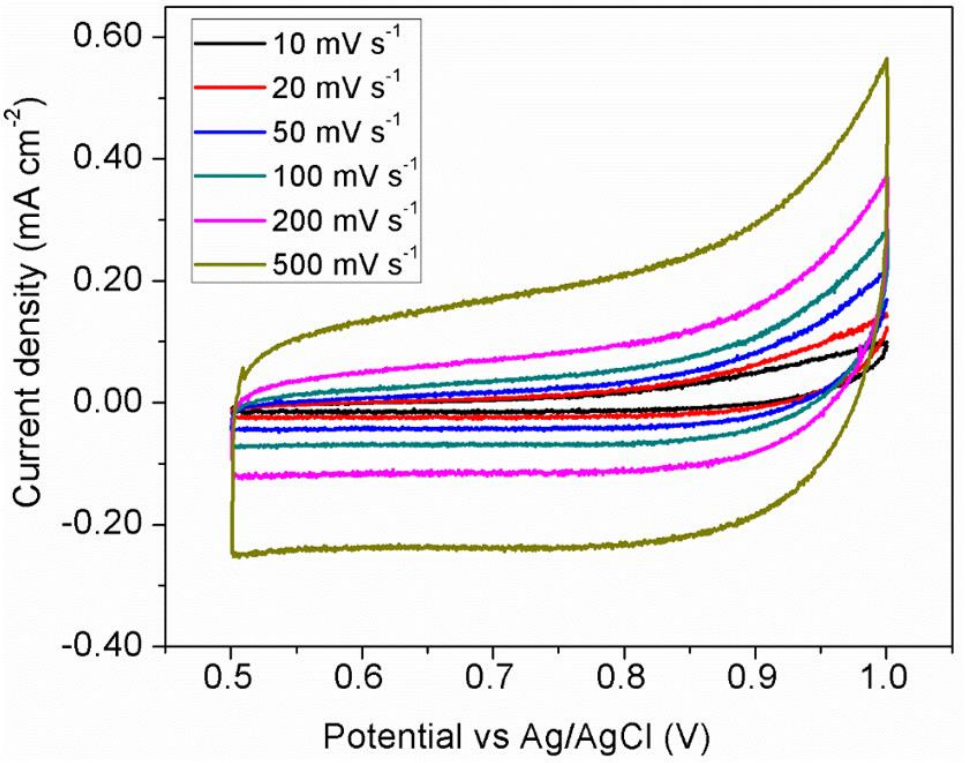


**Figure 5-15.** Cyclic voltammogram (CV) of the $NiO_2H_x$ thin film model electrode with different scan rates in a 2 M $KNO_3$ aqueous electrolyte.

For the Raman spectroscopic investigation, it is observed that the Raman bands were broadened as soon as the $NiO_2H_x$ was immersed in the 2 M $KNO_3$ electrolyte (Figure 5-16). The band broadening is a clear indication of cation incorporation between the interlayer spacing, because the incorporated cations will lead to break of the lattice symmetry, leading to structural disorder and thus band broadening effect.[40,114,115,173] Similar band broadening effects related to cation incorporation has been reported in different works related to Li-ion battery and pseudocapacitive charge storage.[40,114,115,173]

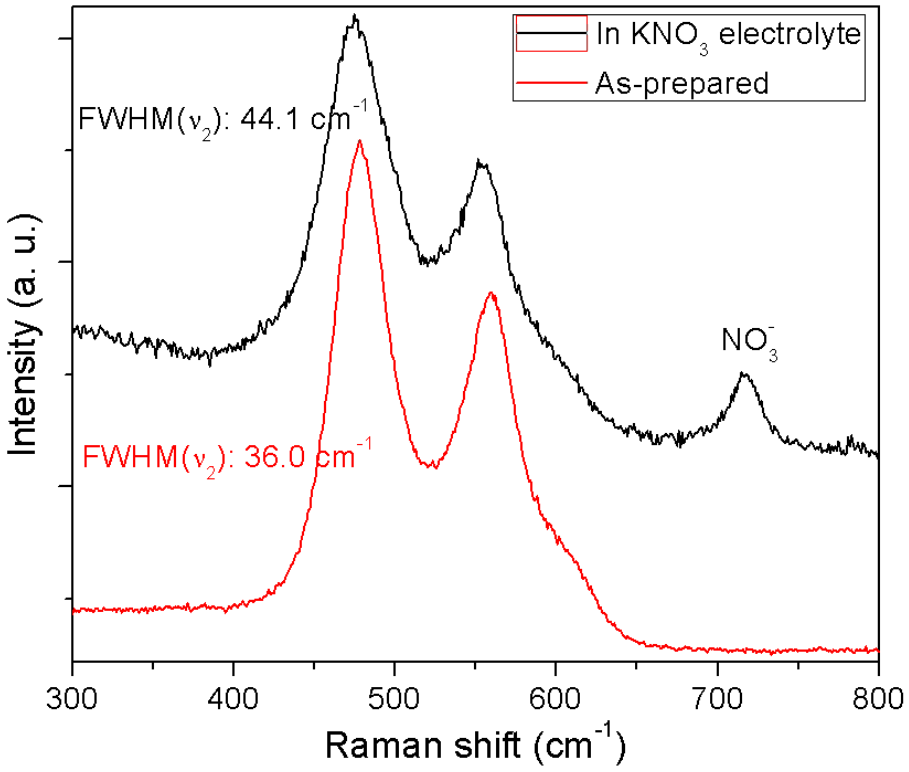


**Figure 5-16.** Comparison of the Raman spectra of the as-prepared $NiO_2H_x$ model electrode and the electrode immersed in a 2 M $KNO_3$ electrolyte at OCV condition.

However, it is obvious that the CV current density (Figure 5-17) was much lower than that of the CV tested in the 2 M KOH electrolyte (Figure 5-12). Moreover, during the operation of the $NiO_2H_x$, the Raman spectra of $NiO_2H_x$ didn't exhibit noticeable feature changes (Figure 5-17); $\omega(E_g)$ and $\omega(A_{1g})$ were retained to be 476 $cm^{-1}$ and 554 $cm^{-1}$, respectively, while $I(A_{1g})/I(E_g)$ was calculated to be 0.57. These experimental facts suggest the charge storage caused by cation incorporation can't cause significant evolution of phonon energies and phonon polarizabilities, implying the properties of Ni-O bond and electron cloud distribution within $NiO_2$ layer remain static during cycling. Meanwhile, the static spectroscopic evolution is in accordance with the limited current density observed in the CV profile, which qualitatively indicates the cation incorporation cannot lead to massive charge storage proven by both electrochemical and structural analyses.

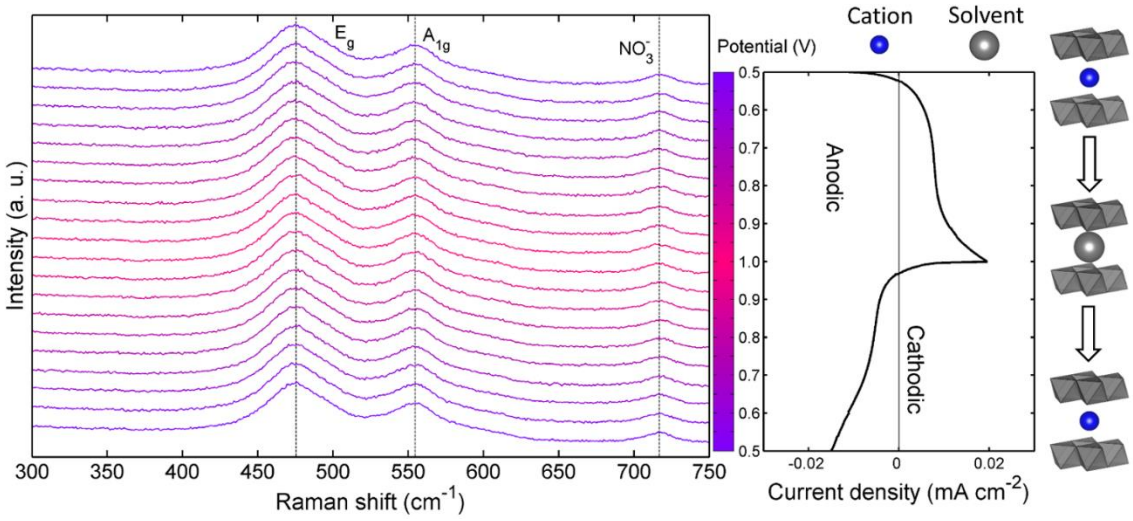


**Figure 5-17.** *In operando* Raman spectroscopic evolution of the $NiO_2H_x$ thin film model electrode operated in a 2 M $KNO_3$ aqueous electrolyte. The corresponding CV profile (10 mV $s^{-1}$) is shown on the right panel. The potential of each spectrum is indicated by the color bar located between the spectra and the CV curves. The color bar is separated into 20 grids. Each grid represents a potential interval of 0.05 V, over which, the spectrum was acquired during the *in operando* measurements. A schematic sketch of interlayer cation insertion/extraction is also shown to illustrate the redox behavior in the $KNO_3$ electrolyte on the basis of quantitative analyses.

## 5.4. Quantitative analyses

To quantitatively analyze the charge storage contribution of the two redox mechanisms, quantitative Raman spectroscopic analyses were performed to correlate the structural features and charge storage. The two Raman bands ($A_{1g}$ and $E_g$) were fitted using a Lorentzian profile (equation (72)) and the stored charge density were calculated by integrating the CV profile acquired during *in operando* experiments shown in Figure 5-12 and Figure 5-17 . Figure 5-18 shows the energy of $E_g$ mode, energy of $A_{1g}$ mode, $I(A_{1g})/I(E_g)$, and the charge storage density as functions of the potential of WE for both KOH and $KNO_3$ electrolytes. In the KOH electrolyte (Figure 5-18a-d) , the evolution of $\omega(E_g)$, $\omega(A_{1g})$, and $I(A_{1g})/I(E_g)$ are in excellent quantitative agreement with the profile of stored charge as a function of the potential, proving that the amount of charge storage is

quantitatively associated to phonon energies and phonon polarizabilities. To be specific, in the potential range where no significant charge is stored/released, the phonon band properties remain largely static; as significant amount of charge is stored/released, the phonon band energy ($\omega(E_g)$ and $\omega(A_{1g})$) exhibit systematic stiffening/softening and band intensity ratio $I(A_{1g})/I(E_g)$ show systematic increase/decrease as a same profile of charge storage (Figure 5-18a-d). On the other hand, in the $KNO_3$ electrolyte, all of the band features basically retained the same values as functions of potentials, also quantitatively consistent with the limited stored charge (about 4 % of the stored charge in the KOH electrolyte based on the enlarged plot). Thus, it can be concluded that the structural features and charge storage in the KOH electrolyte shown in Figure 5-18 are essentially contributed by the breaking/formation of O-H bond (as marked in Figure 5-12) with the minor contribution from cation insertion/extraction (marked in Figure 5-17).

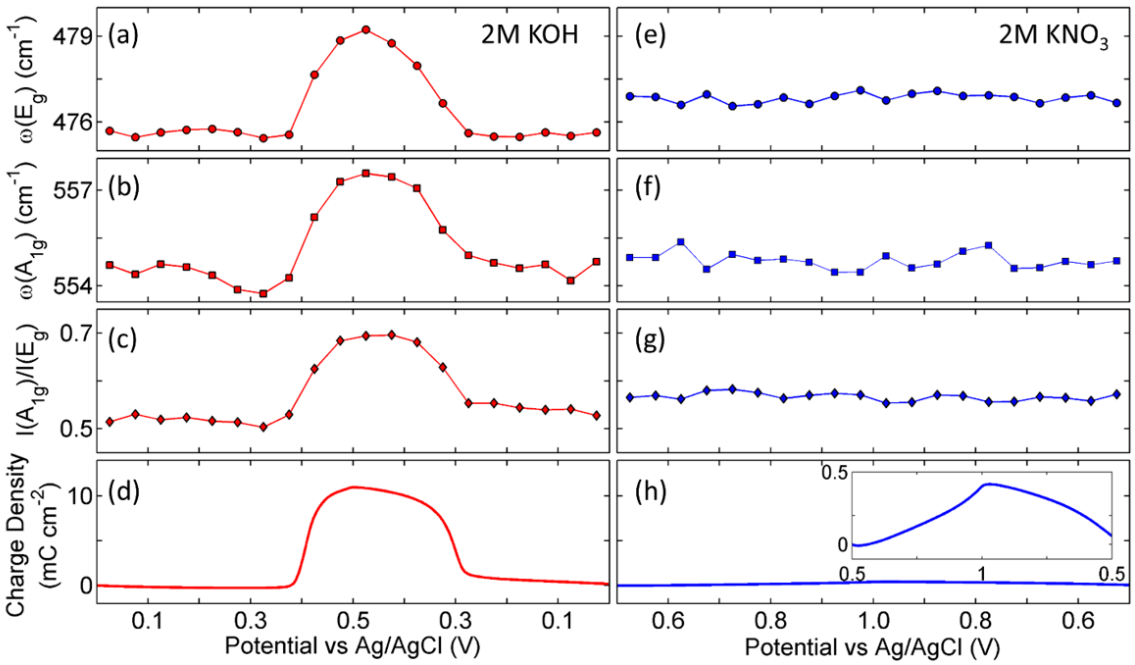


**Figure 5-18.** Quantitative correlation between key spectroscopic features and stored charge density of the $NiO_2H_x$ model electrode when 2 M KOH and 2 M $KNO_3$ were used as electrolytes. (a - d) The energy of the $E_g$ mode (**i.e.,** $\omega(E_g)$), energy of the $A_{1g}$ mode (**i.e.,** $\omega(A_{1g})$), intensity ratio of $A_{1g}$

and $E_g$ (**i.e.,** $I(A_{1g})/I(E_g)$), and stored charge density as functions of the WE potential when KOH was used as the electrolyte, respectively. (e - h) The values of $\omega(E_g)$, $\omega(A_{1g})$, $I(A_{1g})/I(E_g)$, and stored charge density as functions of the WE potential when $KNO_3$ was used as the electrolyte, respectively.

## 5.5. Conclusions

In this chapter, a systematic *in operando* resonance Raman spectroscopic study of thin-film $NiO_2H_x$ model electrodes was performed to investigate the contributions of two possible redox mechanisms of $NiO_2H_x$ during cycling. Depending on resonance enhancement effect, it is found that the phonon properties of $NiO_2H_x$, including $\omega(E_g)$, $\omega(A_{1g})$, and $I(A_{1g})/I(E_g)$, exhibited systematic evolution along with massive redox charge storage in the 2 M KOH electrolyte, whereas limited charge storage and spectroscopic evolution were observed in the 2 M $KNO_3$ electrolyte. Quantitative Raman band analyses indicate that phonon properties ($\omega(E_g)$, $\omega(A_{1g})$, and $I(A_{1g})/I(E_g)$) show strong quantitative dependence on charge storage, confirming that the breaking/formation of O-H bond provides a major contribution to charge storage while cation insertion/extraction playing a much less important role, thus offering important insight into energy storage behavior of $NiO_2H_x$.

# 6. UNRAVELING THE NATURE OF ANOMALOUSLY FAST ENERGY STORAGE IN T-NIOBIUM OXIDE

## 6.1. Introduction

In previous two chapters, charge storage mechanisms of two types of pseudocapacitive materials were investigated using *in operando* Raman spectroscopy and vibrational analyses. As mentioned in chapter 1 and chatter 2, beside supercapacitors, Li-ion batteries are another category of energy storage devices for transportation power supplies and portable electronics. The commercialization of Li-ion batteries is more successful than that of pseudocapacitors. In recent decades, tremendous efforts have been devoted to the developments of extraordinarily high-rate Li-ion battery materials,[143,174-177] in order to make the rate capability comparable to that of pseudocapacitors and develop a new-generation of high-power energy storage devices. The most remarkable progress in this pursuit is the discovery of the anomalously fast energy storage behavior of T-$Nb_2O_5$.[174,178,179] In contrast to the mainstream intercalation-type energy storage materials (e.g., $LiCoO_2$, $LiMn_2O_4$, and $LiFePO_4$), the rate of Li ion intercalation into T-$Nb_2O_5$ (even for a very thick composite electrode) increased almost linearly with the scan rate (equation (17)),[174,180-182] which indicates extremely fast Li ion intercalation that Li ion diffusion doesn't limit the kinetics. Also, this linear relation between the CV current and the scan rate is believed to be the exclusive characteristic of surface-bound capacitive reactions. This unique energy storage behavior of T-$Nb_2O_5$ was defined as "intercalation pseudocapacitance".[174,180] Therefore, T-$Nb_2O_5$ holds a great perspective on the development of thick electrodes with high volumetric energy densities without

compromising power densities,[174] and has been utilized by various works related to device engineering.[183-188] However, the fundamental principles of "intercalation pseudocapacitance" of T-$Nb_2O_5$ remain unsolved.

Unravelling the Li ion intercalation mechanism is a challenging task because the crystal structure of T-$Nb_2O_5$ is complex, as shown in Figure 6-1. In the T-$Nb_2O_5$ crystal, Nb ions are coordinated with either six or seven oxygen ions, forming either tilted octahedral ($NbO_6$) or tilted pentagonal bipyramids ($NbO_7$).[189,190] These $NbO_6$ and $NbO_7$ polyhedra share either corners or edges, constituting an orthorhombic structure (space group: *Pbam*, No. 55).[189,190] Since the discovery of its anomalously fast energy storage behavior, various state-of-art characterization techniques have been applied to probing the Li ion storage mechanism in T-$Nb_2O_5$. Unfortunately, the understanding of the Li ion intercalation mechanism is still at a preliminary stage because of the complexity of the structure.[181,191-193] *In situ* X-ray diffraction (XRD) revealed that Li ion incorporation into T-$Nb_2O_5$ forms a solid solution, resulting in lattice expansion/contraction during lithiation/delithiation.[181,191,192] *In situ* X-ray absorption spectroscopy (XAS) analysis confirmed the change of oxidation state of Niobium ions as well as evolution of Nb-O bond length under cycling conditions.[174,192] Very recently, *ex-situ* nuclear magnetic resonance (NMR) analyses further confirmed the ultrafast kinetics of T-$Nb_2O_5$.[194] Nonetheless, the exact Li ion intercalation mechanism, which is responsible for the above-mentioned changes in lattice parameters, changes in Nb oxidation states, as well as the ultrafast kinetics, is yet to be determined.

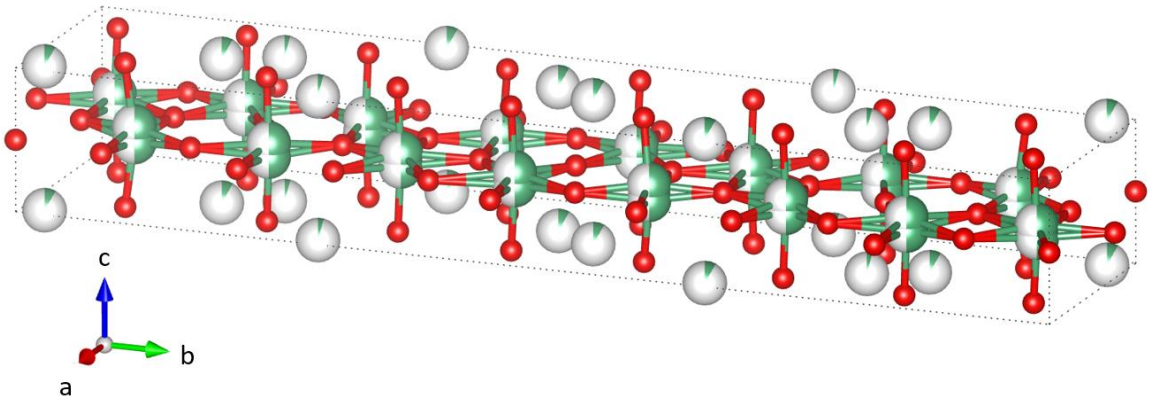


**Figure 6-1.** A sketch of the crystalline structure of T-$Nb_2O_5$.

In previous two chapters, *in operando* Raman spectroscopy has been successfully applied to the study of two supercapacitor materials ($MnO_2$ and $NiO_2H_x$).[40,41] Since the number of vibrational modes is limited for these simple crystal structures, the evolution of a Raman peak or band can be directly linked to a specific structural change, thus offering critical insight to the mechanism of charge storage in electrode materials. This rationale was also applied to previous *in operando* Raman studies on classic Li-ion-based energy storage materials ($LiCoO_2$, $LiMn_2O_4$, $LiFePO_4$, and Li-graphite),[173,195-200] and catalysts.

For a material with a complex structure like T-$Nb_2O_5$, however, the vibrational structures are so complex that it becomes extremely difficult, if not impossible, to straightforwardly correlate a single vibrational band with a specific structural change in the material. Therefore, it is necessary to systematically probe the detailed structural information of the complex material using *in operando* Raman spectroscopy performed on a well-designed model cell under well-controlled operating conditions, together with a comprehensive theoretical analysis of the vibrational structures. On the basis of the model of Li ion incorporation, it is found that the *in operando* Raman spectroscopic evolution is highly consistent with the computed distributions of Raman-active vibrational modes and

vibrational density of states (VDOS), which explains the essential factors of "intercalation pseudocapacitance" in terms of crystallographic sites, type of void, and transport path of Li ions. The detailed experimental and computation investigations are included in following sections.

## 6.2. Sample preparation and characterization

### 6.2.1. Fabrication of thin film T-$Nb_2O_5$

Fabrication of a thin-film model electrode of controlled geometry is the first step for a systematic mechanism study. First, the T-$Nb_2O_5$ powder is synthesized. As a typical synthesis process, 0.691 g of $NbCl_5$ powder (Alfa-Aesar) was dissolved in 2 ml ethanol under ice-bath condition. After the ethanol solution was kept under ice-bath condition for 2 hours, 0.2 ml of cooled DI water was added. Then, the solution was slowly injected by 1 ml of cooled propylene oxide (Alfa-Aesar), forming a transparent gel. Afterwards, the gel was kept in fridge for 24 hours. To remove the organic by-products and chlorides during the above-mentioned steps, 10 ml of acetone was added to the formed gel and was kept being replaced repeatedly for a week. The cleaned gel was dried using Liquid $N_2$ and calcined under 400 $^oC$ in air for 2 hours, forming a dark grey powder, which may contains carbonized species from organic residues. Finally, the powder was calcined in air under 600 $^oC$ for 3 hours, forming crystalline T-$Nb_2O_5$.

For the fabrication of thin-film T-$Nb_2O_5$, first, 10 mg of obtain T-$Nb_2O_5$ powder was firstly dispersed in 20 ml of 1:1 mixture of ethanol and ethylene glycol. After being sonicated aggressively, a total of 75 μL suspension was drop-coated separately in 3 times on a round stainless steel foil (diameter 7/16'') and dried in an oven for 24 hours under 80 $^oC$ each time.

### 6.2.2. Phase characterization

To confirm the phase structure of T-$Nb_2O_5$ powder used for the thin film fabrication. XRD pattern of the obtained T-$Nb_2O_5$ powder was tested (Figure 6-2). The obtained diffraction pattern matches the standard diffraction pattern of T-$Nb_2O_5$ completely (PDF number: 27-1003).[179,191,201,202]

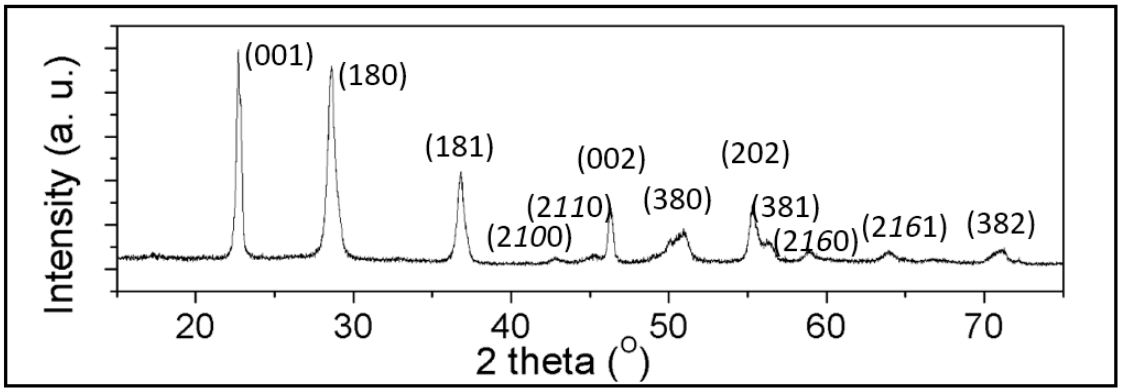


**Figure 6-2.** X-ray diffraction pattern of T-$Nb_2O_5$ powder used in this chapter.

### 6.2.3. Raman spectroscopy

Shown in Figure 6-3 is a typical Raman spectrum of the model electrode. Obviously, the Raman peaks have satisfactory signal-to-noise ratio. However, the broad band widths and irregular band profiles suggest that the observed Raman bands are considerably overlapped, which is a direct indication of the structural complexity of T-$Nb_2O_5$. Since more than 50 atoms exist in the unit cell of T-$Nb_2O_5$, the number of independent vibrational modes will be more than 150.[75-77] A large number of Raman active vibrational modes populated in a particular wavenumber range will inevitably lead to the experimental observation that the Raman spectrum cannot be well-resolved to individual peaks. In this work, such overlapped Raman signal are classified to different band groups: high wavenumber band group ($\nu_{Hi}$) ranging from 570 to 770 $cm^{-1}$, mid wavenumber band group

($\nu_{Mid}$) ranging from 180-360 $cm^{-1}$, and low wavenumber band group ($\nu_{Lo}$) ranging from 80-160 $cm^{-1}$ as marked in Figure 6-3. The key information of these band groups (e.g., positions, profiles, and relative intensities), which is the overall sum of individual Raman modes of T-$Nb_2O_5$, will be traced during *in operando* experiments to reveal structural changes induced by Li ion incorporation. The nature of the Raman bands (symmetry assignments and atomistic motions) of T-$Nb_2O_5$, which compose the observed band groups can be analyzed only through systematic theoretical vibrational analyses. It should be noted that a large number of reported studies have attempted to interpret experimentally overlapped Raman bands for a complicated structure (not limited to T-$Nb_2O_5$) such as assigning high-wavenumber bands as stretching modes.[190,203,204] However, these simple approaches, which can provide only preliminary interpretations, are mostly based on empirical judgements.

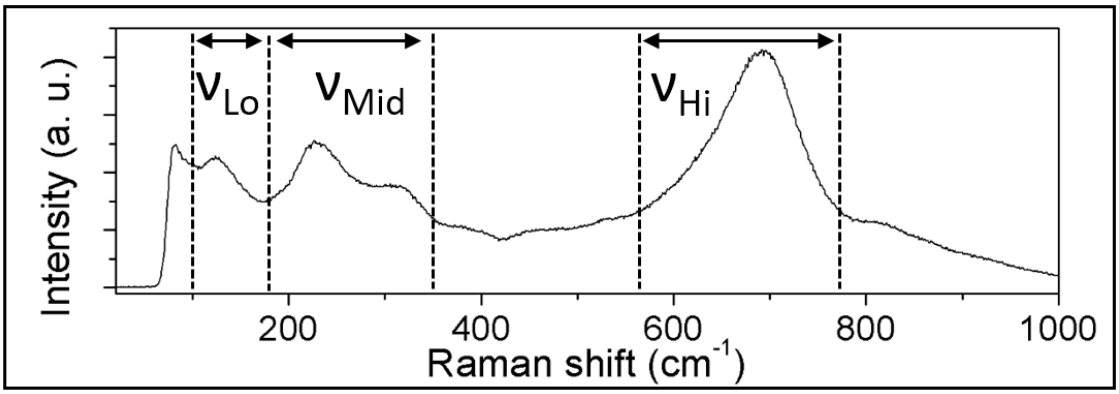


**Figure 6-3.** Raman spectrum of T-$Nb_2O_5$ thin film used in this study. The ranges for major band groups are defined.

### 6.2.4. Electrochemical behavior

The *in operando* Raman cell for Li-ion battery application is shown in Figure 3-4. To confirm the reliability of *in operando* cell, it is necessary to compare the long-term stability of a well-developed material using the *in operando* Raman cell and a standard Li-ion battery set-up. In this study, the long-term cycling stability of $LiMn_2O_4$ using a C/10

rate was compared (Figure 6-4). The $LiMn_2O_4$ is deposited on carbon fiber paper.[205] The voltage window is from 3.2 V to 4.4 V. The electrolyte is 1 M $LiPF_6$ in 1:1 EC-DMC mixture. It is obvious that the capacity retentions tested in the two configurations are essentially comparable. This experimental fact confirms that the designed *in operando* cell can provide same electrochemical environment as a normal Li-ion battery and reliable *operando* Raman spectroscopic acquisition.

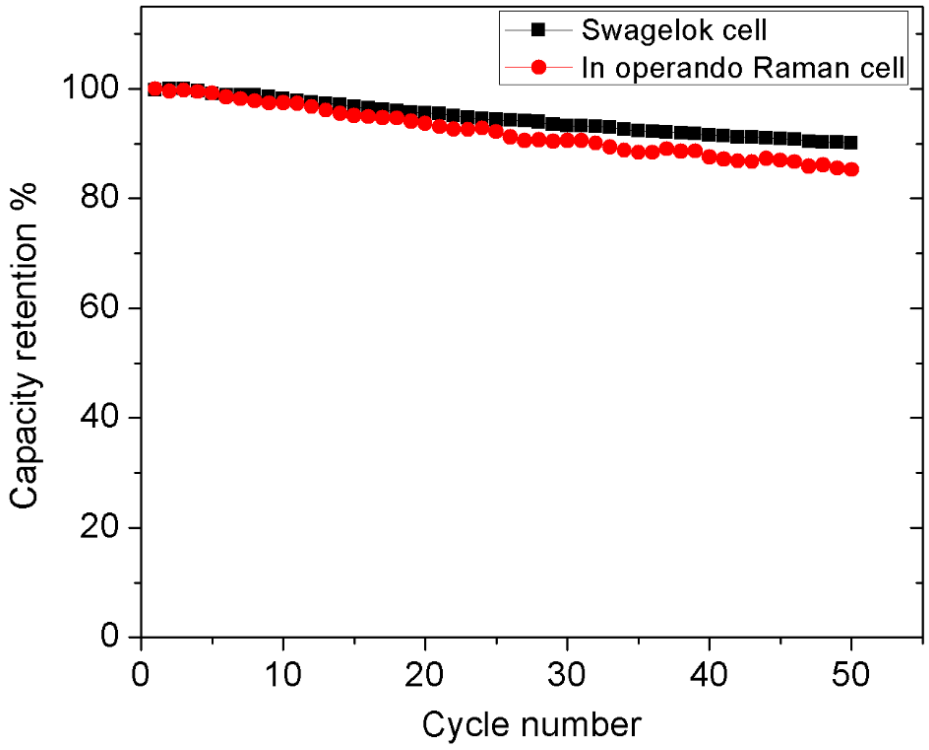


**Figure 6-4.** Capacity retention of a CFP/$LiMn_2O_4$ electrode using normal Swagelok cell and *in operando* Raman cell.

On this basis, cyclic voltammogram (CV) was used to change the stage of Li ion incorporation of T-$Nb_2O_5$ electrochemically, which is performed using 1 M $LiClO_4$ dissolved in dimethyl carbonate (DMC) as the electrolyte in the potential range of 3.0 V to 1.2 V vs $Li^+/Li$. The CV profile is shown in Figure 6-5 and basically agrees with the CV profile of T-$Nb_2O_5$ reported previously.[174,179] The electrochemical current as a function of

potentials indicates that the incorporation of $Li^+$ mainly occurs in low potential range (below 2.0 V approximately). The electrochemical response of Li ion incorporation will be served as an important reference for further *in operando* Raman spectroscopic analyses as a function of cell potentials.

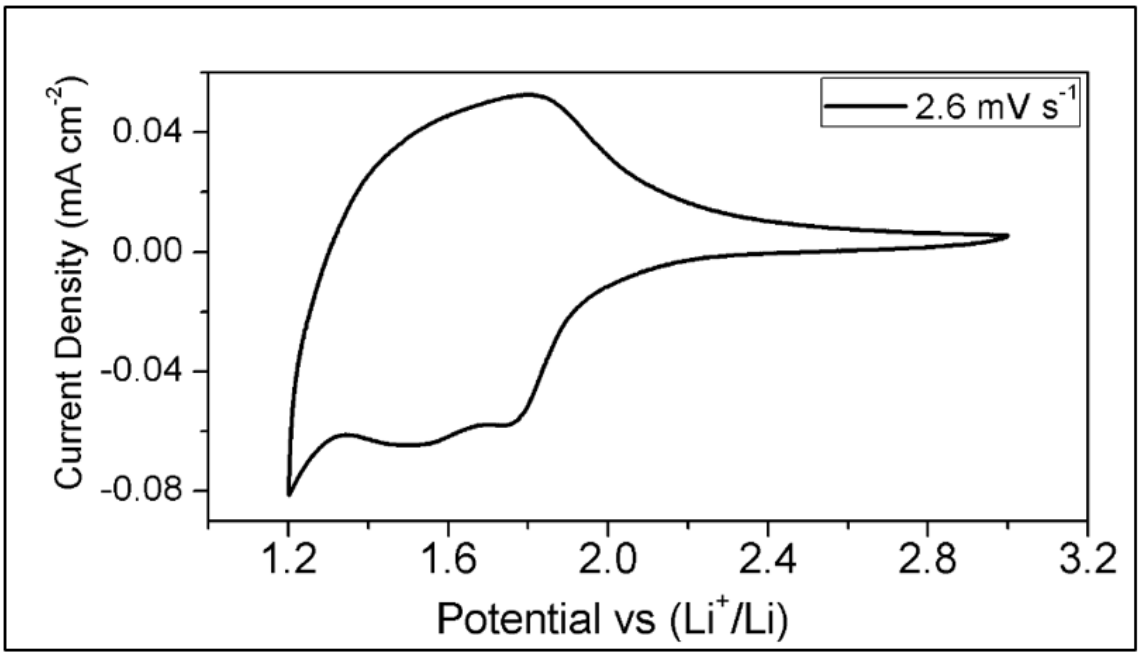


**Figure 6-5.** Cyclic voltammogram (CV) of the T-$Nb_2O_5$ thin film model electrode using the *in operando* Raman cell.

## 6.3. *In operando* Raman spectroscopic evolution

Performed synchronously with CV operations, the *in operando* Raman spectroscopic signal acquired in consecutive electrochemical cycles is shown as a two-dimensional image (Figure 6-6) to examine the general band evolution and reversibility. As shown in Figure 6-5, the CV scan rate is controlled to be 2.6 mV/s so that one Raman spectrum is acquired in a potential interval of 0.1 V. Each *in operando* cycle starts/ends at the potential of 3.0 V (high potential state). In Figure 6-6, Raman spectra near each cycle number represent the higher potential states, whereas Raman spectra in between each cycle

number represent the lower potential states. Obviously, the Raman spectroscopic evolution is completely reversible and consistent for different cycles. During the cycling between the high potential state and the low potential state, the $\nu_{Hi}$ band group exhibits periodic intensity increase and decrease, respectively. Also, the $\nu_{Mid}$ and $\nu_{Lo}$ band groups show obvious reversible evolution as well, as the intensity distribution of the two band groups greatly changed periodically in each cycle. This reversible evolution of the Raman band groups of T-$Nb_2O_5$ is undoubtedly a convincing indication of the reversible structural evolution induced by Li ion intercalation/deintercalation. On the basis of such reversibility, the Raman spectra at each potential can to be analyzed individually to further investigate the vibrational features at different stages of Li ion storage.

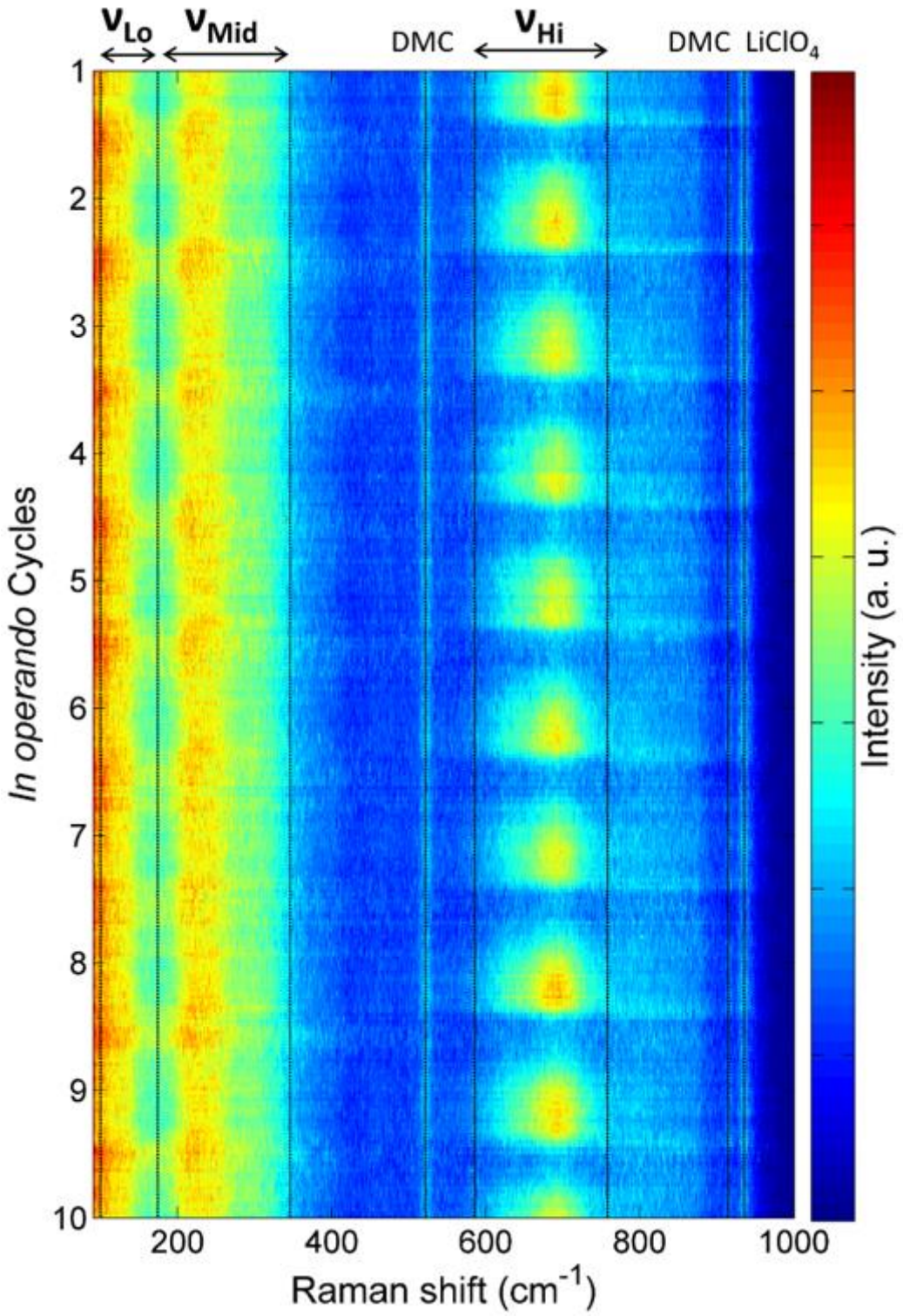


**Figure 6-6.** *In operando* Raman spectroscopic evolution of the T-$Nb_2O_5$ thin film electrode acquired in ten cycles. The evolution is shown as a two dimensional image and the Raman intensity is depicted using a color bar. In each cycle, the electrochemical potential is cycled from 3.0 V to 1.2 V and back to 3.0 V while Raman acquisition is performed simultaneously with an interval of

0.1 V. Raman spectra near each cycle number represent the higher potential states, whereas Raman spectra acquired at the lower potential states lie in the middle between each cycle number. Major Raman band groups of T-$Nb_2O_5$ and electrolyte bands are marked.

To evaluate the details of Raman evolution, Raman spectra at each individual potential interval in different cycles are summed up, generating the spectroscopic evolution shown in Figure 6-7. During the cathodic process (potential sweep from 3.0 V to 1.2 V), the evolution of each band group can be summarized as follows. First, $\nu_{Hi}$ band group basically remains static during the potential sweep from 3.0 V to 2.0 V approximately, which is consistent with the fact that the CV current in this potential range is not significant (Figure 6-5). As the potential continues to approach 1.2 V, the relative intensity of $\nu_{Hi}$ band group greatly decreases and eventually almost vanishes. Second, similar to $\nu_{Hi}$ band group, $\nu_{Mid}$ band group presents no obvious evolution during the potential sweep from 3.0 V to 2.0 V. Afterwards, $\nu_{Mid}$ band group presents significant splitting gradually (marked with dash lines). The maximized splitting for $\nu_{Mid}$ band group is observed at 1.2 V approximately. Third, for $\nu_{Lo}$ band group, after being static from 3.0 V to 2.0 V, the position of $\nu_{Lo}$ experiences a minor blue shift with the maximized shift at 1.2 V. The overall effect of the evolution of the three band groups makes the Raman spectrum of the low potential state (1.2 V) drastically different from that of the high potential state (3.0 V). During the following anodic process, the three band groups displayed a reverse behavior of cathodic process, including the intensity increase of $\nu_{Hi}$, band merging of $\nu_{Mid}$, and red shift of $\nu_{Lo}$. For the Raman bands of the electrolyte (DMC and $LiClO_4$), the band properties (position, width, intensity, and profile) remain totally static during the entire process, indicating that the electrochemical operation has no influence on electrolyte properties at all.

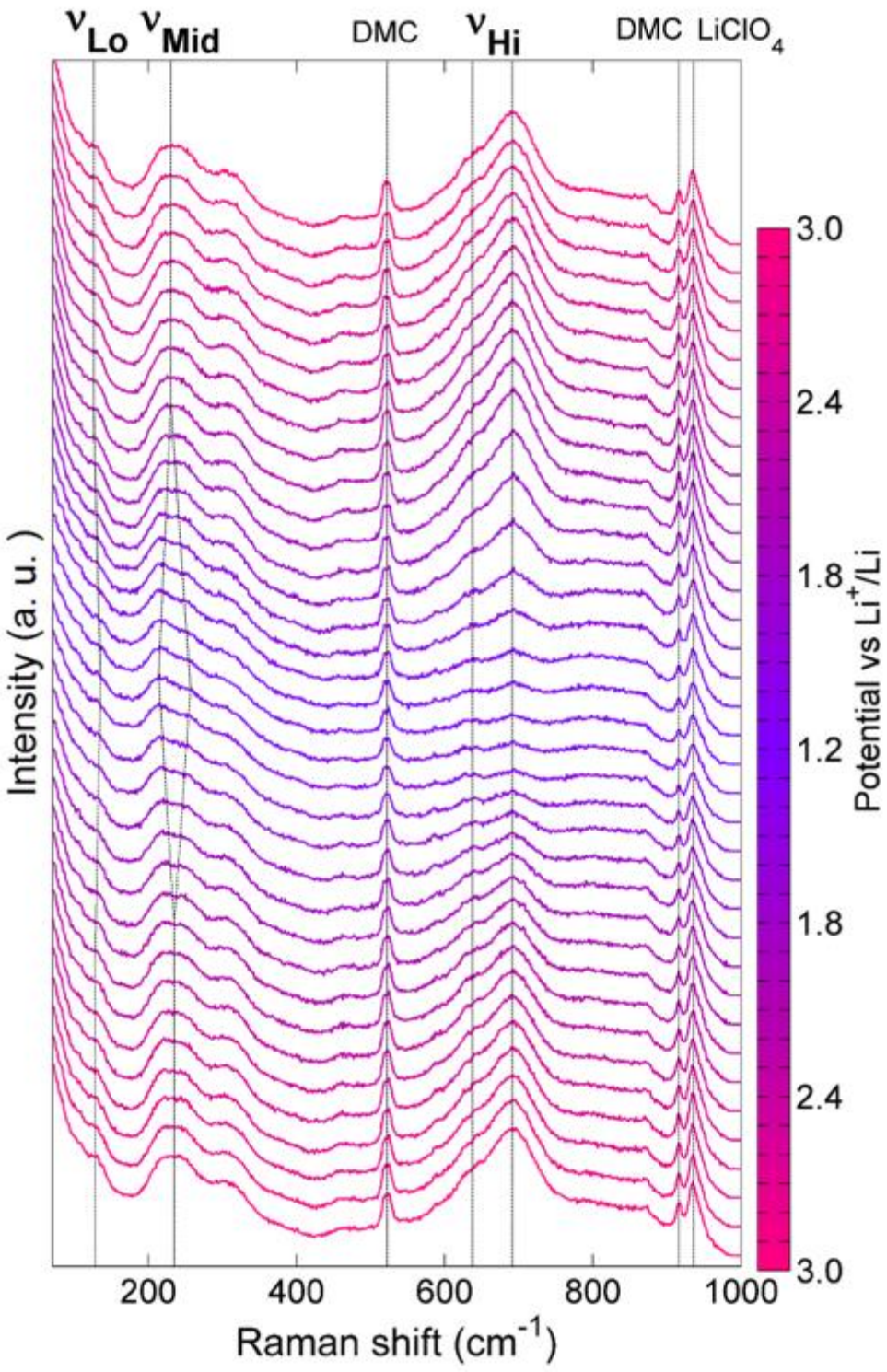


**Figure 6-7.** *In operando* Raman spectroscopic evolution of the T-$Nb_2O_5$ thin film electrode when the WE is cycled between 3 V, 1.2 V, and 3 V. The dash lines are applied to show the evolution of major band groups. The potential of each spectrum is indicated by the color bar. The color bar is

separated into 36 grids. Each grid represents a potential interval of 0.1 V, over which, the spectrum was acquired during the *in operando* measurements.

## 6.4. Quantitative analyses

The exact values of vibrational properties as a functional of electrochemical operations can be considered as a quantitative indication of structural evolution induced by incorporation of Li ion. To perform accurate correlation with electrochemical properties, systematic band fitting was performed to quantitatively describe the band group evolution. The intensity decrease of $\nu_{Hi}$ band group is quantified by calculating the integrated intensity ratio of $\nu_{Hi}$ band group and $\nu_{Mid}$ band group. The splitting of $\nu_{Mid}$ band group is depicted by values of band fitting results. To ensure consistency, three Gaussian bands were used to fit the $\nu_{Mid}$ regardless of the profile of $\nu_{Mid}$ (split or merged, Figure 6-8).

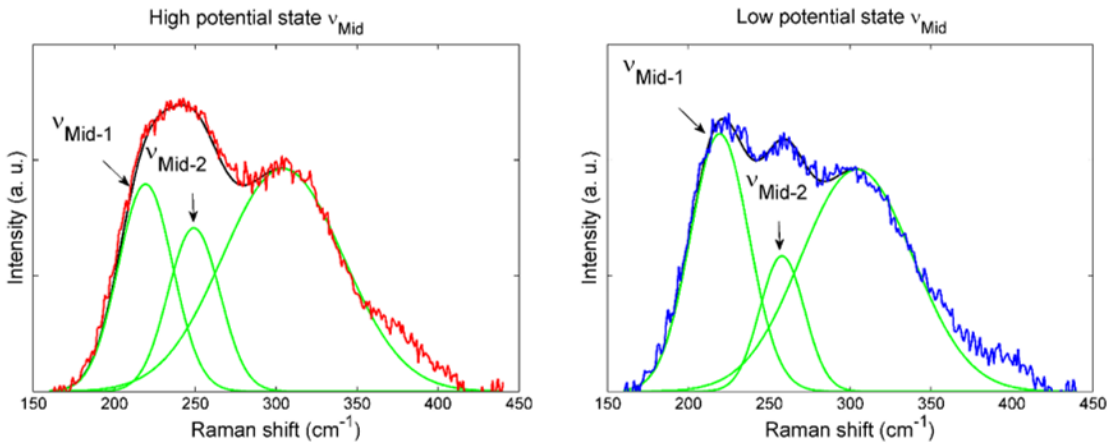


**Figure 6-8.** Fitting of $\nu_{Mid}$ band group for the high potential state and the low potential state. The individual Gaussian bands are plot as green lines. The fitted spectra are shown as black lines. The doublets ($\nu_{Mid-1}$ and $\nu_{Mid-2}$) are marked.

Combining all of the quantifications mentioned above, Figure 6-9 shows the positions of $\nu_{Mid}$ doublets ($\nu_{Mid-2}$ and $\nu_{Mid-1}$) and intensity ratio between $\nu_{Hi}$ and $\nu_{Mid}$ as well as the stored charge density (integrated from Figure 6-5) as a function of electrochemical

potentials. The evolution of these band properties are in good agreement quantitatively with stored charge density. To be specific, in the potential range where charge storage/release is not significant, the $\nu_{Mid}$ band group remained merged and $\nu_{Hi}$ band group is of considerably high intensity. As charge is stored/released, positions of $\nu_{Mid-1}$ and $\nu_{Mid-2}$ separates/merges and $I(\nu_{Hi})/I(\nu_{Mid})$ decreases/increases accordingly.

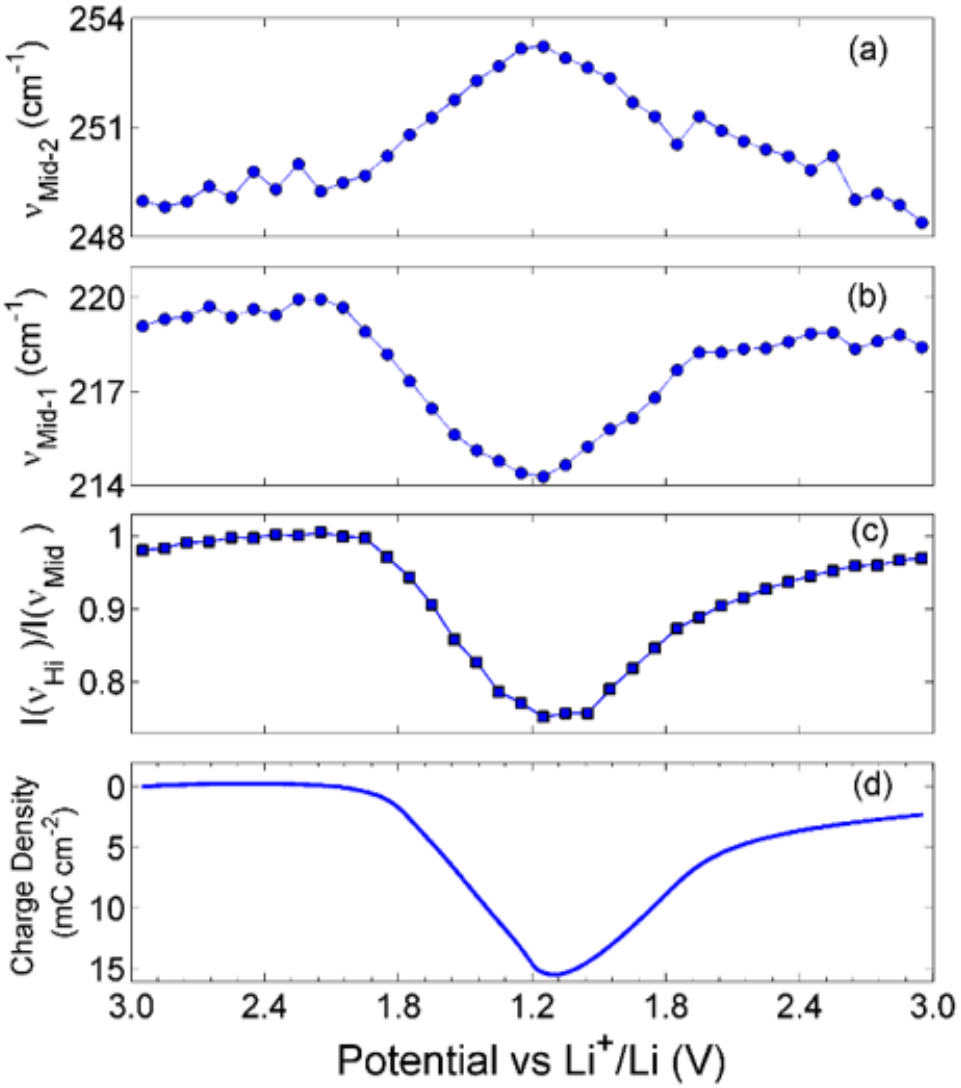


**Figure 6-9.** Quantitative correlation between key features of *in operando* Raman spectra and stored charge density. (a-b) The positions of $\nu_{Mid-2}$ and $\nu_{Mid-1}$ doublet as function of cell potentials. (c) Intensity ratio of $\nu_{Hi}$ and $\nu_{Mid}$ as a function of cell potentials. (d) Electrochemical charge storage density of the T-$Nb_2O_5$ thin film electrode as a function of cell potentials, respectively.

## 6.5. Model of Li ion storage and transport for T-$Nb_2O_5$

Undoubtedly, the Raman spectroscopic evolution as a function of electrochemical potentials mentioned above is a direct consequence of the consecutive structural change of T-$Nb_2O_5$ at different stage of Li ion incorporation. However, such structural changes responsible for fast Li-ion storage cannot be feasibly interpreted from vibrational evolution since the nature of the experimental Raman band groups is unknown. To reveal the structural information conveyed by spectroscopic evolution, a hypothetical model of Li-incorporated T-$Nb_2O_5$ is needed to calculate the vibrational structure and the effect of Li incorporation on the vibrational structure, and to correlate with experimental Raman spectroscopic evolution. The incorporation mechanism will be investigated in terms of both crystallographic sites, the local Nb-O bonding structure, and the kinetics of Li ion incorporation.

### 6.5.1. The structure of unlithiated T-$Nb_2O_5$

The structure of pristine T-$Nb_2O_5$ (unlithiated) is shown in Figure 6-1. The stoichiometry of the cell is $Nb_{16.8}O_{42}$. In one unit cell, 0.8 out of 16.8 Nb (less than 5% amount of Nb) is randomly distributed in the crystalline structure. To make the calculation of the unlithiated T-$Nb_2O_5$ executable, a few approximations have to be applied. First, the small amount of the randomly distributed Nb can't be considered for theoretical calculation since the location is not defined and stoichiometry is fractioned. Second, since the 0.8 Nb is not considered, 2 oxygen ions out of 42 in one unit cell (less than 5% amount of oxygen) have to be removed at the same time to balance the charge of the entire unit cell. To be specific, the two oxygen ions at 2b Wyckoff position are removed in the model cell since the 2b Wyckoff position doesn't have any Raman active modes. The overall effect is that

the model of unlithiated T-$Nb_2O_5$ is $Nb_{16}O_{40}$, slightly different from the actual $Nb_2O_5$ ($Nb_{16.8}O_{42}$). To make theoretical calculations on T-$Nb_2O_5$ executable, such simplification is inevitable. However, the deviation caused by this simplification is expected to be inconsequential since the major framework of T-$Nb_2O_5$ is not affected. In addition, for the theoretical calculation, the Nb positions have to be determined, in contrast to the slight uncertainty of Nb positions (0.3 Å) shown in Figure 6-1.

After these necessary approximations, the unlithiated T-$Nb_2O_5$ model was constructed, as shown in Figure 6-10 (orthorhombic, space group *Pbam* No. 55). After the geometry optimization process, the lattice parameters for unlithiated $Nb_2O_5$ model are a=6.37 Å, b=29.78 Å, c=3.92 Å, $\alpha=\beta=\gamma=90^o$ (orthorhombic). Judging from its cell structure, T-$Nb_2O_5$ has a large number of spacious voids between Nb-O bonds that are potentially suited for Li ion accommodation. Despite the structural complexity, these voids can be categorized into two types according to the local Nb-O bonding structure. For the first type, Li ions can be accommodated into the three-dimensional voids lying in the triangular prism-like cages formed by 6 Nb and 9 O (Figure 6-10). For the second type, Li ions can be attached to the two-dimensional voids on the facets of Nb-O bonds formed by 4 Nb and 4 O (Figure 6-10).

For the technical details of computation, all the calculations for structural optimization, charge analysis and vibrational frequency analysis have been carried out with the Vienna Ab Initio Simulation Package (VASP) at the density functional theory (DFT) based with 3D periodic conditions.[206-208] The exchange-correlation function was treated by generalized gradient approximation with Perdew-Wang 1991 formula (GGA-PW91).[209,210] The electron-ion interaction was treated by the projector-augmented wave method (PAW)

that the core electrons were treated with cost-effective pseudopotentials implemented in VASP and the valence electron were expanded by plane-wave basis with the kinetic cutoff energy of 600 eV.[211,212] Brillouin-Zone (BZ) integration was sampled by Monkhorst-pack scheme at 0.05 × 2 (1/Å) interval in the reciprocal space.[213] The structural optimization and energetic calculations were computed by quasi-Newton method with the energetic and gradient convergences of $1 \times 10^{-4}$ and $1 \times 10^{-2}$ eV, respectively.

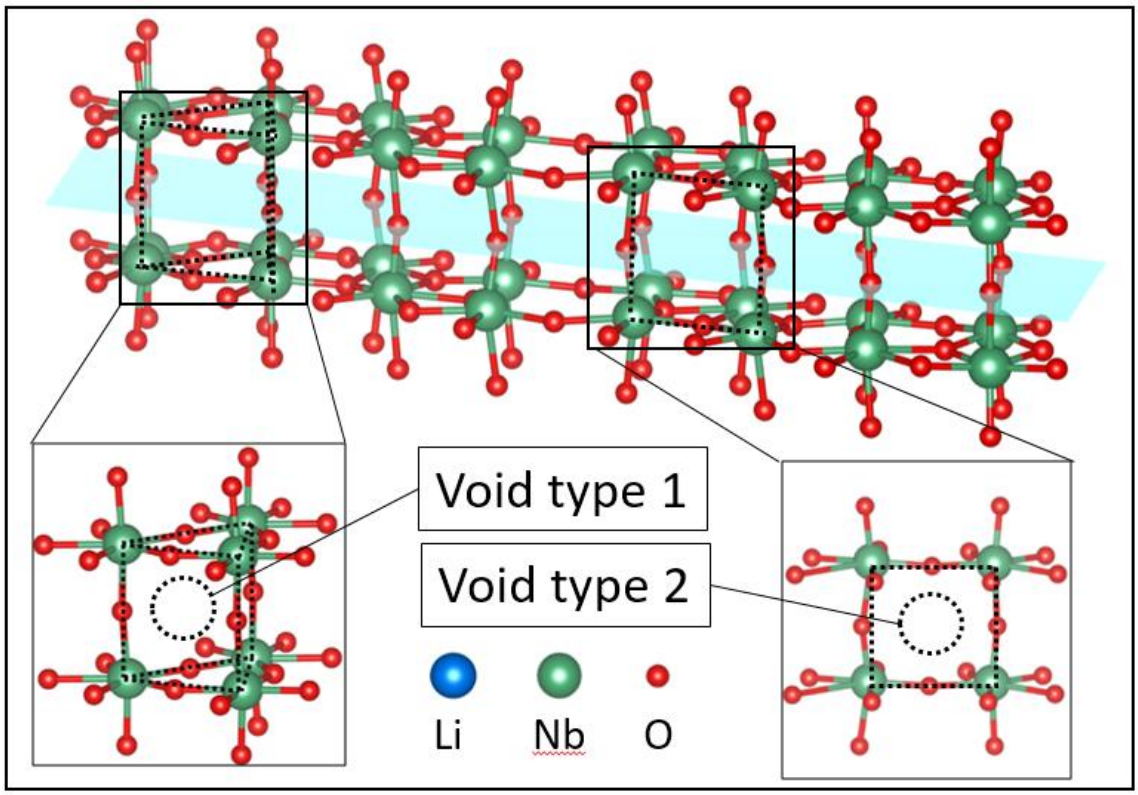


**Figure 6-10.** Structure of unlithiated T-$Nb_2O_5$. Two local bonding structures are shown to demonstrate the type of possible voids for Li accommodation: triangular bipyramid (3D void) and Nb-O bonding facet (2D void).

### 6.5.2. Li ion incorporation behavior

For the model of lithiated T-$Nb_2O_5$, first, it is necessary to determine the stoichiometry of incorporated Li ions for the model cell. According to previous studies, it is suggested that the $Nb_2O_5$ forms a stable solid solution up to 1.25 $Li^+$ per one $Nb_2O_5$

formula.[191,192] The electrochemical testing results (Figure 6-9) indicate the amount of $Li^+$ incorporated in one $Nb_2O_5$ formula is approximately 1.1 (about 8.8 Li+ per unit cell). For the other works, this value is generally similar with slight variations.[174,179] Therefore, to make the calculation executable, it is determined that the stoichiometry of Li for the lithiated model is 1 per $Nb_2O_5$ (eight Li ions in one unit cell).

Through computational investigation, the structure of lithiated T-$Nb_2O_5$ with minimized energy is shown in Figure 6-11. First, with regard to the crystallographic structure, it is found that all Li ions are located at the same plane, which is right in the middle between the two layers of niobium atoms. To make it clear, this plane preferred by Li ion incorporation is highlighted in Figure 6-10. Crystallographically, this plane is where 4g Wyckoff sites (space group *Pbam*, No. 55) are generally located. It is obvious that this plane has the lowest atomic density, thus offering least steric effect and repulsion from positively charged niobium atoms. As a direct result of Li ion accommodation, the c-axis of the unit cell expands from 3.92 Å to 3.98 Å, which is consistent with a previous *in operando* XRD measurement (3.91 Å to 4.02 Å).[181] Second, with regard to the local bonding structure, interestingly, all Li ions are found exclusively located at the 2D voids on the facets formed by Nb-O bonds (Figure 6-11).

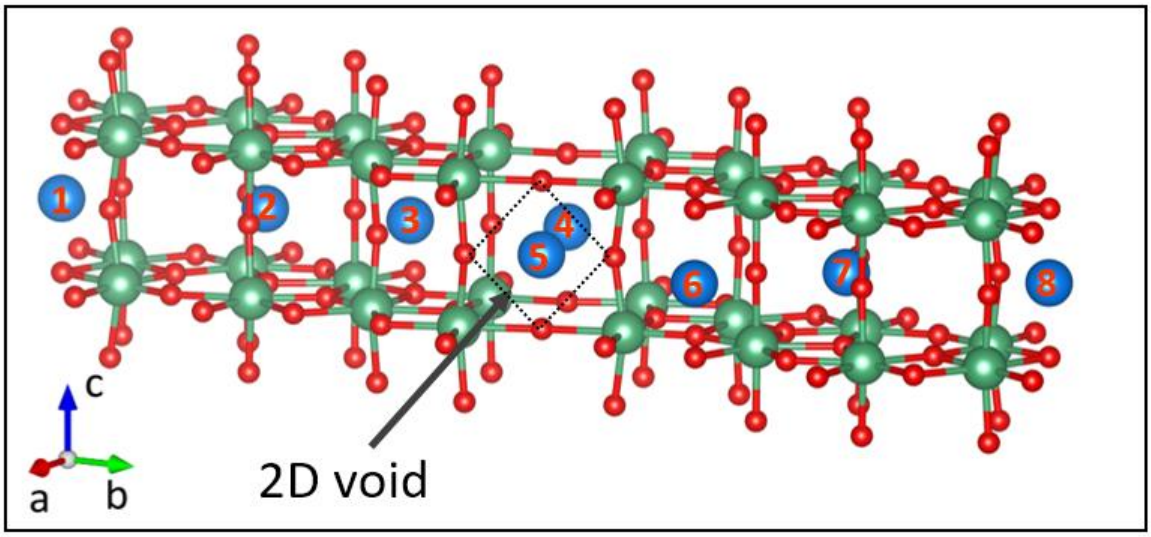


**Figure 6-11.** The structure of lithiated T-$Nb_2O_5$ after geometry optimizations. The eight incorporated Li ions in one unit cell are labeled.

To further demonstrate the exclusive selectivity of the void for Li incorporation in Figure 6-11, the lithiated structure (2x2x1 expanded) is projected from [001] direction as shown in Figure 6-12. It is obvious that all of the incorporated Li ions are preferably located at the voids on the facet constructed by Nb-O bonds. Since the facet is perpendicular to (001) plane, when viewed from [001] direction, Li ions are appeared to be stacked under oxygen ions (Figure 6-12).

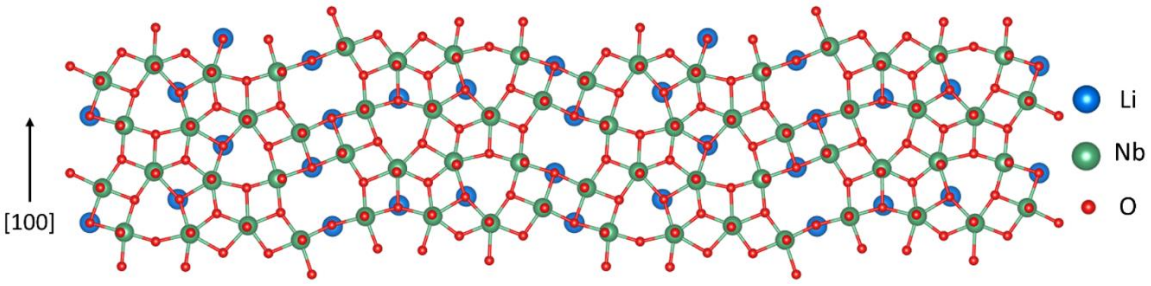


**Figure 6-12.** Lithiated T-$Nb_2O_5$ model cell after geometry optimization viewed from [001] direction.

The adsorption energies for each incorporated Li ion in these voids (labeled in Figure 6-11) were calculated. The calculation is based on equation (87):

$$E_{ads} = E[surface - adsorbate] - E[surface] - E[adsorbate] \ . \qquad (87)$$

The calculated adsorption energies range from -3.23 eV to -3.53 eV (Table 6-1), indicating that the accommodated Li ions are highly stable.

**Table 6-1. Adsorption Energies of Li ions labelled in Figure 6-11**

| Label number | 1 | 2 | 3 | 4 | 5 | 6 | 7 | 8 |
|---|---|---|---|---|---|---|---|---|
| Adsorption energy (eV) | -3.45 | -3.25 | -3.53 | -3.50 | -3.45 | -3.23 | -3.47 | -3.46 |

To further evaluate the selectivity of Li ion accommodation, the adsorption energies of one specific Li ion placed at a 2D or a 3D void were also calculated, as shown in Figure 6-13. The adsorption energy for one Li ion placed at a 3D void (Figure 6-13) is -3.11 eV whereas those for a Li ion placed at each of the three neighboring 2D voids (Figure 6-13) are -3.47 eV, -3.32 eV, and -3.29 eV, respectively, further indicating that accommodation of a Li ion at a 2D void is energetically more favorable than that at a 3D void.

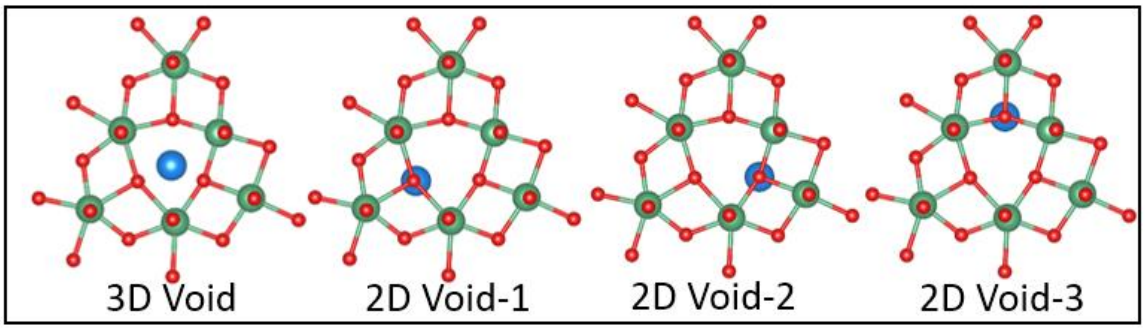


**Figure 6-13.** Local structures of $Nb_2O_5$ when one Li ion is adsorbed on one 3D void or each of three neighboring 2D voids. The viewing direction is [001] and upward vector is [100].

As a general schematic of Li ion incorporation for T-$Nb_2O_5$, Figure 6-14 shows the change of local Nb-O bonding before and after a Li ion (labeled 7 in Figure 6-11) is

incorporated on the 2D facet. The charge difference image of the facet clearly shows the reduction of Nb and oxidation of Li for the Li ion incorporation process.

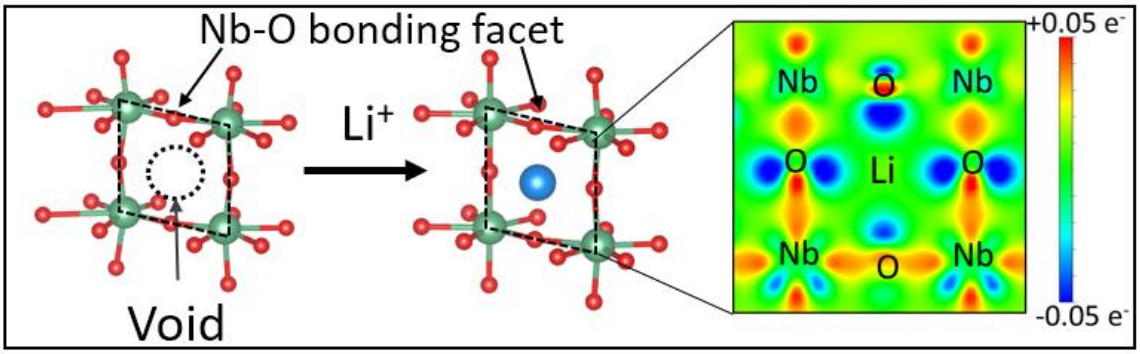


**Figure 6-14.** A schematic of adsorption of a Li ion on a 2D void formed by Nb-O bonding facet and the distribution of the induced charge change on a Nb-O facet (highlighted by dash lines) as a result of lithiation process.

### 6.5.3. Li ion Transport behavior

Based on the Li ion adsorption mechanism mentioned above, the transport of Li ions in T-$Nb_2O_5$ can be interpreted accordingly. The diffusion of Li ions involves a series of elementary steps (Figure 6-15) during which a Li ion adsorbed on a 2D void migrates to another neighboring 2D void.

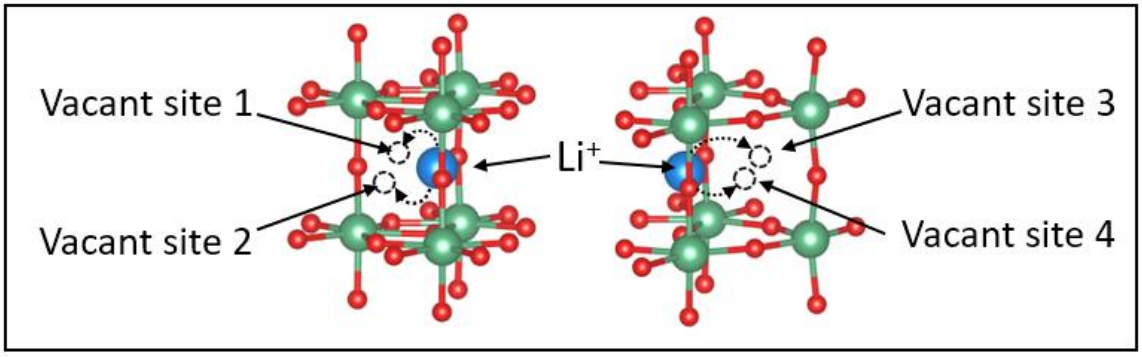


**Figure 6-15.** A schematic of elementary steps for Li ion transport. Each Li ion can migrate to four neighboring 2D voids.

Each adsorbed Li has four neighboring 2D voids (Figure 6-15) and the connection between these voids (distance ~2-3 Å) forms a large variety of tunnels without any obstructing oxygen ions (Figure 6-16). Since all of these tunnels are parallel to (001) plane, the combination of these tunnels forms a quasi-2D pathway for $Li^+$ transport, which is a unique characteristic for T-$Nb_2O_5$ and clearly unraveled the Li-ion transport pathway. Furthermore, the quasi 2D network connected by 2D voids explains the fundamental reason of the recently reported bond valence sum simulation results, which suggested degenerate diffusion pathways for T-$Nb_2O_5$. [194] To evaluate the feasibility of Li ion transport, calculations of kinetic energies were performed. The calculated energy barriers that must be overcome for a selected Li ion to transport to the neighboring 2D voids (numbered one to four in Figure 6-15) are 0.36 eV, 0.25 eV, 0.39 eV, and 0.26 eV, respectively. It should be noted that these energy barriers are consistently lower than 0.4 eV regardless of the direction of transport, which is comparable to the state-of-art Li ion conductors.[214,215] Moreover, considering the fact that the differences in adsorption energy of each Li ion are fairly small (< 0.3 eV, Table 6-1), the incorporated Li ions are not likely trapped in fixed locations and diffusion of Li ions is both thermodynamically and kinetically favorable. Therefore, the stable adsorption of Li ions on the 2D voids with fast kinetics resembles a capacitive surface adsorption behavior, which is the unique feature for T-$Nb_2O_5$.

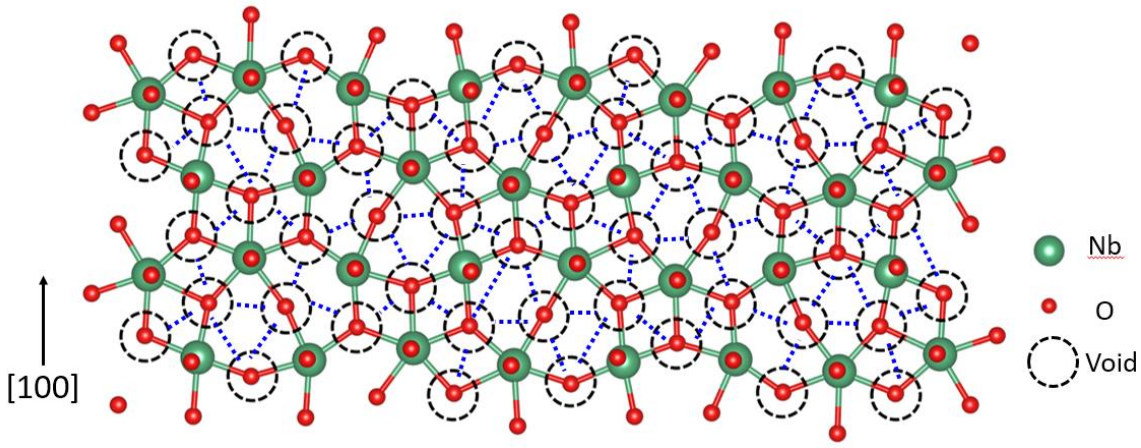


**Figure 6-16**. The structure of T-$Nb_2O_5$ viewed from [001] direction. The voids located on Nb-O bonding facets preferred for Li ion incorporation are highlighted. The connections between the voids are highlighted as blue dash lines.

## 6.6. Validation of Li ion incorporation mechanism of T-$Nb_2O_5$

To validate our proposed mechanism of Li-ion incorporation, theoretical calculations of the vibrational modes of the lithiated and unlithiated T-$Nb_2O_5$ model mentioned above were performed to understand Raman spectroscopic evolution from high to low potential states. As mentioned previously, because of the structural complexity of T-$Nb_2O_5$, simple correlation of a single Raman mode and structural evolution is impossible. Instead, a comprehensive vibrational analysis is applied. To be specific, first, the frequency values of Raman active modes at the Γ-point were calculated, resulting in a number of discrete theoretically Raman-active frequency points. Then, the continuous distribution of vibrational density of states (VDOS) integrated at Γ-point from phonon dispersion was calculated. Both discrete Raman frequencies and VDOS will be compared with experimental Raman spectra.

### 6.6.1. Vibrational analyses

Prior to detailed calculation of vibrational frequencies, the analyses of mechanical representations (phonon modes) of the unlithiated and lithiated T-$Nb_2O_5$ model were performed on the basis of cell structures shown in Figure 6-10 and Figure 6-11. The *Pbam* space group (No. 55) is based on 3D point group $D_{2h}$. The character table of point group $D_{2h}$ is shown in Table 6-2. Of all the normal modes, the $A_g$, $B_{1g}$, $B_{2g}$, and $B_{3g}$ modes (for space group *Pbam*) are theoretically Raman active.[131]

**Table 6-2. The character table of the point group $D_{2h}$.**

| $D_{2h}$(mmm) | E | $C_{2z}$ | $C_{2y}$ | $C_{2x}$ | i | $\sigma_z$ | $\sigma_y$ | $\sigma_x$ | functions |
|---|---|---|---|---|---|---|---|---|---|
| $A_g$ | 1 | 1 | 1 | 1 | 1 | 1 | 1 | 1 | $x^2$, $y^2$, $z^2$ |
| $B_{1g}$ | 1 | 1 | -1 | -1 | 1 | 1 | -1 | -1 | xy, $J_z$ |
| $B_{2g}$ | 1 | -1 | 1 | -1 | 1 | -1 | 1 | -1 | xz, $J_y$ |
| $B_{3g}$ | 1 | -1 | -1 | 1 | 1 | -1 | -1 | 1 | yz, $J_x$ |
| $A_u$ | 1 | 1 | 1 | 1 | -1 | -1 | -1 | -1 | · |
| $B_{1u}$ | 1 | 1 | -1 | -1 | -1 | -1 | 1 | 1 | z |
| $B_{2u}$ | 1 | -1 | 1 | -1 | -1 | 1 | -1 | 1 | y |
| $B_{3u}$ | 1 | -1 | -1 | 1 | -1 | 1 | 1 | -1 | x |

For unlithiated T-$Nb_2O_5$ model cell, one unit cell contains 56 atoms/ions. Therefore, the degree of freedom (DOF) is 168. The mechanical representation can be expressed as:

$$\Gamma = 28A_g + 14A_u + 28B_{1g} + 14B_{1u} + 14B_{2g} + 28B_{2u} + 14B_{3g} + 28B_{3u} \ . \quad (88)$$

The Raman active modes are:

$$\Gamma_{Raman} = 28A_g + 28B_{1g} + 14B_{2g} + 14B_{3g} \ . \quad (89)$$

For lithiated T-Nb2O5, one unit cell contains 64 atoms. Therefore, the degree of freedom is 192. The mechanical representation can be expressed as:

$$\Gamma = 32A_g + 16A_u + 32B_{1g} + 16B_{1u} + 16B_{2g} + 32B_{2u} + 16B_{3g} + 32B_{3u} \ . \quad (90)$$

The Raman active modes are:

$$\Gamma = 32A_g + 32B_{1g} + 16B_{2g} + 16B_{3g} \ . \tag{91}$$

On the basis of vibrational analyses mentioned above, vibrational modes and frequencies of unlithiated and lithiated T-$Nb_2O_5$ were computed by the finite displacement approach,[216,217] in which the force constant (Hessian) matrix was derived by slightly displacing each atom from its equilibrium position for the symmetry-inequivalent displacements. The frequencies as a function of normal modes were obtained via the diagonalization of Hessian matrix and computed at the Γ-point of the Brillouin zone to compare with the spectroscopic result. The vibrational density of state at the Γ-point of the Brillouin zone was analyzed by PHONONY.[218]

### 6.6.2. Vibrational calculation and Raman spectroscopic evolution

On the basis of vibrational calculations, the discrete frequency values of these Raman modes at Γ-point as well as the continuous VDOS integrated at the Γ-point are plotted for both lithiated and unlithiated model of T-$Nb_2O_5$ (Figure 6-17 Right panel). To compare with these theoretical calculations, the experimental Raman spectra acquired at the high potential state and the low potential state are highlighted (Figure 6-17 left).

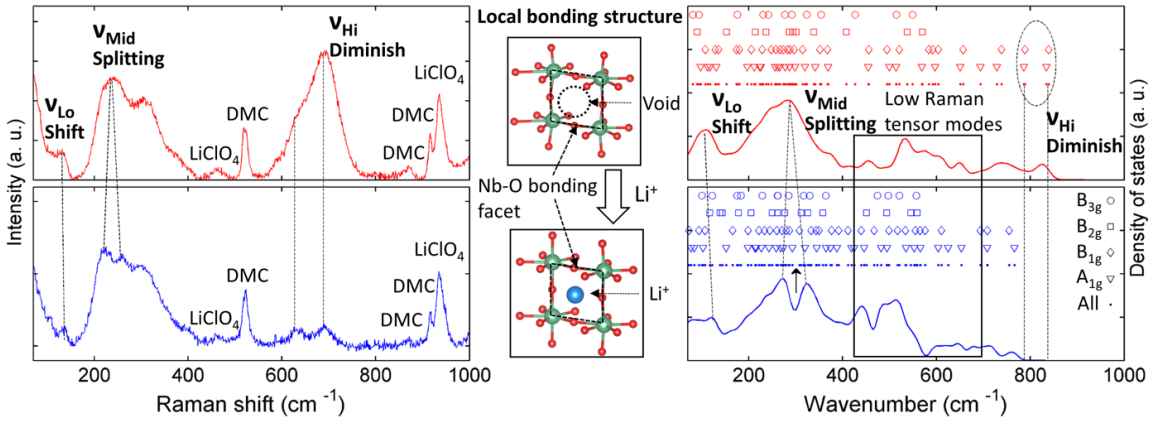

**Figure 6-17.** Correlation between experimental Raman spectroscopic evolution and theoretical calculation of vibrational structures. Left panel: Raman spectra corresponding to high (top) and low (bottom) potential states. The evolution of key band groups are labeled. Right panel: Calculated Γ-point frequencies of Raman active modes and calculated VDOS integrated at Γ-point for unlithiated (top) and lithiated (bottom) T-$Nb_2O_5$. Symbols for Raman active modes: Triangle: $A_g$, Diamond: $B_{1g}$, Square: $B_{2g}$, Circle: $B_{3g}$, sum of all Raman active modes: dot. The evolution of key part of VDOS profile and key changes on Raman modes population distributions are marked. Middle panel; the change of the local Nb-O bonding structure corresponding to lithiation process.

The comparison of experimental Raman spectroscopic evolution (Figure 6-17 left) with computed vibrational calculations (Figure 6-17 right) is performed in different ranges of vibrational frequencies. First, the intensity of $\nu_{Hi}$ band group greatly decreases and almost diminishes from high to low potential states in the experiment. For the corresponding theoretical calculations, in the high-wavenumber region, it can be found that the VDOS distribution also disappears for lithiated model. The essential reason for the loss of VDOS in high wavenumber region is because all four discrete Raman modes (two $A_g$ modes and two $B_{1g}$ modes, marked in the circle, Figure 6-17 Right) disappeared in the high-wavenumber region. Furthermore, the computation revealed that these disappeared high-wavenumber modes belong to stretching vibrations of Nb-O. The result provides a direct evidence that Li ions two-dimensionally adsorb on the Nb-O bonding facet (Figure 6-17 middle panel) and retard the stretching vibration of Nb-O bonds. Second, the Raman signal demonstrates significant band splitting in the $\nu_{Mid}$ band group when cycling from high to low potential states. Comparing this phenomenon with calculated VDOS in the mid-wavenumber range, the distribution also exhibits significant profile splitting when T-$Nb_2O_5$ is lithiated (Figure 6-17 Right). Responsible for the notch in VDOS profile is the change of distribution of discrete Raman frequencies when T-$Nb_2O_5$ model is lithiated; a narrow range of frequency where no Raman mode is populated appears (marked by an

arrow in Figure 6-17 Right panel), which strongly supports the experimental splitting of $\nu_{Mid}$ band group. Finally, a blue shift is observed in the $\nu_{Lo}$ band group. As a comparison, the VDOS profile in the low-frequency range demonstrated considerable blue shift as well. Through the comparison mentioned above, the consistency between Raman spectroscopic evolution and the calculations of discrete Raman frequencies and VDOS validates our proposed mechanism of Li-ion incorporation, which is responsible for the anomalously fast energy storage behavior.

It should be noted that the experimental Raman spectra and vibrational calculations are subjected to minor differences. The exact values of band groups are moderately different for experimental results and theoretical calculations due to the approximations have to be applied to make the theoretical calculations executable, and also because current vibrational theoretical calculation technique is not absolutely perfect. Also, the absolute intensity of experimental Raman spectra and the density or population of vibrational modes cannot match perfectly, which is most obvious for $\upsilon_{Hi}$ band group. This effect is because VDOS calculation cannot consider the Raman tensor of each mode (i.e. mode polarizability). The vibrational modes contribute to the $\nu_{Hi}$ band group may have significantly high Raman tensor values, which lead to the considerably strong intensity of $\upsilon_{Hi}$ band group even though vibrational modes are not densely populated in this frequency range. Also, similar rationale account for the phenomena that a number of vibrational modes predicted by calculation cannot be detected by Raman spectrum experimentally (marked by a rectangular in Figure 6-17 Right panel), most likely due to the low polarizability of these modes. However, despite the discrepancies regarding to the absolute values (positions and intensities) of experimental Raman spectra and vibrational

calculations, the agreement between experimental spectroscopic evolution and effect of lithiation on the vibrational properties offers solid corroboration on our proposed mechanism of Li ion incorporation for T-$Nb_2O_5$.

## 6.7. Insight from the Li ion storage mechanism of T-$Nb_2O_5$

### 6.7.1. Insight from aspects of Li ion storage behavior

It is undoubtedly that intercalation-type transition metal oxide-based Li-ion storage materials dominate the field of secondary energy storage applications. As an essential part of Li ion intercalation mechanism for transition metal oxide family, our proposed model for $Nb_2O_5$ should be compared with Li-ion intercalation mechanisms for classic Li ion storage materials, including commercialized cathode materials ($LiCoO_2$, $LiMn_2O_4$, and $LiFePO_4$) and classic fast-rate Li ion storage materials ($Li_4Ti_5O_{12}$ and $LiTiS_2$). The mechanism will be compared in terms of the type of void for Li ion accommodation, the size of the void, as well as the tunnel that connects the void for Li ion diffusion. For the type of voids, it is well-known that Li ions are generally incorporated in the three-dimensional polyhedra formed by oxygen ions (tetrahedral site for $LiMn_2O_4$, octahedral site for $LiCoO_2$, $LiFePO_4$, $Li_4Ti_5O_{12}$, and $LiTiS_2$).[15,59,219,220] As a contrast, for T-$Nb_2O_5$, Li ions are attached on two-dimensional facet formed by Nb and O. Because of the analogy of a capacitive surface adsorption behavior as mentioned in previous part, the 2D attachment/detachment should provide faster kinetics than intercalation/deintercalation into three-dimensional polyhedra, which is an important factor responsible for the exceptionally fast energy storage. Also for T-$Nb_2O_5$, the average size of the void (measured from the optimized structure shown in Figure 6-11, the void is also marked in Figure 6-11) is approximately 3 Å, which is considerably larger than the void sizes for classic cathode

materials: $LiMn_2O_4$ (1.6 Å),[221] $LiCoO_2$ (2.4 Å),[222] and $LiFePO_4$ (2.5 Å),[223] as well as classic fast-rate $Li_4Ti_5O_{12}$ (2.6 Å) and $LiTiS_2$ (2.8 Å).[219,220] The void sizes are defined by the distance between edges of tetrahedral coordination (e.g., $LiMn_2O_4$) or distance between faces of octahedral coordination (e.g., $LiCoO_2$). Judging from such rough comparison, spacious accommodation for attachment/detachment of Li ions on Nb-O bonding facet can be further more advantageous to faster Li ion transport. Finally, for the tunnel connected by the voids, $LiCoO_2$ and $LiTiS_2$ have a 2D transport pathway,[15,59] which makes $LiCoO_2$ and $LiTiS_2$ have higher Li ion conductivity and diffusivity generally.[15,44] For T-$Nb_2O_5$, the combination of tunnels for T-$Nb_2O_5$ forms a quasi 2D transport pathway as mentioned earlier, similar to the 2D tunnel for $LiCoO_2$, $LiTiS_2$ and novel MXene intercalation-type materials.[224-227] Therefore, through the comparisons mentioned above, the unique combination of facile Li ion adsorption on 2D Nb-O bonding facet, large void size, and quasi-2D diffusion pathway determines the exceptionally fast Li ion transport behavior of T-$Nb_2O_5$, and clearly defines the term "intercalation pseudocapacitance" mentioned by previous reports. [174,180]

### 6.7.2. Rational design of T-$Nb_2O_5$

Furthermore, understanding of the key attributes to fast ionic transport may provide important insight into the design and engineering novel intercalation-type energy storage materials. For T-$Nb_2O_5$-based electrodes, it is unlikely that the rate of Li ion storage may be enhanced by engineering the bulk phase to nano-size particles or to other morphologies, since the impedance of grain boundaries to ionic transport will definitely slow down Li ion transport, as proven by Griffith *et al.* very recently.[194] However, as mentioned above, since

T-$Nb_2O_5$ has a defined plane (quasi 2D) for Li ion diffusion, similar to layered materials (e.g., $LiCoO_2$), aligning the crystalline orientation may considerably enhance the kinetics.

This strategy may further enhance the rate capability and capacity utilization of T-$Nb_2O_5$, similar with the rational design strategy mentioned in chapter 4 regarding the energy storage mechanism of layer-structured $MnO_2$.[40] As shown in Figure 6-18, if the diffusion plane (quasi 2D) is perpendicular to the plane of the current collector, the exposure of diffusion plane to the electrolyte is maximized, which can fully utilize the fast kinetics of Li ion transport. On the contrary, if the diffusion plane is parallel to the surface of the current collector, the accessibility of diffusion plane is mostly blocked from the electrolyte, which may lead to sluggish kinetics as a result. In fact, engineering the crystalline direction has been successfully applied to various layer-structured materials.[137,140,228,229] It is expected that strategy is applicable to T-$Nb_2O_5$ because of the intrinsic similarity on ionic transport pathway.

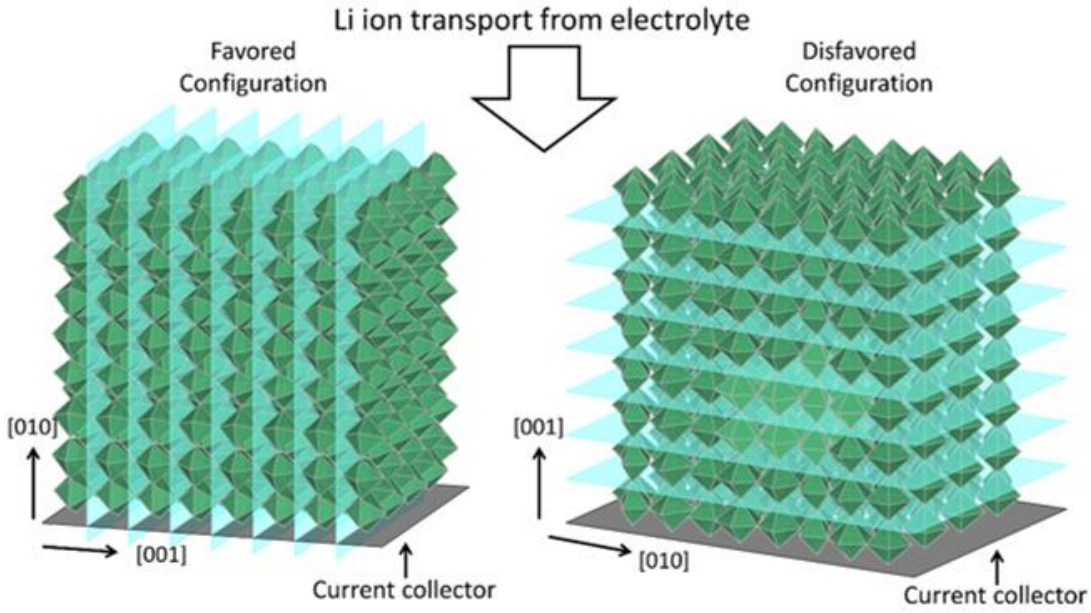

**Figure 6-18.** Schematics of effect of crystalline orientation of T-$Nb_2O_5$ on Li ion transport. The plane for quasi 2D Li ion diffusion is highlighted. Left, Plane of diffusion pathway is perpendicular to surface of the current collector. Right, Plane of diffusion pathway is parallel to surface of the current collector.

### 6.7.3. Rational design of novel Li ion storage materials

For the design and search of novel fast-rate Li ion intercalation materials, it is found that, for a considerable number of state-of-art fast-rate Li ion storage and conductors, such as T-$Nb_2O_5$, $Li_{10}GeP_2S_{10}$, and $Li_7La_3Zr_2O_{12}$, the Li ions are not accommodated at the voids with well-defined tight 3D coordination of neighboring anions (i.e., S or O). For T-$Nb_2O_5$, Li ions are stored at 2D voids similar to a capacitor; for $Li_7La_3Zr_2O_{12}$, a large portion of the Li ions are stored at the sites with the lowest symmetry (site 96h, space group *Ia-3d*), which doesn't guarantee a specified type of coordination for Li ions.[214,230] For $Li_{10}GeP_2S_{10}$, although neighboring S form a tetrahedral-like coordination of Li, the tetrahedral coordination is significantly distorted with a long Li-S bond length.[231,232] These unique types of Li accommodation mentioned above may contribute to the favorable condition for fast-rate Li ion storage and transport. Future efforts on the development of fast-rate Li ion storage materials may focus on creating similar structural motifs, such as using elements with large radius and a complicated stoichiometry to form a spacious environment for Li ion storage and transport. In addition to the factors mentioned above, extensive computational material design is vitally needed to successfully achieve rational design of a new-generation of intercalation-type Li-ion storage materials.[215,233]

## 6.8. Conclusions

In this chapter, a combination of experimental and computational investigations into the vibrational property of T-$Nb_2O_5$ upon incorporation of Li ion has offered deeper

understanding of the mechanism of anomalously fast Li ion storage in T-$Nb_2O_5$. In particular, *in operando* Raman spectroscopy performed on a well-designed platform under realistic cycling conditions is vital to probing the reversible evolution of several key Raman band groups ($\nu_{Hi}$, $\nu_{Mid}$, and $\nu_{Lo}$) of T-$Nb_2O_5$ during reversible Li ion storage. The progression of the charge storage process was further quantified through correlation between analyses of band group properties and the amount of stored charge as a function of electrochemical potentials. To correlate the structural change of T-$Nb_2O_5$ with its Raman spectroscopic evolution, a model depicting the mechanism of Li ion incorporation into T-$Nb_2O_5$ was proposed. The computational results suggest that Li ion storage is preferred at 4g Wyckoff positions of T-$Nb_2O_5$ and Li ions are preferably adsorbed on the 2D voids formed by Nb-O bonds. The transport of Li is based on a quasi-2D network with facile kinetics. Vibrational modes and VDOS calculations agree very well with experimental Raman spectroscopic evolution in different range of vibrational frequencies, confirming that the proposed model of Li-ion incorporation accounts for the charge storage mechanism of T-$Nb_2O_5$. The understanding of detailed energy storage mechanism may offer new insights into the design of novel materials with exceptional electrochemical energy storage performance.

# 7. CONCLUSIONS AND RECOMMENDATIONS

## 7.1. Conclusions

This dissertation investigated the electrochemical energy storage mechanisms of a few important electrode materials for pseudocapacitors and Li-ion batteries. Vibrational structures as a function of electrochemical operations revealed structural evolution of the electrode materials. Experimentally, *in operando* Raman spectroscopy conducted on well-designed *in operando* Raman platforms realized the investigation of mechanisms.

Chapter 4 describes the probing of the electrochemical energy storage mechanism of pseudocapacitive $MnO_2$. *In operando* analyses showed similar Raman spectroscopic evolution of $MnO_2$ when using electrolyte cations of different sizes ($Li^+$, $Na^+$, and $K^+$). The correlation between spectral features under degrees of discharge in electrolytes with different cations revealed significant cation size effects on Raman spectroscopic evolution. Further, the theoretical calculations of phonon energies for a model $MnO_2$ incorporated with various sizes of cations validated the experimental cation-size effects, further confirming the analyses of the electrochemical charge storage mechanism.

Chapter 5 describes a systematic electrochemical energy storage mechanism study of thin-film $NiO_2H_x$ model electrodes to investigate the contributions of two possible redox mechanisms of $NiO_2H_x$. Depending on the resonance enhancement effect, this study found that the phonon properties of $NiO_2H_x$ exhibited systematic evolution along with massive redox charge storage in the 2 M KOH electrolyte, whereas limited charge storage and spectroscopic evolution were observed in the 2 M $KNO_3$ electrolyte. Further Raman band analyses indicated that phonon properties show strong quantitative dependence on charge storage, which confirms that the breaking/formation of the O-H bond provides a major

contribution to charge storage while cation insertion/extraction plays a much less important role, thus offering important insights into the energy storage behavior of $NiO_2H_x$.

Chapter 6 investigates the nature of the exceptionally fast Li ion storage mechanism of T-$Nb_2O_5$. Experimentally, *in operando* Raman spectroscopy exhibited systematic band evolution, revealing the effects of Li ion storage on the vibrational structure of T-$Nb_2O_5$. Theoretically, a model T-$Nb_2O_5$ was proposed, which describes the behavior of Li ion incorporation. Through computational analyses, this study found that Li ions are preferably stored at the 2D voids on the Nb-O bonding facets, which is fundamentally analogous to capacitor behavior. The diffusion of Li is based on the quasi-2D transport path with very fast kinetics. The agreement between the experimental Raman spectroscopic evolution and the computed effects of lithiation on the vibrational structure confirmed the validity of the model of Li ion incorporation in T-$Nb_2O_5$, which revealed the nature of the exceptionally fast Li ion storage mechanism.

The unraveled mechanisms of electrochemical energy storage in this dissertation serve as significant discoveries for fundamental energy science. Also, the information of energy storage mechanisms can be applied as general guides for systematic rational designs of electrochemical energy storage materials.

## 7.2. Recommendations for future work

In this section, a few on-going directions of research and recommendations for future work are discussed in terms of more aspects of electrochemical energy storage mechanisms, applications of advanced Raman spectroscopy, and more advanced *in operando* mechanism probing.

### 7.2.1. More aspects of energy storage/conversion mechanisms

First, the methodology of *in operando* Raman spectroscopy can be incorporated with surface-enhanced techniques (Section 2.2.6. ). The surface of an electrode for electrochemical energy storage can be modified by SERS-active nanoparticles. With the SERS effect, the Raman signal from the electrode surface or the interface between an electrode and an electrolyte can be potentially enhanced. Under the *in operando* condition, more information about the dynamics of chemical reactions bound on electrode-electrolyte interfaces can be revealed via the surface enhancement technique. The crucial requirement of the application of the technique is that applied SERS-active nanoparticles must be chemically inert. SERS-active nanoparticles should not react with an electrode and an electrolyte in the applied potential window either spontaneously or electrochemically. The *in operando* observation of interfacial reactions can offer valuable information such as performance degradation, side reactions, and other processes related to the behavior of electrochemical energy storage.

Moreover, the methodology applied in this dissertation can be readily applied to other electrochemical energy storage materials as long as the probed material is sufficiently Raman-active. In recent years, a few other types of novel materials have emerged with impressive electrochemical behavior but with little information regarding their energy storage mechanisms. The application of the methodology of this dissertation can potentially unravel the energy storage mechanisms of these novel materials. The obtained information can form a categorized knowledge database for fundamental physical science in the field of energy storage.

The *in operando* Raman spectroscopic technique elaborated in this dissertation can also be utilized for the probing of catalytic reaction mechanisms. Besides electrochemical

energy storage, electrochemical catalytic energy conversion is another important topic for the modern energy industry. Similarly, the catalytic reaction mechanism is directly associated with its catalytic performance, and the evaluation of the mechanism requires systematic physical probing. *In operando* Raman spectroscopy is also suited to this area by revealing the key intermediate chemical species involved in catalytic processes at different electrochemical potentials. In recent years, various types of novel catalytic materials have been fabricated. The application of *in operando* Raman spectroscopy has a significant perspective on the study of the reaction mechanisms of these novel materials.

### 7.2.2. Advanced Raman spectroscopic technique

Besides the study of other fields of fundamental energy science, another category of future work of this dissertation is the advanced Raman spectroscopic technique.

#### *7.2.2.1. Raman mapping of the dynamics of heterostructured electrode material*

As mentioned Section 3.2.1. in this dissertation, Raman spectroscopic measurements were carried out at particular spots of electrode materials. Since the electrodes used in this dissertation are all homogeneous thin films instead of complicated structures, the dynamics of the particular spot could reflect the structural evolution of the entire electrode. In a more complicated case, complex electrode structures with a heterogeneous distribution of materials (e.g., a composite) can be probed by the *in operando* Raman technique to examine the progression of energy storage as a function of locations of an electrode. This case requires Raman mapping, which is the spatial distribution of Raman spectra. Technically, in a classic Raman microspectroscopic system, a Raman map can be generated by a spot-by-spot Raman spectroscopic measurement in the same electrochemical condition. However, this measurement is likely to be extremely time-

consuming since it is inefficient to construct an image from individual pixels. Such a slow rate generally cannot match the corresponding rate of electrochemical operations, thus making the classic point-by-point *in operando* Raman mapping not executable. Realizing Raman mapping under the *in operando* condition requires a more advanced Raman spectroscopic technique. First, a better signal detection system can be applied to shorten the time it takes for Raman spectroscopic acquisition, such as enhancing the sensitivity of a CCD camera. Second, laser illumination can be modified to a line profile instead of a spot, which can greatly improve the efficiency of *in operando* Raman mapping.

#### *7.2.2.2. Eliminating the fluorescence effect*

As mentioned in Section 2.2.5. , fluorescence commonly exists during Raman spectroscopic measurements when an electronic state transition occurs. Fluorescence typically leads to a very broad profile of light emission and often overwhelms the Raman spectroscopic signal, leading to severe difficulties for spectroscopic analyses. Technically, for an *in operando* Raman measurement, if one component (e.g., an electrode or an electrolyte) is fluorescence-active, the entire *in operando* Raman measurement will be influenced. The experiments in this dissertation were not affected by the fluorescence effect. However, future work that is likely to involve fluorescence-active electrodes or electrolytes should entail fluorescence-removing techniques. First, the simplest method of reducing the fluorescence effect is to adjust the excitation wavelength, as mentioned in Section 2.2.5. A higher-energy incident laser can separate the fluorescence profile from the frequencies of Raman scattering; a lower-energy incident laser can prevent the excitation of electronic states. Second, if adjusting the laser frequencies cannot remove fluorescence efficiently, adjusting the optical illumination and acquisition system can be applied. While, the lifetime

of emissions of a Raman scattering process falls in the range of $10^{-16}$s, the lifetime of fluorescence emissions falls in the range of $10^{-9}$s. When using a pulse-wave laser with an extremely short pulse period as excitation, the intensity of Raman scattering decays much faster than that of fluorescence. On this basis, by using the spectroscopic acquisition with a specified short delay time relative to the laser pulse (i.e., the approximate lifetime of the Raman scattering process), the majority of Raman scattering intensity can be captured while a large portion of the fluorescence signal remains uncaptured,[234-236] greatly reducing the fluorescence effect. However, this method is subject to a few drawbacks. First, because of the short period of the laser pulse, the overall intensity of Raman scattering will be lower than it is when using a continuous-wave laser. Second, if the laser pulse is too short, according to the uncertainty principle, the laser energy (e.g., frequency) is subject to considerable uncertainty. Therefore, the monochromaticity of a laser, which is vital for the accurate measurement of the Raman shift, is affected, thus leading to more errors in Raman band position measurements.

#### *7.2.2.3. Application of non-first order Raman scattering*

In this dissertation, Raman scattering processes are all first-order scattering processes. For first-order Raman scattering, in terms of classic electromagnetics, polarization is assumed to have linear relation with electric field (equation (61)); in terms of quantum theory, only one photon is involved in a Raman scattering process. In reality, higher orders of scattering processes can occur (i.e., polarization has non-linear term with respect to electric field or multiple photons can involve in scattering processes). For a two-photon scattering process, the process is named Hyper Raman scattering (Figure 7-1, left).[237-239] Theoretically, all vibration modes are Hyper-Raman active, thus potentially

offering more information of structural changes under *in operando* conditions. Of course, application of Hyper Raman scattering under *in operando* conditions strongly depends on the Hyper-Raman activities of probed materials. A careful selection of excitation laser wavelengths to utilize the resonance effect,[240] or surface enhancement technique are needed to enhance signal intensities of Hyper Raman scattering.[241,242] Besides Hyper Raman scattering, three-photon scattering processes are also possible. The most common three-photon scattering configuration is coherent anti-stokes Raman scattering (Figure 7-1 right).[243,244] By careful tuning the incident photon frequencies $\omega_1$ and $\omega_2$, to make frequency difference between $\omega_1$ and $\omega_2$ match the frequency of a particular vibrational energy level $\omega_i$. A strong anti-stokes emission will occur (with respect to $\omega_1$), thus revealing the information of energy level $\omega_i$. In recent years, applications of this technique are successful,[245-247] and have perspective in the field of *in operando* mechanism probing for electrochemical energy storage.

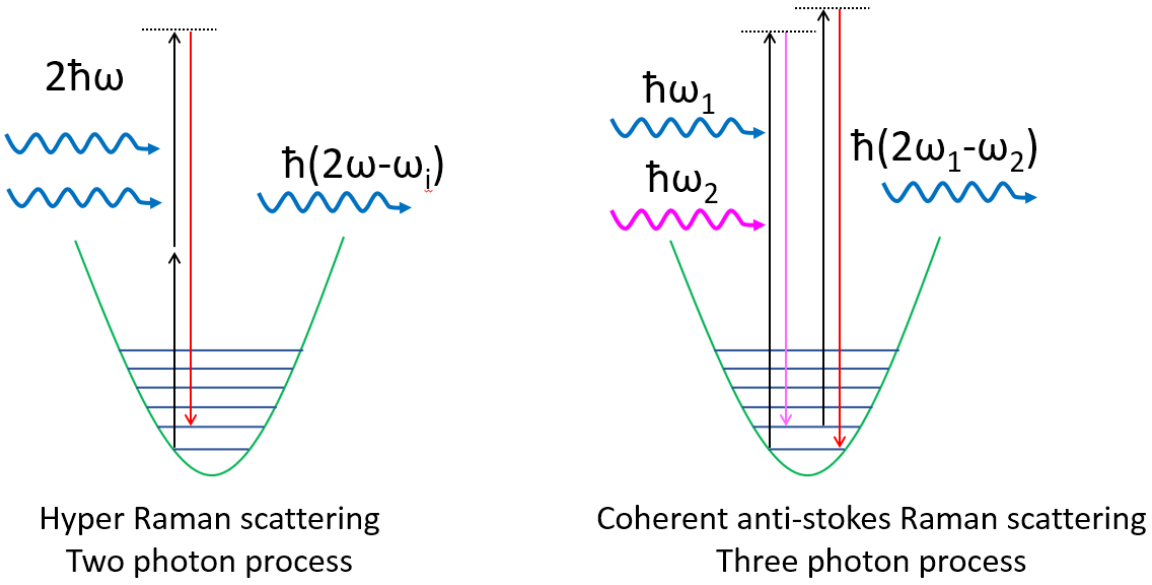


**Figure 7-1.** Schematics of two non-first-order Raman scattering processes. Left: Hyper Raman scattering (two-photon process). Right: coherent anti-stokes Raman scattering (three-photon process).

### 7.2.3. Advanced *in operando* mechanism probing

In this dissertation, Raman spectroscopy is the only physiochemical method applied to probe electrochemical energy storage mechanisms under *in operando* configurations. As mentioned in Section 2.2. , Raman spectroscopy is a very powerful technique. However, Raman spectroscopy itself has a few limitations. The major limitation is that Raman spectroscopy cannot directly provide neither information of oxidation states nor information of lattice parameters and Raman spectroscopy strongly relies on Raman activities (i.e., Raman tensor for each vibrational mode). These limitations of Raman spectroscopy can be compensated by other diffraction or absorption spectroscopic techniques. With regard to this dissertation, the mechanism probing (relying on *in operando* Raman spectroscopy) also made use of previously reported results, such as information about evolution of lattice parameters or evolution of oxidation states. Besides this dissertation, in most cases, a complete and systematic mechanism study for a specific material strongly relies on the combination of "information fragments" acquired by different groups using different samples and different experimental configurations. The information fragments from different works often have considerable inconsistencies, because of the variations on samples, facilities, *in operando* setups, or even methods of data acquisition and data interpretation.

For an ideal probing of electrochemical energy storage mechanism, the advanced *in operando* configuration should be compatible with all types of physiochemical methods. In this case, all types of *in operando* analyses could be conducted under the exactly same condition and the energy storage mechanism will be conceived as an integral rationale rather than combination of "information fragment" from different reports, which will

greatly reduce variations and thus achieve optimum consistency. Practically, this ideal *in operando* configuration needs to take all requirements of different techniques into consideration (e.g., working distance requirement for Raman measurements and transparency for absorption measurements). Experimentally, to be specific, diffraction based-techniques (X-ray and neutron) can offer direct information about long range ordering (e.g., lattice parameter). Moreover, scattering techniques (Raman scattering, X-ray scattering, and neutron scattering) can reveal properties of vibrational (phonon) modes. Furthermore, light absorption (IR, Vis, UV, and X-Ray) can provide valuable information about electronic states (e.g., oxidation states of elements). These analyses from different techniques based on the same *in operando* configuration will offer a comprehensive rationale, which can unravel electrochemical energy storage mechanisms with optimum consistency and accuracy.

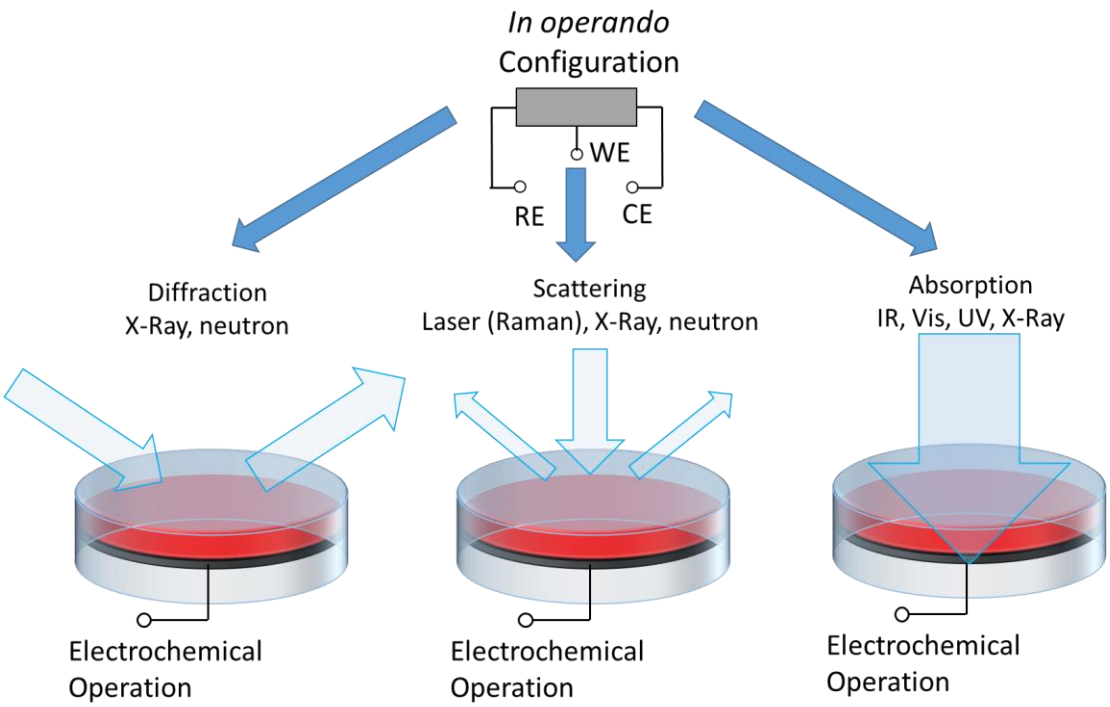


**Figure 7-2.** A schematic of an advanced *in operando* configuration compatible with all physiochemical methods: light diffraction, light scattering, and light absorption.

# REFERENCES


1. Chu, S., Majumdar, A., "Opportunities and challenges for a sustainable energy future," *Nature*, 2012, 488, 294-303.

2. Lund, J. W., "Characteristics, development and utilization of geothermal resources," *GHC Bulletin*, 2007, 28, 1-9.

3. Fridleifsson, I. B., Bertani, R., Huenges, E., Lund, J. W., Ragnarsson, A., Rybach, L. "The possible role and contribution of geothermal energy to the mitigation of climate change," IPCC scoping meeting on renewable energy sources, Luebeck, Germany, 2008; 59-80.

4. Lenzen, M., "Life cycle energy and greenhouse gas emissions of nuclear energy: A review," *Energy Conversion and Management*, 2008, 49, 2178-2199.

5. IEA, NEA, "Projected costs of generating electricity: 2015 edition — Executive summary," International Energy Agency (IEA), Nuclear Energy Agency (NEA), and Organization for Economic Co-operation and Development (OECD). Paris, France, 2015.

6. Buonocore, J. J., Luckow, P., Norris, G., Spengler, J. D., Biewald, B., Fisher, J., Levy, J. I., "Health and climate benefits of different energy-efficiency and renewable energy choices," *Nature Clim. Change*, 2016, 6, 100-105.

7. Schmidt, T. S., Born, R., Schneider, M., "Assessing the costs of photovoltaic and wind power in six developing countries," *Nature Clim. Change*, 2012, 2, 548-553.

8. Sandalow, D. B., "Plug-In Electric Vehicles, What Role for Washington?" Brookings Institution Press: 2009.

9. Wahnschafft, R., "Two Billion Cars: Driving towards Sustainability," *Natural Resources Forum*, 2009, 33, 250-251.

10. Davis, S., "The Vehicle Technologies Market Report," *Center for Transportation Analysis*, 2012, 865, 1256.

11. Crompton, T. R., 2 - Guidelines to battery selection. In *Battery Reference Book (Third Edition)*, Newnes: Oxford, 2000; pp 1-23.

12. Winter, M., Brodd, R. J., "What Are Batteries, Fuel Cells, and Supercapacitors?," *Chem. Rev. (Washington, DC, U. S.)*, 2004, 104, 4245-4270.

13. Whittingham, M. S., "Electrical Energy Storage and Intercalation Chemistry," *Science*, 1976, 192, 1126-1127.

14. Mizushima, K., Jones, P. C., Wiseman, P. J., Goodenough, J. B., "LixCoO2 (0<x<-1): A new cathode material for batteries of high energy density," *Mater. Res. Bull.*, 1980, 15, 783-789.

15. Whittingham, M. S., "Lithium Batteries and Cathode Materials," *Chem. Rev. (Washington, DC, U. S.)*, 2004, 104, 4271-4302.

16. Pistoia, G., "Lithium-ion batteries: advances and applications." Newnes: 2013.

17. Yoshio, M., Brodd, R. J., Kozawa, A., "Lithium-Ion Batteries." Springer: 2009; Vol. 1.

18. Scrosati, B., Garche, J., "Lithium batteries: Status, prospects and future," *J. Power Sources*, 2010, 195, 2419-2430.

19. Schmid, R., Pillot, C., "Introduction to energy storage with market analysis and outlook," *AIP Conf. Proc.*, 2014, 1597, 3-13.

20. Venkatarama, S., Gartner, J., "Electric vehicle batteries," *Pike Research*, 2011.

21. Gaines, L., Nelson, P. "Lithium-ion batteries: possible materials issues," 13th international battery materials recycling seminar and exhibit, Broward County Convention Center, Fort Lauderdale, Florida, 2009; 16.

22. Miller, J. R., Simon, P., "Electrochemical Capacitors for Energy Management," *Science*, 2008, 321, 651-652.

23. Miller, J. R., "Valuing Reversible Energy Storage," *Science*, 2012, 335, 1312-1313.

24. Simon, P., Gogotsi, Y., "Materials for electrochemical capacitors," *Nat. Mater.*, 2008, 7, 845-854.

25. Kötz, R., Carlen, M., "Principles and applications of electrochemical capacitors," *Electrochim. Acta*, 2000, 45, 2483-2498.

26. Burke, A., "Ultracapacitors: why, how, and where is the technology," *J. Power Sources*, 2000, 91, 37-50.

27. Conway, B. E., "Electrochemical supercapacitors: scientific fundamentals and technological applications." Springer Science & Business Media: 2013.

28. Goodenough, J. B., "Evolution of Strategies for Modern Rechargeable Batteries," *Acc. Chem. Res.*, 2013, 46, 1053-1061.

29. Chung, D., James, T., Elgqvist, E., Goodrich, A., Santhanagopalan, S., "Automotive Lithium-ion Battery (LIB) Supply Chain and US Competitiveness Considerations; Clean Energy Manufacturing Analysis Center (CMAC), NREL (National Renewable Energy Laboratory)," NREL (National Renewable Energy Laboratory (NREL), Golden, CO (United States)): 2015.

30. Chung, D., Elgqvist, E., Santhanagopalan, S., "Automotive Lithium-ion Cell Manufacturing: Regional Cost Structures and Supply Chain Considerations," *Contract*, 2016, 303, 275-3000.

31. Landsberg, G., Mandelstam, L., "Eine neue Erscheinung bei der Lichtzerstreuung in Krystallen," *Naturwissenschaften*, 1928, 16, 557-558.

32. Raman, C. V., Krishnan, K. S., "A new type of secondary radiation," *Nature*, 1928, 121, 501-502.

33. Smekal, A., "Zur Quantentheorie der Dispersion," *Naturwissenschaften*, 1923, 11, 873-875.

34. Colthup, N., "Introduction to infrared and Raman spectroscopy." Elsevier: 2012.

35. Keresztury, G., Raman Spectroscopy: Theory. In *Handbook of Vibrational Spectroscopy*, John Wiley & Sons, Ltd: 2006.

36. Ferrari, A. C., "Raman spectroscopy of graphene and graphite: Disorder, electron-phonon coupling, doping and nonadiabatic effects," *Solid State Commun.*, 2007, 143, 47-57.

37. Kneipp, K., Kneipp, H., Itzkan, I., Dasari, R. R., Feld, M. S., "Ultrasensitive chemical analysis by Raman spectroscopy," *Chem. Rev. (Washington, DC, U. S.)*, 1999, 99, 2957−2975.

38. Kneipp, K., Kneipp, H., Itzkan, I., Dasari, R. R., Feld, M. S., "Surface-enhanced Raman scattering and biophysics," *Journal of Physics-Condensed Matter*, 2002, 14, R597-R624.

39. Movasaghi, Z., Rehman, S., Rehman, I. U., "Raman spectroscopy of biological tissues," *Appl. Spectrosc. Rev.*, 2007, 42, 493-541.

40. Chen, D., Ding, D., Li, X., Waller, G. H., Xiong, X., El-Sayed, M. A., Liu, M., "Probing the charge storage mechanism of a pseudocapacitive MnO2 electrode using in operando Raman spectroscopy," *Chem. Mater.*, 2015, 27, 6608-6619.

41. Chen, D., Xiong, X., Zhao, B., Mahmoud, M. A., El-Sayed, M. A., Liu, M., "Probing Structural Evolution and Charge Storage Mechanism of NiO2HxElectrode Materials using In Operando Resonance Raman Spectroscopy," *Advanced Science*, 2016, 3, 1500433.

42. Chen, D., Wang, J.-H., Chou, T.-F., El-Sayed, M., Liu, M., "Unraveling the nature of anomalously fast energy storage in T-Nb2O5," *Submitted*, 2016.

43. Bard, A. J., Faulkner, L. R., Leddy, J., Zoski, C. G., "Electrochemical methods: fundamentals and applications." Wiley New York: 1980; Vol. 2.

44. Park, M., Zhang, X., Chung, M., Less, G. B., Sastry, A. M., "A review of conduction phenomena in Li-ion batteries," *J. Power Sources*, 2010, 195, 7904-7929.

45. Simonnet, C., Grandjean, A., "Mixed ionic and electronic conductivity of RuO2–glass composites from molten state to glassy state," *J. Non-Cryst. Solids*, 2005, 351, 1611-1618.

46. Xu, K., "Nonaqueous Liquid Electrolytes for Lithium-Based Rechargeable Batteries," *Chem. Rev. (Washington, DC, U. S.)*, 2004, 104, 4303-4418.

47. Bisquert, J., Garcia-Belmonte, G., Fabregat-Santiago, F., Bueno, P. R., "Theoretical models for ac impedance of finite diffusion layers exhibiting low frequency dispersion," *J. Electroanal. Chem.*, 1999, 475, 152-163.

48. Lai, W., Ciucci, F., "Small-Signal Apparent Diffusion Impedance of Intercalation Battery Electrodes," *J. Electrochem. Soc.*, 2011, 158, A115-A121.

49. Song, J., Bazant, M. Z., "Effects of Nanoparticle Geometry and Size Distribution on Diffusion Impedance of Battery Electrodes," *J. Electrochem. Soc.*, 2013, 160, A15-A24.

50. Frackowiak, E., Béguin, F., "Carbon materials for the electrochemical storage of energy in capacitors," *Carbon*, 2001, 39, 937-950.

51. Aoki, K., Tokuda, K., Matsuda, H., "Theory of linear sweep voltammetry with finite diffusion space," *Journal of Electroanalytical Chemistry and Interfacial Electrochemistry*, 1983, 146, 417-424.

52. Aoki, K., Tokuda, K., Matsuda, H., "Theory of linear sweep voltammetry with finite diffusion space," *Journal of Electroanalytical Chemistry and Interfacial Electrochemistry*, 1984, 160, 33-45.

53. Orazem, M. E., Tribollet, B., "Electrochemical impedance spectroscopy." John Wiley & Sons: 2011; Vol. 48.

54. Jossen, A., "Fundamentals of battery dynamics," *J. Power Sources*, 2006, 154, 530-538.

55. Goodenough, J. B., Kim, Y., "Challenges for Rechargeable Li Batteries," *Chem. Mater.*, 2010, 22, 587-603.

56. Maier, J., "Thermodynamics of Electrochemical Lithium Storage," *Angew. Chem., Int. Ed.*, 2013, 52, 4998-5026.

57. Crompton, T. R., 1 - Introduction to battery technology. In *Battery Reference Book (Third Edition)*, Newnes: Oxford, 2000; pp 1-64.

58. Huggins, R., "Advanced batteries: materials science aspects." Springer Science & Business Media: 2008.

59. Ellis, B. L., Lee, K. T., Nazar, L. F., "Positive Electrode Materials for Li-Ion and Li-Batteries†," *Chem. Mater.*, 2010, 22, 691-714.

60. Manthiram, A., Fu, Y., Chung, S.-H., Zu, C., Su, Y.-S., "Rechargeable Lithium–Sulfur Batteries," *Chem. Rev. (Washington, DC, U. S.)*, 2014, 114, 11751-11787.

61. Xu, K., "Electrolytes and Interphases in Li-Ion Batteries and Beyond," *Chem. Rev. (Washington, DC, U. S.)*, 2014, 114, 11503-11618.

62. Randles, J. E. B., "Kinetics of rapid electrode reactions," *Discussions of the faraday society*, 1947, 1, 11-19.

63. Zhang, S., Pan, N., "Supercapacitors Performance Evaluation," *Adv. Energy Mater.*, 2015, 5, n/a-n/a.

64. Lota, G., Fic, K., Frackowiak, E., "Carbon nanotubes and their composites in electrochemical applications," *Energy Environ. Sci.*, 2011, 4, 1592-1605.

65. Wang, G., Zhang, L., Zhang, J., "A review of electrode materials for electrochemical supercapacitors," *Chem. Soc. Rev.*, 2012, 41, 797-828.

66. Chmiola, J., Yushin, G., Gogotsi, Y., Portet, C., Simon, P., Taberna, P. L., "Anomalous Increase in Carbon Capacitance at Pore Sizes Less Than 1 Nanometer," *Science*, 2006, 313, 1760-1763.

67. Zhu, Y., Murali, S., Stoller, M. D., Ganesh, K. J., Cai, W., Ferreira, P. J., Pirkle, A., Wallace, R. M., Cychosz, K. A., Thommes, M., Su, D., Stach, E. A., Ruoff, R. S., "Carbon-Based Supercapacitors Produced by Activation of Graphene," *Science*, 2011, 332, 1537-1541.

68. El-Kady, M. F., Strong, V., Dubin, S., Kaner, R. B., "Laser Scribing of High-Performance and Flexible Graphene-Based Electrochemical Capacitors," *Science*, 2012, 335, 1326-1330.

69. Conway, B. E., "Transition from “Supercapacitor” to “Battery” Behavior in Electrochemical Energy Storage," *J. Electrochem. Soc.*, 1991, 138, 1539-1548.

70. Conway, B. E., Birss, V., Wojtowicz, J., "The role and utilization of pseudocapacitance for energy storage by supercapacitors," *J. Power Sources*, 1997, 66, 1-14.

71. Ho, C., Raistrick, I. D., Huggins, R. A., "Application of A‐C Techniques to the Study of Lithium Diffusion in Tungsten Trioxide Thin Films," *J. Electrochem. Soc.*, 1980, 127, 343-350.

72. Chun, S. E., Pyun, S. I., Lee, G. J., "A study on mechanism of charging/discharging at amorphous manganese oxide electrode in 0.1 M Na2SO4 solution," *Electrochim. Acta*, 2006, 51, 6479-6486.

73. Levine, I. N., "Quantum chemistry (7th Edition)." Boston : Pearson: 2013.

74. Ashcroft, N. W., Mermin, N. D., "Solid state physics." Saunders College, Philadelphia: 1976; p 120.

75. Halford, R. S., "Motions of Molecules in Condensed Systems: I. Selection Rules, Relative Intensities, and Orientation Effects for Raman and Infra - Red Spectra," *The Journal of Chemical Physics*, 1946, 14, 8-15.

76. Hornig, D. F., "The Vibrational Spectra of Molecules and Complex Ions in Crystals. I. General Theory," *The Journal of Chemical Physics*, 1948, 16, 1063-1076.

77. Rousseau, D. L., Bauman, R. P., Porto, S. P. S., "Normal mode determination in crystals," *J. Raman Spectrosc.*, 1981, 10, 253-290.

78. Mulliken, R., "Report on notation for the spectra of polyatomic molecules," *J. chem. Phys*, 1955, 23, 1997.

79. Kroumova, E., Aroyo, M. I., Perez-Mato, J. M., Kirov, A., Capillas, C., Ivantchev, S., Wondratschek, H., "Bilbao Crystallographic Server : Useful Databases and Tools for Phase-Transition Studies," *Phase Transitions*, 2003, 76, 155-170.

80. Long, D. A., "Intensities in Raman Spectra. I. A Bond Polarizability Theory," *Proceedings of the Royal Society of London. Series A. Mathematical and Physical Sciences*, 1953, 217, 203-221.

81. Allemand, C. D., "Depolarization ratio measurements in Raman spectrometry," *Appl. Spectrosc.*, 1970, 24, 348-353.

82. Hollas, J. M., "Modern spectroscopy." John Wiley & Sons: 2004.

83. Smith, E., Dent, G., "Modern Raman spectroscopy: a practical approach." John Wiley & Sons: 2013.

84. Jabłoński, A., "Efficiency of anti-Stokes fluorescence in dye s," *Nature*, 1933, 131, 21.

85. Fleischmann, M., Hendra, P. J., McQuillan, A. J., "Raman spectra of pyridine adsorbed at a silver electrode," *Chem. Phys. Lett.*, 1974, 26, 163-166.

86. Jeanmaire, D. L., Van Duyne, R. P., "Surface raman spectroelectrochemistry," *Journal of Electroanalytical Chemistry and Interfacial Electrochemistry*, 1977, 84, 1-20.

87. Airy, G. B., "On the diffraction of an object-glass with circular aperture," *Transactions of the Cambridge Philosophical Society*, 1835, 5, 283.

88. Wei, W., Cui, X., Chen, W., Ivey, D. G., "Manganese oxide-based materials as electrochemical supercapacitor electrodes," *Chem. Soc. Rev.*, 2011, 40, 1697-1721.

89. Sassin, M. B., Chervin, C. N., Rolison, D. R., Long, J. W., "Redox Deposition of Nanoscale Metal Oxides on Carbon for Next-Generation Electrochemical Capacitors," *Acc. Chem. Res.*, 2012, 46, 1062-1074.

90. Brousse, T., Toupin, M., Dugas, R., Athouël, L., Crosnier, O., Bélanger, D., "Crystalline MnO2 as Possible Alternatives to Amorphous Compounds in Electrochemical Supercapacitors," *J. Electrochem. Soc.*, 2006, 153, A2171-A2180.

91. El-Kady, M. F., Ihns, M., Li, M., Hwang, J. Y., Mousavi, M. F., Chaney, L., Lech, A. T., Kaner, R. B., "Engineering three-dimensional hybrid supercapacitors and microsupercapacitors for high-performance integrated energy storage," *Proc. Natl. Acad. Sci. U. S. A.*, 2015, 112, 4233-4238.

92. Bach, S., Henry, M., Baffier, N., Livage, J., "Sol-gel synthesis of manganese oxides," *J. Solid State Chem.*, 1990, 88, 325-333.

93. Goff, P. L., Baffier, N., Bach, S., Pereira-Ramos, J.-P., "Structural and electrochemical properties of layered manganese dioxides in relation to their synthesis: classical and sol-gel routes," *J. Mater. Chem.*, 1994, 4, 875-881.

94. Nakayama, M., Konishi, S., Tagashira, H., Ogura, K., "Electrochemical Synthesis of Layered Manganese Oxides Intercalated with Tetraalkylammonium Ions," *Langmuir*, 2005, 21, 354-359.

95. Nakayama, M., Tagashira, H., "Electrodeposition of layered manganese oxide nanocomposites intercalated with strong and weak polyelectrolytes," *Langmuir*, 2006, 22, 3864-3869.

96. Yu, G., Xie, X., Pan, L., Bao, Z., Cui, Y., "Hybrid nanostructured materials for high-performance electrochemical capacitors," *Nano Energy*, 2013, 2, 213-234.

97. Song, M.-K., Cheng, S., Chen, H., Qin, W., Nam, K.-W., Xu, S., Yang, X.-Q., Bongiorno, A., Lee, J., Bai, J., Tyson, T. A., Cho, J., Liu, M., "Anomalous Pseudocapacitive Behavior of a Nanostructured, Mixed-Valent Manganese Oxide Film for Electrical Energy Storage (vol 12, pg 3483, 2012)," *Nano Lett.*, 2012, 12, 4416-4416.

98. Peng, L., Peng, X., Liu, B., Wu, C., Xie, Y., Yu, G., "Ultrathin Two-Dimensional MnO2/Graphene Hybrid Nanostructures for High-Performance, Flexible Planar Supercapacitors," *Nano Lett.*, 2013, 13, 2151-2157.

99. Long, J. W., Young, A. L., Rolison , D. R., "Spectroelectrochemical Characterization of Nanostructured, Mesoporous Manganese Oxide in Aqueous Electrolytes," *J. Electrochem. Soc.*, 2003, 150, A1161-A1165.

100. Julien, C., Massot, M., Baddour-Hadjean, R., Franger, S., Bach, S., Pereira-Ramos, J. P., "Raman spectra of birnessite manganese dioxides," *Solid State Ionics*, 2003, 159, 345-356.

101. Ghodbane, O., Pascal, J.-L., Fraisse, B. I. M., Favier, F. d. r., "Structural in Situ Study of the Thermal Behavior of Manganese Dioxide Materials: Toward Selected Electrode Materials for Supercapacitors," *ACS Appl. Mater. Interfaces*, 2010, 2, 3493-3505.

102. Ghodbane, O., Ataherian, F., Wu, N.-L., Favier, F., "In situ crystallographic investigations of charge storage mechanisms in MnO2-based electrochemical capacitors," *J. Power Sources*, 2012, 206, 454-462.

103. Athouël, L., Moser, F., Dugas, R., Crosnier, O., Bélanger, D., Brousse, T., "Variation of the MnO2 Birnessite Structure upon Charge/Discharge in an Electrochemical Supercapacitor Electrode in Aqueous Na2SO4 Electrolyte," *J. Phys. Chem. C*, 2008, 112, 7270-7277.

104. Luo, J., L. Suib, S., "Formation and transformation of mesoporous and layered manganese oxides in the presence of long-chain ammonium hydroxides," *Chem. Commun. (Cambridge, U. K.)*, 1997, 1031-1032.

105. Julien, C. M., Massot, M., "Lattice vibrations of materials for lithium rechargeable batteries III. Lithium manganese oxides," *Mater. Sci. Eng., B*, 2003, 100, 69-78.

106. Julien, C. M., Massot, M., Poinsignon, C., "Lattice vibrations of manganese oxides: Part I. Periodic structures," *Spectrochim. Acta, Part A*, 2004, 60, 689-700.

107. Nam, K.-W., Kim, M. G., Kim, K.-B., "In Situ Mn K-edge X-ray Absorption Spectroscopy Studies of Electrodeposited Manganese Oxide Films for Electrochemical Capacitors," *J. Phys. Chem. C*, 2006, 111, 749-758.

108. Hu, C.-C., Tsou, T.-W., "Ideal capacitive behavior of hydrous manganese oxide prepared by anodic deposition," *Electrochem. Commun.*, 2002, 4, 105-109.

109. Hu, C.-C., Tsou, T.-W., "Capacitive and textural characteristics of hydrous manganese oxide prepared by anodic deposition," *Electrochim. Acta*, 2002, 47, 3523-3532.

110. Young, M. J., Holder, A. M., George, S. M., Musgrave, C. B., "Charge Storage in Cation Incorporated alpha-MnO2," *Chem. Mater.*, 2015, 27, 1172-1180.

111. Yeager, M., Du, W., Si, R., Su, D., Marinković, N., Teng, X., "Highly Efficient K0.15MnO2 Birnessite Nanosheets for Stable Pseudocapacitive Cathodes," *J. Phys. Chem. C*, 2012, 116, 20173-20181.

112. Hsu, Y.-K., Chen, Y.-C., Lin, Y.-G., Chen, L.-C., Chen, K.-H., "Reversible phase transformation of MnO2 nanosheets in an electrochemical capacitor investigated by in situ Raman spectroscopy," *Chem. Commun. (Cambridge, U. K.)*, 2011, 47, 1252-1254.

113. Ruther, R. E., Callender, A. F., Zhou, H., Martha, S. K., Nanda, J., "Raman Microscopy of Lithium-Manganese-Rich Transition Metal Oxide Cathodes," *J. Electrochem. Soc.*, 2015, 162, A98-A102.

114. Julien, C., Massot, M., "Spectroscopic studies of the local structure in positive electrodes for lithium batteries," *Phys. Chem. Chem. Phys.*, 2002, 4, 4226-4235.

115. Inaba, M., Iriyama, Y., Ogumi, Z., Todzuka, Y., Tasaka, A., "Raman study of layered rock-salt LiCoO2 and its electrochemical lithium deintercalation," *J. Raman Spectrosc.*, 1997, 28, 613-617.

116. Shao, J., Li, X., Qu, Q., Wu, Y., "Study on different power and cycling performance of crystalline KxMnO2·nH2O as cathode material for supercapacitors in Li2SO4, Na2SO4, and K2SO4 aqueous electrolytes," *J. Power Sources*, 2013, 223, 56-61.

117. Baddour-Hadjean, R., Pereira-Ramos, J.-P., "Raman Microspectrometry Applied to the Study of Electrode Materials for Lithium Batteries," *Chem. Rev. (Washington, DC, U. S.)*, 2010, 110, 1278-1319.

118. Doeff, M. M., Anapolsky, A., Edman, L., Richardson, T. J., De Jonghe, L. C., "A High-Rate Manganese Oxide for Rechargeable Lithium Battery Applications," *J. Electrochem. Soc.*, 2001, 148, A230-A236.

119. Armstrong, A. R., Bruce, P. G., "Synthesis of layered LiMnO2 as an electrode for rechargeable lithium batteries," *Nature*, 1996, 381, 499-500.

120. Hwang, S.-J., Park, H.-S., Choy, J.-H., Campet, G., Portier, J., Kwon, C.-W., Etourneau, J., "Micro-Raman Spectroscopic Study on Layered Lithium Manganese Oxide and Its Delithiated/Relithiated Derivatives," *Electrochem. Solid-State Lett.*, 2001, 4, A213-A216.

121. Park, H.-S., Hwang, S.-J., Choy, J.-H., "Relationship between Chemical Bonding Character and Electrochemical Performance in Nickel-Substituted Lithium Manganese Oxides," *J. Phys. Chem. B*, 2001, 105, 4860-4866.

122. Tompsett, D. A., Islam, M. S., "Electrochemistry of Hollandite α-MnO2: Li-Ion and Na-Ion Insertion and Li2O Incorporation," *Chem. Mater.*, 2013, 25, 2515-2526.

123. Baddour-Hadjean, R., Pereira-Ramos, J. P., "Raman Microspectrometry Applied to the Study of Electrode Materials for Lithium Batteries," *Chem. Rev. (Washington, DC, U. S.)*, 2010, 110, 1278-1319.

124. Ammundsen, B., Paulsen, J., "Novel Lithium-Ion Cathode Materials Based on Layered Manganese Oxides," *Adv. Mater. (Weinheim, Ger.)*, 2001, 13, 943-956.

125. Post, J. E., Veblen, D. R., "Crystal structure determinations of synthetic sodium, magnesium, and potassium birnessite using TEM and the Rietveld method," *Am. Mineral.*, 1990, 75, 477-489.

126. Clark, S. J., Segall, M. D., Pickard, C. J., Hasnip, P. J., Probert, M. I., Refson, K., Payne, M. C., "First principles methods using CASTEP," *Z. Kristallogr.*, 2005, 220, 567-570.

127. Lee, C., Yang, W., Parr, R. G., "Development of the Colle-Salvetti correlation-energy formula into a functional of the electron density," *Phys. Rev. B: Condens. Matter Mater. Phys.*, 1988, 37, 785-789.

128. Perdew, J. P., Burke, K., Ernzerhof, M., "Generalized Gradient Approximation Made Simple," *Phys. Rev. Lett.*, 1996, 77, 3865-3868.

129. Refson, K., Tulip, P. R., Clark, S. J., "Variational density-functional perturbation theory for dielectrics and lattice dynamics," *Phys. Rev. B: Condens. Matter Mater. Phys.*, 2006, 73, 155114.

130. Aroyo, M., Perez-Mato, J., Orobengoa, D., Tasci, E., De La Flor, G., Kirov, A., "Crystallography online: Bilbao crystallographic server," *Bulg. Chem. Commun*, 2011, 43, 183-197.

131. Aroyo, M. I., Perez-Mato, J. M., Capillas, C., Kroumova, E., Ivantchev, S., Madariaga, G., Kirov, A., Wondratschek, H., "Bilbao crystallographic server: I. Databases and crystallographic computing programs," *Z. Kristallogr.*, 2006, 221, 15-27.

132. Aroyo, M. I., Kirov, A., Capillas, C., Perez-Mato, J. M., Wondratschek, H., "Bilbao Crystallographic Server. II. Representations of crystallographic point groups and space groups," *Acta Crystallographica Section A*, 2006, 62, 115-128.

133. Wen, S., Lee, J.-W., Yeo, I.-H., Park, J., Mho, S.-i., "The role of cations of the electrolyte for the pseudocapacitive behavior of metal oxide electrodes, MnO2 and RuO2," *Electrochim. Acta*, 2004, 50, 849-855.

134. Qu, Q., Zhang, P., Wang, B., Chen, Y., Tian, S., Wu, Y., Holze, R., "Electrochemical Performance of MnO2 Nanorods in Neutral Aqueous Electrolytes as a Cathode for Asymmetric Supercapacitors," *J. Phys. Chem. C*, 2009, 113, 14020-14027.

135. Ji, C.-C., Xu, M.-W., Bao, S.-J., Cai, C.-J., Wang, R.-Y., Jia, D.-Z., "Effect of alkaline and alkaline–earth cations on the supercapacitor performance of MnO2 with various crystallographic structures," *J. Solid State Electrochem.*, 2013, 17, 1357-1368.

136. Misnon, I. I., Aziz, R. A., Zain, N. K. M., Vidhyadharan, B., Krishnan, S. G., Jose, R., "High performance MnO2 nanoflower electrode and the relationship between solvated ion size and specific capacitance in highly conductive electrolytes," *Mater. Res. Bull.*, 2014, 57, 221-230.

137. Wei, G.-Z., Lu, X., Ke, F.-S., Huang, L., Li, J.-T., Wang, Z.-X., Zhou, Z.-Y., Sun, S.-G., "Crystal Habit-Tuned Nanoplate Material of Li[Li1/3–2x/3NixMn2/3–x/3]O2 for High-Rate Performance Lithium-Ion Batteries," *Adv. Mater. (Weinheim, Ger.)*, 2010, 22, 4364-4367.

138. Chen, H., Grey, C. P., "Molten Salt Synthesis and High Rate Performance of the "Desert-Rose" form of LiCoO2," *Adv. Mater. (Weinheim, Ger.)*, 2008, 20, 2206-2210.

139. Bouwman, P. J., Boukamp, B. A., Bouwmeester, H. J. M., Notten, P. H. L., "Structure-related intercalation behaviour of LiCoO2 films," *Solid State Ionics*, 2002, 152–153, 181-188.

140. Mukhopadhyay, A., Guo, F., Tokranov, A., Xiao, X., Hurt, R. H., Sheldon, B. W., "Engineering of Graphene Layer Orientation to Attain High Rate Capability and Anisotropic Properties in Li-Ion Battery Electrodes," *Adv. Funct. Mater.*, 2013, 23, 2397-2404.

141. Kurra, N., Alhebshi, N. A., Alshareef, H. N., "Microfabricated Pseudocapacitors Using $Ni(OH)_2$ Electrodes Exhibit Remarkable Volumetric Capacitance and Energy Density," *Adv. Energy Mater.*, 2015, 5, 1401303.

142. Wang, H., Casalongue, H. S., Liang, Y., Dai, H., "Ni(OH)2 Nanoplates Grown on Graphene as Advanced Electrochemical Pseudocapacitor Materials," *J. Am. Chem. Soc.*, 2010, 132, 7472-7477.

143. Zhang, H., Yu, X., Braun, P. V., "Three-dimensional bicontinuous ultrafast-charge and -discharge bulk battery electrodes," *Nat Nano*, 2011, 6, 277-281.

144. Corrigan, D. A., Knight, S. L., "Electrochemical and Spectroscopic Evidence on the Participation of Quadrivalent Nickel in the Nickel Hydroxide Redox Reaction," *J. Electrochem. Soc.*, 1989, 136, 613-619.

145. Brousse, T., Bélanger, D., Long, J. W., "To Be or Not To Be Pseudocapacitive?," *J. Electrochem. Soc.*, 2015, 162, A5185-A5189.

146. Qu, L., Zhao, Y., Khan, A. M., Han, C., Hercule, K. M., Yan, M., Liu, X., Chen, W., Wang, D., Cai, Z., Xu, W., Zhao, K., Zheng, X., Mai, L., "Interwoven Three-Dimensional Architecture of Cobalt Oxide Nanobrush-Graphene@NixCo2x(OH)6x for High-Performance Supercapacitors," *Nano Lett.*, 2015, 15, 2037-2044.

147. Mai, L., Dong, Y., Xu, L., Han, C., "Single Nanowire Electrochemical Devices," *Nano Lett.*, 2010, 10, 4273-4278.

148. Hercule, K. M., Wei, Q., Khan, A. M., Zhao, Y., Tian, X., Mai, L., "Synergistic Effect of Hierarchical Nanostructured MoO2/Co(OH)2 with Largely Enhanced Pseudocapacitor Cyclability," *Nano Lett.*, 2013, 13, 5685-5691.

149. Cheng, S., Yang, L., Chen, D., Ji, X., Jiang, Z.-j., Ding, D., Liu, M., "Phase evolution of an alpha $MnO_2$-based electrode for pseudo-capacitors probed by in operando Raman spectroscopy," *Nano Energy*, 2014, 9, 161-167.

150. Li, H. B., Yu, M. H., Wang, F. X., Liu, P., Liang, Y., Xiao, J., Wang, C. X., Tong, Y. X., Yang, G. W., "Amorphous nickel hydroxide nanospheres with ultrahigh capacitance and energy density as electrochemical pseudocapacitor materials," *Nat. Commun.*, 2013, 4, 1894.

151. Huang, L., Chen, D., Ding, Y., Feng, S., Wang, Z. L., Liu, M., "Nickel–Cobalt Hydroxide Nanosheets Coated on NiCo2O4 Nanowires Grown on Carbon Fiber Paper for High-Performance Pseudocapacitors," *Nano Lett.*, 2013, 13, 3135-3139.

152. Xiong, X., Ding, D., Chen, D., Waller, G., Bu, Y., Wang, Z., Liu, M., "Three-dimensional ultrathin Ni(OH)2 nanosheets grown on nickel foam for high-performance supercapacitors," *Nano Energy*, 2015, 11, 154-161.

153. Salunkhe, R. R., Lin, J., Malgras, V., Dou, S. X., Kim, J. H., Yamauchi, Y., "Large-scale synthesis of coaxial carbon nanotube/Ni(OH)2 composites for asymmetric supercapacitor application," *Nano Energy*, 2015, 11, 211-218.

154. Oliva, P., Leonardi, J., Laurent, J. F., Delmas, C., Braconnier, J. J., Figlarz, M., Fievet, F., Guibert, A. d., "Review of the structure and the electrochemistry of nickel hydroxides and oxy-hydroxides," *J. Power Sources*, 1982, 8, 229-255.

155. Portemer, F., Delahaye‐Vidal, A., Figlarz, M., "Characterization of Active Material Deposited at the Nickel Hydroxide Electrode by Electrochemical Impregnation," *J. Electrochem. Soc.*, 1992, 139, 671-678.

156. Hall, D. S., Lockwood, D. J., Poirier, S., Bock, C., MacDougall, B. R., "Applications of in Situ Raman Spectroscopy for Identifying Nickel Hydroxide Materials and Surface Layers during Chemical Aging," *ACS Appl. Mater. Interfaces*, 2014, 6, 3141-3149.

157. Singh, D., "Characteristics and Effects of γ‐NiOOH on Cell Performance and a Method to Quantify It in Nickel Electrodes," *J. Electrochem. Soc.*, 1998, 145, 116-120.

158. Bode, H., Dehmelt, K., Witte, J., "Zur kenntnis der nickelhydroxidelektrode—I.Über das nickel (II)-hydroxidhydrat," *Electrochim. Acta*, 1966, 11, 1079-IN1.

159. Glemser, O., Einerhand, J., "Die Struktur höherer Nickelhydroxyde," *Zeitschrift für anorganische Chemie*, 1950, 261, 43-51.

160. Ohzuku, T., Ueda, A., Nagayama, M., "Electrochemistry and Structural Chemistry of LiNiO2 ($R\bar{3}m$) for 4 Volt Secondary Lithium Cells," *J. Electrochem. Soc.*, 1993, 140, 1862-1870.

161. Yang, S. B., Wu, X. L., Chen, C. L., Dong, H. L., Hu, W. P., Wang, X. K., "Spherical alpha-Ni(OH)(2) nanoarchitecture grown on graphene as advanced electrochemical pseudocapacitor materials," *Chem. Commun. (Cambridge, U. K.)*, 2012, 48, 2773-2775.

162. Kim, M. S., Hwang, T. S., Kim, K. B., "A Study of the Electrochemical Redox Behavior of Electrochemically Precipitated Nickel Hydroxides Using Electrochemical Quartz Crystal Microbalance," *J. Electrochem. Soc.*, 1997, 144, 1537-1543.

163. Lee, J.-W., Han, J.-N., Seo, M., Pyun, S.-I., "Transport of alkaline cation and neutral species through the α-Ni(OH)2/γ-NiOOH film electrode," *J. Solid State Electrochem.*, 2001, 5, 459-465.

164. Cordoba - Torresi, S. I., Gabrielli, C., Hugot - Le Goff, A., Torresi, R., "Electrochromic Behavior of Nickel Oxide Electrodes: I . Identification of the Colored State Using Quartz Crystal Microbalance," *J. Electrochem. Soc.*, 1991, 138, 1548-1553.

165. Bode, H., Dehmelt, K., Witte, J., "Zur Kenntnis der Nickelhydroxidelektrode. II. Über die Oxydationsprodukte von Nickel(II)-hydroxiden," *Z. Anorg. Allg. Chem.*, 1969, 366, 1-21.

166. Bartl, H., Bode, H., Sterr, G., Witte, J., "Zur kenntnis der nickelhydroxidelektrode—IV. Kristallstrukturuntersuchung des hochoxidierten γ1-Nickelhydroxids," *Electrochim. Acta*, 1971, 16, 615-621.

167. Beverskog, B., Puigdomenech, I., "Revised Pourbaix diagrams for nickel at 25–300 °C," *Corros. Sci.*, 1997, 39, 969-980.

168. Melendres, C. A., Xu, S., "In Situ Laser Raman Spectroscopic Study of Anodic Corrosion Films on Nickel and Cobalt," *J. Electrochem. Soc.*, 1984, 131, 2239-2243.

169. Jeong, D. J., Kim, W.-S., Choi, Y.-K., Sung, Y.-E., "Intercalation/deintercalation characteristics of electrodeposited and anodized nickel thin film on ITO electrode in aqueous and nonaqueous electrolytes," *J. Electroanal. Chem.*, 2001, 511, 79-87.

170. Cornilsen, B. C., Karjala, P. J., Loyselle, P. L., "Structural models for nickel electrode active mass," *J. Power Sources*, 1988, 22, 351-357.

171. Merrill, M., Worsley, M., Wittstock, A., Biener, J., Stadermann, M., "Determination of the "NiOOH" charge and discharge mechanisms at ideal activity," *J. Electroanal. Chem.*, 2014, 717–718, 177-188.

172. Yang, G.-W., Xu, C.-L., Li, H.-L., "Electrodeposited nickel hydroxide on nickel foam with ultrahigh capacitance," *Chem. Commun. (Cambridge, U. K.)*, 2008, 6537-6539.

173. Dokko, K., Shi, Q., Stefan, I. C., Scherson, D. A., "In Situ Raman Spectroscopy of Single Microparticle Li+−Intercalation Electrodes," *J. Phys. Chem. B*, 2003, 107, 12549-12554.

174. Augustyn, V., Come, J., Lowe, M. A., Kim, J. W., Taberna, P.-L., Tolbert, S. H., Abruña, H. D., Simon, P., Dunn, B., "High-rate electrochemical energy storage through Li+ intercalation pseudocapacitance," *Nat. Mater.*, 2013, 12, 518-522.

175. Kang, B., Ceder, G., "Battery materials for ultrafast charging and discharging," *Nature*, 2009, 458, 190-193.

176. Ghidiu, M., Lukatskaya, M. R., Zhao, M.-Q., Gogotsi, Y., Barsoum, M. W., "Conductive two-dimensional titanium carbide 'clay' with high volumetric capacitance," *Nature*, 2014, 516, 78-U171.

177. Augustyn, V., Simon, P., Dunn, B., "Pseudocapacitive oxide materials for high-rate electrochemical energy storage," *Energy Environ. Sci.*, 2014, 7, 1597-1614.

178. Brezesinski, K., Wang, J., Haetge, J., Reitz, C., Steinmueller, S. O., Tolbert, S. H., Smarsly, B. M., Dunn, B., Brezesinski, T., "Pseudocapacitive Contributions to Charge Storage in Highly Ordered Mesoporous Group V Transition Metal Oxides with Iso-Oriented Layered Nanocrystalline Domains," *J. Am. Chem. Soc.*, 2010, 132, 6982-6990.

179. Kim, J. W., Augustyn, V., Dunn, B., "The Effect of Crystallinity on the Rapid Pseudocapacitive Response of Nb2O5," *Adv. Energy Mater.*, 2012, 2, 141-148.

180. Simon, P., Gogotsi, Y., Dunn, B., "Where Do Batteries End and Supercapacitors Begin?," *Science*, 2014, 343, 1210-1211.

181. Come, J., Augustyn, V., Kim, J. W., Rozier, P., Taberna, P. L., Gogotsi, P., Long, J. W., Dunn, B., Simon, P., "Electrochemical Kinetics of Nanostructured Nb2O5 Electrodes," *J. Electrochem. Soc.*, 2014, 161, A718-A725.

182. Girard, H.-L., Dunn, B., Pilon, L., "Simulations and Interpretation of Three-Electrode Cyclic Voltammograms of Pseudocapacitive Electrodes," *Electrochim. Acta*, 2016, 211, 420-429.

183. Lim, E., Kim, H., Jo, C., Chun, J., Ku, K., Kim, S., Lee, H. I., Nam, I.-S., Yoon, S., Kang, K., Lee, J., "Advanced Hybrid Supercapacitor Based on a Mesoporous Niobium Pentoxide/Carbon as High-Performance Anode," *ACS Nano*, 2014, 8, 8968-8978.

184. Wang, X., Li, G., Chen, Z., Augustyn, V., Ma, X., Wang, G., Dunn, B., Lu, Y., "High-Performance Supercapacitors Based on Nanocomposites of Nb2O5 Nanocrystals and Carbon Nanotubes," *Adv. Energy Mater.*, 2011, 1, 1089-1093.

185. Wang, X., Yan, C., Yan, J., Sumboja, A., Lee, P. S., "Orthorhombic niobium oxide nanowires for next generation hybrid supercapacitor device," *Nano Energy*, 2015, 11, 765-772.

186. Kong, L., Zhang, C., Wang, J., Qiao, W., Ling, L., Long, D., "Nanoarchitectured Nb2O5 hollow, Nb2O5@carbon and NbO2@carbon Core-Shell Microspheres for Ultrahigh-Rate Intercalation Pseudocapacitors," *Scientific Reports*, 2016, 6, 21177.

187. Li, H., Zhu, Y., Dong, S., Shen, L., Chen, Z., Zhang, X., Yu, G., "Self-Assembled Nb2O5 Nanosheets for High Energy–High Power Sodium Ion Capacitors," *Chem. Mater.*, 2016, 28, 5753-5760.

188. Zhang, C., Kim, S. J., Ghidiu, M., Zhao, M.-Q., Barsoum, M. W., Nicolosi, V., Gogotsi, Y., "Layered Orthorhombic Nb2O5@Nb4C3Tx and TiO2@Ti3C2Tx Hierarchical Composites for High Performance Li-ion Batteries," *Adv. Funct. Mater.*, 2016, 26, 4143-4151.

189. Nowak, I., Ziolek, M., "Niobium Compounds: Preparation, Characterization, and Application in Heterogeneous Catalysis," *Chem. Rev. (Washington, DC, U. S.)*, 1999, 99, 3603-3624.

190. Jehng, J. M., Wachs, I. E., "Structural chemistry and Raman spectra of niobium oxides," *Chem. Mater.*, 1991, 3, 100-107.

191. Kumagai, N., Koishikawa, Y., Komaba, S., Koshiba, N., "Thermodynamics and Kinetics of Lithium Intercalation into Nb2 O 5 Electrodes for a 2 V Rechargeable Lithium Battery," *J. Electrochem. Soc.*, 1999, 146, 3203-3210.

192. Kodama, R., Terada, Y., Nakai, I., Komaba, S., Kumagai, N., "Electrochemical and In Situ XAFS-XRD Investigation of Nb2O5 for Rechargeable Lithium Batteries," *J. Electrochem. Soc.*, 2006, 153, A583-A588.

193. Lubimtsev, A. A., Kent, P. R. C., Sumpter, B. G., Ganesh, P., "Understanding the origin of high-rate intercalation pseudocapacitance in Nb2O5 crystals," *Journal of Materials Chemistry A*, 2013, 1, 14951-14956.

194. Griffith, K. J., Forse, A. C., Griffin, J. M., Grey, C. P., "High-Rate Intercalation without Nanostructuring in Metastable Nb2O5 Bronze Phases," *J. Am. Chem. Soc.*, 2016, 138, 8888-8899.

195. Nanda, J., Remillard, J., O'Neill, A., Bernardi, D., Ro, T., Nietering, K. E., Go, J.-Y., Miller, T. J., "Local State-of-Charge Mapping of Lithium-Ion Battery Electrodes," *Adv. Funct. Mater.*, 2011, 21, 3282-3290.

196. Jing, W., Gopi Krishna Phani, D., Chunwen, S., Murali, G. T., Danielle, A., Anthony, G. D., Arumugam, M., Graeme, H., John, B. G., Keith, J. S., "In situ Raman spectroscopy of LiFePO 4 : size and morphology dependence during charge and self-discharge," *Nanotechnology*, 2013, 24, 424009.

197. Dokko, K., Mohamedi, M., Anzue, N., Itoh, T., Uchida, I., "In situ Raman spectroscopic studies of LiNiMn2 - O4 thin film cathode materials for lithium ion secondary batteries," *J. Mater. Chem.*, 2002, 12, 3688-3693.

198. Kalbac, M., Farhat, H., Kong, J., Janda, P., Kavan, L., Dresselhaus, M. S., "Raman Spectroscopy and in Situ Raman Spectroelectrochemistry of Bilayer 12C/13C Graphene," *Nano Lett.*, 2011, 11, 1957-1963.

199. Huang, W., Frech, R., "In Situ Roman Studies of Graphite Surface Structures during Lithium Electrochemical Intercalation," *J. Electrochem. Soc.*, 1998, 145, 765-770.

200. Pollak, E., Geng, B., Jeon, K.-J., Lucas, I. T., Richardson, T. J., Wang, F., Kostecki, R., "The Interaction of Li+ with Single-Layer and Few-Layer Graphene," *Nano Lett.*, 2010, 10, 3386-3388.

201. Waring, J., Roth, R., Parker, H., "Temperature-pressure phase relationships in niobium pentoxide," *J. Res. Natl. Bur. Stand., Sect. A*, 1973, 77, 705-711.

202. Kato, K., Tamura, S., "Die Kristallstruktur von T-Nb2O5," *Acta Crystallographica Section B*, 1975, 31, 673-677.

203. Jehng, J.-M., Wachs, I. E., "The molecular structures and reactivity of supported niobium oxide catalysts," *Catal. Today*, 1990, 8, 37-55.

204. Jehng, J. M., Wachs, I. E., "Molecular structures of supported niobium oxide catalysts under in situ conditions," *J. Phys. Chem.*, 1991, 95, 7373-7379.

205. Waller, G. H., Lai, S. Y., Rainwater, B. H., Liu, M., "Hydrothermal synthesis of LiMn2O4 onto carbon fiber paper current collector for binder free lithium-ion battery positive electrodes," *J. Power Sources*, 2014, 251, 411-416.

206. Kresse, G., Furthmüller, J., "Efficient iterative schemes for ab initio total-energy calculations using a plane-wave basis set," *Phys. Rev. B: Condens. Matter Mater. Phys.*, 1996, 54, 11169-11186.

207. Kresse, G., Hafner, J., "Ab initio molecular dynamics for liquid metals," *Phys. Rev. B: Condens. Matter Mater. Phys.*, 1993, 47, 558-561.

208. Kresse, G., Hafner, J., "Ab initio molecular-dynamics simulation of the liquid-metal-amorphous-semiconductor transition in germanium," *Phys. Rev. B: Condens. Matter Mater. Phys.*, 1994, 49, 14251-14269.

209. Ceperley, D. M., Alder, B. J., "Ground State of the Electron Gas by a Stochastic Method," *Phys. Rev. Lett.*, 1980, 45, 566-569.

210. Perdew, J. P., Wang, Y., "Accurate and simple analytic representation of the electron-gas correlation energy," *Phys. Rev. B: Condens. Matter Mater. Phys.*, 1992, 45, 13244-13249.

211. Blöchl, P. E., "Projector augmented-wave method," *Phys. Rev. B: Condens. Matter Mater. Phys.*, 1994, 50, 17953-17979.

212. Kresse, G., Joubert, D., "From ultrasoft pseudopotentials to the projector augmented-wave method," *Phys. Rev. B: Condens. Matter Mater. Phys.*, 1999, 59, 1758-1775.

213. Monkhorst, H. J., Pack, J. D., "Special points for Brillouin-zone integrations," *Phys. Rev. B: Condens. Matter Mater. Phys.*, 1976, 13, 5188-5192.

214. Thangadurai, V., Narayanan, S., Pinzaru, D., "Garnet-type solid-state fast Li ion conductors for Li batteries: critical review," *Chem. Soc. Rev.*, 2014, 43, 4714-4727.

215. Wang, Y., Richards, W. D., Ong, S. P., Miara, L. J., Kim, J. C., Mo, Y., Ceder, G., "Design principles for solid-state lithium superionic conductors," *Nat. Mater.*, 2015, 14, 1026-1031.

216. Gonze, X., "First-principles responses of solids to atomic displacements and homogeneous electric fields: Implementation of a conjugate-gradient algorithm," *Phys. Rev. B: Condens. Matter Mater. Phys.*, 1997, 55, 10337-10354.

217. Kresse, G., Furthmüller, J., Hafner, J., "Ab initio Force Constant Approach to Phonon Dispersion Relations of Diamond and Graphite," *EPL (Europhysics Letters)*, 1995, 32, 729.

218. Togo, A., Tanaka, I., "First principles phonon calculations in materials science," *Scr. Mater.*, 2015, 108, 1-5.

219. Dahn, J. R., McKinnon, W. R., Haering, R. R., Buyers, W. J. L., Powell, B. M., "Structure determination of LixTiS2 by neutron diffraction," *Can. J. Phys.*, 1980, 58, 207-213.

220. Zhao, B., Ran, R., Liu, M., Shao, Z., "A comprehensive review of Li4Ti5O12-based electrodes for lithium-ion batteries: The latest advancements and future perspectives," *Materials Science and Engineering: R: Reports*, 2015, 98, 1-71.

221. Mosbah, A., Verbaere, A., Tournoux, M., "Phases LixMnO2λ rattachees au type spinelle," *Mater. Res. Bull.*, 1983, 18, 1375-1381.

222. Lin, Q., Li, Q. a., Gray, K. E., Mitchell, J. F., "Vapor Growth and Chemical Delithiation of Stoichiometric LiCoO2 Crystals," *Cryst. Growth Des.*, 2012, 12, 1232-1238.

223. Streltsov, V. A., Belokoneva, E. L., Tsirelson, V. G., Hansen, N. K., "Multipole analysis of the electron density in triphylite, LiFePO4, using X-ray diffraction data," *Acta Crystallographica Section B*, 1993, 49, 147-153.

224. Levi, M. D., Lukatskaya, M. R., Sigalov, S., Beidaghi, M., Shpigel, N., Daikhin, L., Aurbach, D., Barsoum, M. W., Gogotsi, Y., "Solving The Capacitive Paradox of 2D MXene using Electrochemical Quartz-Crystal Admittance and In Situ Electronic Conductance Measurements," *Adv. Energy Mater.*, 2015, 5, 11.

225. Ling, Z., Ren, C. E., Zhao, M.-Q., Yang, J., Giammarco, J. M., Qiu, J., Barsoum, M. W., Gogotsi, Y., "Flexible and conductive MXene films and nanocomposites with high capacitance," *Proc. Natl. Acad. Sci. U. S. A.*, 2014, 111, 16676-16681.

226. Lukatskaya, M. R., Mashtalir, O., Ren, C. E., Dall'Agnese, Y., Rozier, P., Taberna, P. L., Naguib, M., Simon, P., Barsoum, M. W., Gogotsi, Y., "Cation Intercalation and High Volumetric Capacitance of Two-Dimensional Titanium Carbide," *Science*, 2013, 341, 1502-1505.

227. Zhao, M.-Q., Ren, C. E., Ling, Z., Lukatskaya, M. R., Zhang, C., Van Aken, K. L., Barsoum, M. W., Gogotsi, Y., "Flexible MXene/Carbon Nanotube Composite Paper with High Volumetric Capacitance," *Adv. Mater. (Weinheim, Ger.)*, 2015, 27, 339-345.

228. Ramana, C. V., Zaghib, K., Julien, C. M., "Highly Oriented Growth of Pulsed-Laser Deposited LiNi0.8Co0.2O2 Films for Application in Microbatteries," *Chem. Mater.*, 2006, 18, 1397-1400.

229. Gao, S., Sun, Y., Lei, F., Liang, L., Liu, J., Bi, W., Pan, B., Xie, Y., "Ultrahigh Energy Density Realized by a Single-Layer β-Co(OH)2 All-Solid-State Asymmetric Supercapacitor," *Angewandte Chemie International Edition*, 2014, 53, 12789-12793.

230. Buschmann, H., Dolle, J., Berendts, S., Kuhn, A., Bottke, P., Wilkening, M., Heitjans, P., Senyshyn, A., Ehrenberg, H., Lotnyk, A., Duppel, V., Kienle, L., Janek, J., "Structure and dynamics of the fast lithium ion conductor "Li7La3Zr2O12"," *Phys. Chem. Chem. Phys.*, 2011, 13, 19378-19392.

231. Kuhn, A., Kohler, J., Lotsch, B. V., "Single-crystal X-ray structure analysis of the superionic conductor Li10GeP2S12," *Phys. Chem. Chem. Phys.*, 2013, 15, 11620-11622.

232. Kamaya, N., Homma, K., Yamakawa, Y., Hirayama, M., Kanno, R., Yonemura, M., Kamiyama, T., Kato, Y., Hama, S., Kawamoto, K., Mitsui, A., "A lithium superionic conductor," *Nat. Mater.*, 2011, 10, 682-686.

233. Ceder, G., "Opportunities and challenges for first-principles materials design and applications to Li battery materials," *MRS Bull.*, 2010, 35, 693-701.

234. Matousek, P., Towrie, M., Ma, C., Kwok, W. M., Phillips, D., Toner, W. T., Parker, A. W., "Fluorescence suppression in resonance Raman spectroscopy using a high-performance picosecond Kerr gate," *J. Raman Spectrosc.*, 2001, 32, 983-988.

235. Matousek, P., Towrie, M., Parker, A. W., "Fluorescence background suppression in Raman spectroscopy using combined Kerr gated and shifted excitation Raman difference techniques," *J. Raman Spectrosc.*, 2002, 33, 238-242.

236. Matousek, P., Towrie, M., Stanley, A., Parker, A. W., "Efficient rejection of fluorescence from Raman spectra using picosecond Kerr gating," *Appl. Spectrosc.*, 1999, 53, 1485-1489.

237. Cyvin, S. J., Rauch, J. E., Decius, J. C., "Theory of Hyper-Raman Effects (Nonlinear Inelastic Light Scattering): Selection Rules and Depolarization Ratios for the Second-Order Polarizability," *J. Chem. Phys.*, 1965, 43, 4083-&.

238. Kelley, A. M., "Hyper-Raman Scattering by Molecular Vibrations," *Annu. Rev. Phys. Chem.*, 2010, 61, 41-61.

239. Denisov, V. N., Mavrin, B. N., Podobedov, V. B., "Hyper-Raman scattering by vibrational excitations in crystals, glasses and liquids," *Physics Reports-Review Section of Physics Letters*, 1987, 151, 1-92.

240. Wu, Y., Wen, L. L., Zhu, Y. F., "Efficient hyper-Raman scattering in resonant coherent media," *Opt. Lett.*, 2003, 28, 631-633.

241. Butet, J., Martin, O. J. F., "Surface-Enhanced Hyper-Raman Scattering: A New Road to the Observation of Low Energy Molecular Vibrations," *J. Phys. Chem. C*, 2015, 119, 15547-15556.

242. Kneipp, J., Kneipp, H., Wittig, B., Kneipp, K., "One- and two-photon excited optical pH probing for cells using surface-enhanced Raman and hyper-Raman nanosensors," *Nano Lett.*, 2007, 7, 2819-2823.

243. Cheng, J. X., Volkmer, A., Xie, X. S., "Theoretical and experimental characterization of coherent anti-Stokes Raman scattering microscopy," *Journal of the Optical Society of America B-Optical Physics*, 2002, 19, 1363-1375.

244. Cheng, J. X., Xie, X. S., "Coherent anti-Stokes Raman scattering microscopy: Instrumentation, theory, and applications," *J. Phys. Chem. B*, 2004, 108, 827-840.

245. Zumbusch, A., Holtom, G. R., Xie, X. S., "Three-dimensional vibrational imaging by coherent anti-Stokes Raman scattering," *Phys. Rev. Lett.*, 1999, 82, 4142-4145.

246. Duncan, M. D., Reintjes, J., Manuccia, T. J., "Scanning Coherent anti-stokes Microscope," *Opt. Lett.*, 1982, 7, 350-352.

247. Evans, C. L., Potma, E. O., Puoris'haag, M., Cote, D., Lin, C. P., Xie, X. S., "Chemical imaging of tissue in vivo with video-rate coherent anti-Stokes Raman scattering microscopy," *Proc. Natl. Acad. Sci. U. S. A.*, 2005, 102, 16807-16812.